UNIVERSITÄT OSNABRÜCK

Insulator-Assisted Regular Arrays of Metal Centres via Metal-Organic Compounds

Dissertation

zur Erlangung des Doktorgrades
"Doctor rerum naturalium"

am Fachbereich Physik der Universität Osnabrück

vorgelegt von

Linda Laflör

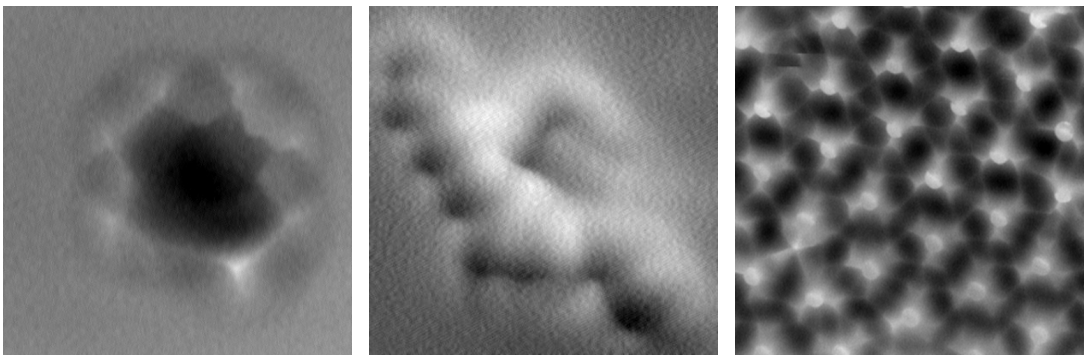

Osnabrück 2022

Contents

Abbreviations

Abbreviation	Explanation
AFM	Atomic Force Microscopy
AM	Amplitude Mode
Cp	Cyclopentadienyl
DAS	Dimer-Adatom-Stacking fault
DFG	German Research Foundation
DFT	Density-functional theory
DNA	Deoxyribonucleic acid
EFM3T	Electron Beam Evaporator, Focus
fcc	face-centered cubic
FDCA	Ferrocene Dicarboxylic Acid
FM	Frequency Mode
geo 1	naming of staggered FDCA conformer
geo 2	naming of eclipsed FDCA conformer
GGA	Generalised Gradient Approximation
GTH	Goedecker-Teter-Huttler
hcp	hexagonal close-packed
HON	Honeycomb
HOMO	Highest Occupied Molecular Orbital
HSAB	Hard Soft Acid Base
IUPAC	International Union of Pure and Applied Chemistry
LT	Low Temperature
LUMO	Lowest Unoccupied Molecular Orbital
ML	Monolayer
NC-AFM	Non-contact Atomic Force Microscopy
NTCDI	Naphthalenetetracarboxylic diimide
PBE	Perdew-Burke-Ernzerhof
PI	Proportional Integral
PPIX	Protoporphyrin IX
PPM	Probe Particle Model
PTCDA	Perylenetetracarboxylic dianhydride
PTCDI	Perylenetetracarboxylic acid diimide

Abbreviation	Explanation
QCM	Quartz Crystal Microbalance
REA	Research Executive Agency
RHK VT - 750	Variable Temperature AFM from RHK
RT	Room Temperature
SMON	Surface Metal-Organic Network
SPM	Scanning Probe Microscopy
STM	Scanning Tunnelling Microscopy
SubPc	chloro[subphthalocyaninato]boron(III)
TCNB	1,2,4,5-tetracyanobenzene
TMA	Trimesic acid
UC110	Unit Cell 110
UC75-1	Unit Cell 75 - 1 Molecule
UC75-3	Unit Cell 75 - 3 Molecules
UC75-4	Unit Cell 75 - 4 Molecules
UC-Fe	Unit Cell with Iron
UHV	Ultrahigh Vacuum
XPS	X-Ray Photoelectron Spectroscopy
3D	three dimensional

1 Introduction

The term "nanotechnology" is used to describe those disciplines that exploit the properties of matter at the atomic and molecular scale are exploited and where tools are employed to manipulate nano scaled building blocks such as molecules. The nano scaled regime covers a wide span from about 0.1 nm to several hundred nanometers. Nanotechnology includes the fields of nanoelectronics, nanobiotechnology, or nanomedicine. Nanotechnology is an important driver for developments in information storage, cosmetics, and pharmaceuticals [1, 2, 3].

The concept of nanotechnology has first been envisioned by Richard P. Feynman in his famous speech "*There is plenty of room at the bottom*" in 1959 [4]. Therein, Feynman elucidated the possibilities emerging if one is able to control tiny building blocks, or even atoms. Additionally, he envisioned strategies towards miniaturisation and stated technical requirements for the characterisation of nano devices.

Today, two opposite strategies are pursued towards the manufacturing of nano materials, namely the top-down and the bottom-up approach. The top-down approach starts with macroscopic specimen and relies on the carving of smaller sized components. Typical procedures are lithography techniques, in particular light and electron lithography [5, 6]. Optical lithography methods are the established standard for construction of nano scaled materials such as computer chips [2].

In contrast, the bottom-up approach starts with single atoms and molecules to build nano scaled devices. This approach has been followed in both liquid phase and on surfaces [7]. The liquid phase approach has, for example, been used for the synthesis of graphene nano ribbons [7]. Typical surface-assisted bottom-up procedures are self-assembly [8], and on-surface synthesis [9], as well as the manipulation of single building blocks into larger arrangements [2]; yet, this serial procedure is rather time-consuming in comparison to the parallel approaches of self-assembly or synthesis.

An important aspect in the field of nanotechnology is the characterisation of nano structures. Because optical microscopy is restricted by the Abbe limit, access to the "nano world" has been hindered for a long time until specific techniques were developed that allow the investigation of single atoms [1]. Among these techniques, scanning probe microscopy

is now established as arguably the most important tool in nano science for real space imaging and manipulation of atoms and molecules. Two central variants of scanning probe microscopy are scanning tunnelling microscopy (STM) and atomic force microscopy (AFM). For both techniques, an atomically sharp tip rasters a surface. Either the current flowing (STM) or the force acting (AFM) between tip and sample is used as the main measurement observable. Both variants can achieve resolution in the picometer range, thus enabling imaging of single atoms and submolecular structures in real space [10].

A prerequisite for the fabrication of nano scaled devices via the surface-assisted bottom-up approach is the availability of small building blocks on surfaces. These can be atoms, single molecules, as well as clusters of atoms or molecules. For the on-surface availability it is important that these building blocks adsorb on the surface. For the benefit of a confined two dimensional system and the possibility of investigations using scanning probe microscopy, the adsorption of single molecules and two dimensional molecular assemblies are preferred. These assemblies are observed for the Frank-van-der-Merwe growth mode, which commonly occurs on surfaces with a high surface energy [11, 12]. This is typically the case for metal surfaces. However, molecular adsorbates on metal surfaces can (electronically) couple with the underlying surface, which can result in a loss of functionality. To fully exploit the functionalities of nano scaled devices, such as harvesting electrical functionality for nanoelectronic applications, decoupling from the surface is required [13]. Decoupling can be obtained by using insulator surfaces.

In comparison to metal surfaces, insulator surfaces have significantly lower surface energies. The molecule-molecule interaction is often stronger than the molecule-surface interaction on surfaces having a low surface energy. This relation results in the formation of three dimensional accumulations of the molecular adsorbates, which is often referred to as dewetting [14]. Nevertheless, firm adsorption of molecules on insulating surfaces has been established via anchoring in the past years. Anchoring describes the specific attraction of molecular functional groups to specific surface sites. Anchoring aids the growth of wetting molecular films on insulating surfaces [14]. The functional groups acting as anchor groups are typically polar. Examples of such anchor groups are carboxylic acid groups [15, 16], nitriles [17], or halogenides [18]. The majority molecules that have been reported to anchor to insulating surfaces are organic molecules.

Metal-organic compounds express unique properties, including magnetism [19], chargeability [20], optoelectronic properties [21], and tunable reactivity [22]. For future exploitation of the listed properties, the formation metal-organic compounds is desired on insulating surfaces. So far, first examples of metal-organic compounds have been studied on insulating surfaces [20, 23, 24, 25].

A key to successfully utilise the properties of metal-organic compounds is to establish tar-

geted strategies to obtain metal-organic assemblies on insulating surfaces. Three different strategies towards on-surface metal-organic assemblies have successfully been pursued, however, mostly on conducting surfaces.

First, pre-synthesised metal-organic molecules have been deposited onto surfaces, where they adsorb and can form assembled structures [20, 26, 27]. The pre-synthesised metal-organic molecules contain an intramolecular coordinate bond.

Second, on-surface synthesis has been successfully used to form intramolecular coordinate bonds, whereby metal-organic molecules are formed [28].

Third, metal-organic networks have been constructed via self-assembly, where organic molecules form networks via intermolecular coordinate bonds [22].

All three approaches have been successfully realised on metal surfaces. In the following, a representative example is given for each approach on a metal sample:

For the deposition and assembly approach, the metal-organic molecule 1,1'-ferrocene dicarboxylic acid was deposited to the Ag(111) surface. The formation of an assembly has been observed [27].

An on-surface reaction has been the metallation of porphyrin molecules. A porphyrin molecule like tetraphenylporphyrin reacts with a single metal atom, such as cobalt, via coordinate bond formation between the four pyrole rings of the porphyrin and the metal centre under elimination of molecular hydrogen [29, 30].

A metal-organic network has been formed using terephtalate acid as organic molecule and the metal centre, iron, on Cu(100) surfaces. The combination of terephtalate acid and iron have resulted in a square planar coordination geometry, which ultimately lead to a network with a rectangular structure [31].

First metal-organic compounds have been deposited on insulating surfaces, via the deposition and assembly approach. Typical examples are petroporphyrin molecules metallated with vanadium oxide [24] and magnesium-phthalocyanine [25] on NaCl thin films, where single molecules are observed on the surface. Another example is ferrocene dicarboxylic acid on calcite (104), where assemblies of the molecule have been observed [20].

To the best of my knowledge, on-surface synthesis of a metal-organic molecule via metallation of a porphyrin molecule has not been established on an insulating surface.

The formation of a metal-organic network on insulating surfaces has, to the best of my knowledge, been established for only one example. A network has been formed between biphenyl-4,4'-dicarboxylic acid molecules and iron on calcite(104) [23]. The formation of the networks has been found to be strongly dependent on the deposition order, and the networks match with the underlying lattice periodicity of the calcite(104) surface [23].

In this work, the three different approaches are investigated towards metal-organic compounds on both metal and insulating surfaces with the ultimate aim of the fabrication of

regular metal arrays: (1) the deposition and assembly of pre-synthesised metal-organic molecules, (2) the on-surface synthesis of individual metal-organic molecules, and (3) the on-surface formation of metal organic networks via coordinate bonds.

For the first approach, 1,1'-ferrocene dicarboxylic acid is investigated on CaF_2 bulk and thin film surfaces. Towards the second approach, the metallisation of protoporphyrin IX and copper is studied on Ag(111) and CaF_2 surfaces. The third approach towards the formation of a metal-organic network is pursued using trimesic acid and iron.

In this thesis an experimental approach is followed based on STM and non-contact atomic force microscopy (NC-AFM) to investigate metal-organic compounds on metal and insulator surfaces. A focus is set on high-resolution NC-AFM with CO functionalised tips towards determining the presence of coordinate bonds.

This thesis is organised as follows:

The chemical fundamentals of relevant metal-organic and on-surface chemistry, as well as molecules on surfaces are presented in chapter 2. More precisely, porphyrin metallisation as the prototypical example for on-surface metal-organic synthesis is described in section 2.2, molecular adsorption on (insulating) surfaces is presented in section 2.3, and the formation of on-surface metal-organic networks is discussed in section 2.4.

Chapter 3 introduces the experimental methods used in this thesis, STM and NC-AFM. The fundamentals of both techniques are described. Details on the experimental set up utilised in this work are given in section 3.2.

Chapter 4 gives a brief description of the sample systems and the experimental preparations used throughout this work. The chapter is split into a section focussing on surface properties and preparation (section 4.1), a section on molecule deposition (section 4.2.1), and a section on metal deposition (section 4.2.2).

The experimental results, analysis and discussion are presented in chapters 5 to 8, whereby steps towards the three approaches (deposition and assembly, synthesis, and network formation) are followed.

Chapter 5 discusses the $CaF_2/CaF_1/Si(111)$ thin film surface as well as copper on the $CaF_2/CaF_1/Si(111)$ thin film. As copper is used as an educt in the approach of metal-organic synthesis, an investigation of the mobility of copper on CaF_2 thin films is addressed in section 5.2. It is shown that the number of metal clusters is reduced and larger clusters are formed upon tip induced displacement (section 5.3.1). A reduction in cluster density and an increase in cluster size is also observed upon stepwise heating the sample system to 573 K (section 5.3.2). This behaviour indicates a low barrier for lateral surface mobility.

In chapter 6, the influence of flexible side groups on NC-AFM and STM imaging of molecules is investigated towards the approach of on-surface synthesis. NC-AFM and STM measurements are conducted after depositing protoporphyrin IX (PPIX), a porphyrin

derivate with multiple flexible side groups, on an Ag(111) surface. Three different shapes at position of PPIX molecules are observed repeatedly in STM and NC-AFM images, and different molecular conformers are proposed as cause of these different shapes (section 6.2). The addition of copper to PPIX on Ag(111) results in the formation of clusters, which indicates a change of either intermolecular or molecule-surface interaction (section 6.3). As an outlook, PPIX is deposited onto CaF_2 surfaces (section 6.5).

Chapter 7 discusses the approach of pre-synthesised molecule deposition and assembly on the example of 1,1'-ferrocene dicarboxylic acid (FDCA) on CaF_2 bulk and thin film surfaces. A focus is set on the anchoring of the metal-organic molecule via carboxylic acid moieties to CaF_2 surfaces. With the support from density functional theory (DFT) calculations it is determined that FDCA forms a quadruped anchoring motif to the underlying CaF_2 surface (section 7.1). One of the key findings is that no difference in molecular adsorption is observed for bulk and thin film surfaces. FDCA shows a distinct dumbbell shape in experimental NC-AFM data, which is in excellent agreement with NC-AFM image calculations. The contrast results from repulsive interaction between NC-AFM tip and the topmost hydrogen atoms (section 7.2).

Last, the assembly of trimesic acid (TMA) and iron is investigated towards the approach of metal-organic network formation in chapter 8. In section 8.2.2, iron deposition and heating of iron on the Au(111) surface is investigated. The formation of iron islands confirms the Volmer-Weber growth of iron on Au(111) surfaces [32, 33, 34]. Heating experiments of up to 383 K result in the formation of an iron-gold near-surface alloy, indicating that an alloy formation indeed occurs upon small heating temperatures [35] in section 8.2.2.1. Next, in section 8.3, the formation of hydrogen-bonded trimesic acid networks is investigated. A focus is set on NC-AFM imaging and on mapping the axial force of the hydrogen-bonded intermolecular area. Based on the axial force maps, the influence of electrostatic interaction between the negatively charged cloud in front of the CO tip and the molecule is revealed. In section 8.4, TMA networks are investigated, upon heating the TMA on Au(111) sample system. Furthermore, section 8.4 addresses the influence of iron contaminations in the Au(111) surface on the trimesic acid network structure, showing the formation of novel molecular assemblies. Finally, the co-deposition of TMA and iron is investigated in section 8.5. The influence of deposition order and temperature on the network formation is discussed in chapter 8.5.1. A long-range ordered structure is reoccurringly observed throughout all probed deposition parameters. A rectangular unit cell is determined for the TMA-Fe network. To determine the bonding situation within the unit cell, in section 8.5.2 an analysis of oxygen-oxygen distance is performed based on high-resolution constant-height NC-AFM images. The data gives strong evidence for a non-planar coordination geometry and the formation of a regular array of TMA and iron.

This work advances the three different approaches towards the on-surface fabrication of metal-organic compounds on insulating samples. In particular, a metal-organic network is formed by TMA and iron on Au(111) surfaces. The network has a three dimensional coordination geometry with a subjacent metal atom, forming a regular array of iron. Furthermore, small clusters of metal-organic molecules (FDCA) are established on insulating surfaces, where a firm anchoring mechanism of a metal-organic molecule is determined. These results push the field of metal-organic compounds on insulating surfaces and pave the way for future exploitation of the properties of metal-organic compounds on insulating surfaces.

2 Metal-Organic Compounds on Surfaces

Molecules typically are categorised as organic or inorganic [36]. Organic molecules are generally defined as molecules which contain carbon and hydrogen atoms [36]. The term inorganic molecule summarises essentially the remaining molecules, especially molecules containing metals, and molecules which do not contain carbon and hydrogen atoms. However, not every molecule can be strictly categorised into one of the two categories. Many compounds contain carbon and hydrogen atoms and could thus be labelled organic, yet, these compounds contain metal atoms and show properties and reaction behaviour of inorganic chemicals. An example of such molecules are organometallic molecules. Organometallic molecules are complexes of organic ligands and at least one metal centre, where at least one bond is formed between a carbon and the metal centre [37]. However, a variety of complexes exist, where an organic ligand coordinates to a metal centre from other elements than the carbon. For these compounds, the term "metal-organic" compounds is commonly utilised, especially in the community of metal-organic framework, three dimensional crystalline metal-organic compounds, but the term is also often read in context of surface science [22, 37]. Therefore, in this work the category "metal-organic" is defined as follows:

A **metal-organic compound** consists of at least one metal atom as well as at least one, usually functionalised, organic ligand. In metal-organic compounds, the bond between metal and ligand stems either from an atom of the functional group or a carbon atom of the ligand [22, 37]. Hence, the category metal-organic also comprises organometallic compounds.

The aim of this work is to fabricate ordered arrays of metal-organic compounds on surfaces, especially on insulator surfaces. Towards this aim, three approaches will be followed: the on-surface synthesis of a metal-organic molecule, adsorption and assembly of pre synthesised metal-organic molecules, and the formation of a metal-organic network. In this chapter, the chemical fundamentals of metal-organic chemistry will be briefly explained first (section 2.1). Next, the fundamentals and examples found in literature will be given

for each strategy. In section 2.2, the strategy of on-surface synthesis will be elucidated vy discussing literature examples of on-surface metallisation of porphyrin molecules. Next, basics of molecular adsorption on metal and insulator surfaces will be given in section 2.3. Following, in section 2.4, fundamentals of the formation of regular arrays on surfaces will be discussed with a focus set on the formation of surface metal-organic networks.

2.1 Chemical Fundamentals

Coordination compounds were first characterised by Alfred Werner, describing the octaedric geometry of cobalt complexes CoL_6 (L=ligand) and introducing the modern comprehension of metal-ligand bonding in the late nineteenth century. Nowadays, the chemical basics of metal-ligand bonding and complex chemistry are text book knowledge. The following has been compiled from different textbooks: *"Riedel Moderne Anorganische Chemie"* by Christoph Janiak et al., *"Lehrbuch der Anorganischen Chemie"* by Arnold F. Hollemann and Nils Wiberg and *"Chemie: Das Basiswissen der Chemie"* by Charles E. Mortimer [36, 37, 38].

A **complex** is formed by a central metal atom (M) and several ligands (L). The metal-ligand bond can be either of covalent or coordinate type. In a covalent bond, both bonding partners (in case of a complex M and L) equally contribute an electron to the bond as depicted in figure 2.1a. In a coordinate bond, both electrons in the bond stem from only one bonding partner. The lone pair of the electron donating partner overlaps with an empty orbital of the electron accepting bonding partner. This type of bond between ligand and metal is known as the **coordinate bond**, in literature, this bond is also often referred to as coordinate covalent bond, dative bond, or simply as coordination. In comparison with classic covalent bonds, coordinate bonds are more polar, longer, yet also weaker.
Similar to covalent bonds, coordinate bonds can be divided into σ and π bonds, which are distinguished by the involved orbitals. The orbitals of the σ bond are rotationally symmetric to the metal-ligand bond axis, while a node is present in the plane of the metal-ligand bond for a π bond. This is illustrated in figure 2.1b, where the orbitals involved in a σ bond are highlighted in pastel green, and the orbitals in a π bond are coloured in light and dark blue. The ligand is always the σ donor. The ligand has at least one lone pair making electrons available towards the bond. Some ligands have more than one lone pair of electrons for donating more than one bond, allowing these ligands to act as π donor. Ligands with an empty orbital can act as π acceptor, which accept the electron of the metal. In organometallic complexes, the ligand often acts as σ bond donor and π bond acceptor, as depicted in figure 2.1. For the π back bond, the ligand has an empty orbital and the

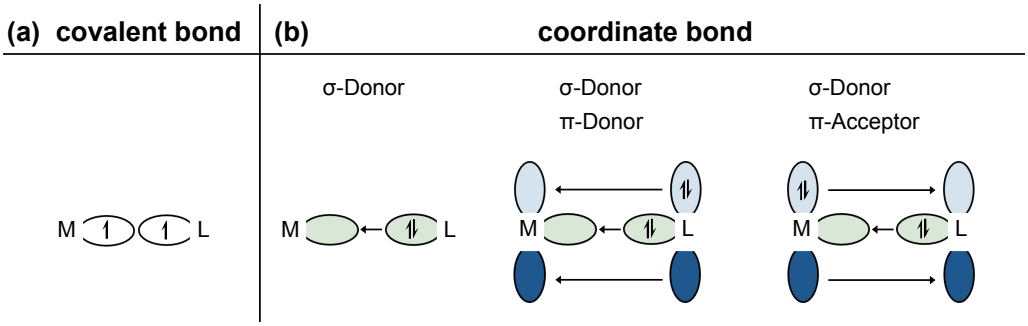

Figure 2.1: Electron distribution in (a) covalent and (b) coordinate bonds. σ and π bond donor and acceptors are distinguished. Adapted from [37].

metal is in an oxidation state between -I and +I.

Oxidation state is a conceptual comprehension of assigning electrons to atoms with the stronger electronegativity within a molecule. Oxidation state of elements amounts to zero, of ionic atoms the oxidation state equals the charge.

The variety of complexes cannot solely be traced back to different types of bonds and oxidation state, but strongly depends on an interplay of factors such as the number of ligands, the ligands geometry, and the electron distribution within the metal centre. The number of donor atoms of a ligand coordinating to the metal centre varies in complexes, this is described by the **coordination number**. Compounds with coordination numbers between two and twelve are known, but the most common compounds represent coordination compounds of 2, 4, or 6. The coordination number can either be equal or larger than the number of ligands, as ligands can form one or multiple coordinate bonds to the central metal atom. The number of coordinate bonds formed by a ligand is described by the **denticity**, a ligand forming one coordinate bond is called monodentate, while a ligand forming two coordinate bonds is called bidentate. Ligands with more coordinate bonds are referred to as polydentate ligands. These often act as chelate ligands, where one ligand forms multiple bonds to one metal centre. Additionally, polydentate ligands can connect multiple metal cores, the ligands are then referred to as bridging ligands or linkers. Furthermore, for ligands with multiple neighbouring atoms coordinating to one metal centre, the term **hapticity** describes the number of atoms coordinating to the metal. Hapticity is often used in context of aromatic hydrocarbons, like pentadienyl or benzene, where a different number of carbons can be involved in the coordination.

Coordination complexes can have a variety of **coordination geometries**, which on the one hand depend on the coordination number, on the other hand depend on the number of electrons filling the d-orbitals of the metal centre. Here, the different coordination geometries are classified into one, two and three dimensional geometries. There is a large number of three dimensional coordination complexes, a few of the most common coordination ge-

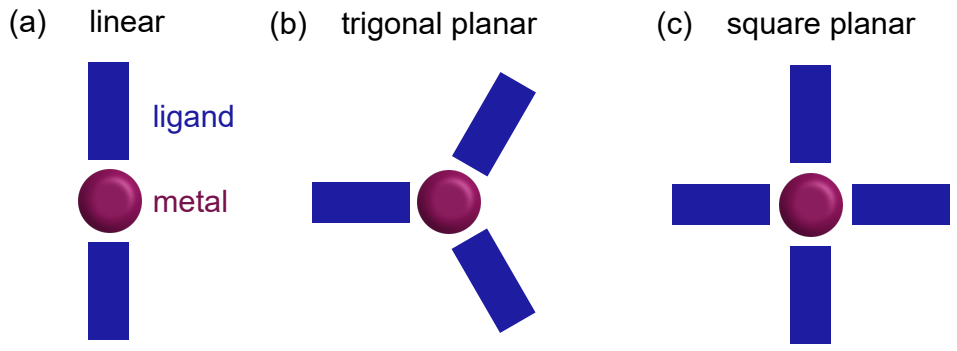

Figure 2.2: Schematic of one and two dimensional coordination geometries. (a) linear, (b) trigonal planar, (c) square planar. The metal centre is represented in a purple colour, the ligands are shown in blue.

ometries are octahedral (coordination number: 8), square pyramidal (coordination number: 5), and tetrahedral (coordination number: 4). Fewer examples exist for two dimensional coordination complexes. The most common ones are square planar (coordination number: 4), and trigonal planar (coordination number: 3). The only one dimensional coordination geometry is the linear geometry (coordination number: 2). Schematics of the one and two dimensional coordination geometries are given in figure 2.2.

Taking a closer look at complexes with a coordination number 4, two different coordination geometries occur: Tetrahedral and square planar geometry. The tetrahedral geometry is a three dimensional geometry, while the square planar geometry is two dimensional. Whether a complex shows a tetrahedral or a square planar geometry is strongly dependent on the electron distribution in the d-orbitals of the metal centre. Thus, a tetrahedral geometry is adapted for d-orbitals of the metal centre filled with 0, 5 (high-spin), and 10 electrons, while a square planar geometry is often observed for d-orbitals filled with 8 or 9 electrons. To understand this effect, a deeper understanding of the d-orbitals, crystal field theory, and electron distribution is required.

Transition metals contain electrons in the s, p, and d orbitals. The d orbitals are usually filled partially, a characteristic which renders them suitable for a stable bond formation. The five atomic d orbitals are denoted as d_{xy}, d_{xz}, d_{yz}, d_{z^2}, and $d_{x^2-y^2}$. In an isolated metal, the orbitals' energies are degenerate. In contrast, the d orbitals split in their energy, when the metal is coordinated to ligands forming a coordination complex. This splitting can be described by the crystal field theory, which is a rather coarse model, which describes ligands by negative point charges. The negative point charges interact with the electron filled d orbitals via electrostatic interaction. This interaction causes an energetic splitting of the orbitals into different energy levels, which is illustrated in figure 2.3. The splitting depends on the adapted complex geometry. In this section, orbital splitting will be described

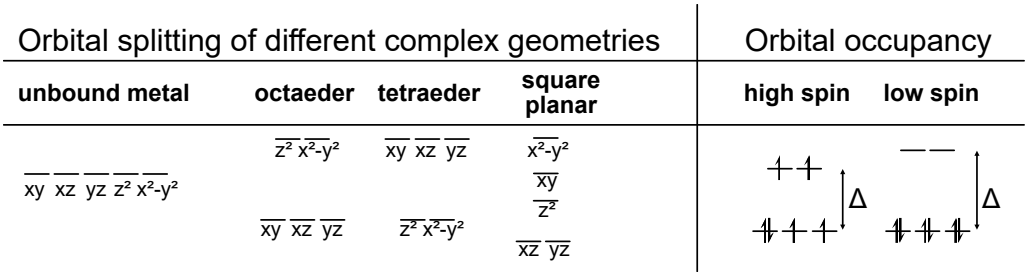

Figure 2.3: Orbital splitting for some of the most common complex geometries: octaeder, tetraeder, and square planar after ligand field splitting theory. Furthermore, the electron distribution in high and low spin complexes is illustrated.

using the widely known examples of an octahedral and tetrahedral coordination geometries, as well as the two dimensional example of a square planar geometry (see figure 2.3). The *d* orbitals split into two sets of orbitals in an octahedral complex: d_{z^2}, and $d_{x^2-y^2}$ are destabilized by bonding ligands and therefore have a higher energy, while d_{xy}, d_{xz}, and d_{yz} are stabilised by the ligand field and therefore have a lower energy. The reason for the (de)stabilisation of the orbitals originates from the geometry of the the negative point charges with the *d* orbitals. The interaction between the negative point charges and the d_{xy}, d_{xz}, and d_{yz} orbitals is energetically more stable than the interaction between the point charges and the spherical d_{z^2}, and $d_{x^2-y^2}$ orbitals.

For a tetrahedral geometry, the orbitals are also split. Due to the coordination geometry the d_{xy}, d_{xz}, and d_{yz} orbitals are closer to the negative point charges and therefore, energetically destabilised. For the square planar geometry, the orbital energies split into four energy levels. The most stable states are formed by the degenerate orbitals d_{xz}, and d_{yz}. Energetically next favourable is d_{z^2}, followed by d_{xy}. The most destabilised orbital is the $d_{x^2-y^2}$ orbital. The energy difference between the two levels of degenerate orbitals in octahedral and tetrahedral coordination geometries is often referred to as Δ. While the exact value of Δ depends on the individual ligands, it can be generally stated that a higher Δ indicates a stronger metal-ligand bond. The *d* orbitals are (partially) filled with electrons, and for four to seven electrons, high and low spin complexes can exist. The concept of **high and low spin** complexes describes the way electrons are distributed in the split *d* orbitals. A maximum of two electrons can occupy each orbital, hereto the electrons require a different spin. For the spin pairing one electron has to flip from up to down spin, which requires a certain amount of energy, the spin pairing energy. When the electrons are distributed in the *d* orbitals of a metal in a complex, the lower degenerate orbitals are filled with one electron each. For the residual electrons two possible electron distributions exist: First, if Δ is smaller than the spin pairing energy, the electrons fill the higher degenerate orbitals with up spin electrons before residual electrons are spin paired in the energetically lower orbitals.

This distribution of electrons is known as high spin. Second, for a low spin complex, Δ is larger than the spin pairing energy. In this case, the electrons are flipped to down spin, filling the lower degenerate orbitals. In figure 2.3, an example is given for a complex with six electrons. In the high spin complex, two electrons are located at the higher degenerate orbitals, while the low spin complex has all six electrons paired in the lower degenerate orbitals.

The **Lewis acid base concept**, named after the chemist Gilbert N. Lewis, extends the classic conception of acids and bases by Brønsted; Brønsted acids and bases depend on the presence of protons. Instead, the Lewis acid base concept classifies compounds into acids and bases depending on the presence of lone pairs of electrons. Reactions between Lewis acids and bases result in coordinate bond formation. A Lewis base has a lone pair of electrons, it is therefore acting as electron donor, and has a nucleophilic nature. A Lewis acid has an empty orbital. A Lewis acid acts as electron acceptor and has a electrophilic nature. Within complex chemistry, metals are usually classified as Lewis acids, while ligands are usually classified as Lewis bases. Based on the hard soft acid base (HSAB) concept lewis acids and bases are further categorised into hard and soft compounds. Using the HSAB concept allows a rough prediction of the stability of a complex. The most stable compounds are formed between acid and base pairs of a similar hardness. The bonding between hard compounds is more ionic, while the bonding between soft compounds is more of a covalent nature. The categorisation of a compound as hard or soft depends on the atomic or ionic radius, the oxidation state of the compound and on its the polarisability. A hard compound has a small radius, a high oxidation state, and a low polarisability. The opposite properties are required to classify compounds as soft. While most compounds can be easily classified as hard or soft, few compounds are known to not completely fit the concept.

Summarising, a metal-organic compound is defined as a complex, in which a coordinate bond is formed between an organic ligand and a metal centre. Complexes show different coordination geometries, depending on coordination number and electronic structure of the metal. The coordination geometries can be categorised as one, two and three dimensional.

2.2 On-Surface Synthesis of Metal-Organic Molecules

One of the strategies towards metal-organic molecules on surfaces is the on-surface synthesis with organic molecules and metals as educts. A versatile group of organic educts, which can undergo on-surface synthesis, are porpyhrin molecules. Porphyrin molecules can react with a large variety of metals forming metal-organic molecules. Furthermore, different functional groups can be added to the prophyrin core to create desired molecular properties. Functionalised porphyrins can be found in biochemical context, especially as chlorophyll or haem [24]. Both, chlorophyll and haem are metallated, chlorophyll contains a magnesium centre, while haem is metallated with iron.
In solution, porphyrin forms complexes with all transition metals, alkali metals, most alkaline earth metals, post transition metals, selected metalloids, as well as lanthanoides and actinoides [29, 39]. However, on-surfaces the reaction has so far been accomplished with a smaller variety of metals. These metals, either surface metal adatoms or co-deposited metal atoms, include Ag, Au, Ce, Co, Cu, Fe, Mn, Ni, Rh, Ru, or Zn. [29, 30, 40, 41, 42, 43, 44, 45, 46]. On-surface metalation has been realised with a number of hydrogenated porphyrin derivates on metal surfaces including Ag(111), Au(111), Cu(111), Cu(110), Cu(100), Fe(110) or Ni(111) [30, 40, 47, 45, 48].
As depicted in figure 2.4a, the porphyrin molecule is a cyclic, aromatic molecule, consisting of four pyrole rings connected via methine groups. Two of the four pyrole rings are hydrogenated. Porphyrins can be functionalised in both meso and beta positions. In sum, substitutions at twelve positions are possible. For a metallated porphyrin, the four nitrogen atoms coordinate to a central metal atom forming a square planar coordination geometry (see figure 2.4 d). So far, the metallisation on surfaces of porphyrin molecules

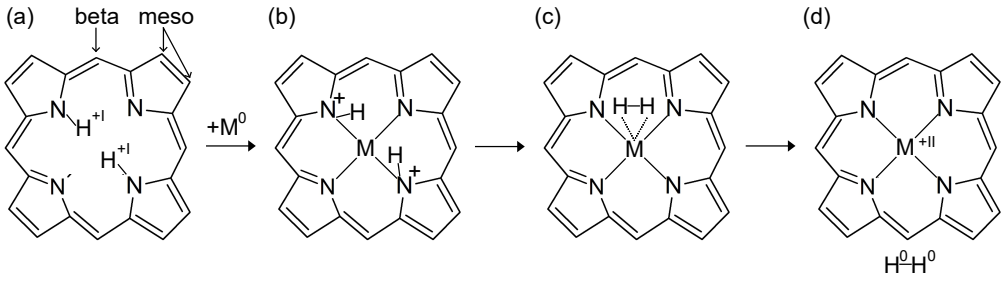

Figure 2.4: On-surface reaction pathway of porphyrin with a metal M.

follows the same reaction path regardless of metal centre or porphyrin derivate [30]: A simplified reaction pathway is depicted in figure 2.4. Prior the reaction (a), the metal has an oxidation state of zero, both hydrogen atoms are bound to the nitrogen atoms of the porphyrin molecule and have an oxidation state of +I. As first reaction step (b), the metal coordinates to the four nitrogen atoms, while the hydrogen bonds are still bound to the

nitrogen atoms, resulting in a positive charge at the nitrogen atoms. In the next steps, the hydrogen atoms form coordinate bonds to the metal centre. A covalent bond now connects the two hydrogen atoms, after the covalent bond between nitrogen and hydrogen is cleaved. This results in the intermediate shown in figure 2.4c. In the final reaction step (d), the coordinate bond between hydrogen and the metal centre is cleaved and the hydrogen is eliminated as molecular hydrogen. The products of this reaction are a metalated porphyrin, containing a metal with oxidation state +II, and molecular hydrogen with an oxidation state of zero. This process is a redox reaction, whereby the hydrogen is reduced from oxidation state +I to 0 and the oxidation state of the metal is increased from 0 to +II.
A requirement for a metal centre undergoing metallisation of a porphyrin is the ability of the metal centre to adopt an oxidation state of +II. When other ligands coordinate to the metal centre, higher oxidation states are also feasible for the metal centre [29]. The activation energy of the metallisation strongly depends on the metal centre and increases with the atomic number of the metal centre [29].
The on-surface reaction has been monitored with STM and also XPS experiments. With STM experiments differences in the imaged features at the molecule positions have been observed for specific porphyrin derivates. For these derivates the metalated form of the molecule appears brighter than the unmetalated molecule in STM topography. The metalated molecule shows a bright protrusion at its centre, while the unmetalated molecule usually exhibits a dark centre [29]. One prototypical example is the metallisation of tetraphenylporphyrin: The porphyrin centre of the educt is imaged as a dark depression in the STM image. After the metallisation with iron, the molecules centre is imaged as a bright protrusion [49]. This allows to differentiate single reacted molecules from unreacted molecules. However, for some porphyrin-substrate combinations the unreacted educt and the metalated product show a similar feature within the STM image [42, 47]. Therefore, STM data is not always suitable to monitor the reaction. For the case that STM is not suitable, the combination of STM with XPS experiments has been used to successfully determine if a reaction has occurred. With XPS, a shift of the energy is observed between the educt and product data for photoelectrons emitted from the nitrogen 1s orbital as well as of the metal centre 2p orbital [42, 47].
So far, the on-surface reaction path is well understood, and the reaction has been successfully monitored by STM and XPS experiments. To this day, porphyrin metallisation, to the best of my knowledge, has only been realised on metal surfaces.

2.3 Molecular Adsorption on Surfaces

To study molecules on surfaces with scanning probe microscopy, a stable adsorption is desired. When reactions or molecular assembly is investigated, molecules should not desorb from the surface at room temperature or during heating experiments. Furthermore, the growth of ordered molecular monolayers is desired. This is achieved by an interplay of molecule-substrate interactions, as well as intermolecular interactions [11]. First, general concepts of growth and molecule-substrate interaction are elucidated. Second, the molecule-molecule interaction is described and different order inducing mechanisms. Third, the peculiarities of molecular structure formation on insulating surfaces is discussed. A focus is set on anchoring molecules to an insulating surface.

The growth mode of molecular layers (the adsorbates) on a surface can be predicted based on the simplified approach using the surface energies, a macroscopic material quantity, of the bulk crystal of the adsorbate (γ_A), and the substrate (γ_S), and additionally the energy of the interface layer. (γ_I) [11, 12]. For the thermodynamic equilibrium, three different growth modes are described:

A layer-by-layer growth, also known as Frank-van-der-Merwe growth, is observed, when the sum of the interface energy and the surface energy of the adsorbate are smaller than the surface energy ($\gamma_A + \gamma_I < \gamma_S$). Frank-van-der-Merwe growth is characterized that one layer is completely formed before the next layer starts to form [11, 12]. This is also described as wetting behaviour of the adsorbate.

When the sum of the surface energy of the adsorbate and the interface energy is larger than the substrate energy ($\gamma_A + \gamma_I > \gamma_S$), dewetting occurs. Dewetting describes the process of multilayer islands formation before a full monolayer has formed. This growth mode is known as Volmer-Weber growth [11, 12].

Stranski-Krastanov growth describes the formation of a layer of the adsorbate followed by island growth [11, 12].

A second model to characterise molecule adsorption is the distinction between physisorption and chemisorption.

Physisorption condenses the interactions between adsorbate and surface, where only minor perturbances of the electronic state of adsorbate and surface occurs. Physisorption is often caused by van-der-Waals interaction, especially by London dispersion forces [50]. An example for physisorption of a molecule on a metal surface is molecular nitrogen (N_2) on Ag(111) surfaces. A very weak interaction exists between N_2 and the Ag(111) surface. Therefore, N_2 shows a very unreactive behaviour on the Ag(111) surface [51].

Chemisorption denotes adsorption where a change in the electronic state occurs in either adsorbate, surface, or both species. This includes the formation of a chemical bond. Typical

bonds formed by chemisorbed molecules are covalent or ionic bonds [50]. A prototypical example of chemisorption is the adsorption of thiol molecules on Au(111) surfaces. The thiol group forms a covalent bond between the sulfur atom and a gold surface atom creating a thiol ether [52].

The intermolecular interaction also strongly determines the growth of molecular on-surface structures. Intermolecular interaction is induced by for example bonds, including hydrogen bonds, coordinate, and covalent bonds, but also different types of dipole interaction. Intermolecular interactions can cause the formation of ordered molecular arrangements, within this thesis commonly referred to as ordered structures. The arrangement can be induced by different thermodynamic processes, the most common ones are likely self-assembly and self-organisation. **Self-assembly** describes the spontaneous formation of a stable structure in an equilibrium state. It is formed through non-covalent intermolecular interaction [8, 53]. Thus, the molecular building blocks are only weakly bound. This allows forming and breaking bonds. If an equilibrium can be achieved, an equilibrium structure is formed.

When the molecular arrangement is trapped kinetically, the process of forming ordered structures is called **self-organisation**. A self-organised structure can transform into a self-assembled structure, by increasing the kinetic energy, so a restructuring occurs and the equilibrium structure is formed [54, 55]. To obtain the equilibrium structure, diffusion can be increased by increasing the surface temperature during deposition. Furthermore, a reduction of the deposition flux results in an increase of adsorbate mobility, allowing the formation of an equilibrium structure.

An interplay of intermolecular and molecule-substrate interactions is responsible for the formation of molecular assemblies. To study molecules on a surface and for ordered on-surface molecular structures layer-by-layer growth is desired. Therefore, substrates with a high surface energy are the most suitable. This is the case for most metal surfaces, nevertheless, two dimensional molecular assemblies are also desired on substrates with other properties, such as insulators. However, insulating substrates commonly have very small surface energies in comparison with metal substrates [56]. Differences in surface energies are observed for different insulating substrates: A comparably low surface energy is found for alkali salts. A relatively high surface energy is found for calcite(104) and CaF_2(111) surfaces [56]. To form layer-by-layer growing structures, the molecule-substrate interaction is required to be strong enough to inhibit dewetting, on insulators the specific molecule-substrate interaction between single atoms of the molecule and specific regions on the surface is often described as **anchoring** [14]. The interaction between the functional groups and the substrate include covalent bonds, hydrogen bonding, dipole interaction and ionic bonding. Therefore, anchoring includes both physisorption and chemisorption.

So far, anchoring has been studied mainly on alkali salts, calcite(104), and CaF_2(111) surfaces. A variety of functional groups has been used as anchor groups. Examples for oxygen containing anchoring groups are carboxylic acid (-COOH) [16, 57], hydroxyl (-OH) [16, 58], anhydride (-C(O)-O-C(O)-) [59], and aldehyde (-C=O) [58] moieties. Nitrogen containing anchoring groups include nitriles (-C≡N), amines (-CNH_2), and imides (-C(O)-NR-C(O)-) [17, 60]. Examples of anchoring groups based on other elements are halogenides [18] and thiol (-SH) [17] moieties.

Anchor groups unite their polar properties, as they all contain negatively polarized elements. Additionally, the hydroxyl, thiol, and amine moieties have the ability to form hydrogen bonds.

Based on various experimental insights, different strategies have been proposed to tune the molecule-substrate interactions [14]. First, the type of anchoring can be changed, by either using a different anchoring group, or altering the anchoring group. For example, the deprotonation of an anchor group changes the chemical interaction [61]. Second, the geometric fit of the molecular anchor groups to their specific bonding sites, also known as molecule-substrate matching, can be altered, so that the anchor groups have an optimized geometry in relation with their site-specific anchoring position. One example is changing the molecular structure, so the anchor group sits at a different position. Another example to optimise the molecule-substrate matching is the addition of hydrocarbons between the molecule and the anchor groups [62, 63]. Third, the strength of an anchor can be varied by changing the number of functional groups, to either stronger anchoring via more anchors or weaker anchoring via fewer anchor groups. This has been shown on the example of helicene molecules, where, simply put, a higher number of anchor groups resulted in stronger anchoring [18].

Nowadays, first examples exist, where experimental data on anchoring is strengthened by density functional theory (DFT). The combination of experimental and theoretical approaches gives insights into the bonding situation of the anchoring mechanism of molecules onto insulators. DFT helps unravel the character of the involved bonding mechanisms into several contributions, like van-der-Waals interaction, electrostatic interaction, as well as hydrogen, or coordinate bonding [17, 25, 58, 64]. To learn about the different types of interaction can help categorising anchoring as physisorption or chemisorption [25, 64]. An example, where a combination of AFM experiments and DFT calculations unravelled the influence of different anchor groups on adsorption strength, is the adsorption of helicene molecules on NaCl(001) surfaces. The helicene molecules were functionalised with bromine or cyano groups. DFT linked influence of the anchors' dipole strengths and the number of anchors in relation to the anchor strength. Furthermore, the combination of AFM and DFT did reveal, that stronger adsorption can also be achieved, when the

molecule adsorbs in a different geometry and additional to the anchoring, van-der-Waals interaction of the non-anchoring part of the adsorbate can occur [18]. Therefore, combining experimental data with DFT calculation improves the comprehension of anchoring processes.
For metal-organic molecules, an additional anchor moiety has been discovered [25]. For the case of magnesium-phthalocyanine, anchoring to the NaCl surface has been found via the magnesium centre. The magnesium atom anchors to the chloride via chemisorption. A chemical bond was confirmed with density functional theory calculations. The calculations showed a charge density shift at the positions of magnesium and chloride, indicating hybridisation of the p-orbitals of both ions [25].
Summarising, while an interplay of interaction is required to form stable ordered structures on surfaces, specific interaction between adsorbate and substrate is required for molecular adsorption on insulating surfaces. This can be achieved by anchoring. Anchor groups are usually polar functional groups. For metal-organic molecules, anchoring has been achieved via the metal centre.

2.4 On-Surface Formation of Metal-Organic Networks

Organic molecules and metal atoms can form surface metal-organic networks (SMONs) through the self-assembly process. With SMONs, self-assembly is specifically achieved through coordinate bond formation [22, 65].
For SMONs, the organic molecule, also known as linker, requires a functionalisation that allows for the formation of coordinate bonds [22]. The number of functional groups and their arrangement within the molecule are important for the structure, which is obtained by the self-assembled networks. Furthermore, the network structure depends on the different coordination geometries of the metal centre, which in turn depends on the oxidation state of the metal [22]. Typical, 1D and 2D coordination geometries are linear, trigonal planar, and square planar. However, two dimensional coordination geometries have been observed on surfaces with coordination numbers of up to eight [22]. Combining metals with different coordination geometries with different types of linker molecules results in the formation of different types of networks [22] (see figure 2.5). In the schematic in figure 2.5, the non-bonding part of the linker molecules are depicted in grey, while blue and red illustrate the functional moieties. The metal centres are sketched by purple circles, and for the case of two different metals, the second type of metal is sketched as green circles.
In the following, prominent examples of different networks will be given. 1D chains are formed by a **linear** coordination geometry. The metal is required to have the possibility to adapt a coordination of two, while the organic linker molecule contains two functional

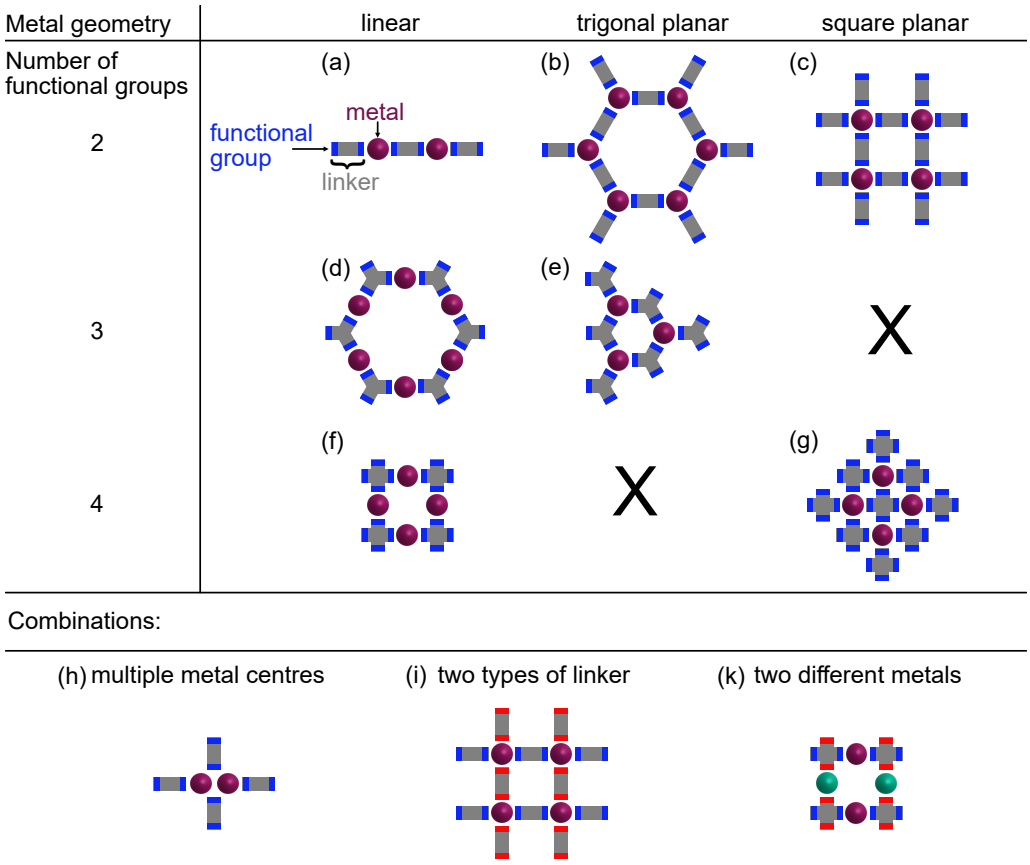

Figure 2.5: Schematic drawing of typical SMON geometries. (a-g) Metal (purple) geometries linear, trigonal planar and square planar are depicted. Organic linkers are depicted in grey with two to four functional groups (blue). (h-k) Common examples for network geometries with multiple metal cores, different linkers or different metals.

groups that act as reactive sites (see 2.5a). For example, a SMON has been formed by porphyrin molecule functionalised with two pyridyl rings on opposite sites which coordinate to copper atoms on a Au(111) surface [66]. When combining a metal having a linear coordination geometry with a threefold functionalised organic linker, a hexagonal network instead of a chain is formed [67] as sketched in figure 2.5d. The geometry of the linker is similarly adopted by the SMON when combining the metal centre with a linear coordination geometry with a fourfold functionalised linker: now a network with a rectangular lattice is obtained [45] (see figure 2.5f).

Trigonal planar geometries require metals with the possibility to form three coordinate bonds. The combination with a linker functionalised with two moieties delivers also a hexagonal network, yet with the metal atoms located at the vertices (see figure 2.5b). In combination with threefold functionalised molecules, a triangular arrays of metal centre can be formed (see figure 2.5e). The network shows hexagonal pores. A notable example for this case is the combination of iron with 1,3,5-trispydridylbenzene, leading to a triangular

array of the iron atoms and a network with hexagonal pores [67]. However, examples for networks based on trigonal planar coordination geometry are very scarce [22].

Square planar coordination geometries are formed by metal centres with the ability to form four coordinate bonds. In combination with twofold functionalised linkers, rectangular networks are obtained as depicted in figure 2.5c. An example is the combination of iron atoms with 1,4-benzenedicarboxylate. Four organic linkers coordinate to one iron centre via one carboxylate moiety each. This combination results in a rectangular network [31] A similar network is achieved, when combining a metal with a square planar coordination geometry with fourfold functionalised linkers (see figure 2.5g). An example of the combination of a fourfold linker with a metal with a square planar coordination geometry is 5,10,15,20-tetrakis-(4-pyridyl)-porphyrin coordinating to iron. In this example, a rectangular arrangement of both metal centres and network can be observed [68].

Up to this point within this section, examples with only one type of metal centre coordinating to the respective ligand have been described. Examples of SMONs with multiple metal atoms in one centre, combination of different linker molecules, or introduction of different metal centres are also possible and sketched in figure 2.5h-k.

Several examples exist for SMONs with multiple (chemically equivalent) metal atoms in one centre. One example has been observed for iron and diterephthalate molecules, where two iron atoms interact with four molecules forming a rectangular network [69] (see figure 2.5h).

Furthermore, networks have been successfully formed with different organic linkers, which is sketched in figure 2.5i. One example is the combination of functionalised porphyrins with terpyridyl ($C_{29}H_{18}N_3Br$) compounds, resulting in a network with square pores. The porphyrin molecules have four coordination sites, to each one, one iron atom coordinates. Within this example, the iron centres coordinate to the bridging terpyridyl ligand [70].

Additionally, metal-organic networks have been established with two different types of metal centres (see figure 2.5k). Exemplary is the stepwise assembly and reaction of tetra[(4-cyano phenyl)phen-4-yl]porphyrin with gadolinium and cobalt. First, the fourfold functionalised organic linker forms a square planar coordination geometry with the gadolinium metal centres, resulting in a rectangular network. Second, after exposure to cobalt, the porphyrin undergoes metallisation (see section 2.2), resulting in a network with two different metal centres [71].

To this point, a large variety of SMONs have been established on metal surfaces. The structure of the SMONs strongly depends on both the metal centre and the geometry of the organic ligand. Only recently, first steps towards SMONs have been established on insulator surfaces by Schüller et al. [23]. For this example, SMONs have been fabricated of biphenyl-4,4'-dicarboxylic acid and iron on calcite(104). The formation of the SMONs

depends on the deposition order. If the metal is deposited first, the metal atoms form clusters on the surface resulting in a hindered diffusivity. Only the deposition of the molecules prior to the metal results in SMONs. These SMONs grow along the [010] substrate direction indicating a templating effect of the calcite surface. A lattice match of the SMON facilitates the growth along the [010] direction [23].

3 Scanning Probe Microscopy: Theoretical Background and Experimental Set Up

3.1 Introduction to NC-AFM and STM

Scanning Probe Microscopy (SPM) is the umbrella term for microscopy techniques which use physical probes instead of light as in optical microscopy. Historically, the first scanning probe microscope developed was the scanning tunnelling microscope, soon followed by the invention of the atomic force microscope [72, 73]. Scanning Tunnelling Microscopy (STM) was invented in 1982 by Gerd Binnig and Heinrich Rohrer, who later on developed Atomic Force Microscopy (AFM) with Calvin Quate and Christopher Gerber in 1985. Nowadays, both STM and AFM allow the operation in ultra high vacuum (UHV), in liquids, or in ambient conditions. Both crystalline and amorphous surfaces can be investigated by SPM. Furthermore, SPM has been utilised to investigate molecules, cells, and membranes [74, 75, 76]. SPM enables imaging the atomic structure of crystalline surfaces, including structural defects of surfaces like point defects, as well as adsorbates such as molecules [77, 78]. In this chapter, the focus is set on investigating crystalline surfaces, as well as imaging adsorbed molecules in UHV.

The basic set up is similar for both STM and AFM: A sharp tip scans over a surface in very close proximity while a measurement signal is detected. The tip movement is performed in x,y, and z direction by piezoelectric actuators. Piezoelectric materials mechanically deform when applying a voltage and allow precise positioning of the tip with picometre precision [79].

Different physical quantities between tip and sample are measured with the different SPM techniques. For STM, a tunnelling current between tip and sample is the main observable. For AFM, the forces between tip and sample are used for imaging and force measurements. Therefore, a major difference in applicability between STM and AFM is the requirement of conducting surfaces for STM measurements, as electron tunnelling is not feasible on

insulating surfaces. In contrast, as AFM does not require conductivity, it can be performed on both conducting and insulating surfaces. The basic principles of both techniques are explained in the following sections.

3.1.1 Scanning Tunnelling Microscopy

Effectively, the scanning tunnelling microscope images the electronic structure of a surface from exploiting the quantum mechanical tunnelling effect between a tip and a surface [73, 80, 81]. The tunnelling effect can be described starting from the wave function of a quantum mechanical particle, an electron in case of STM. The tunnelling effect is illustrated

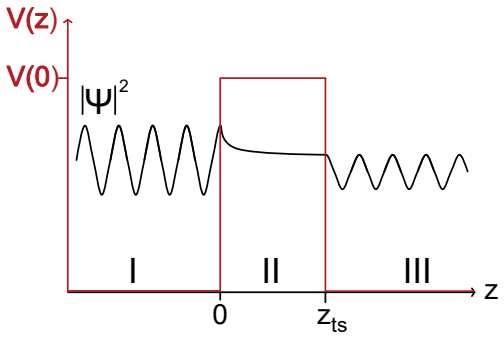

Figure 3.1: Illustration of the quantum mechanical tunnelling effect: Region I: The wave function of a particle in front of a barrier. Region II: Tunnelling through potential barrier V(0) with a thickness z_{ts}, the wave function decays exponentially. Region III: The wave function with a reduced amplitude behind the barrier.

in figure 3.1. When the wave function hits a potential barrier at z=0, the probability of finding the electron within region II is not zero, but decays exponentially. Therefore, the probability density remains larger than zero in the area behind the barrier (region III) [79]. In STM, region I corresponds to the tip and region III to the sample (or vice versa). The potential barrier (region II) represents the vacuum gap between tip and sample. When tip and sample are close enough, a sufficient amount of electrons can tunnel between tip and sample and a net current can thus be measured. The tunnelling current, usually denoted as I_t, is exponentially dependent on the tip-sample distance z_{ts}, also described as barrier width. Different theoretical descriptions of the tunnelling effect in the context of STM have been developed. First, the description by Wentzel, Kramers and Brillouin (WKB-model) gives a solution for the one dimensional Schrödinger equation [82, 83, 84, 79]. The WKB model allows to determine the probability of a quantum mechanical particle tunnelling through a potential barrier. Within the WKB model, the shape of potential barriers can vary. Second, the tunnelling effect has also been described by the Bardeen-model [85]. In this model, the probability of one electron tunnelling through the barrier is calculated with the help of the density of states of both tip and sample, as well as perturbation theory. In the Bardeen-model two systems are defined: tip and barrier are defined as one area, sample and barrier as a second area [85, 79]. This allows the separation of two wave functions. Combining both areas in the Schrödinger equation allows solving the one dimensional Schrödinger

equation for this situation. Out of this the tunnelling rate and ultimately the tunnelling current passing through the potential gap is determined. Third, the Bardeen-model has been refined by Tersoff and Hamann to adapt to the specific requirements of STM [86]. Within the model by Tersoff and Hamann, the wave function of the tip is described by a s-orbital wave function, thus the tip is described as a spherical shape. The model by Tersoff and Hamann uses the local density of states ρ of the Fermi level to describe the STM measurement [86].

The description of the tunnelling current by the Bardeen model is established in dependence from the bias voltage V applied between tip and sample, the local density of states of the sample ρ_s and the tip ρ_t, the energy differences between the fermi levers of tip and sample ϵ, and a Matrix element M.

$$I = \frac{4\pi e}{\hbar} \int_0^{eV} \rho_t(\epsilon - eV)\rho_s(\epsilon)|M(\epsilon)|^2 d\epsilon \tag{3.1}$$

The matrix element M describes the tunnelling probability T, which can be approximated by the work functions of both tip Φ_t and sample Φ_s, the tip-sample distance z_{ts}, as well as the mass of the particle (electron) m.

$$|M(\epsilon)|^2 = T(\epsilon, V, z_{ts}) \propto \exp\left(-2z_{ts}\sqrt{\frac{2m}{\hbar^2}\left(\frac{\Phi_t + \Phi_s}{2} + \frac{eV}{2} - \epsilon\right)}\right) \tag{3.2}$$

This equation shows, that with an increasing tip-sample distance z_{ts}, the tunnelling current I_t decreases.

The operation of a scanning tunnelling microscope requires positioning of the STM tip. The tip is systematically rastered along above the sample's surface in all three dimensions with piezoelectric actuators.

Two operation modes exist in STM: Constant-height mode and constant-current mode. In constant-height mode, the tip moves laterally at a constant height above the surface and differences in the current are measured [87]. This mode can be operated faster than constant-current mode, but has a higher risk of tip crashes due to sample tilt or protruding objects.

All STM data presented in this work has been acquired in constant-current mode. In this mode, the tunnelling current is kept constant by varying the tip-sample distance [73, 81]. A feedback circuit varies the tip-sample distance by constantly comparing tunnelling current set point to the measured current. This mode results in so-called topography images, which will be indicated with "Z_I" throughout this work. However, the term topography can be misleading, as the tunnelling current depends not only on the surface structure, but also on the surface's local density of states. As soon as adsorbates or impurities with a different

local density of states than the underlying surface are present on the surface, the measured heights can differ from the expected height of an adsorbate [87]. An example for a false height measurement is the imaging of CO molecules on metal surfaces [78, 87], as will be discussed in section 3.2.1 for the case of CO adsorbed on Au(111). For CO adsorption on Cu(111), a single CO molecule adsorbs preferably at an on-top position with the molecule pointing away from the surface without tilt [88]. However, STM imaging of a single adsorbed molecule represents a depression [88].

3.1.2 Non-Contact Atomic Force Microscopy

Atomic force microscopy (AFM) measurements are based on the forces acting between a scanning tip and the surface of the sample. AFM operation modes can fundamentally be separated into two cases, namely: static and dynamic AFM [79, 89]. The static mode relies on Hooke's law $F = k \cdot q$ with the spring constant k and the deflection q of the cantilever, therefore the force F can directly be measured from the deflection of the cantilever. In the dynamic mode the cantilever is excited to oscillate. The dynamic mode can be further divided into amplitude modulated AFM (AM-AFM), also known as intermittent contact mode, and the frequency modulated AFM (FM-AFM), which is commonly denoted as non-contact AFM (NC-AFM) [79]. NC-AFM is the mode of AFM utilised in this thesis. Therefore, the description of AFM will focus on NC-AFM in the following.

General Principles of NC-AFM

NC-AFM is based on an oscillating movement of the AFM tip above a surface. When the AFM tip is not in range of the sample, the cantilever oscillates at its resonance, upon approaching the surface interactions between tip and sample cause a change in resonance frequency, which ultimately, results in a frequency shift Δf in NC-AFM.

Sensors for NC-AFM

Technically, the tip is attached to an oscillator, usually in the form of a cantilever. Physically, these cantilevers can be described as a spring. There are different types of cantilevers using different technical realisations of oscillation excitation and signal detection [79, 90, 91]. In this work, two types are utilised: First, for room-temperature measurements in this work, silicon cantilevers are used. These cantilevers are equipped with silicon tips. The deflection of a Si-cantilever is detected by the optical beam detection method, while the excitation is mechanically induced by a piezo [79].

Second, the low-temperature measurements in this work are performed using a quartz tuning fork, commercially known as qPlus sensor [90, 91]. This type of sensor has been developed from using a tuning fork resonator with one fixated prong, whereby an

electrochemically etched tungsten tip is attached to the free prong of the quartz tuning fork. Excitation is performed mechanically, while detection is performed electrically by using the piezoelectric effect.

Mathematical Description of NC-AFM

At large tip-sample distance, where the tip oscillates without the presence of tip-sample forces F_{ts}, the tip deflection $q(t)$ is described by an harmonic, externally driven, damped oscillator. The equation of motion can be written as [89]:

$$\ddot{q} + \gamma\dot{q} + 4\pi^2 f_0^2 q = 4\pi^2 f_0^2 q_{drive} = 4\pi^2 f_0^2 \cdot A_{drive} cos(2\pi f t) \tag{3.3}$$

whereby q describes the displacement relative to the equilibrium position of the tip, which describes the position of the cantilever without a sample present. And q_{drive} is the externally driven oscillation also written as $q_{drive} = A_{drive} cos(2\pi f t)$. The damping is described by γ. The relation between the eigenfrequency f_0 and the cantilever properties is given via the spring constant k and the mass of the cantilever m: $f_0 = 2\pi\sqrt{\frac{k}{m}}$. The damped, harmonic oscillator is described by the resonance frequency f. One possible solution, namely the harmonic movement of the equation of motion is [89]:

$$q = A \cdot cos(2\pi f t + \phi) \tag{3.4}$$

Here, the phase shift ϕ describes the shift between the resonance frequency and the oscillation signal. To describe the damped harmonic oscillator, the phase shift can also be expressed by the normalised frequency $\frac{f}{f_0}$ as well as the quality factor Q.

$$\phi = arctan\left(\frac{-\frac{f}{f_0}}{Q[1-(\frac{f}{f_0})^2]}\right) \tag{3.5}$$

This description of the phase shift is only valid for a normalised frequency smaller than 1. The amplitude $A(f)$ describes the harmonic, damped, driven oscillator by using the resonance frequency f, as well as the excitation amplitude A_{drive}, and the quality factor Q

$$A(f) = \sqrt{\frac{A_{drive}^2}{(1-\frac{f}{f_0})^2 + \frac{1}{Q^2}(\frac{f}{f_0})^2}} \tag{3.6}$$

To determine the maximum for equation 3.6 the partial derivation is $\frac{dA}{df} = 0$, therefore the resonance frequency can be described as following [89]:

$$f = f_0 \sqrt{1 - \frac{1}{2Q^2}} \tag{3.7}$$

Based on equation 3.6, the dependency between the amplitude and the quality factor can be expressed by the simplified term $A = QA_{drive}$ for the case of small damping. The quality factor of the cantilever is defined by the spring constant and the damping constant γ, as well as the mass m.

$$Q = \frac{\sqrt{km}}{\gamma} \tag{3.8}$$

For qPlus sensors quality factors typically have values of 10000 or higher in an environment of 5 K, maximum values of up to 1500000 have been reported [91]. As the quality factor is strongly dependent on the temperatures, smaller values are expected for the quality factor, when measurements are conducted at higher temperatures, such as 77 K and room temperature [91].

Expression of the Frequency Shift

The frequency shift $\Delta f = f_{res} - f_0$ is the main signal used in NC-AFM. The given description via the damped harmonic oscillator in the prior section is only valid at large tip-sample distances where tip-sample forces are negligible. As soon as a force acts between tip and sample, this interaction force has to be included in the equation of motion [79, 89]. Therefore, the tip position, in particular the tip-sample distance $z_{ts}(t)$ has to be introduced as a parameter. The piezo position can be expressed as $z_{ts}(t) = Acos(2\pi ft + \phi)$, as in frequency mode the oscillation is always at resonance, $\phi = -90°$. Therefore, $z_{ts}(t)$ can also be expressed by $z_{ts}(t) = Asin(2\pi ft)$. In proximity to the sample, the riven, damped harmonic oscillator can be described by the non-linear interaction force between tip and sample $F_{ts}(d + z_{ts})$ [89]. When considering this change for the expression of the frequency shift, a time average of the force times the tip position $\langle F_{ts}(z_{ts}(t)) \cdot z_{ts}(t) \rangle_t$ over one oscillation period $T = \frac{1}{f}$ is required with [89]

$$\langle F_{ts}(t) \cdot z_{ts}(t) \rangle_t = \frac{1}{T} \int_0^T F_{ts}(d + z_{ts}(t)) \cdot z_{ts}(t)\, dt \tag{3.9}$$

The frequency shift can be derived from expression 3.9 by using $T = \frac{1}{f_0}$ and $m = \frac{k}{4\pi f_0^2}$ [89].

$$\Delta f = -\frac{f_0}{A^2 k} \langle F_{ts}(t) \cdot z_{ts}(t) \rangle_t \tag{3.10}$$

However, taking into consideration that the largest contribution to the frequency shift occurs at the turnaround points, where the velocity is the lowest, a more suitable description is achieved by replacing the time average by a spatial average [89]. The spatially averaged force can be expressed from equation 3.9.

$$\langle F_{ts}(d+z)\cdot z\rangle = \frac{1}{\pi}\int_{-A}^{A}\frac{F_{ts}(d+z)z}{\sqrt{A^2-z^2}}dz \tag{3.11}$$

Combining equations 3.10 and 3.11 allows to express the frequency shift in spatial dependency [89].

$$\Delta f = -\frac{f_0}{\pi A^2 k}\int_{-A}^{A}F_{ts}(d+z)\frac{z}{\sqrt{A^2-z^2}}dz \tag{3.12}$$

The expression $\frac{z}{\sqrt{A^2-z^2}}$ causes weighting, so a larger contribution is given by the turnaround points. Additional to the weighted contribution of the turnaround points the tip-sample force F_{ts} is also considered in equation 3.12.
For small amplitudes both turnaround points contribute to the frequency shift [89]. For very large amplitudes, for the upper turnaround point F_{ts} adapts very small values, therefore only the contribution from the lower turnaround point is considered.

Imaging Modes in NC-AFM

In NC-AFM, the frequency shift is the main signal, while the oscillation amplitude is kept constant. In topography mode, a feedback loop is in control of the z position between tip and sample to maintain $\Delta f = f - f_0$ at a pre-set value. The z position is then recorded also denoted as the topography signal. In this work, the images obtained in NC-AFM topography mode are denoted as "$Z_{\Delta f}$". NC-AFM can also be operated in constant-height mode, where the feedback loop is turned off, and the changes in Δf are recorded and frequency shift images are obtained. Within this thesis, constant-height AFM images are denoted with "Δf" in the image.

Forces in AFM

The total force acting on the tip is usually composed of different long- and short-range contributions. Interactions at tip-sample distances smaller than approximately 1 nm are often considered short-ranged, while interactions measurably being present at distances larger than 1 nm are commonly referred to as long-ranged [89]. Furthermore, forces are commonly categorised into attractive and repulsive forces. In the following, a brief overview of common tip-sample interactions is given:
An omnipresent contribution originates from van-der-Waals interaction, which is commonly classified as long-range force. Van-der-Waals interaction is a hypernym for the London

dispersion force, Keesom interaction, and Debye interaction. London dispersion force describes the interaction between electrically neutral atoms, molecules, or bodies without a permanent dipole; the interaction results from induced dipoles [92]. In contrast, Keesom interactions describe the interaction between two permanent dipoles, and the Debye interaction describes the interaction between a permanent and an induced dipole [93].

Electrostatic interactions can be either attractive or repulsive. Electrostatic interactions describe the tip-sample interaction between tip and sample with electric charges trapped at either position, or the interaction between tips and samples with different potentials. Electrostatic interactions include Coulomb forces.

Chemical interactions are typically short-ranged. Strong attractive short-range interactions are for example caused by covalent bonds formed between tip and sample. The exact description of these is difficult and usually requires quantum chemical calculations. Strong repulsive short-range interaction is Pauli repulsion. Pauli repulsion is based on the Pauli exclusion principle, which states that the same state cannot be occupied by two electrons. When two atoms are in close proximity, an overlap of their orbitals occurs, but the electrons in occupied orbitals are not allowed in the other occupied orbitals state, causing strong repulsion [89]. The description of the short-range interactions is difficult, as it is not only highly system-specific, but a description requires theoretical approaches like density functional theory [94].

High-Resolution AFM of Molecules

A significant advance of NC-AFM has been the controlled functionalisation of the AFM tip with defined molecules or atoms and the understanding of the imaging mechanisms. Tip functionalisation of the AFM tip enables sub-molecular resolution and one of its first applications has been the clarification of the chemical structure of on-surface molecules [95, 96, 97].

Various molecules and atoms have been used for tip functionalisation: examples are CO, NO, Xe, Cl, Br, O, and larger organic molecules like C_{60} or NTCDI (Naphthalenetetracarboxylic diimide) [95, 98, 99, 100, 101, 102]. Tip functionalisation generally requires low temperature set ups, usually 5 K systems, only for copper tips functionalised with oxygen (commonly known as CuOx tips) experiments at 78 K allow a stable tip functionalisation [100]. The most commonly used molecule for tip functionalisation in NC-AFM is CO. Due to the fact that CO functionalised tips have been utilised in this work, tip functionalisation will be discussed for CO terminated tips in detail.

The total forces between the functionalised tip and sample change the resonance frequency of the cantilever, which results in a frequency shift. The total force is a composite of different long- and short-range forces. Interactions, such as van-der-Waals and electrostatic

interactions, contribute to the overall image, by adding an attractive background to the AFM measurement [103, 104]. However, sub-molecular resolution with NC-AFM is achieved in the short-range regime, where a repulsive interaction between tip and sample occurs, mainly, caused by the repulsive Pauli interaction [103, 104]. The repulsive interaction stems from the overlap of the electric densities of both tip and sample. The repulsive interaction is detected via a frequency shift change, when measuring in constant-height mode. At positions where a very strong repulsive interaction occurs due to, for example a high electron density, like bond or atom positions, a larger frequency shifts occurs. Within the constant-height NC-AFM image, these positions with a strong interaction are observed as bright features resembling the molecular structure.

A distinctiveness of the CO-functionalised tip is the lateral deflection of the CO molecule. The deflection of the CO tip stems from the relatively weak lateral spring constant of the CO tip of $0.24\,\mathrm{Nm}^{-1}$, which is, for example, weaker than the spring constant of a molecule bound to a surface [105]. The deflection of the CO tip occurs at positions of strong repulsion, like bonds, which results in a sharpening of the imaged bond [106]. However, the deflection of the CO tip can also result in a distortion of imaged features [106].

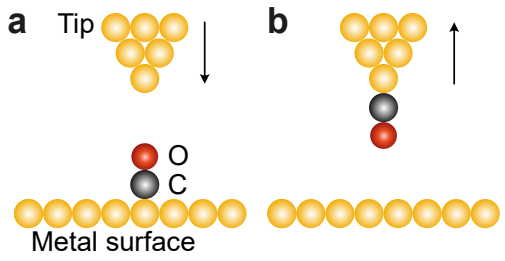

Figure 3.2: Schematic of CO pick up with metal atoms (yellow), carbon atoms (grey), oxygen atoms (red). (a) Metallic tip is approached (black arrow) towards a CO molecule adsorbed on surface. (b) Functionalised tip moves away from the surface (black arrow).

CO terminated tips have been established with an STM in 1997 by L. Bartels et al. [88]. For functionalisation of tips, CO molecules have to be deposited onto the metal sample, where single CO molecules adsorb in on top position for the example of the noble metal surfaces Cu(111), Ag(111), and Au(111) [107]. Here, the carbon atom points towards the surface, leaving the oxygen atom pointing away from the surface perpendicularly [107], this is depicted in figure 3.2a. In the initial experiments, CO molecules have been transferred to the tip by a combination of height and voltage ramps [88]. In particular, the protocol was as follows: CO molecules have been picked up from the metal sample by the sharp metal tip via a voltage and a tip-sample distance decrease [88]. When the tip-sample distance is increased again, the CO has adsorbed at the tip apex in more than half of the attempts [88]. (The procedure of CO pick-up within this thesis is described in detail in section 3.2.1.)

As illustrated in figure 3.2, the CO molecule flips during the process, such that the carbon

atom is binding to the tip apex after transfer [88]. A common control to assess the quality of the CO tip is imaging another CO molecule on the surface. For the case of a tip with a perfectly adsorbed, perpendicular CO molecule, the STM image of the surface-adsorbed molecule consists of a circular shape with a bright centre and surrounding halo [88].

A significant advance in resolution has been achieved after using CO terminated tips in NC-AFM, in particular, CO functionalised tips delivered unprecedented, sub-molecular contrast when imaging molecules.

The very first molecule resolved with a CO terminated tip has been pentacene on Cu(111) in 2009 [95]. The carbon-carbon as well as the carbon-hydrogen bonds of the planar molecule have been resolved by NC-AFM in constant-height mode; the bonds are imaged in the form of sharp lines [95]. In the following years, CO functionalised tips soon facilitated identification of chemical structures of molecules, with Breitfussin and fuel compounds being representative examples [96, 97]. Furthermore, chemical reaction steps have been monitored with CO functionalised tips and different intermediate states and by-products have been identified [108]. Additionally, bond order discrimination has been presented for the example of single and double bonds within a C_{60} molecule [109]. Moreover, NC-AFM imaging with CO functionalised tips enabled chemical discrimination for the case of azines, where the number and position of the nitrogen atoms in six-membered rings has be determined from NC-AFM data [109].

An intensively investigated - and initially strongly disputed - topic in high-resolution imaging with functionalised tips concerns the intermolecular features, especially bond-like features between molecules. Intermolecular features can stem from imaging intermolecular bonds, but also from imaging artefacts resulting in apparent bonds.

One example for intermolecular features, where indeed hydrogen bonds are present, is the intermolecular region between naphthalene tetracarboxylic diimide molecules [102]. Here, sharp bond-like features are imaged at the position of the hydrogen bonds formed between the molecules' oxygen atoms and the hydrogen atoms of the imide moiety. Another example are the bonds observed in the intermolecular regions between bis-(para-benzoicacid) acetylene molecules, where hydrogen bonds are formed between two carboxylic acid moieties [74]. Yet, it is still under debate which physical interactions cause the bond-like features at the hydrogen bond position.

However, bond-like features have also been observed between chemically non-bonded atoms, these features are referred to as apparent bonds. A prominent example of imaging an apparent bond is dibenzo[a,h]thianthren, where the apparent bond is observed intramolecular. This molecule contains two sulfur atoms, which are not connected by a chemical bond directly. However, a bond-like feature is imaged between the two sulfur atoms with NC-AFM [110]. Furthermore, apparent bonds have been observed in the intermolecular

regions between bis(para-pyridyl)acetylene molecules, in particular between two nitrogen atoms, where a bond is chemically impossible [111]. These examples demonstrate that imaging bond-like features with NC-AFM is not thorough evidence for the existence of a chemical bond.

To further understand the contributions to NC-AFM imaging in general, and at intermolecular regions in particular, a theoretical description is required. In particular, this approach has the benefit that the well-defined tip geometries can be used for modelling the contrast formation. Over the last years, two theoretical approaches have been developed: The probe particle model (PPM) by Hapala et al. [106] and the DFT-based model by Ellner et al. [109].

The PPM relies on a simple mechanical model to explain the contrast formation of high-resolution imaging with functionalised tips in general [106]. The original PPM describes the functionalised tip as a flexible apex consisting of a probe particle bound to the last atom of the metal tip (tip base). Lateral and radial spring constants describe the harmonic potential in which the probe particle moves. The interaction between the probe particle and the sample atoms (usually, the geometry from a DFT geometry optimisation) is described by a force-field model using pairwise Lennard-Jones potential. The force between probe particle and the surface is the sum of all Lennard-Jones interactions between the probe particle and sample atoms. Furthermore, two other forces act on the probe particle: First, the radial force between probe particle and the tip base causes the probe to stay attached to the tip base. Second, the lateral harmonic force is contributing to the total force acting on the probe particle. Furthermore, the electrostatic interaction between probe particle and surface has been included in the PPM. Differently sized probe particles showed a variation of imaging contrast depending on the van-der-Waals radii of the probe particle [106].

In contrast to the mechanical PPM model, Ellner et al. proposed a model, where the total interaction is decomposed into electrostatic, van-der-Waals, and short-ranged interactions. This separation of the interactions allows an in depth examination of the individual contribution of each interaction to the contrast formation [109, 112]. The determination of electrostatic and short-ranged interactions is based on the total charge densities of both tip and sample, which are separately calculated via *ab-initio* calculations. The short-range potential is determined via an integral over the charge densities [109, 112].

The combination of different approaches leads to the consensus that a complex interplay of different effects is responsible for NC-AFM contrast formation [106, 109, 112, 113]. The different contributions can be grouped into three categories: electrostatic interaction [112], short-ranged repulsive tip-sample interaction [109], and attractive van-der-Waals interaction. Additionally, the deflection of the flexible CO tip contributes to the contrast [106]. In the following, these four effects will be described in more detail.

The first contribution originates in the electrostatic interaction between tip and sample [112]. The CO functionalised tip expresses an electrostatic multipole: the metal tip is often modelled by a dipole with the negative end pointing towards the CO molecule, while a negative charge cloud surrounds the oxygen atom of the CO molecule. This tip interacts with the sample, which is electrostatically described by the surface electrostatic potential. The electrostatic interaction contributes primarily in the long and medium ranged tip-sample distance of 500 pm or larger [112].
Second, short-ranged repulsive tip-sample interactions contribute to the intermolecular contrast formation [109]. The short-range contributions have been described within the model of Ellner et al. by the overlap of the wave functions of tip and sample.
The third contribution are attractive van-der-Waals interactions between tip and sample. van-der-Waals interactions are usually weak and are characterised as a long-range interaction. At larger tip-sample distances, van-der-Waals interaction are the main contribution to the total interaction, at smaller tip-sample distances the electrostatic and short-range interactions dominate [109]. van-der-Waals interactions can be described by dispersion correction terms within *ab-initio* calculations [113].
Fourth, tip relaxation is observed above electron dense regions like bonds at close tip-sample distance, as the Pauli repulsion is strong in this regime [106]. This causes the tip to move away from the electron dense regions. The tip relaxation results in a sharp ridge within the contrast. Tip relaxation is not only observed above bonds, but at regions with two atoms in close proximity, which are not connected via a bond [106]. The close atoms interact simultaneously with the probe particle. This causes an increased repulsion leading to a sidewise tip relaxation, increasing bond like features. The sharpening of the intermolecular contrast has been described by the PPM [106].
Summarising, tip functionalisation of NC-AFM tips has been a milestone in AFM resolution. Imaging with a functionalised tip enables high-resolution imaging giving unprecedented sub-molecular contrast. The tip functionalisation facilitated identifying molecular structures and reactions with NC-AFM. Nowadays, combining experimental and theoretical approaches leads to the consensus, a synergy of four effects results in the high-resolution NC-AFM images, namely electrostatic, short range, and van-der-Waals interactions, as well as tip deflection. These effects do also contribute to the intermolecular contrast.

3.2 Low-temperature Scanning Probe Microscope "Amaryllis"

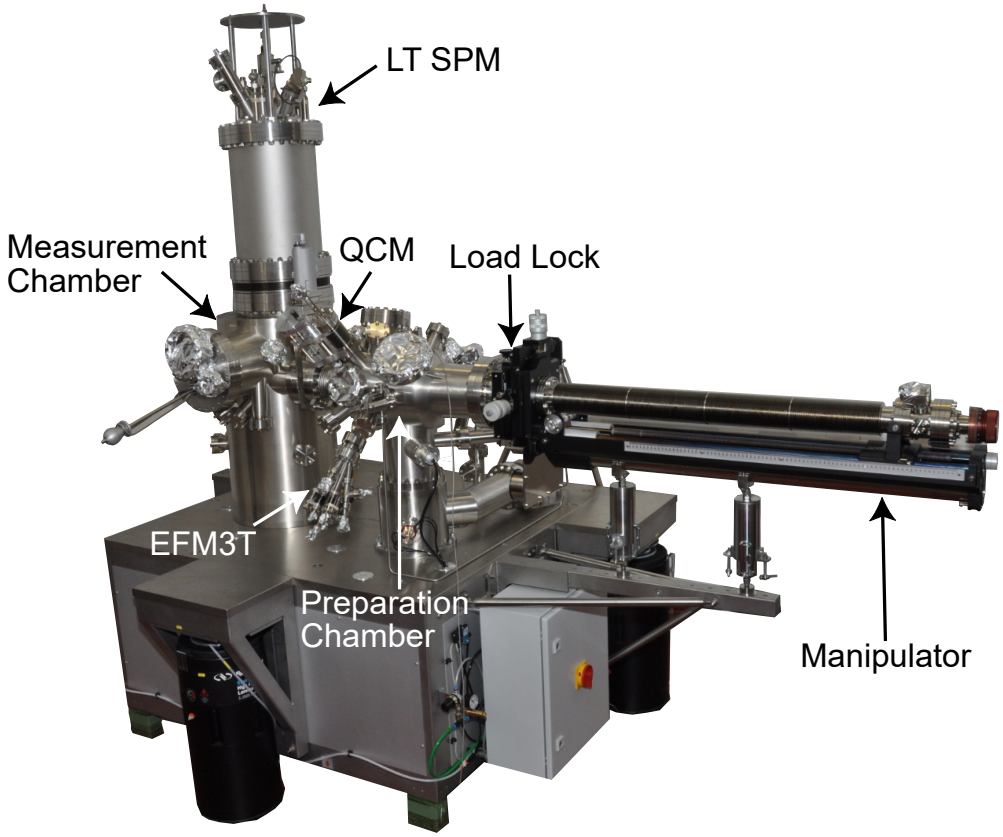

Figure 3.3: Photograph of the LT-SPM system "Amaryllis" housing a Scienta Omicron LT STM qPlus gen. III microscope. The three chambers of the apparatus are labelled as measurement chamber, preparation chamber, and load lock. The crucial equipment of the preparation chamber is labelled as well: Manipulator, EFM3T, and QCM.

The majority of the experiments within this work have been performed with a low temperature scanning probe microscope, namely a Scienta Omicron LT STM gen. III (Scienta Omicron GmbH, Taunusstein, Germany). The room temperature (RT) measurements in chapter 7 have been conducted with a RHK VT AFM 750 (RHK Technology Inc., Troy, MI, USA). The latter system has been described in detail by Temmen, Lübbe and Schnieder [114, 115, 116], the respective measurements will be marked accordingly. Here, I will focus on describing the LT-SPM system, which is mounted in an UHV system consisting of three recipients.

The UHV System

The base pressure of the UHV system is typically in below 3×10^{-10} mbar (preparation

chamber) and 1×10^{-10} mbar (measurement chamber). The low base pressure is obtained by a combination of vacuum pumps. A rotary pump is used as the first stage (RV3, Edwards High Vacuum International, West Sussex, U.K.) in combination with a turbo pump (Hipace 300, Pfeiffer Vacuum Technology AG, Asslar, Germany) as the second stage. Additionally, ion getter pumps (Gamma Vacuum, Shakopee, MN, USA) and titan sublimation pumps (TSP ST22, Gamma Vacuum, Shakopee, MN, USA) are placed in both preparation and measurement chamber. As shown in figure 3.3, the preparation chamber connects the load lock and the measurement chamber. The load lock is a recipient for transferring samples and tips in and out of the system without breaking the vacuum of the full system. It can be pumped separately from the rest of the chamber, which allows quick and easy transfers. The preparation chamber is typically used for sample preparation. The chamber is equipped with a manipulator arm (Omniax 800,Vacgen LTD, Hailsham, U.K.) with heating and cooling facilities for sample preparation and transport. A temperature sensor (T1) is at the manipulator close to the sample position. A calibration has been performed for heating and cooling of the manipulator by Rostislaw Baurichter, where the sensor temperature (which will be given in the experiments) is compared with a thermocouple and a Pt100 element mounted to a sample holder [117]. For temperatures below 400 K, a deviation of <10 K is observed. The sensor temperature deviates from the sample temperature for higher temperatures by up to 50 K at about 570 K [117]. However, these temperatures were only used for surface preparation.

For metal surface preparation, an ion source (IS 40C1, Prevac sp., Rogów, Poland) is attached to the preparation chamber. For metal and CaF_2 deposition, an e-beam evaporator (EFM3T, Focus GmbH, Huenstetten, Germany) is mounted to the preparation chamber. For molecule deposition, home-build molecule evaporators equipped with Knudsen cells are attached to this chamber. The Knudsen cells are fabricated out of glass tubes with a thermocouple wire melted into the closed end and a Tantal wire wrapped around for heating. The cell is supported by a thermocouple and power feed through (Allectra, Schönfliess bei Berlin, Germany), which in turn is mounted to a linear motion feed through (MDC Vacuum Limited, Miron Keynes, U.K.). This construction allows simultaneous heating of the molecules as well as temperature measurement.

To monitor deposition rates, a quartz crystal microbalance, QCM (Quartz Balance Q0 40A1, Prevac sp., Rogów, Poland) is mounted to the preparation chamber. The quartz sensor of the QCM can be moved inside the preparation chamber to be located at the same position a sample would be placed during deposition. This allows to determine the deposition rates at the sample site.

A gas inlet via leak valve is mounted to the preparation chamber as part of the ion source. Typically, this leak valve is used for dosing Argon. Additionally, this leak valve is used

for CO deposition required for CO-tip functionalisation. Last, the preparation chamber is equipped with a home build apparatus for crystal cleaving. It consists of a blade mounted to a wobble stick [118].
The measurement chamber is equipped with the LT microscope, which is mounted to a LHe/LN_2 cryostat. Additionally, a wobble stick is available for tip and sample transfers, as well as a carousel for sample and tip storage at room temperature.

Scan Head and Electronics

The LT microscope is mounted to the bottom of a cryostat, which can be cooled with liquid helium or liquid nitrogen, which is surrounded by a second cryostat for liquid nitrogen. Typical scanning temperatures are 4.6 K (cooling with liquid helium) and 77 K (cooling with liquid nitrogen). Room temperature and heating measurements would also be possible, but have not been conducted in this work. For all experiments qPlus sensors with attached tungsten tips are used, as supplied by the manufacturer (Scienta Omicron, Taunusstein, Germany). Resonance frequencies of qPlus sensors in this work are usually around f_0=26 500 Hz and quality factors usually vary between about 5000 and 40000 at 4.6 K and between about 500 and 2000 at 77 K.
The system is equipped with a STM preamplifier and a qPlus preamplifier (SPM PRE 4E and qPlus PRE, Scienta Omicron, Taunusstein, Germany).
A Matrix 4.0 system (Scienta Omicron, Taunusstein, Germany) is used as SPM electronics, which includes a phase locked loop (PLL) hardware. In addition, an atom tracking device [119] is used to monitor and compensate the z-position of the tip in between constant-height NC-AFM scans.

Performance Amaryllis

STM and AFM imaging have been performed reliably and reproducible results can be achieved with the LT microscope. A minor fraction of the measurement data presented in this thesis is subject to a reduced performance of the LT microscope. In the following, a brief discussion will be delivered on the different aspects that temporarily reduced the system stability until repairs were performed by the manufacturer. Affected data will be accordingly marked throughout this thesis. However, all scientific conclusions are unaffected by these limitations.
Initially, the apparatus has been decoupled from floor vibrations by passive damping systems (S-2000 Stabilizer, Newport Spectra-Physics GmbH, Darmstadt, Germany) at delivery, which are visible in figure 3.3. In this configuration, tiny air movements, such as opening doors remotely located from the laboratory, have caused a ringing in the STM topography channel, expressed by a damped oscillation at a frequency between

1.5-2 Hz and an amplitude of 10 pm or more. This problem has likely been caused by a resonant amplification due to coupling between the damping legs and the internal damping within the microscope. Therefore, the passive damping systems have been replaced by active damping systems (HALCYONICS_DUO, ACCURION, Göttingen, Germany). The disturbances at 1.5-2 Hz, due to air movements, are removed with these isolators.
A disturbance at frequencies of 50 Hz and multiples partly have impacted the protoporphyrin experiments (see chapter 6). The disturbances have caused artificial, regular patterns in the topography images (cf. figures 6.3a, 6.4e, 6.6a). The disturbances have been caused by the measurement electronics (MATRIX system) as well as defect cabling. This problems has been solved by recabling and replacing electronic components by the manufacturer.
Another problem, likely caused by a defective part inside the scan head, concerns disturbances in the range of 450 Hz to 600 Hz and around 1800 Hz. These disturbances have been observed with different magnitudes in the different areas of the sample. Near disturbance free measurements have been possible in one corner of the sample, specifically in the lower right corner (see section 8.2.2, figure 8.3 region I). where most of the data acquisition has been performed. These disturbances have been apparent in some of the iron and TMA measurements, which have been performed at different regions of the sample (chapter 8, disturbances in different areas are visible in images 8.3b-d).
Last, intermittent z instabilities of up to 10 pm have occurred during the TMA and iron experiments. Sharp spikes with a short ring down have been observed, causing instabilities of the tip, especially when using functionalised tips.

3.2.1 CO terminated Tip

A significant advance of SPM experiments during the last years has been the introduction of functionalised tips [95, 96, 97]. The benefit of a well defined reference as well as the capability of high-resolution imaging is also used in this thesis by employing CO terminated tips. CO tip preparation requires four steps: (i) CO deposition of a sub-monolayer coverage on the metal surface, (ii) shaping the metal tip apex, (iii) vertical manipulation for CO pick-up, and (iv) characterisation of the CO-terminated tip by inverse imaging for quality assessment.

(i) CO Deposition
In the first step of this protocol, CO is deposited onto the cold sample by dosing via a leak valve. Here, the leak valve mounted to the preparation chamber is used. A pressure of 9×10^{-6} mbar is set by opening the leak valve. Then, the gate valve between preparation and measurement chamber is opened, together with the shields enclosing the liquid Helium

cooled scan head.
The pressure in the preparation chamber reduces to 2×10^{-6} mbar due to additional pumping by the LT cryostat and the getter pump while the pressure in the measurement chamber raises to 5×10^{-8} mbar. CO is typically dosed for 30 s. Therefore, the shields and valves are closed again after 30 s.

(ii) Shaping the Metal Tip

The second step concerns the preparation of a sharp metal tip whereby mainly three tip enhancement procedures are used: tip pulling, z-ramps, and voltage pulses. For strong reconstruction of the tip apex, or in case the two latter techniques fail, **tip pulling** can be used. This procedure requires the following protocol: First, the topography feedback loop is switched off and the tip is retracted from the surface by 10 nm. The bias voltage is is set to either plus or minus 8 V and the current gain is set to 333 nA. Next, the tip is manually moved towards the surface until the tunnelling current reaches saturation. Finally, the tip is manually withdrawn slowly from the surface until no tunnelling current is observed. As tip pulling causes surface contaminations a new area of the surface is approached after tip pulling. Tip pulling is often followed by both z-ramps and voltage pulses. **Z-ramps** are usually performed, when the tip is having multiple ends (i.e. when imaged data includes ghost images) or when the tip appears blunt (i.e. when no strong contrast is achieved). In this process, the tip is driven into the surface with specified ramp speed and indentation depth. The height of the z-ramp is chosen regarding the degree of change desired. **Voltage pulses** are usually performed, when the tip is showing a frequency shift smaller than −2 Hz, which is another indicator of the tip quality. For a voltage pulse, the tip is retracted from the sample by 1 nm relative to the STM position and pulses of either plus or minus 8 V are applied. This procedure has usually to be repeated multiple times. It was found that an average frequency shift between −2 Hz to 0 Hz is measured in dynamic STM for a sharp tip. Consequently, if the measured average frequency shift falls within the range after a voltage pulse, no further pulses are performed.

(iii) Tip Functionalisation

A suitable tip for CO functionalisation is usually formed when the frequency shift Δf is between 0 Hz and −2 Hz in dynamic STM mode. As soon a suitable tip is obtained, tip functionalisation can be attempted. STM measuring parameters with the most successful CO pick ups were found to differ for the different metal surfaces: While for Au(111) reliable CO pick up is achieved, using V_{bias}=−25 mV and I_t=5 pA as set point, V_{bias}=−5 mV and I_t=15 pA are used for Ag(111). However, differing pick up parameters have been chosen, mostly due to the fact that other adsorbates hinder imaging at the stated parameters. For

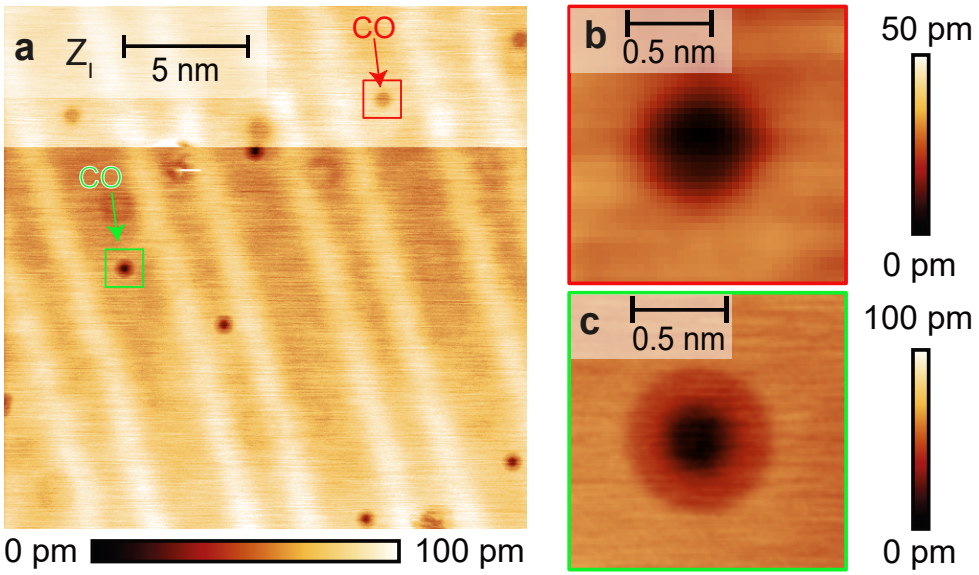

Figure 3.4: (a) Image of CO molecules on Au(111) imaged without (red) and with (green) CO terminated tip. (b) Close up of a CO molecule imaged without a CO terminated tip, the molecule in the overview image is marked in red. (c) Close up of a CO molecule imaged a CO terminated tip, the molecule in the overview image is marked in green. Imaging parameters: (a-c) $I = 100\,\text{pA}$, $U_S = -5\,\text{mV}$, $T_S = 4.6\,\text{K}$.

example, parameters for CO pick up at a TMA/Au(111) sample have been set between V_{bias}=−25 mV and I_t=100 pA, and V_{bias}=−5 mV and I_t=5 pA. For CO pick up, the tip is placed above a CO molecule. Then, a z-ramp is performed with a reduction of the tip-sample distance by 0.3 nm. Imaging is continued directly afterwards.
A successful CO pick up is usually accompanied by a Δf change of about −0.3 Hz, a clear change in height, and a change in contrast of other CO molecules. If the pick up was not successful the pick up procedure is repeated on the same or another on-surface CO molecule.

(iv) Tip Characterisation

In the last step, the quality of a CO terminated tip is assessed by imaging a CO molecule adsorbed at the surface with the CO tip. The CO imaged with a CO tip is described ideally as round with a halo surrounding it [88]. A typical difference in imaging contrast at a surface adsorbed CO with a metal and with a CO terminated tip is shown in figure 3.4. With a metal tip, CO is imaged as a dark depression as highlighted by a red arrow and box in figure 3.4a and b. A CO molecule imaged with a CO functionalised tip is marked by a green box (see figure 3.4a and c).
Three examples of imaging surface-adsorbed CO molecules with three CO tips of different quality are shown in figure 3.5. Figure 3.5a presents an example of imaging with a high

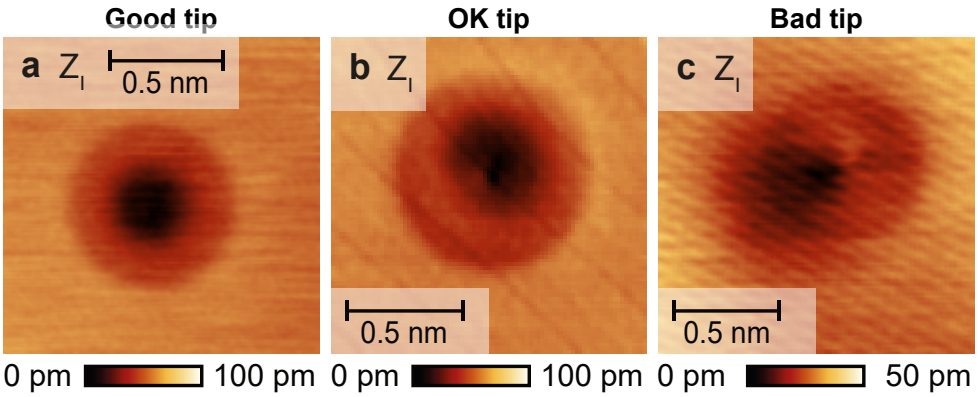

Figure 3.5: Images of CO molecules with different quality CO functionalised tips on Au(111) and Ag(111). (a) CO imaged with a high quality tip on Au(111), (b) CO imaged with a reasonable tip on Ag(111), suitable for test measurements, and (c) CO imaged with a low quality tip on Ag(111), further tip preparation is required. Imaging parameters: (a) $I = 100\,\text{pA}, U_S = -5\,\text{mV}, T_S = 4.6\,\text{K}$, (b,c) $I = 15\,\text{pA}, U_S = 5\,\text{mV}, T_S = 4.6\,\text{K}$.

quality tip. The CO image shows a circular shape, the dark centre is placed in the centre of the less dark halo. In this example, the inner shape is perfectly symmetric. Second, an example of a CO molecule imaged with a reasonable CO terminated tip is given in figure 3.5b. The imaged CO shows a circular halo, however the dark centre is not placed perfectly in the centre of the halo. The dark centre shows an asymmetry. Third, an image taken with an asymmetric CO tip is shown in figure 3.5c. The image of the CO molecule does not represent the previously observed halo with a dark centre, but instead expresses a bright centre in a circular halo, accompanied by a dark shadow. This quality of CO functionalised tip is not suitable for measurements. Therefore, the tip requires reforming and a new attempt of CO pick-up. Various different shapes of CO acquired with low quality asymmetric CO tips have been observed. Still, contrast differing from the symmetric contrast on Au(111) and Ag(111), with one exemplary contrast given in figure 3.5 a, can usually be considered to result from a low quality tip which requires re-preparation After evaluating the quality of the CO tip, the CO tip is either used for STM and AFM measurements or the CO is discarded by applying a z-ramp of -0.7 pm. And the CO pick up protocol is restarted at step two.

3.3 Data Analysis, Correction, and Presentation

All STM and AFM data acquired with the LT-SPM gen III are stored in Omicron's proprietary MATRIX file format. Analysing and data processing is performed with the open source software Gwyddion [120]. The topography (Z) data (both STM (Z_I) and AFM ($Z_{\Delta f}$) is plane-subtracted raw data unless stated otherwise. The gwyddion.net colour scale

(yellow-brown) is used to represent topography images, while the grey scale is used for constant-height NC-AFM data (Δf). Constant-height data is shown as raw data unless stated otherwise. As the microscope calibration of x and y scale was found to be inaccurate at 5 K, all acquired data taken requires a correction in x and y scale with a factor of 1.08. This correction value is based on calibration measurement from atomic resolution images of CaF_2, Si(111)-(7×7), and Au(111), where the unit cell sizes are well-known from literature.

4 Properties and Preparation of the Sample Systems

4.1 Surfaces

To investigate the on-surface fabrication of metal-organic compounds, four different surfaces were utilised in this thesis: Au(111), Ag(111), Si(111)-(7×7), and CaF_2(111). Au(111) surfaces were used for experiments with trimesic acid and iron towards the formation of metal-organic networks (see chapter 8). Ag(111) surfaces were utilised for experiments aiming towards the metallisation of protoporphyrin IX with copper (chapter 6). Si(111)-(7×7) surfaces were utilised as the base substrate for CaF_2 thin films (see chapters 5, 6 and 7). Both CaF_2(111) thin film and bulk crystal surfaces were used for studying the adsorption of ferrocene dicarboxylic acid (chapter 7). Furthermore, CaF_2 thin films were used for studying the adsorption of copper as well as protoporphyrin IX molecules (chapters 5, 6). The properties and the preparation of the utilised surfaces will be discussed in the following sections.

4.1.1 Au(111)

Properties

Crystalline gold has a face-centred cubic (fcc) crystal structure [38]. This fcc metal can be cut to obtain different surfaces. In this work the (111) surface is utilised. A reconstruction of the Au(111) surface has been observed by many measuring methods [121, 122, 123]. The structure of the reconstruction has been finally explained based on STM data [124]. The reconstruction is denoted as herringbone reconstruction. The herringbone reconstruction shows alternating bright stripes and darker areas in STM (see figure 4.1a,b). The bright stripes run in parallel lines along the $\langle 11\bar{2} \rangle$ directions. The dark areas are either hexagonal close-packed (hcp) or face-centred cubic (fcc) areas [124]. The hcp areas are more narrow than the fcc regions. These regions are separated by domain walls, which appear bright in STM topography [124]. The height difference of the hcp and fcc regions to the domain

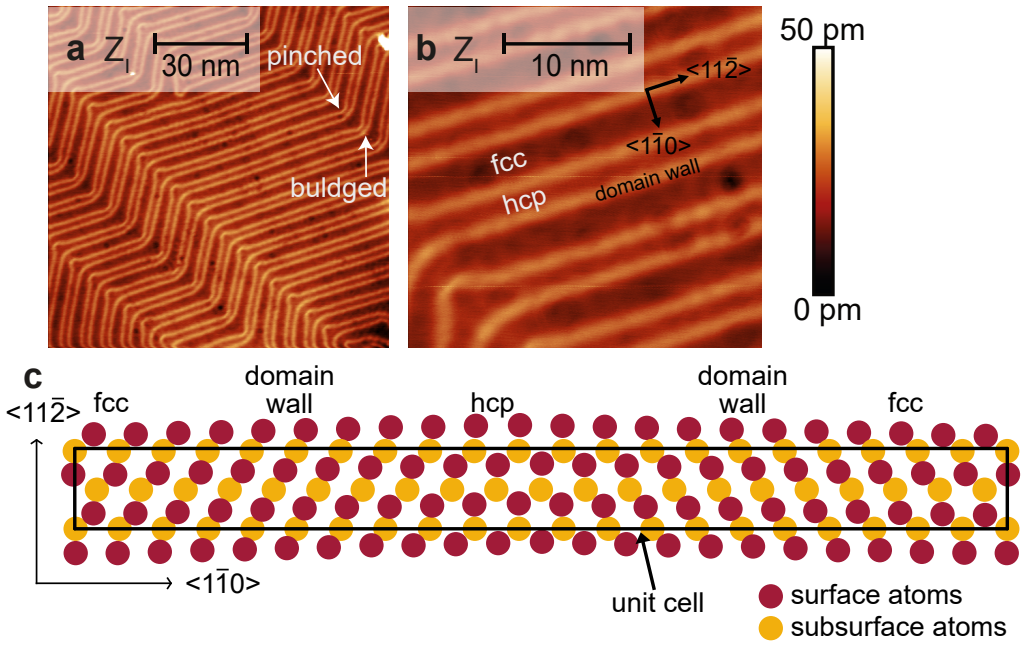

Figure 4.1: Au(111): (a) Overview image, (b) detail image of the herringbone reconstruction. Imaging parameters: $I = 50\,\text{pA}$, $U_S = 5\,\text{mV}$, $T_S = 4.6\,\text{K}$ (c) Top view of the unit cell of the Au(111) herringbone reconstruction. Surface atoms are depicted in red, subsurface atoms in yellow, adapted from Darling et al. [125].

walls depends strongly on scanning parameters and the tip condition. The measured height difference varies between 20 pm and 100 pm [126].

Based on STM images with atomic resolution, the unit cell of the (22x $\sqrt{3}$) Au(111) reconstruction has been determined [125], a top view of a schematic drawing of the unit cell is depicted in 4.1c. The surface atoms are depicted in red, the subsurface atoms in yellow. The unit cell is rectangular with dimensions of 6.3 nm along the $\langle 1\bar{1}0 \rangle$ and 0.47 nm along the $\langle 11\bar{2} \rangle$ direction [126]. The unit cell contains 23 gold atoms at the surface in the area of 22 bulk lattice sites. This results in a contraction of 4.55 % of the topmost layer along the $\langle 1\bar{1}0 \rangle$ [125, 126].

Due to the threefold symmetry of the Au(111) surface, the transition from one domain wall along the $\langle 11\bar{2} \rangle$ direction into another $\langle 11\bar{2} \rangle$ direction is formed by 120 ° bends, so called elbows. The outer (obtuse) site of the elbow is often referred to as bulged elbow site, while the inner (acute) site is referred to as pinched elbow site [32]. These two elbow types are marked with white arrows in figure 4.1a.

Preparation Protocol

Au(111) films deposited on Mica have been used (from Scienta Omicron GmbH, Taunusstein, Germany, and Georg Albert PVD-Beschichtungen, Silz, Germany). The Au(111)/mica

sample is mounted onto a sample holder for resistive heating. Preparation is performed by several sputtering and annealing cycles. The surface is first sputtered using Argon gas at a pressure of about 2×10^{-6} mbar. A Prevac IS40 PS ion source is used for the sputtering process. With a voltage of 1 keV and a current of 10 mA, Argon atoms are accelerated towards the surface for 15 min, resulting in a current between the ion source and the sample of $>2\,\mu$A. After the sputtering process, the Argon inlet is stopped and as soon as the pressure is lower than 10^{-9} mbar, the surface is smoothed by annealing the sample via resistive heating. To heat the sample, it is slowly warmed up by increasing the heater voltage in steps. The sample is first heated at 10 V and 0.4 A for 5 min, the voltage is then increasing to 13 V with a current increasing to 0.8 A for another 5 min, and finally to 16 V and 1.1 A for 15 min. A temperature of about 580 K is achieved at maximum heating power. The temperature is determined by a thermocouple mounted next to the sample holder on the manipulator arm (see section 3.2). Afterwards, the voltage is decreased slowly over the course of 5 min to 10 min. The surface cools down and as soon as the measured temperature falls below 353 K, another preparation cycle is started or the sample is loaded into the LT microscope. Three sputtering and annealing cycles are usually sufficient to obtain a clean and nearly defect free surface, an example is given in figure 4.1.

4.1.2 Ag(111)

Properties

Silver is a precious metal with a face-centred cubic (fcc) crystal structure [38], a model of a fcc crystal is given in figure 4.2a. The fcc crystal can be cut to obtain different surfaces. The (111) plane is indicated by a yellow triangle. A model of the (111) surface is given in figure 4.2b. The top layer is indicated in green, the second layer in yellow and the third layer in blue. The surface has a threefold geometry, a unit cell is highlighted by dashed lines. Its inert (111) surface renders it as an ideal candidate for studying molecular deposition, a large variety of SPM experiments has been conducted on molecules adsorbed on Ag(111) surfaces [24, 106, 127].

Preparation Protocol

Ag(111) films (from Georg Albert PVD-Beschichtungen, Silz, Germany) deposited on mica are prepared by sputtering and annealing cycles, similar to the procedure for Au(111). While sputtering is performed with the identical parameters as used for Au(111), annealing is realised with one difference: The Ag(111)/mica sample is mounted on top of a silicon sample and supported by a direct heating plate sample holder. Therefore, annealing is performed by direct heating through the silicon sample. A cut is made into the Ag film to

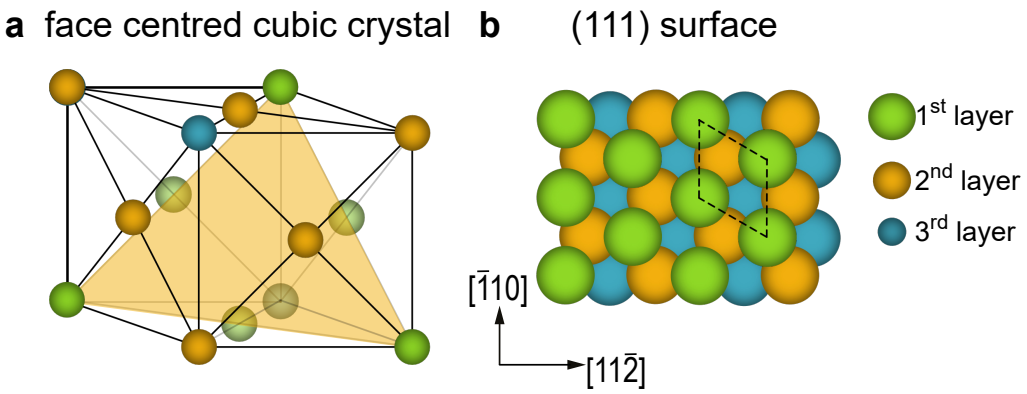

Figure 4.2: (a) Model of the face-centred cubic crystal structure, the (111) plane is indicated by a yellow triangle. The atoms are coloured differently to illustrate the different layers in the (111) surface, which is shown in (b). In (b) the radii indicate the height of the atoms, the top layer atoms (green) are depicted as largest, second layer silver atoms are coloured yellow, third layer is coloured blue.

increase the electrical resistance across the Ag(111) film. To anneal Ag(111), a current of 1.75 A is passed through the silicon for 5 min. The current is increased step wise by 0.25 A every 5 min until a current of 2.3 A is reached. Annealing is performed for 20 min. Finally, the current is ramped down over the course of 10 min. Similar to the procedure for the gold surface, Ag(111) has to cool to 353 K or below before a new sputter and anneal cycle can be started or the sample is loaded into the LT. Three sputtering and annealing cycles are usually sufficient to obtain a clean and near defect free surface, an example is given in figure 4.3.

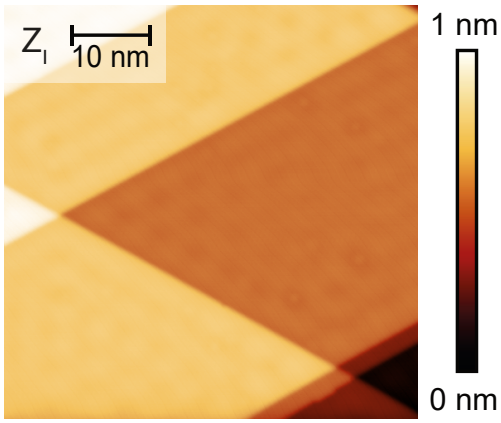

Figure 4.3: Overview image of a Ag(111) surface. STM imaging parameters: $I = 15\,\mathrm{pA}, U_S = 5\,\mathrm{mV}, T_S = 4.6\,\mathrm{K}$.

4.1.3 Si(111)-(7×7)

Due to the small lattice mismatch of 0.6 % between the Si(111) and the CaF_2 crystals, CaF_2 thin films are commonly grown on Si(111) surfaces [128, 129].

Properties

A natural oxide terminates silicon surfaces in atmospheric conditions. Heating the surface to 1073 K results in a desorption of the oxide [130]. To remove surface contaminations the Si(111) sample requires heating to about 1473 K [131]. The formation of the Si(111)(7×7) reconstruction occurs at temperatures of below 1123 K, at higher temperatures a (1×1) reconstruction forms. The formation of both reconstructions is reversible, therefore, upon cooling through the transition phase (7×7) reconstruction forms again [132]. Unravelling the microscopic geometry of the (7×7) reconstruction has been a challenge for many years

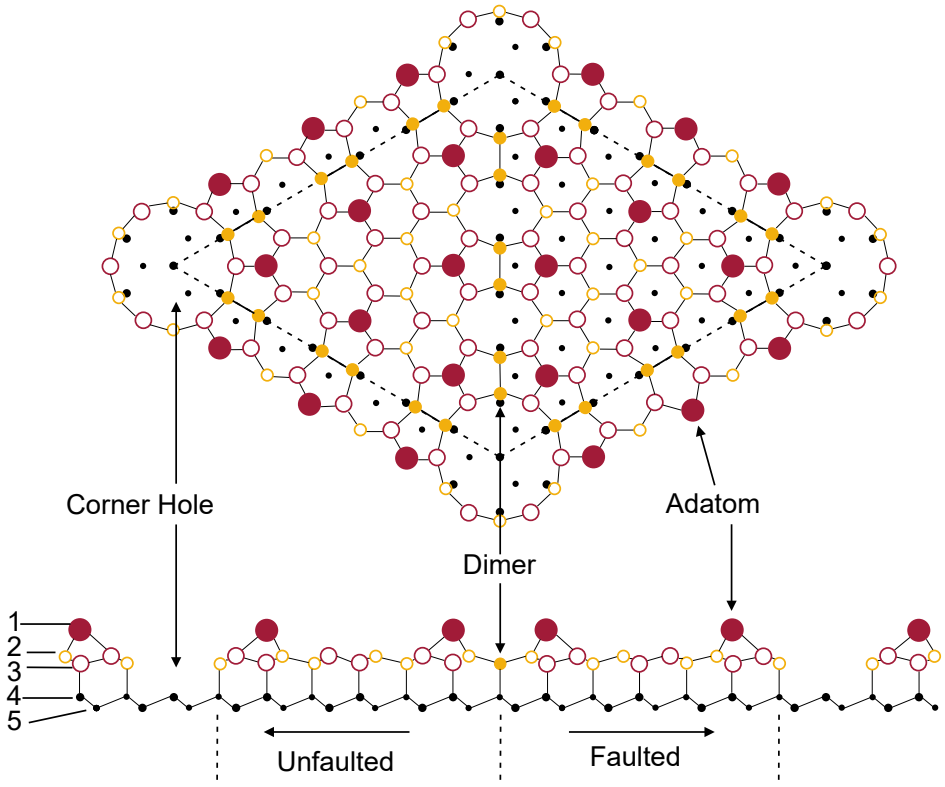

Figure 4.4: Top and side view of the DAS model. Layers 1-5 are indicated by different sized circles. The adatoms of the first layer are depicted as red, filled circles, the dimers as yellow, filled circles. The Si atoms of the bulk layers (4 and 5) are depicted in black. The (7×7) unit cell is indicated by a black dashed line. The faulted and unfaulted halves are indicated by arrows, an exemplary corner hole, dimer and adatom is highlighted by arrows in both top an side view. Adapted from Takayanagi et al. [133].

and has finally been achieved by real space imaging, using STM and later AFM [77, 134]. Today, it is a broad consensus that the geometry of the top layers of the Si(111)-(7×7) reconstruction are described by the dimer-adatom-stacking fault (DAS) model [133, 135]. A schematic model is given in figure 4.4. The DAS model, as the name implies, has three characteristic properties: 9 dimers, 12 adatoms, and a stacking fault area. The driving force of this reconstruction is the reduction of the number of dangling bonds. The silicon bulk crystal forms a fcc lattice (black dots in figure 4.4). The top three layers are reconstructed as described by the DAS model. The (7×7) unit cell is indicated by a dashed line. Located on top of the bulk crystal are two triangular islands (third layer), either bound in faulted or unfaulted stacking. This layer is indicated by yellow lined circles. Each of these islands contains 21 atoms in the third layer. The islands are connected by 18 atoms forming dimers (yellow, filled circles). The second layer consists of rest atoms (red lined circles). The first, or top layer consists of 12 adatoms (red, filled circles). Characteristic of the Si(111)-(7×7) reconstruction are the vacancies in the top three layers named corner holes [133, 135].
As shown in figure 4.5 a and b, two different contrast modes are obtained with STM depending on the bias voltage. A positive sample voltage results in the contrast observed in figure 4.5a, characteristic of this contrast are the depressions, which are also denoted as corner holes. Within one unit cell 12 protrusions are observed at the same height, which match to the 12 adatoms of the dimer-adatom-stacking fault model described in the next paragraph. At a negative sample voltage results in the contrast shown in figure 4.5b, the corner holes are also observed in this contrast, as are the twelve adatoms, however, the adatoms are imaged in two different apparent heights, the ones imaged darker are the adatoms of the unfaulted half, the adatoms imaged brighter are part of the faulted half of the unit cell, as the faulted half obtains a higher charge density [136].

Preparation

Silicon samples (<0.006 Ωcm, b-doped, p-type from Institute of Electronic Materials Technology, Warsaw, Poland; and ceded by AG Wollschläger (0.1° miscut, manufacturer unknown, p-type determined via hot-probe method [137])) are mounted to direct heating sample holders. Prior to all experiments, samples are degassed first via resistive heating at about 680 K. The sample is kept at this state for several hours. Second, the sample is further cleaned via direct heating for about 15 hours. To this end, the current through the silicon sample is slowly increased to 2.16 A. At these parameters the surface has just started to faintly glow.
For each preparation, several flash annealing cycles are performed, where a current of 7.18 A is passed through the sample to eliminate surface contaminations. This results in a substrate temperature of about 1480 K. The sample is kept at this temperature for

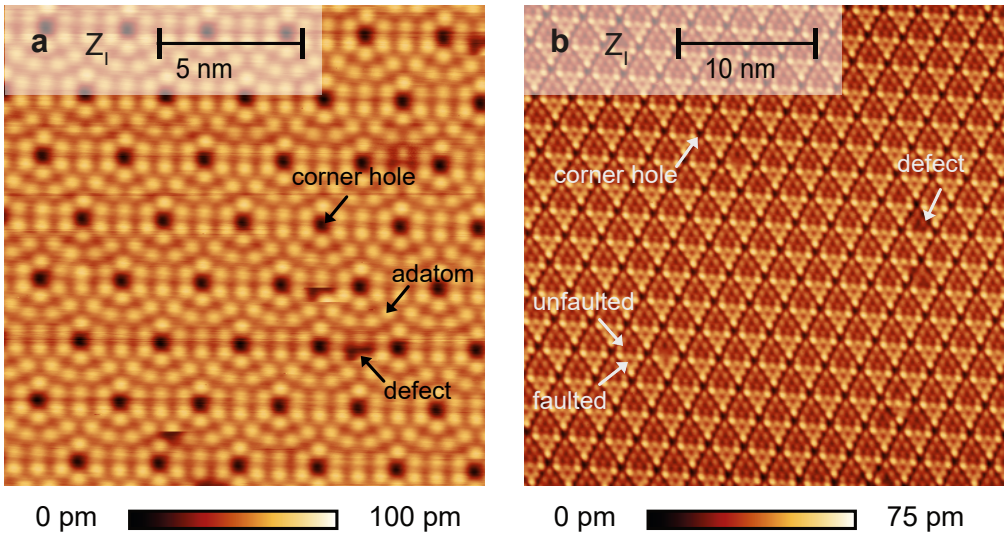

Figure 4.5: STM topography images of the Si(111)-(7×7) reconstruction at (a) positive sample bias voltage and (b) negative sample bias voltage. STM imaging parameters: (a) $I = 400\,\text{pA}, U_S = 1.8\,\text{V}, T_S = 4.6\,\text{K}$, (b) $I = 200\,\text{pA}, U_S = -2\,\text{V}, T_S = 77\,\text{K}$.

maximum of 20 s or until the pressure rises above 10^{-9} mbar. This step needs to be repeated until the pressure does not exceed 10^{-9} mbar for 20 s, so the components of the residual gas in the vacuum do not contaminate the surface. Next, the current is decreased instantly to about 3 A, and then the current is slowly decreased to zero over the course of 5 min. This step allows the formation of the (7×7) reconstruction.

A successful preparation is indicated by a low defect density including the absence of contaminations. This can be observed by atomic resolution STM images. Representative, topography images of STM (Z_I) at positive and negative bias voltage are given in figure 4.5a and. Both show the (7×7) reconstruction, an example of the characteristic corner holes as well as an exemplary adatom are marked by arrows in figure 4.5a and b. Additionally, exemplary defect sites are marked in both images, verifying true atomic resolution.

4.1.4 $CaF_2(111)$

Large Fluorite (CaF_2) crystals can synthetically be grown with very high purity [138]. The material can also be grown as a thin film, as will be discussed in chapter 5.

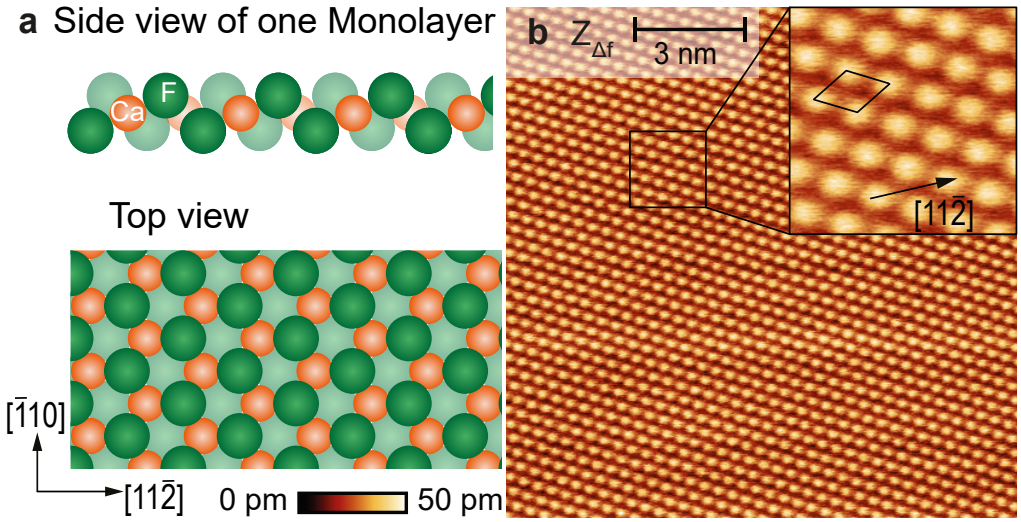

Figure 4.6: (a) Side and top view of a $CaF_2(111)$ surface model, (b) NC-AFM image of CaF_2, the inset shows a magnification of the highlighted area. Imaging parameters: $\Delta f = -2\,\text{Hz}$, $U_S = 4\,\text{V}$, $f_0 = 26\,640.9\,\text{Hz}$, $T_S = 4.6\,\text{K}$.

Properties

CaF_2 grows in a face-centred cubic crystal structure. The $CaF_2(111)$ surface terminates with fluoride as the topmost layer. In $CaF_2(111)$ a monolayer consists of three layers of atoms, a fluoride layers as top layer, followed by one calcium cation layer, then followed by another fluoride layer. A side view of one monolayer of the crystal is illustrated in figure 4.6a. Fluoride atoms are depicted in green, calcium cations are illustrated in orange. The (111) surface is shown in figure 4.6. $[11\bar{2}]$ and $[\bar{1}10]$ surface directions are also indicated in the model. The CaF_2 surface follows a threefold rotational symmetry.

Atomic resolution of the $CaF_2(111)$ surface was first obtained by Barth et al. in 2001 [139]. It was found that the contrast formation in NC-AFM strongly depends on the electrostatic interaction between tip and sample. Therefore, the tip termination influences the imaging contrast. Positively charged tips image the negatively charged fluorine anions as "bright" in the topography, while a negatively charged tip maps the positive calcium cations as "bright" in the topography images. The contrast with the negative tip shows round protrusions, while the contrast obtained with the positive tip images triangular features [114]. An example of atomic resolution obtained with a negatively charged tip is shown in figure 4.6b.

Preparation using Bulk Crystals

Bulk CaF_2 crystals (Korth Kristalle, Altenholz, Germany) have been used for experiments using both a room temperature NC-AFM system from RHK, and for low temperature experiments a LT-SPM instrument from ScientaOmicron (see section 3.2). For the room temperature experiments, a crystal sample holder as described by Tröger et al. [118] was used. For low temperature experiments, a double sample holder, as described by Heggemann et al. [140] was used. This double sample holder supports a metal sample mounted next to a bulk crystal [140]. In both experimental set-ups, the crystals were first degassed together with the sample holder by heating to 600 K for 3 h. Second, each crystal was cleaved along a direction of the $\langle \bar{1}10 \rangle$ family by a blade providing a {111} plane in the preparation chamber [118]. After cleaving, two different procedures have been followed: (i) For experiments at room temperature, the crystal is placed into the scan head directly after cleaving. (ii) For low temperature NC-AFM measurements, the crystal is heated to 330 K for one hour to remove trapped charges from the surface before inserting the sample holder to the scan head.

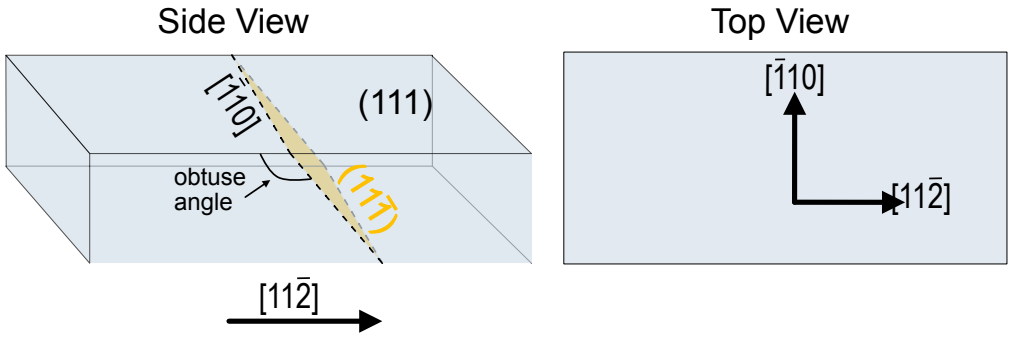

Figure 4.7: Illustration of the cleaving process of the CaF_2 crystal to determine surface orientation. In the sketch of the side view a black, dashed line marks the cleaving position along the $[\bar{1}10]$, in yellow the $(11\bar{1})$ cleavage surface is indicated. The $[11\bar{2}]$ direction is indicated by an arrow. In the top view the resulting surface orientations are marked by arrows.

The absolute orientation of a $[11\bar{2}]$ surface direction is determined after the experiments by a second cleaving process. This is illustrated in figure 4.7: the crystal is removed from the holder and cleaving is performed in the centre of the crystal's surface. The crystal cleaves along a $[\bar{1}10]$ direction forming two more {111} planes, which are highlighted in yellow in figure 4.7. The $[11\bar{2}]$ direction can be determined by the orientation of the newly cleaved $(11\bar{1})$ plane to the (111) plane of the surface. The $[11\bar{2}]$ direction points towards the obtuse angle between the two planes (see figure 4.7). Due to the crystal structure, the $[11\bar{2}]$ direction is perpendicular to the $[\bar{1}10]$ direction, as illustrated in the top view of the crystal, the crystal cleaving and direction determination has been described in detail in the

thesis of Pieper [141]. An example of a successfully prepared CaF_2 surface is given in figure 4.6b. The NC-AFM image of a $CaF_2(111)$ surface has a size of 13.6 nm and shows atomic resolution. In the inset, a magnified image of the atomic structure is given with a unit cell and a $[1\,1\,\bar{2}]$ direction included.

Preparation of $CaF_2(111)$ Thin Films on Si(111)
In this thesis, $CaF_2(111)$ surfaces are also prepared by deposition of thin films on clean Si(111) surfaces. In a first step, Si(111) surfaces were prepared as described in section 4.1.3. Next, the Si(111) sample is heated to about 873 K and CaF_2 (Alfa Aesar, cleanliness 99.9%) is deposited from an e-beam evaporator (EFM3Ts, Focus GmbH, Huenstetten, Germany). The CaF_2 is heated in the e-beam evaporator with a filament current of 1.96 A and an acceleration voltage of 270 V, the CaF_2 thin film structure is described in detail in chapter 5.

4.2 Deposition of Molecules, Metals, and CaF_2

Experiments in this thesis require the deposition of molecules, metals, and CaF_2. A Knudsen cell was used for sublimation of different molecules (see section 4.2.1). An electron beam evaporator was used for CaF_2 as well as for copper and iron sublimation (see section 4.2.2). For some experiments multiple components were deposited onto the sample in steps or parallel. To obtain a predictable coverage of the receptive material, sublimation parameters are calibrated prior to the deposition using a quartz crystal micro balance (QCM, Quartz Balance Q0 40A1, Prevac sp., Rogów, Poland), which is equipped with a thickness monitor sensor (TM14, Prevac sp., Rogów, Poland). Furthermore, the QCM contains a quartz crystal resonator with a resonance frequency between 4.8 MHz to 6.0 MHz (Prevac sp., Rogów, Poland), the exact resonance frequency depends on the mass on the resonator. When material is deposited onto the QCM the crystal's resonance frequency changes and based on the frequency change, the mass and layer thickness of the material is determined. The mass of material can then be translated into the number of molecules deposited on the crystal.
For measurements with the QCM, first, the QCM is positioned by a linear UHV manipulator at the sample preparation position in the preparation chamber. Second, the temperature of the QCM is stabilised by water cooling. Third, the material is slowly heated to the lowest sublimation temperature, where a rate is observed with the QCM. At this sublimation temperature, measurements are conducted, where the QCM measures the mass change. Fourth, the sublimation temperature is increased, and the rate is determined for a higher sublimation temperature. Several different sublimation temperatures are investigated.

The experiment is repeated several times for each temperature, to proof reproducibility of the measurements. As multiple measurements were conducted for each sublimation temperature, the rate and temperature are determined over a set time frame, the error is determined by standard deviation of the different measurements.
The final calibration of the sublimation was performed in the preparation chamber prior to the experiment. Experiments to find initial parameters were also performed at a separate test chamber, which consisted of a pumping system, a QCM (ALD-Sensor, Inficon, Bad Ragaz, Switzerland), and the respective Knudsen cell. The general set up was similar to the one in the preparation chamber. Results of both preparation chamber and test chamber are presented in the following sections.

4.2.1 Deposition using a Knudsen Cell

Organic and metal-organic molecules used in this work were deposited from Knudsen cells. A sketch of a home-build cell as used in this work is shown in figure 4.8. The glass test tube of the Knudsen cell has a thermocouple (type K, NiCr/Ni) melted into its closed end, which allows temperature measurement. Tantalum wire wound as a coil is wrapped around the glass test tube for heating. The tube is heated by passing a current typically of the order of 1.5 A to 2.5 A through the wire. The tube is filled with the molecular material. Glass wool is used as a barrier hindering the molecules to fall out of the tube during handling. The sublimation rate of molecules can be described by the universal Arrhenius law. It describes the temperature dependency of various chemical and physical processes, such as diffusion, reactions, or evaporation [142]. For the sublimation of molecules, the Arrhenius

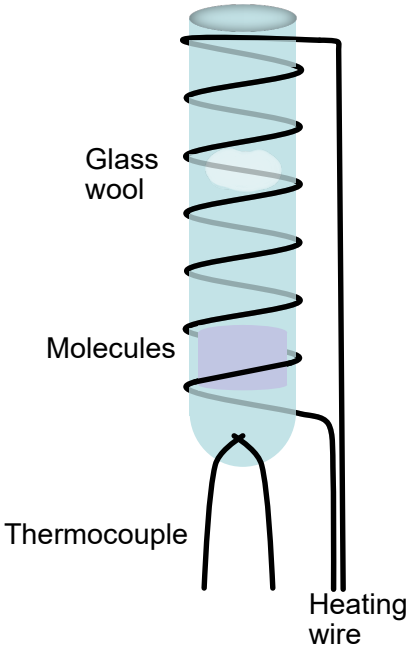

Figure 4.8: Sketch of a home-build Knudsen cell for molecule evaporation: Glass test tube with a thermocouple wire (NiCr, Ni) melted into the closed end. Ta wire is wrapped around the test tube for heating. The test tube is filled with molecules. Glass wool to protect the molecules from accidentally dropping out of the test tube.

law describes the relation of the rate r to the sublimation temperature T.

$$r = r_0 e^{-\frac{E_s}{k_B T}} \tag{4.1}$$

Additionally, rate depends on the sublimation enthalpy (E_S), a molecule specific property, as well as the pre-exponential factor r_0, also known as the attempt frequency. The pre-exponential factor is also a molecule specific property. k_B is the Boltzmann constant ($k_B \approx 8.62 \cdot 10^{-5}\ eVK^{-1}$). The Arrhenius equation is commonly shown in logarithmic form

$$ln(r) = -\frac{E_s}{k_B}\frac{1}{T} + ln(r_0) \tag{4.2}$$

In this form, the linear relation between the inverse temperature and the logarithmic rate is obvious. This is a criterion for a sublimation following Arrhenius law: A linear relation is a sign for a successful evaporation, as a non linear behaviour usually indicates either the presence impurities or the decomposition of the evaporating molecules. To rule these effects out, the logarithmic rate is plotted over the inverse temperature and the linear relation is checked. Results are shown in figure 4.9.

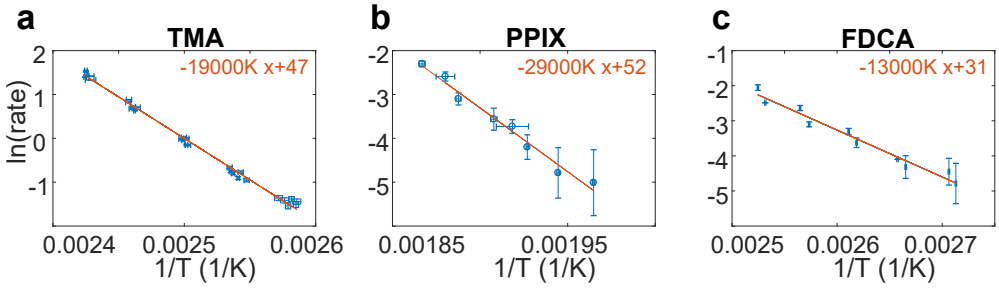

Figure 4.9: Arrhenius plots of the deposition rates of (a) TMA, (b) PPIX, and (c) FDCA molecules with lines of best fit in orange, fit parameters are included in each graph.

The data for all three molecules, trimesic acid, protoporphyrin IX, and ferrocene dicarboxylic acid, were collected during repeated measurements.

- trimesic acid, TMA, *1,3,5-benzenetricarboxylic acid*, $C_9O_6H_6$
  (Source: Sigma Aldrich, Darmstadt, Germany; purity: 95%)

- protoporphyrin IX, PPIX, *3-[18-(2-carboxyethyl)-8,13-bis(ethenyl)-3,7,12,17-tetramethyl-22,23-dihydroporphyrin-2-yl]propanoic acid*, $C_{34}H_{34}N_4O_4$
  (Source: Enzo Life Sciences, Lörrach, Germany; purity: ≥95%)

- ferrocene dicarboxylic acid, FDCA, *1,1'-Dicarboxyferrocene*, $C_{12}H_{10}FeO_4$
  (Source: Alfa Aesar, Kandel, Germany; purity: ≥97%)

The data was collected at similar sublimation temperatures, showing the reproducibility of the sublimation, by accumulation of data points at certain temperatures. For PPIX, the difference between the sublimation temperatures was negligibly small, so the measurements were condensed as one data point for each sublimation temperature. A linear fit is performed for each sublimation series and is included as an orange line. The fit parameters are inserted in the plots as well. The sublimation enthalpy E_S can be expressed from the slope m of the linear fit in combination with the Boltzmann constant k_B

$$E_S = mk_B \tag{4.3}$$

The y intercept is the logarithmic of the pre-exponential factor r_0. The results for the sublimation of TMA, PPIX, and FDCA show a linear relation for the logarithmic rate against the inverse temperature. The sublimation enthalpy is listed in table 4.1
A low sublimation rate was chosen for deposition, as a high surface diffusivity was desired, for basics on the relation between sublimation rate and on surface diffusivity see section 2.4. As sub-monolayer coverage was desired, the coverage of molecules is given in units of molecules per square nanometre "$mols/nm^2$". This unit is chosen as the molecules obtain different adsorption geometries depending on coverage, therefore, the unit is more precise than monolayer. In STM and AFM experiments, the coverage can be determined from counting molecules in overview images. The deposition rate is then given as coverage per time unit ($mols/nm^2min^{-1}$). The respective rates are given in table 4.1 along with the deposition temperature.

Table 4.1: List of used molecules and their sublimation properties.

Molecule	T $[K]$	deposition rate $[mols/nm^2min^{-1}]$	sublimation Enthalpy E_S [eV]
TMA	400	0.0028±0.0003	1.6
PPIX	490	0.0002 ± 0.0001	2.5
FDCA	390	0.012 ± 0.003	1.1

4.2.2 Deposition using the Electron Beam Evaporator

An EFM3T (Focus GmbH, Huenstetten, Germany) was used to sublimate calcium fluoride, as well as the metals copper and iron. Both CaF_2 (Korth Kristalle, Altenholz), Germany, and Cu (purity: 99.9995 % from Sigma Aldrich, Darmstadt, Germany) are sublimated from a cruicible, Fe is sublimated from an iron rod (purity: 99.99 % from Focus GmbH, Huenstetten, Germany)
The EFM3T used for sublimation of the listed materials does not have a temperature read out, therefore, an analysis based on the Arrhenius law cannot be performed for these

materials. Instead, the EFM3T has a flux monitor. The principle of the flux monitor is based on the Bayerd-Alpert ionisation Gauge, where a hot filament cathode ionises the sublimated gaseous compounds. A current, also denoted as flux, is detected at the ion detector. Consequently, the flux is used for sublimation calibration along with the rate obtained by the QCM. A linear relation between flux and rate is observed. This is illustrated in the plots in figure 4.10. The parameters of the linear fit are also given in figure 4.10. The error of both rate and flux are determined by standard deviations. Flux is a reproducible quantity that allows predictable material deposition also for the insulator material CaF_2.

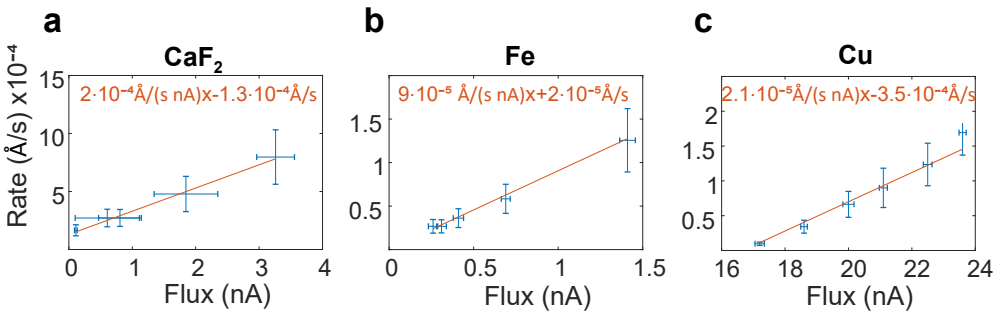

Figure 4.10: Deposition rates determined with the QCM of (a) CaF_2, (b) iron, and (c) copper using the EFM3T shown in the dependence of the measured flux. Best fit is inserted in the plots in orange, fit parameters are included in the plots accordingly.

5 Lateral Mobility of Copper on CaF_2 Thin Films

A requirement to build metal-organic compounds on surfaces via reaction or surface metal-organic network formation (see sections 2.2, 2.4), is the availability of a metal educt. While the reacting metal atoms could directly be provided by the surface of a metal substrate [40, 47], metal atoms need to be deposited onto an insulating surface [23]. To construe the features imaged after a synthesis of a metal-organic compound or after the formation of a SMON, it is important to allocate the adsorbed metal on the surface within the features observed in STM images. Regarding possible reaction processes (see section 2.2) it is vital to know the behaviour of the metal on the surface, especially regarding the adsorption and the resulting mobility of the metal on the surface.

The CaF_2(111) surface is a promising insulating substrate for the study of molecular adsorption. In particular, CaF_2(111) surfaces have a comparably large surface energy when compared to other insulating substrates, especially when compared to alkali halide surfaces [14]. The large surface energy increases the likeliness of molecules to form wetting layers on the underlying surface, which is desired both in the field of molecular self-assembly and for the study of single molecules [14].

The surface energy of an insulator is, however, lower than the surface energy of a metal surface, which commonly leads to dewetting of adsorbates and Volmer-Weber growth, which is characterised by island growth [14]. For a sub-monolayer coverage of adsorbed metal, a few studies have been performed on cobalt, iron, platinum, and silver on CaF_2(111) surfaces, where indeed a Volmer-Weber growth is observed [143, 144, 145].

The CaF_2(111) surface can be formed on bulk crystals, and can also be grown in the form of thin films, especially by growing films on Si(111) [146]. The thin film forms on a calcium monofluoride (CaF_1) interface layer, which is formed on the Si(111) surface. The CaF_2 thin film (111) surface has basically the same structure as a bulk (111) surface, however, with the practical benefit that conductivity-requiring experimental methods such as STM or XPS can be used for the characterisation.

First, the structural properties of CaF_2/CaF_1/Si(111) system are described in section 5.2.

Next, the adsorption of copper on $CaF_2/CaF_1/Si(111)$ is studied in chapter 5.3. A focus is set on the lateral mobility of copper on the CaF_2 surface, with an emphasis on interactions with the scanning tip, as well as the influence of thermal activation.

5.1 Introduction

Due to the small mismatch of 0.6 % between the CaF_2 and the Si lattice constants [147], growth of high-quality $CaF_2(111)$ layers has virtually exclusively been studied on Si(111) surfaces [146].

The preparation of $CaF_2(111)$ thin films is performed by CaF_2 deposition on Si(111) surfaces. Depending on the Si(111) surface temperature during deposition, different growth modes occur for CaF_2 on Si(111) [148]. The deposition of CaF_2 onto a Si(111) sample held at room temperature results in a disordered CaF_2 layer physisorbed on the Si(111)-(7×7) reconstructed surface [149]. Type A-epitaxy is observed for growth at temperatures of about 673 K. In this epitaxy type, the orientation of the CaF_2 layer matches the orientation of the underlying Si crystal [150, 151, 152]. At temperatures above 673 K, the deposition of CaF_2 on Si(111) results in two main chemical and structural changes in surface temperatures of about 673 K: First, the CaF_2 molecules decompose into CaF_1 and fluorine. Both bind to Si and form mixed layers on the Si(111) surface and clusters of SiF_x [150, 151, 152]. Second, due to the reaction with CaF_1 and fluorine, the (7×7) reconstruction is disintegrated and an unreconstructed Si(111)-(1×1) surface begins to form.

Type-B epitaxy has been observed at substrate temperatures between 823 K and 873 K during growth [153]. In this temperature range, a well-ordered CaF_1 interface layer is formed, the residual fluorine atoms react with the Si atoms within the layers of the (7×7) reconstruction to SiF_x, which desorbs from the surface [154]. On top of this CaF_1 layer, ordered layers of $CaF_2(111)$ grow epitaxially as mono- or multilayer upon further deposition. Due to the well-defined and stoichiometric $CaF_2(111)$ termination of samples prepared under these conditions, of the structural properties the surface top layer closely resembles those of a bulk $CaF_2(111)$ surface. Consequently, this growth mode is used for the experiments within this thesis and will be further described later in this section. At higher substrate temperatures of about 923 K, a mixture of a (3×2) and a c(6×2) reconstruction is formed with calcium atoms embedded into the top Si(111) layer, after desorption of further fluorine [155, 156]. At even higher substrate temperatures, calcium also desorbs and the Si(111)-(7×7) reconstruction is restored [157].

With the aim to form ordered $CaF_2(111)$ surfaces for molecule adsorption studies, the type-B epitaxial growth mode with a well-defined CaF_1 interface layer is used throughout

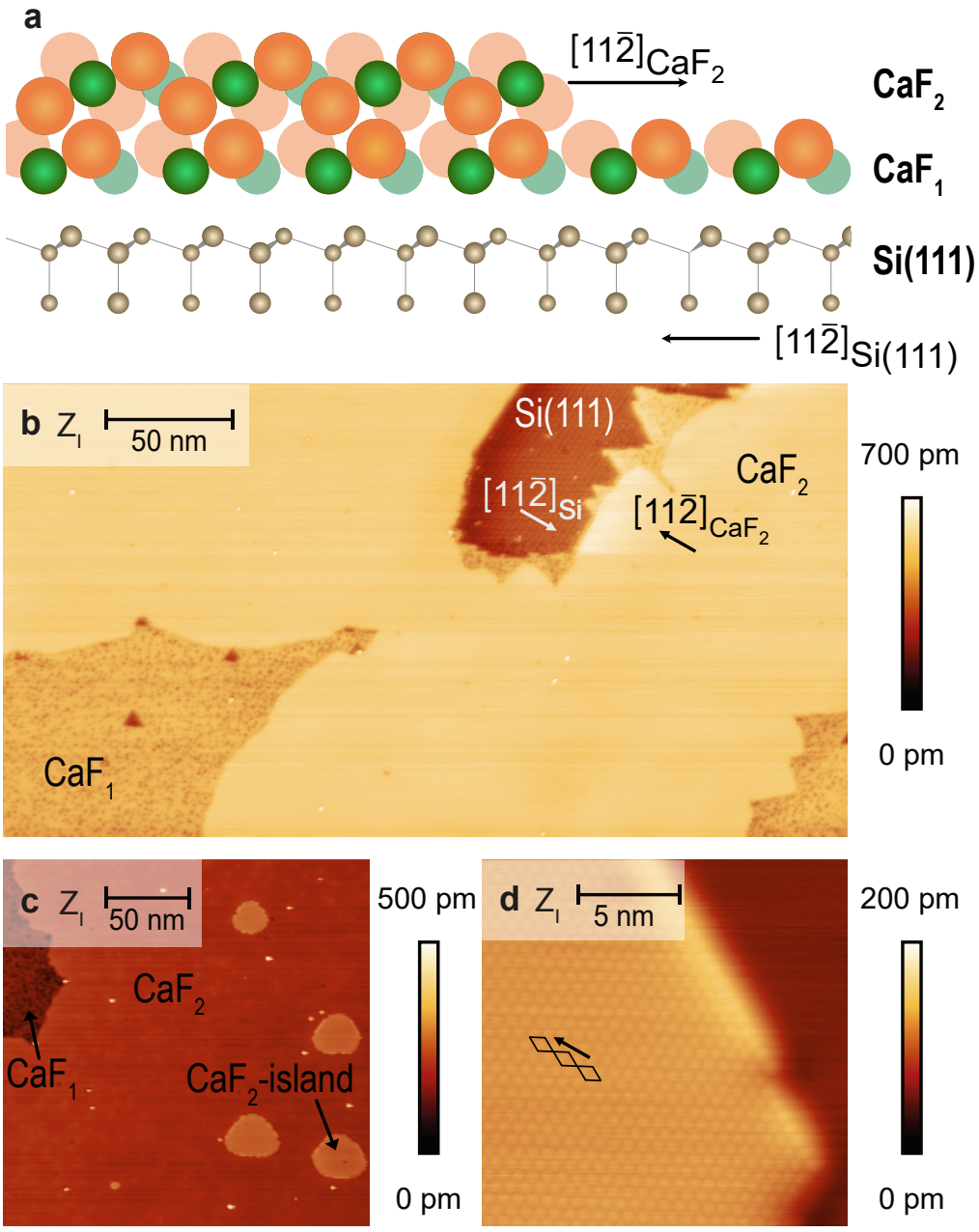

Figure 5.1: (a) Side view of the atomic model of the $CaF_2/CaF_1/Si(111)$ system. Calcium cations are depicted in orange, fluoride in green, and silicon atoms in beige. (b) STM image presenting areas of Si(111), $CaF_1/Si(111)$, and CaF_2/ $CaF_1/Si(111)$. The $[11\bar{2}]$ direction of CaF_2 is indicated by a black arrow, the $[11\bar{2}]$ direction of the Si(111) surface is indicated by a white arrow. (c) STM image of CaF_2 islands on $CaF_2/CaF_1/Si(111)$; CaF_2, CaF_1 surfaces, and an exemplary island are labelled accordingly. (d) Atomic resolution STM imaging on one of the islands, the $[11\bar{2}]$ direction of CaF_2 surface is indicated by a black arrow, unit cells are added as black rhombuses. Imaging parameters: (b) $I = 100\,\text{pA}, U_S = -3\,\text{V}, T_S = 77\,\text{K}$; (c,d) $I = 30\,\text{pA}, U_S = -3\,\text{V}, T_S = 77\,\text{K}$.

this thesis. Such structure can be achieved in the temperature range between 823 K and 873 K. Under these conditions, the CaF_2 molecules react with the Si(111) top layer and form a CaF_1 interface layer. Strong Si-Ca bonds exist between the surface Si atoms and the Ca atoms of the CaF_1 layer [155], while the residual fluorine desorbs, likely as SiF_x molecules [152]. On top of the CaF_1 layer, CaF_2(111) grows stoichiometrically in type-B epitaxy when depositing more CaF_2 material [153, 158].
A model of the side view of the CaF_2/CaF_1/Si(111) system is presented in figure 5.1a. The schematic shows one CaF_2 layer on top of the CaF_1 interface layer, which in turn is formed on top of the (1×1)-reconstructed Si(111) substrate. The calcium cations (fluoride) are coloured in green (orange). Arrows indicate the characteristically opposing $[1\,1\,\overline{2}]$ directions of the Si and CaF_2 crystals in type-B epitaxy.

While there are now few examples of molecular adsorption on CaF_2(111) surfaces presented, including the study of FDCA in chapter 7 of this theses, there are only very few investigations of metal adsorption on CaF_2(111). In this chapter, the focus is set on investigating a sub-monolayer coverage of copper on CaF_2(111) with an emphasis on lateral mobility upon physical influences, in particular interaction with the tip and thermal heating. In the context of on-surface reactions, a high lateral mobility is desired for adsorbed metal. It is expected that a high lateral mobility increases the probability of educt interaction on the surface to allow for the reaction step.
So far, metal adsorption on insulating samples has mostly been studied by using alkali salt substrates [159]. The most common growth mode observed is the Volmer-Weber mode, resulting in metallic islands on the insulator surface at a sub-monolayer coverage [159]. Nucleation sites are commonly step edges or surface defects, in particular vacancy sites[160].
Only very few examples exist where the metal deposition on CaF_2(111) surfaces has been studied. Silver, cobalt, and iron have been studied after deposition on the CaF_2(111) bulk crystal [143], and cobalt as well as platinum have been investigated on CaF_2/CaF_1/Si(111) thin films [144, 145]. On both bulk and thin film substrates, Volmer-Weber growth has been observed for these metals [143, 144, 145]. The observation of Volmer-Weber growth is in agreement with the behaviour of metals on other insulator surfaces, in particular on alkali salts [159]. For Co and Fe on CaF_2(111) surfaces, a high density of nucleation sites is observed. The clusters, formed at the nucleation sites, are thermally stable up to 573 K. It has been suggested that nucleation often occurs at step edges and at defect sites as the studied CaF_2(111) sample showed a high coverage of point defects [143, 144]. Metal atoms are trapped at the defect sites, resulting in increased thermal stability of the adsorbate [143]. For cobalt adsorbed on a CaF_2 thin film, the formation of different sized islands is

observed depending on both the cobalt coverage but foremost on the substrate temperature during metal deposition, which is allocated to the diffusivity of the cobalt material at the surface [145]. At temperatures above 373 K, cobalt material starts to desorb from the surface, and at 773 K only 8 % of deposited material remains on the surface, which has been determined by STM and reflection high-energy electron diffraction measurements. At temperatures below 573 K, cobalt islands are observed to form at the CaF_2 step edges, while at higher temperatures the islands are found to be distributed homogeneously across the surface [145].

5.2 STM Imaging of the CaF_2(111) Thin Film

In course of this thesis, three forms of CaF_2 thin films are grown, namely the CaF_1 interface layer, a CaF_2 monolayer on CaF_1/Si(111), as well as CaF_2 layers on the CaF_1/Si(111) interface layer. In this section, the characteristics of the samples prepared within this thesis are compared to literature results to lay base for ensuing experiments of adsorption of metals and molecules (in sections 5.3, 6.5, and 7).

A prototypical example of a sample, where CaF_2 is deposited for 15 min onto the Si(111) substrate heated to about 873 K is shown by the STM image in figure 5.1b. The image contains Si(111), CaF_1/Si(111), and CaF_2/CaF_1/Si(111) surface regions. An area of bare Si(111)-(7×7) surface is identified by the characteristic surface structure of the (7×7) reconstruction (see section 4.1.3), labelled as Si(111) within the STM image. The CaF_1 is identified by its characteristic high defect-density and accordingly labelled within the STM image in figure 5.1b. The remaining surface, which is near defect-free is allocated as CaF_2 surface.

First, the finding of Si(111)-(7×7) is surprising as, based on literature reports, CaF_1 forms a closed layer before CaF_2 layers grow [161]. However, it is also reported, that the film growth depends strongly not only on the surface temperature during deposition, but also growth rate and miscut of the surface [158, 162]. Thus, the observation of the Si(111)-(7×7) reconstruction can be explained, by not finding the optimum preparation parameters, or the Si(111) sample has a miscut, which inhibits full Frank-van-der-Merwe growth. The atomic resolution of the Si(111)-(7×7) surface allows the determination of the $[1\,1\,\bar{2}]$ direction of Si(111): The faulted (unfaulted) half of the Si(111)-(7×7) can be determined within the STM as the lighter (darker) triangle, due to its higher (lower) density of states (see section 4.1.3) [163]. From the DAS model, it is known that the $[1\,1\,\bar{2}]$ direction points from the faulted to the unfaulted half [133]. This as-determined $[1\,1\,\bar{2}]$ direction is indicated with a white arrow.

Second, the structure to be discussed is the CaF_1 interface layer, which forms on top of the

Si(111)-(1×1) surface. The CaF_1 interface layer can be identified from its characteristic defect-rich surface, which is expressed by plenty depressions. The chemical composition of the CaF_1 layer has previously been confirmed by Wang et al. using XPS [164]. Dark features are observed on the CaF_1 surface areas in the STM images. These features are interpreted as multiple small depressions. In a previous study, these depressions have been allocated to atomic-sized defects in the CaF_1 layer and it was suggested that these are generated by the incorporation of excess Si atoms into the CaF_1 layer [161]. In literature, two types of CaF_1 surface have been reported: rough and smooth layers [148, 165, 166], which are found on terraces or at step edges, and are supposedly caused due to different reaction pathways [148]. Comparing the given example in figure 5.1b to literature results [148, 165, 166], only smooth CaF_1 layers are observed. Smooth CaF_1 layers are reported to allow CaF_2 growth [165].
Third, the CaF_2 layer is discussed. Within the STM images, the CaF_2 layers are the remaining surface, which shows a near defect-free surface, as shown in figure 5.1b. The $[1\,1\,\bar{2}]$ direction of $CaF_2(111)$ is deduced from the $[1\,1\,\bar{2}]$ direction of the Si(111) surface, as the $[1\,1\,\bar{2}]$ directions of both surfaces are opposed in type-B epitaxy. The $[1\,1\,\bar{2}]$ of the CaF_2 surface is indicated with a black arrow. The observation of the formation of a near defect-free $CaF_2(111)$ surface on top of the CaF_1/Si(111) interface layer agrees with the previous studies described in chapter 5.1 [152, 153, 158].
Deposition of more CaF_2 results in the formation of CaF_2 layers on top of the CaF_2/CaF_1/Si(111) sample. The second and subsequent layers of CaF_2 form islands of varying size. An example of CaF_2 islands on a $CaF_2(111)$ surface are given in figure 5.1c and d. In the STM image 5.1c, four CaF_2 islands are imaged (one marked with an arrow). The shape of the islands shown in figure 5.1c is of a hexagon with different edge lengths, which agrees with reports on hexagonal island shapes at the given temperature range [164]. Atomic resolution is achieved on the island (figure 5.1d), it shows a defect free $CaF_2(111)$ surface. Unit cells are highlighted within figure 5.1d. The $[1\,1\,\bar{2}]$ direction of CaF_2 is included as a black arrow. A small area of CaF_1 is also included in the image. In previous works, Volmer-Weber growth has been reported at temperatures of about 773 K and Stranski-Krastanov growth at temperatures of about 1023 K [161] (contradicting studies, which report desorption of fluorine at 923 K[155, 156]). However, as, a surface temperature of 873 K is chosen in this work, it is likely an intermediate growth mode is observed at this intermediate temperature.

5.3 Copper Deposition and Mobility on Insulating CaF_2 Thin Film Surfaces

Copper is deposited on CaF_2/CaF_1/Si(111) surfaces cooled by liquid nitrogen to a temperature of about 105 K. After the metal deposition, the sample is immediately transferred into the scan head and STM measurements are performed at 77 K. A detailed description of the experimental implementation of CaF_2 thin film preparation and metal deposition can be found in sections 4.1.4 and 4.2.2.

Based on previous STM measurements of the CaF_2/CaF_1/Si(111), it is known that the sample expresses CaF_2, CaF_1 and Si(111)-(7×7) regions (see figure 5.2a). After the deposition of copper, a high density of bright spots is observed on the CaF_2/CaF_1/Si(111) surfaces, an overview image is shown in figure 5.2b. Due to the fact that these bright spots only appear after copper deposition, all of these bright spots are categorised as copper, because on the bare CaF_2/CaF_1/Si(111) surfaces (see section 5.2) protrusions are not observed. However, due to the high coverage of the spots, the surface regions can first-hand not be distinguished from one another. Still, as the spots are distributed homogeneously, it can be assumed that the spots are found on the three different surfaces, which is surprising, as due to the higher surface energy of Si(111) and the high defect density of CaF_1, it could be assumed that copper adsorbs stronger on these two surfaces. In figure 5.2d, which was obtained after multiple scans of the same area, an outline of an island is recognised, it is highlighted by a dashed, white line. However, based on the STM images it cannot be determined whether the island is a CaF_2 island on a CaF_1 or CaF_2 surface.

Summarising, after copper deposition bright spots are observed to be distributed homogeneously over the thin film sample. Based on prior STM images it can be concluded, that copper likely adsorbs on the three different surfaces.

Here, the focus is set on studying on-surface mobility of the copper on CaF_2 thin films. Therefore, the presented data are analysed under the consideration of the influence of lateral tip movement in section 5.3.1. In subsequent experiments, the diffusivity is studied by stepwise heating the sample to 573 K. The thermal influence on the cluster mobility is discussed in chapter 5.3.2

5.3.1 Tip-Induced Displacement of Copper Clusters

To probe the cluster stability with respect to the tip presence, the same area is scanned multiple times (four scans in total: two scans from bottom to top; two scans from top to bottom) before the image in figure 5.2d is acquired. The 162×162 nm^2 sized images

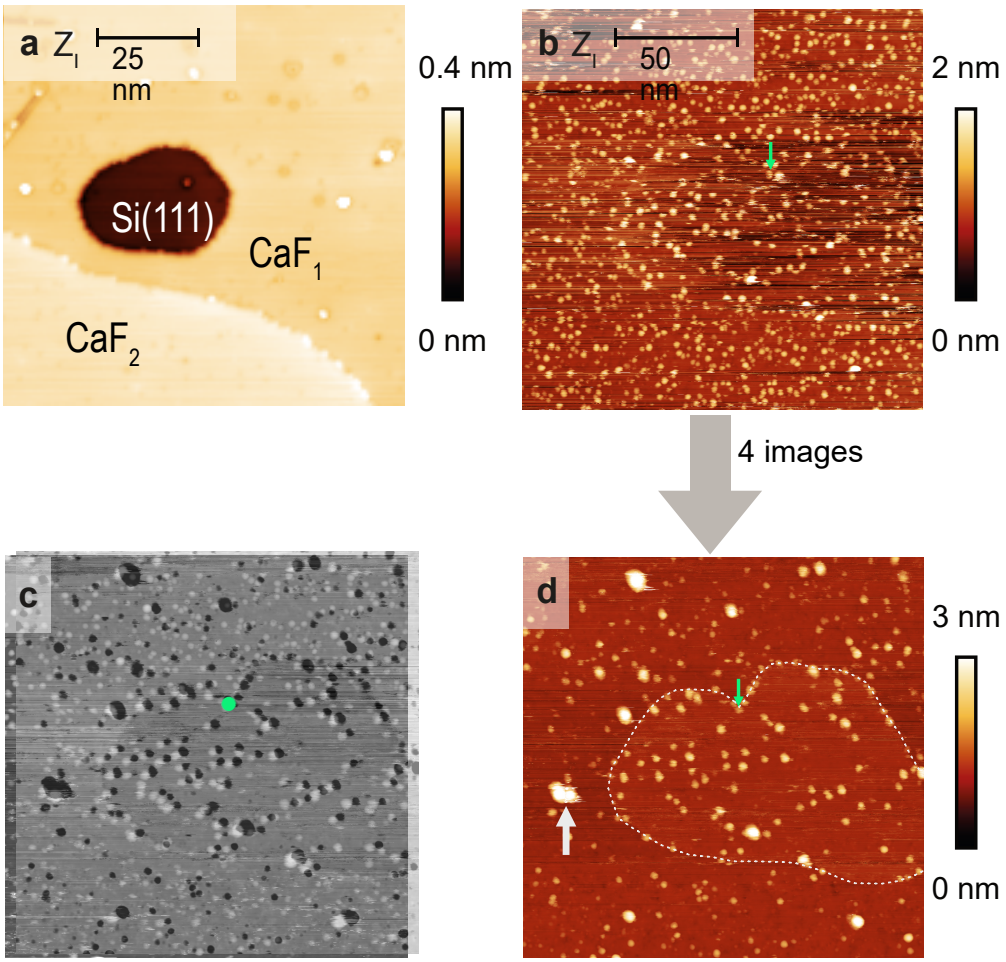

Figure 5.2: Copper on $CaF_2/CaF_1/Si(111)$. (a) Overview image of the $CaF_2/CaF_1/Si(111)$ thin film substrate prior copper deposition. (b) Copper clusters deposited onto thin film surface held at 108 K; (d) four scans of the area later, an island is indicated by a dashed, white line. (c) overlay of images b and d. Imaging parameters: (a) $I = 100\,\text{pA}, U_S = -3\,\text{V}, T_S = 77\,\text{K}$ (b,d) $I = 3\,\text{pA}, U_S = -3\,\text{V}, T_S = 77\,\text{K}$.

are acquired with 1500×1500 pixel^2, the scan speed is set to 9 ms/pixel. The scans are performed at a bias voltage of −3 V and a current set point of 3 pA. The loop gain is set to 5% during the scans.

When comparing the images in figures 5.2b and 5.2d, a reduced number of clusters is observed and some clusters are visibly lager (one example is marked by an arrow in figure 5.2b). This indicates that the smaller clusters are pushed together or collected by the tip. By placing the before and after images one above the other (see figure 5.2c), it is determined that most of the smaller clusters observed in figure 5.2d are not at the same position as the clusters observed in figure 5.1b, but the larger clusters are found at positions where previously clusters adsorb. This is shown by positioning the two images above one another, with one image having an inverted colour scale (see figure 5.2c). The top image is set to

50% transparency, and a precise positioning is achieved by aligning the island edges in both images, a characteristic point is marked in green throughout the images. Therefore, it is likely that the majority of clusters are at least slightly moved during the scans and a lot of the smaller clusters or atoms disappear completely. These observations lead to the conclusion that the copper clusters are weakly bound to the underlying surfaces and lateral tip-induced displacement of the clusters occurs.

5.3.2 Thermal Influence on Copper Mobility

A series of heating experiments is performed with a freshly prepared Cu on $CaF_2/CaF_1/Si(111)$ sample to probe the influence of thermal heating on the copper diffusion, as well as to determine if copper clusters on CaF_2 thin films desorb at temperatures up to 573 K. A very small amount of 0.0004 $\frac{\text{mols}}{\text{nm}^2}$ of PPIX is present on this sample in addition to Cu. The PPIX is deposited onto the freshly prepared CaF_2 thin film, so the PPIX coverage is determined using STM measurements. As a next step Cu is deposited onto the substrate, therefore, the sample is not manipulated with the STM tip prior the presented experiments. The PPIX coverage is negligibly smaller, roughly by a factor 50 to 200, when compared to the copper cluster density. No differences are observed, when comparing the STM images of pure copper (figure 5.2b) and copper with PPIX (figure 5.3a, 0.0004 $\frac{\text{mols}}{\text{nm}^2}$ PPIX). In particular, neither the formation of PPIX clusters is observed, nor decoration of the copper clusters. Therefore, no significant influence of PPIX on the sample system can be determined, and for further interpretation the sample system is treated like a pure copper deposition.

Copper is deposited onto the sample held at 106 K for 15 min with a flux of 24.7 nA. The sample system is heated stepwise in the temperature regime between 196 K and 573 K in the sample position of the manipulator arm, namely using following five temperatures: 196 K, 268 K, 348 K, 403 K and 573 K. The sample is slowly heated to the specified temperatures, and held at the respective temperature for 20 min each. After each heating step, the sample is transferred back into the scan head for STM measurements at 77 K. Representative images are shown for images taken directly after deposition at a temperature of 106 K (figure 5.3a), for a medium temperature of 348 K (figure 5.3b), and for the highest heating temperature of 573 K (figure 5.3c). All three images have a lateral size of 108 nm × 108 nm. On the first sight, the image taken without heating (figure 5.3a) has a higher number of copper clusters than the images after the heating experiments (figure 5.3b,c). This observation is confirmed by determining the cluster density for the different temperatures. The copper cluster density is determined by manually counting the number of clusters within an image, which includes every protrusion due to the fact that defects and impurities have been allocated to depressions in previous experiments (see section 5).

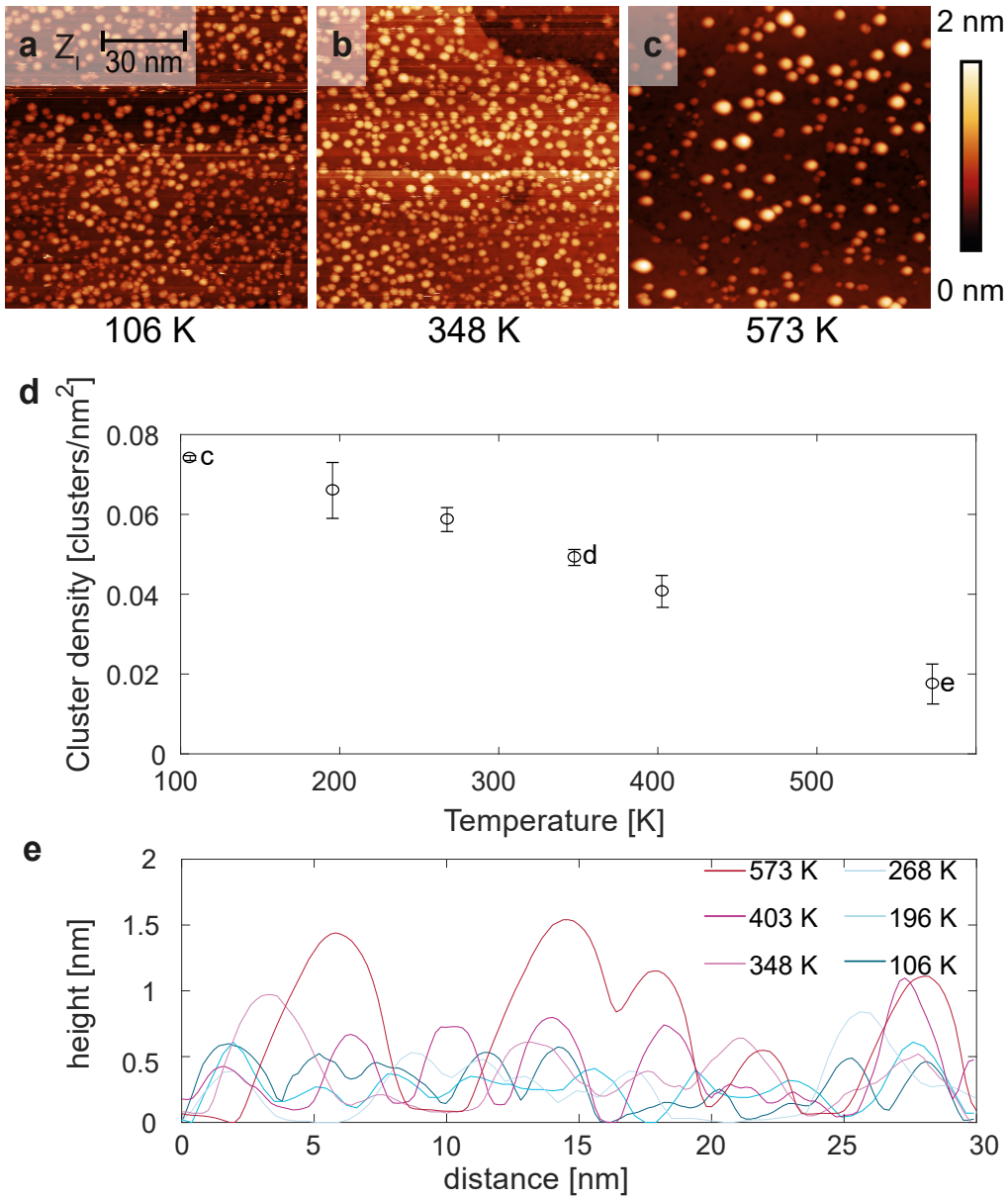

Figure 5.3: Stepwise heating of copper on CaF_2 thin film. (a-c) Heating process of Cu with a low coverage of PPIX on CaF_2 thin films. (d) Plot of Cu cluster density (in clusters/nm^2) at different heating temperatures. (e) Line scans of representative copper clusters of each heating temperature. Imaging parameters: (a-c) $I = 5\,\mathrm{pA}$, $U_S = -4.5\,\mathrm{V}$, $T_S = 77\,\mathrm{K}$.

The cluster density is standardised per square nanometre and averaged over several STM images. The error is determined from the standard deviation of the cluster density of several analysed images. The resulting density for every heating step is shown in figure 5.3d. To reduce an influence of lateral tip-induced displacement, as discussed in the previous section, each sample area is only scanned once. A reduction of the cluster quantity is observed with increasing heating temperatures. The highest cluster density is measured at

106 K with 0.0741±0.0006 clusters/nm^2. A reduction of cluster density is obtained after the deposition from 106 K to 196 K, where a cluster density of 0.066±0.007 clusters/nm^2 is obtained. Heating to 573 K results in an even lower cluster density, which amounts to 0.0175±0.005 clusters/nm^2, which is about 24% of the cluster density observed at 106 K. These observations partly agree with studies of cobalt on CaF_2 surfaces, where higher sample temperatures during the deposition result in a higher diffusivity resulting in larger cobalt clusters, however, desorption starting from temperatures of about 373 K [145]. Therefore, it is debatable, whether the observed reduction of cluster density for copper on the CaF_2 thin film stems from a desorption alone or a combination of desorption and cluster ripening.

In order to address this question, line scans are extracted from representative areas of each sample. The line scans are shown in figure 5.3e, where the apparent cluster height increases with the heating procedure. The clusters formed at 106 K (dark blue) have an apparent height of up to 0.6 nm. An increase in height can be observed beginning at 268 K (light blue), where the apparent height amounts up to 0.9 nm. The clusters formed at 573 K (red) are clearly the highest clusters with an apparent height of up to 1.5 nm. At this heating temperature the clusters are not only higher, but also much broader in shape, which can also be seen in the line scans. The increase in cluster size (height and width) indicates that indeed thermal activation increases the diffusivity of copper on the CaF_2 film with copper ripening and the copper does not solely desorb from the surface. As a result, the increased diffusivity causes the formation of larger clusters. To determine if partial desorption occurs, a further detailed study of the coverage would be required expanding the determination of cluster density to a precise coverage of copper atoms, also considering the height of the copper clusters. However, the shown experiments prove that even after heating to high temperatures of up to 573 K a substantial amount of copper remains on the CaF_2 thin film.

5.4 Conclusions

In summary, $CaF_2/CaF_1/Si(111)$ thin films have been grown. The formed surfaces agree with the previous results reported in literature [148, 161, 165, 166]. The thin film sample shows areas of Si(111), $CaF_1/Si(111)$ and $CaF_2/CaF_1/Si(111)$. The reliable reproduction of CaF_2 thin films allows experiments regarding metal and molecule adsorption. Determination of the $[1\,1\,\bar{2}]$ direction of the $CaF_2(111)$ surface is possible based on determining the Si(111) surface orientation.

Depositing copper onto the $CaF_2/CaF_1/Si(111)$ thin film surface results in the formation of copper clusters. The cluster formation resembles results of other metals on $CaF_2(111)$ surfaces [143, 144, 145]. After performing several STM images of the same surface area, a

reduction of cluster quantity and an increase of cluster size is observed. This indicates that the copper clusters are moved laterally by the tip during the scanning process, which results in pushing clusters together. An additional process causing cluster density reduction can be the pick up of copper by the STM tip. Hence, the copper clusters are weakly bound to the surface, which allows a high mobility on the thin film surface.
When heating the sample system, a reduction of cluster density with increasing temperature is observed. As the cluster size also increases with temperature, a higher diffusivity is one reason for the reduced cluster density. Observations of both tip manipulation and heating lead to the conclusion that the barrier for lateral movement is rather small.
The successful deposition of copper onto the CaF_2 thin films lays a base for reactions of the metal with organic molecules to form metal-organic compounds. The mobility of the copper atoms on the CaF_2 surface can aid the reaction process, as an increased mobility will increase the probability that the different educts meet on the surface. The mobility also allows a fewer copper atoms on the surface, as the likeliness of educts to meet is expected to increase with the mobility of the copper metals.

6 The Challenges of Imaging Flexible Side Groups with NC-AFM

One strategy towards metal-organic molecules on insulating surfaces is on-surface synthesis. An exemplary reaction is the metallisation of prophyrin molecules as described in chapter 2.2. However, and as discussed in section 2.3, a pre-requirement for molecular adsorption on insulating surfaces is the presence of anchor groups that bind the molecule to the insulating surface.
In this chapter, a three dimensional porphyrin molecule will be investigated with NC-AFM using CO-terminated tips. The focus is set on allocating molecular subunits to features in constant-height NC-AFM images.

6.1 Introduction

Protoporphyrin IX (PPIX) is equipped with eight side groups (see fig. 6.1a): two propionic acid moieties (-$C_3O_2H_5$), which can act as anchor groups, two ethylene (-C_2H_3), and four methyl groups (-CH_3). The eight side groups can rotate freely along the sp^3 C-C bonds. These degrees of freedom principally allow a number of different steric conformations. PPIX in its hydrogenated form is the basic building block for several essential biomolecules. In nature, PPIX occurs in its metallised form, either with iron as heme, or with magnesium as chlorophyll [167]. On surfaces, PPIX has been investigated on Cu(110) and Cu(100), where ordered structures are formed at room temperature and metallisation occurs, as was monitored with XPS [47].

The majority of molecules investigated so far with high-resolution NC-AFM using CO functionalised tips exhibit a rather planar shape [168, 169]. However, in recent years, NC-AFM measurements have been extended towards three-dimensional molecules [127, 170, 171, 172, 173]. For the following overview, the three dimensional molecules will be categorized into molecules with rigid moieties and molecules with flexible moieties.
A rigid moiety is classified as chemical group bound to a molecular backbone without

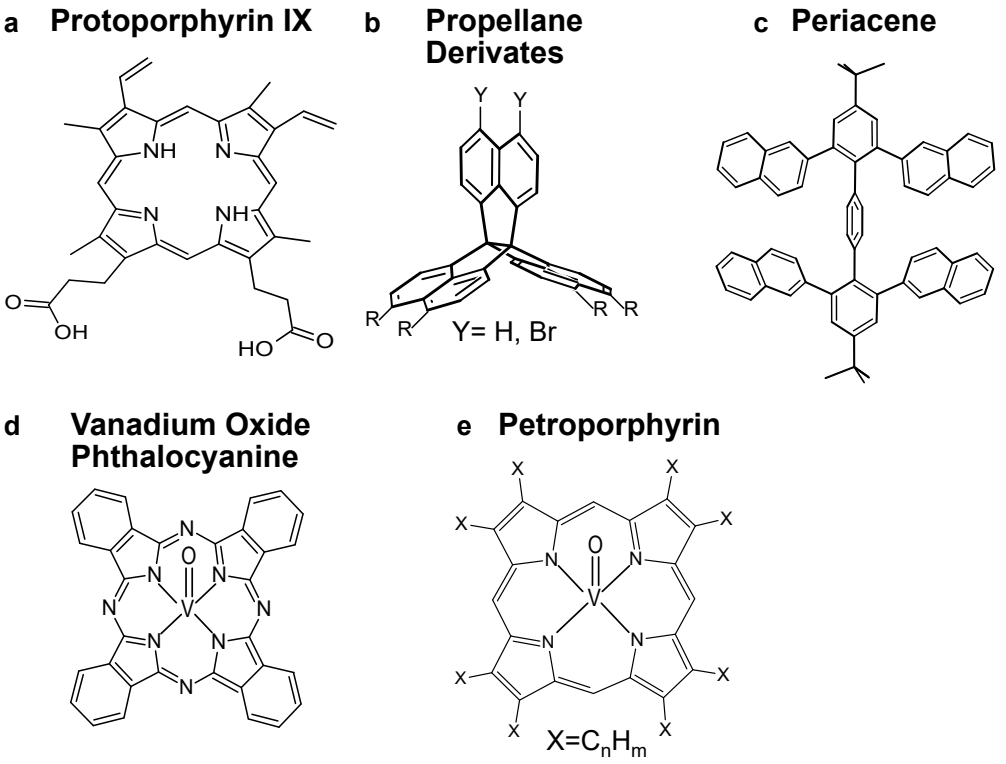

Figure 6.1: Molecular models of (a) protoporphyrin IX, (b) the molecular backbone of propellane derivates substituted at Y-position with either hydrogen or bromine (c) periacene, (d) vanadium oxide phthalocyanine, and (e) petroporphyrin, substituted in meso position with various alkyl chains.

rotational freedom. Examples for rigid moieties include single atoms such as halogens or oxygen atoms, as well as cyclic structures, where more than one atom is attached to the molecular backbone. The absence of a rotational degree of freedom is defined as absence of significant relaxation into another steric conformation. An example, where the absence of relaxation plays an important role during the AFM measurement is when a repulsive interaction is present due to the proximity of a NC-AFM tip.

A flexible moiety contains at least two atoms bound to the molecular backbone via one sp^3 bond, which is the bond type with the highest degree of rotational flexibility. A flexible moiety shows a variety of steric conformations with small energetic difference as a result of the rotational degree(s) of freedom around each bond. Prominent examples are phenyl rings or methyl groups. An increase of the number of steric conformations, resulting in a larger flexibility of the moiety, can stem from multiple sp^3 or sp^2 bonds within the moiety. An example of a moiety with this increased flexibility is an alkyl chain such as propyl or hexyl [174].

The adsorption of molecules on surfaces likely reduces the flexibility of the side group, as

steric conformations may be energetically inhibited due to surface interactions.

Here, I will highlight four prominent examples of NC-AFM imaging of three dimensional molecules with either rigid or flexible side groups. First, three examples of molecules with rigid moieties are discussed, namely, vanadium oxide metallated porphyrin and phthalocyanine molecules, as well as propellane molecules. A unifying property of these molecules is that they have moieties oriented perpendicular to the surface after adsorption. In case of the vanadium oxide metallated porphyrin and phthalocynine molecules, the oxygen atom is sticking out of the molecular plane, where the molecules adopt two main geometries: the vanadium oxide is pointing either up (away from the surface) or down (towards the surface) after adsorption on NaCl thin films on Ag(111) surfaces. [24]. In case of the oxygen pointing away from the surface, the oxygen atom is the topmost point of the molecular structure (see figure 6.1d,e) [24, 175]. In this adsorption geometry of the vanadium oxide metallated porphyrines and phthalocyanines, one protrusion is observed with NC-AFM. High-resolution imaging of the subjacent molecular structures has not been achieved for these examples, as the majority of the molecular structure is located beneath the topmost atoms. Repulsive interactions between tip and the topmost atom hinder imaging at a smaller tip-sample distance [24, 175]. When, investigating the porphyrin molecules in the adsorption geometry, in which vanadium oxide points down, sharp features are observed in high-resolution NC-AFM. Depending on the molecule's side groups, the core of the prophyrin ring can be imaged in the NC-AFM images.

In contrast, the chainlike molecular assembly of propellane molecule (molecular backbone is depicted in figure 6.1b) contains repetitive, cyclic hydrocarbons that point away from both Ag(111) and Au(111) surfaces. Depending on the derivate, the atoms terminating the cyclic hydrocarbons at positions 1 and 8 (indicated with a Y), are either two hydrogen atoms or two bromine atoms. These are the topmost atoms.

Measuring these three-dimensional propellane derivates resulted in particular features in NC-AFM images: The topmost atoms are imaged as a bright protrusion each. When the molecule undergoes partial (full) debromination, one (two) protrusions are missing. Reduced repulsive interactions are measured at these positions when compared to intact molecules [127, 171].

Second, two examples of imaging three-dimensional molecules with flexible side groups are discussed, namely periacenes and petroporphyrins adsorbed on Cu(110) and NaCl/Ag(111) surfaces. Notably, the number of steric conformations differs for the different side groups of the two examples. The first example concerns periacene molecules that contain four naphthalene side groups, three benzene rings, as well as two tert-butyl moieties (see figure 6.1c) [172]. The rotation of each side group is only possible around one sp^3 bond. Therefore, a limited number of steric conformers exist. In particular, the

four naphthalene side groups of periacene can each rotate around one sp^3 C-C bond. Thus, the limiting cases for each naphthalene group are either in-plane with the molecule or rotate into an out-of-plane geometry. The centre benzene ring can adopt an in-plane or out-of-plane geometry as well. As the tert-butyl groups can also each rotate around one sp^3 C-C bond, here, the limiting cases are one or two methyl groups pointing away from the surface. Several protrusions are observed in the NC-AFM images of the periacene derivate on Cu(110), the different features have been assigned to the different side groups by Zhong et al. [172]: sharp, bright lines are observed at the position of two naphthalene groups as well as of the middle benzene ring, allowing to conclude that these groups are positioned in an out-of-plane geometry with C-C bonds being at the topmost positions for each moiety. In contrast, no features are observed in the NC-AFM image at the position of the remaining two naphthalene groups, allowing the conclusion that these groups adopt an in-plane geometry. The tert-butyl groups are imaged as bright protrusions without further substructure, therefore, an allocation of the imaged feature to one or two methyl groups being out of plane has not been achieved [172].

The second example of imaging molecules with flexible side groups is the case of petroporphyrins (see figure 6.1e). Petroporphyrin is the umbrella term for porphyrin molecules found in crude oil. These molecules have a porphyrin core and are typically equipped with alkyl moieties of varying number and length. The alkyl groups have each several rotational degrees of freedom, as multiple sp^3 and sp^2 bonds allow different steric conformers. The metallated form of these molecules can involve Vanadium oxide as discussed before. Prior to NC-AFM experiments, a mixture of these porphyrin molecules has been investigated with mass, infrared, UV-vis, and nuclear magnetic resonance spectroscopy [24]. The spectroscopic investigation allowed the determination of the variety of side groups attached to the different petroporphyrins. Only for specific examples the exact chemical composition has been determined based on the spectroscopic data.

The petroporphyrin molecules have been investigated on NaCl thin films on Ag(111), where the vanadium oxide either points towards or away from the surface. For the molecular adsorption geometry, where the vanadium oxide points towards the surface, bright protrusions are observed at the positions of the molecules' side groups. Zhang et al. have suggested to allocate the protrusions in NC-AFM to specific side groups [24] based on the range of side groups, which have been determined by spectroscopic experiments, and by comparing the protrusions in NC-AFM to previously conducted AFM studies on different model compounds. These model compounds are cyclic molecules such as asphaltenes [176], different polycyclic groups connected via aliphatic linkers [177], as well as the oxygen containing compounds Breitfussin [96] and olympicene derviates, which are cyclic aromatic molecules [178]. Breitfussin contains a methyl group, which is imaged

as one of the brightest protrusions for this molecule in NC-AFM [96]. Based on the comparison between observed NC-AFM features and the model compounds, the features of the side groups are suggested to stem from methyl, ethyl and pentyl moieties.
Additional to these exclusively experimental studies, the analysis of experimental NC-AFM data by combining PPM calculation and artificial intelligence has been performed by Aldritt et al. [173]. In their approach, different characteristics observed in NC-AFM constant-height images observed in NC-AFM are compared to features calculated with PPM for different molecular conformations. A match of the experimental and theoretical contrast allows to allocate specific steric conformations to the experimental data [173].
In conclusion, these examples highlight the difficulty of measuring three-dimensional molecules with NC-AFM. Generally speaking, imaging three-dimensional molecules with rigid moieties usually allows imaging the topmost atoms. This is facilitated by molecules that cannot relax under the NC-AFM tip and, thus, present a strongly repulsive interaction with the tip. With increasing flexibility of the moieties, the number of possible conformation increases and this exacerbates the assignment of features observed in NC-AFM to the molecule's side group.

6.2 The Configurational Flexibility of PPIX on Ag(111) imaged with STM and NC-AFM

PPIX molecules are deposited onto Ag(111) surfaces held at room temperature (see methods 4.2.1 for details). Based on the study of González-Moreno et al.[47], the PPIX molecules remain intact during deposition [47].
The focus in this section is set on unravelling the adsorption geometry of individual molecules on the terraces of Ag(111). To determine the adsorption geometry of single PPIX molecules, first, the position of the different side groups have to be allocated to the features observed in STM and NC-AFM. Second, the orientation of the flexible side groups has to be determined.

Flexibility of the side groups

The PPIX molecule has eight flexible side groups (four methyl, two ethylene, and two propionic acid groups), which can rotate due to the presence of multiple sp^3 bonds. Based on the rotational degrees of freedom, principally, the molecule can exist in different conformations. The different side groups have a different rotational degree of freedom each. As a criteria, I analyse the minimum and maximum heights of atoms in comparison with the prophyrin plane. The height differences of in- and out-of-plane geometry are only

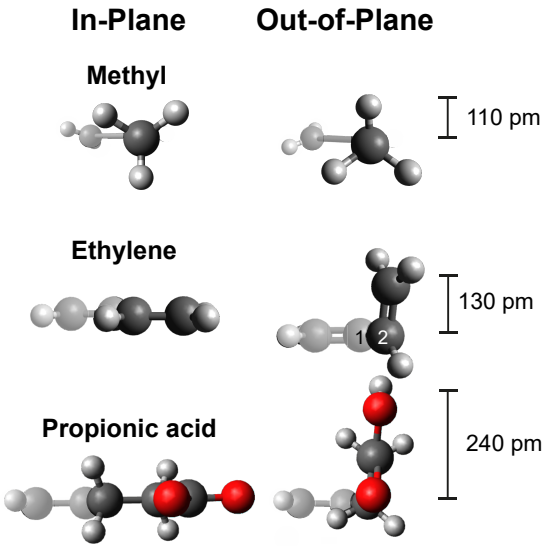

Figure 6.2: Orientation of side groups. Limiting cases of in- and out-of-plane conformations for methyl, ehtylene, and propionic acid side groups.

limiting cases, these are illustrated in figure 6.2. Intermediate rotational configurations are possible. The methyl group can rotate around the single sp^3 C-C bond. The two limiting cases are one or two hydrogen atoms on the top side of the molecular plane. The height difference of both cases are out-of-plane by at maximum roughly 110 pm between the top atomic positions of the different orientations. The ethylene moiety can rotate around the sp^3 C-C bond connecting the carbons indicated as "1" and "2" in figure 6.2. The limiting cases for ethylene are the sp^2 C-C bond pointing out-of-plane or lying within the molecular plane. The height difference between in- and out-of-plane amounts to 130 pm. Propionic acid can express three rotations around the three sp^3 C-C bonds. The limiting cases are on the one hand a situation where all carbon and oxygen atoms are in-plane, and on the other hand a geometry where two carbon and the oxygen atoms are out-of-plane (see figure 6.2). For these cases, the height difference between in- and out-of-plane amounts to about 240 pm.

6.2.1 Results

PPIX molecules decorating the Ag(111) step edges are observed (see figure 6.3a) when imaged with STM, and protrusions of different shapes are present on the surface terraces (see figure 6.3b). The protrusions in figure 6.3b have different shapes. A ball and stick model of PPIX is shown in figure 6.3c, it is in scale with the detail images of the single protrusions (see figure 6.3d-f), highlighting that the size of one protrusion matches the size of a single PPIX molecule. Therefore, due to the protrusions' size, each protrusion is

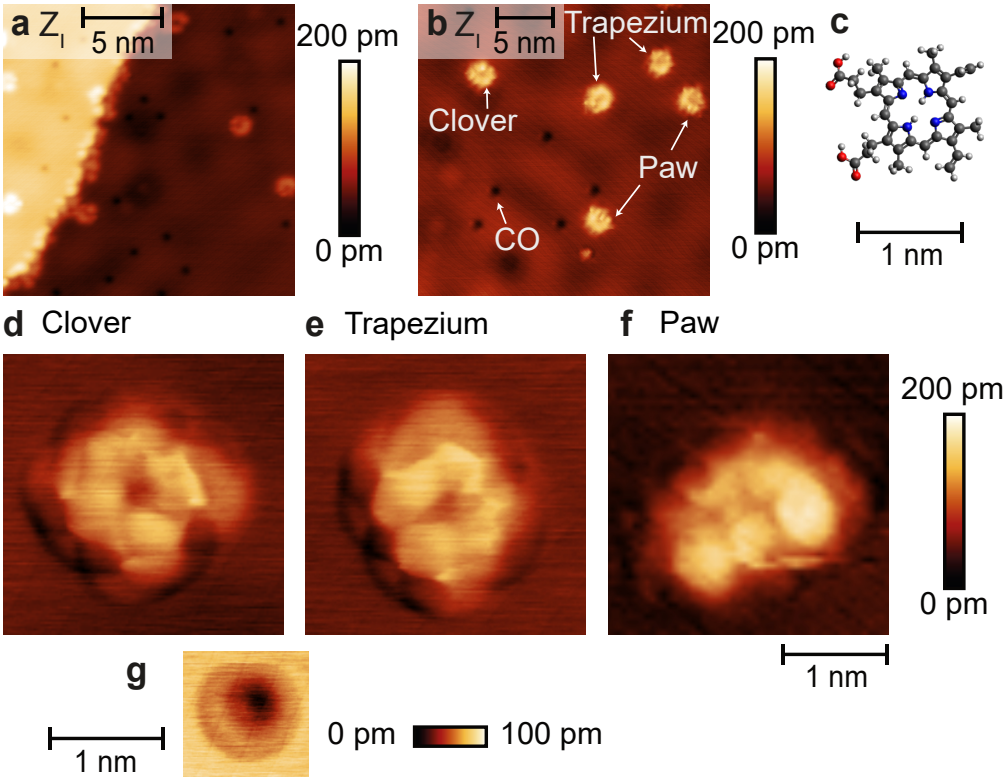

Figure 6.3: (a) Overview STM image of PPIX and CO molecules at an Ag(111) step edge, and (b) overview STM image of five PPIX molecules and five CO molecules on Ag(111). Three different geometries are highlighted: (d) clover-shape, (e) trapezium, and (f) paw. (g) CO molecule imaged with the same CO tip as clover and trapezium. Imaging parameters: (a,b) $I = 12\,\text{pA}$, $U_S = 5\,\text{mV}$, $T_S = 4.6\,\text{K}$; (d,e,f,g) $I = 15\,\text{pA}$, $U_S = 5\,\text{mV}$, $T_S = 4.6\,\text{K}$.

interpreted as a single molecule. The main finding in this and further images is that the molecules are imaged differently. It will be argued below that these differences are due to different orientations of the flexible side groups.

In addition to the PPIX molecules, five CO molecules are visible in figure 6.3b, imaged as dark depressions with a metal tip (an exemplary CO molecule is indicated by a white arrow). As no tip changes are observed throughout the STM image shown in figure 6.3b, a tip dependent imaging effect can be excluded for the following analyisis, as different types of PPIX molecules are observed in the same image.

The different shapes of PPIX molecules are only analysed on the Ag(111) plane to eliminate influence of surface's step edges on the adsorption geometry. Interestingly, from imaging a total of 108 different PPIX molecules with STM, three distinct types have been found that express clear similarities with both metal and CO tips. These three types represent 49 % of 108 molecules imaged, which will be described in the following. Due to their visual shape they will herein be referred to as clover, trapezium, and paw. Of these the predominantly-observed type is the clover type, which is observed in 25 % of the molecules.

Four similarly sized protrusions are imaged in STM, surrounding a dark centre, an example imaged with a CO terminated tip is shown in figure 6.3d. The trapezium, occurring in 12% of the identified cases, is shown in figure 6.3e. This type is characterised by two elongated protrusions in STM imaging. These two protrusions surround a dark centre. An example for the third type, also observed in 12% of the molecules, is shown in figure 6.3f. This paw-like type is distinguished by a larger bulky protrusion on one side of the molecule, with a shape similar to the trapezium, and it exhibits three smaller protrusions on the other side of the molecule. The dark centre in this configuration is not as distinct as in the previous two types.

To investigate the relation between adsorption geometry and imaged features for the three different types, high-resolution NC-AFM with CO functionalised tips is used to investigate PPIX molecules on Ag(111). The constant-height images are taken with an imaging script, where the feedback loop is activated between two images, so a drift correction can be performed using the atom tracking module. The medium value between two feedback positions is given as effective distance. The image with the smallest tip-sample distance is set as zero. Exemplary images are given for different tip-sample distances.

In the images acquired at the largest tip-sample distances, the majority of the molecule is imaged as a dark spot, especially the centre of the porphyrin is imaged as as a dark depression for all three types (see figure 6.4b,f,j). Few, smaller bright protrusions are imaged surrounding the darker area. At this distance, the clover type shows one bright protrusion (see figure P6.4(b)), while the trapezium type shows three protrusions of similar height and size (see figure 6.4(f)). The paw type expresses multiple bright protrusions of similar height (see figure 6.4(j)).

Reducing the tip-sample distance, the number of small bright protrusions increases. The clover shape evolves from a single bright feature (see figure 6.4(b)) into a total of seven bright protrusions (see figure 6.4(c)) upon tip-sample distance reduction. The six additional protrusions are of similar brightness. In comparison with the protrusion observed already at the larger tip-sample distance, the six additional ones are slightly less bright. The trapezium type shows additional three protrusions and incipient sharpening between the protrusions (g) upon a tip-sample distance reduction.

At the smallest tip-sample distances, where imaging the PPIX molecule is possible without destroying the CO functionalised tip, sharp lines are imaged between the bright protrusions. The NC-AFM images at the protrusion positions vary significantly across different types of molecules. The clover type (see figure 6.4(d)) has one protrusion remaining brighter. The sharp lines are connecting the former protrusion positions.

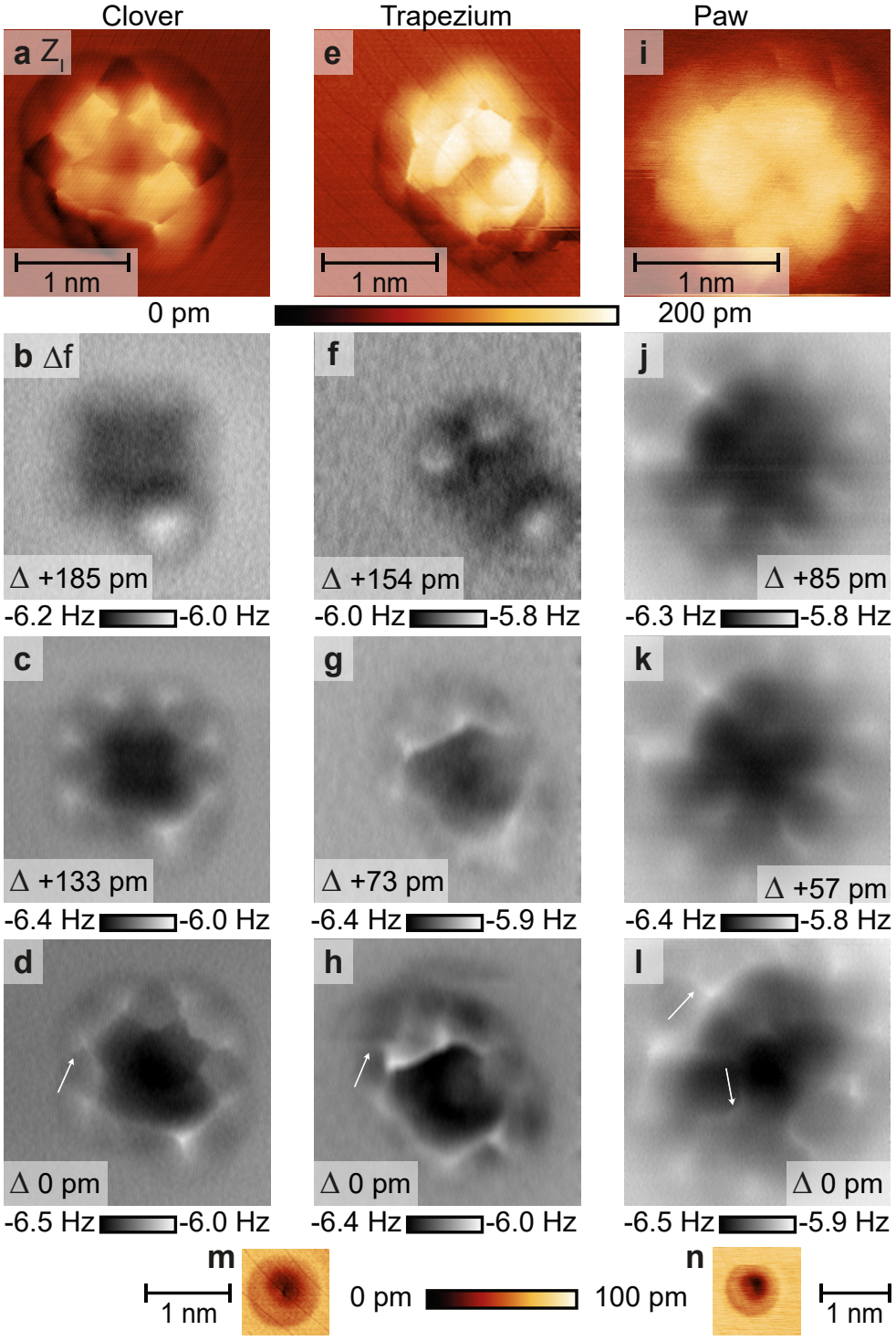

Figure 6.4: Constant-height imaging of three different PPIX geometries with CO functionalised tips. First, the clover geometry is imaged with (a) STM and (b-d) constant-height NC-AFM images. Second, a close up of the trapezium case is imaged in (e) STM mode and (f-h) constant-height AFM. Third an example for the paw geometry is imaged in (i) STM mode and (j-l) constant-height AFM. (m) CO molecule imaged with the same CO tip used for images (a-h). (n) CO molecule imaged with the CO tip used for imaging (i-l). Imaging parameters: STM: $I = 15\,\mathrm{pA}, U_S = 5\,\mathrm{mV}, T_S = 4.6\,\mathrm{K}$, AFM: (b-d) $\Delta f = -6.4\,\mathrm{Hz}, U_S = 0\,\mathrm{V}, f_0 = 26\,654.8\,\mathrm{Hz}, T_S = 4.6\,\mathrm{K}$, 6 pixel mean (f-h;j-l) $\Delta f = -6.2\,\mathrm{Hz}, U_S = 0\,\mathrm{V}, f_0 = 26\,654.8\,\mathrm{Hz} T_S = 4.6\,\mathrm{K}$, 6 pxmean.

From the six less bright protrusions faint features originate at the protrusion position pointing away from the molecular centre, an exemplary line is highlighted with an arrow. The trapezium shape (see figure 6.4(h)) shows three brighter protrusions. Sharp lines are also connecting the different protrusions, and similarly to the clover type faint features are observed at the protrusion position pointing away from the molecule (see arrow in figure 6.4h). The overall arrangement of protrusions and sharp features differs between clover and trapezium type. The paw type (see figure 6.4(l)) also shows bright protrusions connected by sharp lines. Additional to the sharp lines connecting the circular arranged protrusions, sharp lines are observed originating at the protrusion position towards the molecular centre, as well as pointing away from the centre, examples are highlighted with arrows in figure 6.4l. Usually, the CO is lost upon further decrease of the tip-sample distance, based on the three-dimensional character of the moieties.

6.2.2 Discussion

Based on STM and NC-AFM images three types of PPIX molecules occur repeatedly: clover, trapezium, and paw type. As the three types are imaged with both metal and CO tip, it can be concluded that the imaged features are not tip dependent, but the adsorption geometry of PPIX differs between the different types. In this section, the different features observed in NC-AFM constant-height imaging for clover and trapezium types are allocated to the specific side groups based on different criteria. Furthermore, a suggestion for the orientation of the side groups will be made for both types.

Allocating side groups to features in NC-AFM

The observed protrusions in the STM and NC-AFM images do not suffice to lay evidence for allocating the observed details to molecular side groups (methyl, ethylene, propionic acid) directly. Consequently, further criteria are required to finding constraints for determination of the molecules' adsorption geometries for the different types. One possible criteria may be based on the molecular structure, which can be divided into two parts that follow, very roughly, a mirror symmetry. The corresponding mirror symmetry axis is indicated by a dashed line in figure 6.5e. Note, however, that methyl and ethylene groups (highlighted by red and blue ellipses respectively) are interchanged. Additionally, the conformations of the side groups can also break the symmetry. On a side note, the secondary (green) and tertiary (yellow) amino groups are also asymmetrical, however, due to the aromatic character of the porphyrin ring, they are interchangeable. Still, roughly symmetric structures are observed for both clover and trapezium types in the experiments, the shape of the darker inner areas are rather symmetric as shown by CO constant-height imaging in figure 6.5. The darker

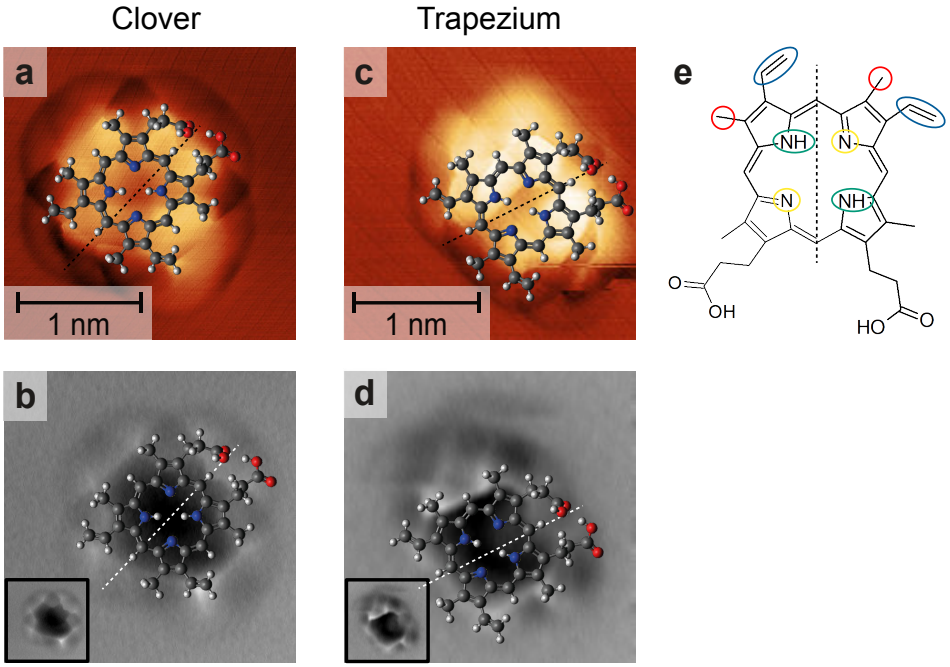

Figure 6.5: (a-d) Possible adsorption geometry for clover and trapezium conformers: The approximative mirror axis is indicated in all images by a dashed line. Ball and stick models of PPIX are positioned onto STM (a,c) and AFM (b,d) images along the approximative mirror axis. The images without molecular model are included in a smaller scale at the bottom of each AFM image. (For larger images please see figure 6.4) (grey: C, white: H, blue: N, red: O) (e) Molecular model. The asymmetric groups are highlighted by coloured ellipses. Methyl groups are indicated by red circles, ethylene groups are highlighted in blue. The secondary and tertiary amino groups are highlighted in green and yellow respectively. Imaging parameters: STM: $I = 15\,\mathrm{pA}, U_S = 5\,\mathrm{mV}, T_S = 4.6\,\mathrm{K}$, AFM: (b) $\Delta f = -6.4\,\mathrm{Hz}, U_S = -0.000\,85\,\mathrm{mV}, f_0 = 26\,654.8\,\mathrm{Hz}, T_S = 4.6\,\mathrm{K}$, 6 pixel mean (d) $\Delta f = -6.2\,\mathrm{Hz}, U_S = 0\,\mathrm{V}, f_0 = 26\,654.8\,\mathrm{Hz}, T_S = 4.6\,\mathrm{K}$, 6 pixel mean.

inner area has a cross shaped form, which can be split into two parts. Yet, the protrusions at the side groups' positions are not perfectly symmetric. Under the assumption that the approximate symmetry axes have the same orientation, only few possibilities for assigning the side groups remain as shown in figure 6.4 and as described in the following.

First, the clover type is discussed: A total of seven protrusions is observed in NC-AFM constant-height imaging. Of the seven protrusions, one protrusion stands out as the brightest. This protrusion is allocated to an ethylene moiety. The remaining six protrusions are allocated to the two propionic acid moieties, the second ethylene group, and three methyl groups. The fourth methyl group, bound to the same pyrrole ring like the ethylene group at the brightest protrusion, sits at a position, where no protrusion is imaged. Perusing the six protrusion by groups, the three methyl groups are distinguished by a similar size and shape. The protrusions allocated to both propionic acids have a broad shape, the area

between the protrusions is imaged bright as well. The second ethylene group is allocated to a protrusion, which is slightly larger than the ones allocated to the three methyl groups. In a similar procedure, the protrusions observed when imaging the trapezium type are allocated to the different side groups. The NC-AFM image of the trapezium type shows also seven protrusions, three of them are imaged slightly brighter than the remaining protrusions. These three are allocated to three methyl moieties. The fourth methyl group is allocated to sit at a region without protrusion. Both ethylene groups sit at positions, where a faint protrusion is observed. The propionic acid moieties are allocated to the protrusions, which are of a similar brightness as the ethylene protrusions, but are slightly bigger.
The constant-height images of the paw type are obtained at a smaller tip-sample distance range. For that reason the images obtained at the different distances are more similar than the images of the other two types. Several bright features are observed, which leads to the assumption that one, or several side groups point out-of-plane and interact with the tip. Further analysis is not possible based on the available data.
Therefore, two orientations of PPIX, one for the clover, and one for the trapezium can be suggested. The differences between clover and trapezium type may be allocated towards different adsorption geometries of the molecule. Nevertheless, I want to emphasise, that these are based on the symmetry assumptions stated in section 6.1 and are only valid for the fact that the PPIX molecules adsorb as intact molecules.

The orientation of the side groups

After allocating the side groups based on symmetry criteria, suggestions on the orientation of each of the side groups will be made based on NC-AFM constant-height series presented in section 6.2.1 and the flexibility of the side groups described in section 6.2.
The large height differences between in- and out-of-plane geometries indicates that only some side groups are visible in AFM. Looking at the contrast observed at large tip-sample distances the number of bright protrusions varies for the different types. This system expresses significant flexibility via the molecules' side groups. A simple count of the circumjacent protrusions in the NC-AFM images at medium distances allows to conclude that the interaction of the molecular side groups with the CO-tip is rather different for the different types. Clearly only some of the side groups are imaged as bright protrusions in all cases. A maximum of seven protrusions is observed for the molecules. The different contrast can stem from different conformations of the side groups. In NC-AFM images most of the moieties are measured at a similar tip-sample distance. The porphyrin core is not imaged in NC-AFM , therefore, the side groups are supposedly pointing out-of-plane. While a maximum height difference of 240 pm (see section 6.1) is possible, a smaller height difference is likely for the side groups imaged. The geometrical differences of the

different side groups, as well as the different conformational states of the specific side groups could explain, why only few groups are observed at larger distances.
For the clover type it can be suggested that the ethylene moiety allocated to the brightest protrusion in NC-AFM points out of the molecular plane, while the second ethylene, and the propionic acid groups are only partially out-of-plane. For the ethylene group a tilted conformation may be possible. The precise structure of propionic acid cannot be suggested, as the moiety has too many degrees of freedom. Three of the four methyl group point out-of-plane with one hydrogen atom, the fourth one being closer in distance to the molecular plane is the one not imaged in the NC-AFM series.
The trapezium type contains three methyl groups, which are depicted as brightest protrusions in NC-AFM, therefore, these are the groups most likely to stick out of the molecular plane. The fourth methyl is not imaged with NC-AFM, therefore, this has to be the moiety with the least interaction with the CO tip. The remaining four moieties (ethylene and propionic acid) are suggested to be partly out-of-plane. The ethylene groups are likely to be tilted. For the trapezium type a general tilt of the entire molecule could be considered, as the sharp line connecting the protrusions of the two methyl groups is depicted brighter in NC-AFM than the line connecting the protrusions of methyl and ethylene groups.
Additionally, it has to be considered that especially the ethylene and propionic acid side groups are flexible. Therefore, when a repulsive tip-sample interaction occurs, the side groups can rotate away from the tip, which causes them to be imaged as less repulsive and therefore less bright.
For further investigations regarding PPIX's adsorption geometry, additional theoretical approaches could be performed. For example, the usage of PPM on DFT optimised PPIX molecules of various adsorption geometries [106]. The comparison of PPM images and experiments could aid to definitely allocate NC-AFM features to specific side groups. This process could be optimised by application of artificial intelligence following the work done by Alldritt et al. [173].

6.3 Investigating Copper and PPIX on Ag(111)

Furthermore, first steps towards the metallisation of PPIX with copper on Ag(111) are performed. The choice of copper follows previous experiments by Gonzalez-Moreno et al., where metallisation has been conducted with copper and PPIX on Cu(110) and Cu(100) [47], details on the reaction pathway are described in section 2.2.
The following experiments are performed after PPIX is deposited at 490 K for 30 min onto the room temperature Ag(111) sample as a first step, in a second step copper is co-deposited onto the sample with a flux of 24.8 nA for 3 min to initiate metallisation.

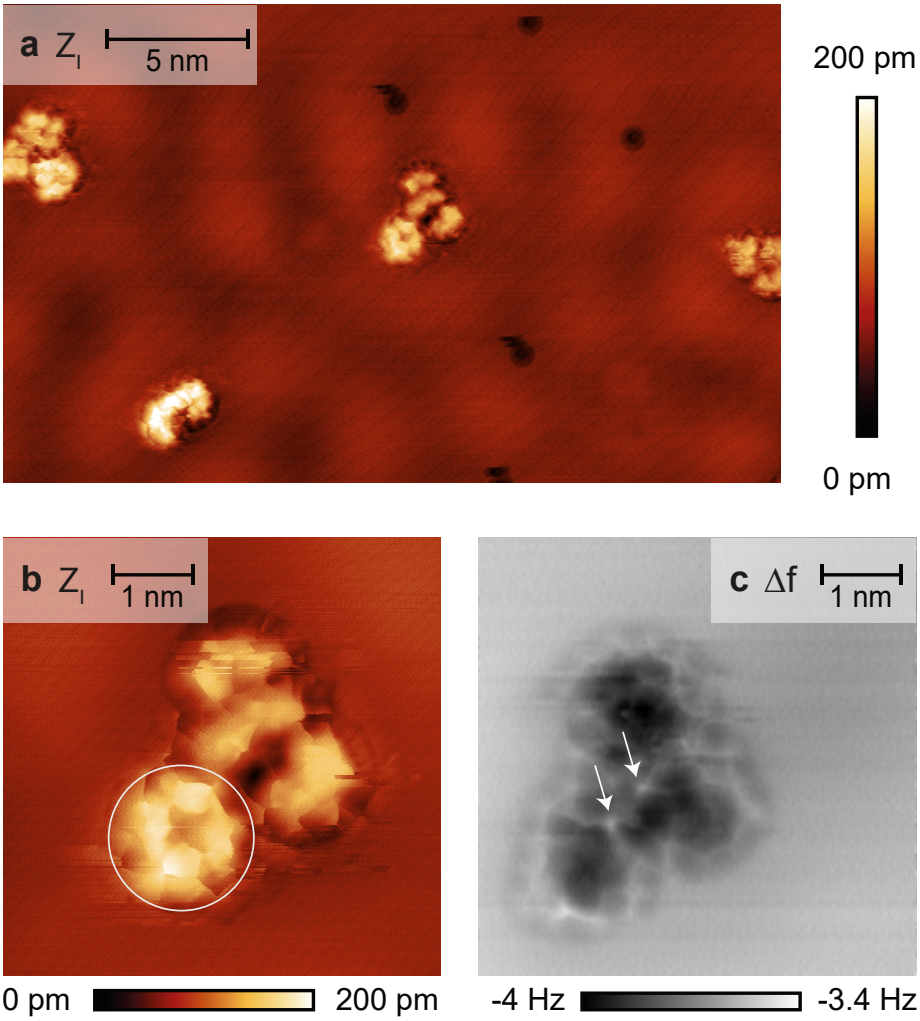

Figure 6.6: Clusters of PPIX and copper. (a) Over view STM image, (b) STM image of a cluster and (b) an AFM image of the same cluster. Image parameters: (a,b) STM: $I = 15\,\text{pA}, U_S = 5\,\text{mV}, T_S = 4.6\,\text{K}$, (b) AFM: $\Delta f = -6.4\,\text{Hz}, U_S = 0\,\text{V}, f_0 = 26\,654.8\,\text{Hz}, T_S = 4.6\,\text{K}$, 6 pixel mean.

The formation of small clusters is the main difference in comparison to PPIX on Ag(111) (see section 6.2). An overview mage of four clusters formed after PPIX and copper

deposition is given in figure 6.6a. An example of one cluster is given in figure 6.6b. The clusters are larger than a single molecule. The size of the clusters varies from about 2 nm to 7 nm, however, only qualitative analysis of cluster size is done, and single clusters can exceed the cluster size. The previously discussed shapes clover, trapezium and paw can be distinguished in some clusters, see for example figure 6.6b, where one clover-shaped PPIX molecule is identified (marked by a white circle). However, in various cases the cluster structure as imaged by STM expresses a complex shape, different to the measurements for pure PPIX on Ag(111) (see figure 6.3).

To yield further insights into the structure of the clusters, constant-height NC-AFM imaging is performed with a CO functionalised tip. Figure 6.6c is a NC-AFM image of the same cluster imaged in (b) by STM. Three darker areas, as well as a few bright protrusions are apparent and sharp lines link some of the bright protrusions. The darker areas resemble the attractive regions of the porphyrin core of pure PPIX. From that observation the presence of three PPIX molecules located at the dark depressions can be suggested. The bright protrusion are repulsive and have been assigned to the molecules' side groups for pure PPIX measurements. Two very bright protrusions in the centre of the cluster (marked by white arrows) are observed in NC-AFM. These two bright protrusions are very prominent and do not resemble previously observed contrast observed for pure PPIX. A possible explanation for these protrusions could be the presence of copper or structural changes induced by copper.

The fundamental challenge in these image data is to relate features in AFM and STM images to the different moieties of PPIX molecules especially the carboxylic acid moieties and to copper atoms or assemblies. The image interpretation is approached by considering the chemical possibilities.

Two possible reaction pathways exist for copper and PPIX: metallisation of the pophyrin core (see section 2.2) or second, coordination via the two carboxylic acid moieties in mono- or bidentate form (see section 2.1). Additional to the chemical reactions, copper atoms can interact with the molecule via weak interactions such as van-der-Waals interactions, for example the metal atoms can interact with the alkyl groups.

First, to monitor a metallisation forming CuPPIX with SPM methods, the porphyrin core has to be imaged (see section 2.2). However, NC-AFM experiments of PPIX with codeposited copper do not show differences in comparison with the PPIX molecules prior the Cu deposition. As concluded in section 6.2, the molecule's side groups inhibit the imaging of the molecule's centre due to their three dimensional character. This leads to the suggestion, that the metal centre is not imaged with STM or AFM. In experiments by Gonzalez-Moreno, the reaction has been monitored with XPS, not SPM methods [47]. Additionally, the formation of clusters is not expected, when metallisation occurs, as the

reaction does not influence the intermolecular interactions. Therefore, it is not possible to conclude, if coordinative bonds have formed in the molecule's centre, unless further experiments with techniques like XPS have been performed.

Second, to determine if intermolecular coordinate bonds between the carboxylic acid moieties and copper atoms or clusters exist, the position of the carboxylic acid moieties needs to be allocated within the imaged features. As shown in section 6.2, side groups of pure PPIX have been proposed to match certain features in the NC-AFM contrast, however the difficulty to clearly identify the components of the clusters exacerbates the allocation of imaged features to the different side groups. Therefore, based on the STM and NC-AFM data, it is not possible to determine if intermolecular coordinate bonds exist within the clusters. A possible approach to clarify, whether intermolecular coordination occurs, is lateral manipulation. Lateral manipulation can be performed with the SPM tip, mechanically separating parts of the cluster. So far, lateral manipulation has been used to dissociate molecules and clusters, allowing the discrimination between hydrogen and coordinate bonds [179].

Third, a non-chemical interaction, such as van-der-Waals interaction, between PPIX molecules and copper could cause the formation of clusters. The copper atoms or clusters can sit between the different side groups, as well as at the outer sides of the prophyrin ring. Imaging of the weak intermolecular interactions with SPM faces similar problems as the imaging intermolecular coordinate bonding. A possible solution is also lateral manipulation.

Additionally, an approach to clarify the position and interaction type of copper with PPIX molecules is the combination of experimental data with theoretical approaches (PPM, DFT calculations), which can be helpful for all three scenarios.

The addition of copper atoms has a clear influence on the molecular assembly: The formation of clusters is observed. This indicates that the molecule-molecule interaction or the molecule-substrate interaction has changed. Due to the three-dimensional character potential coordinate bonds within the porphyrin core have so far not been imaged with STM or AFM. Additional experiments can include heating experiments to eliminate thermal barriers. Inferences could be drawn from the changes in molecular assembly or contrast, if they are observed. Besides, combining SPM methods with additional XPS measurements has been successful in monitoring ongoing metallisation [47], and monitoring the experiments with XPS is promising for this sample system. Additionally, lateral manipulation experiments can give insight on intermolecular interaction. Another possibility is the choice of a porphyrin without protruding side groups. The molecules planar shape should facilitate imaging the metallisation with SPM.

6.4 Summary and Conclusions

In summary, the adsorption of PPIX on Ag(111) is characterised by finding single molecules on flat surface areas. STM imaging reveals a number of molecular shapes, which are explained by different PPIX adsorption geometries. Three types are recurringly observed and herein named clover, trapezium, and paw shape. In constant-height NC-AFM imaging, the single PPIX molecules appear in the form of a dark central area surrounded by a number of bright repulsive features. The number of these protrusions depends on both tip-sample distance as well as the molecular adsorption type. The repulsive interactions are located at the positions of the side groups. The three different side groups have different limiting steric conformations: Methyl can have one or two hydrogen atoms out-of-plane. For ethylene, the complete moiety can be in-plane with the porphyrin ring or the π bond points out-of-plane. Propionic acid has a large variety of steric conformations due to the large number of σ bonds. The limiting cases for propionic acid are in-plane or out-of-plane with the porphyrin core. While the maximum height difference between in and out-of-plane steric conformers amounts to 240 pm, various intermediate conformers exist, where a smaller height difference is possible, which is one reason that the protrusions of the different side groups appear in a very narrow tip-sample distance range. However, based on the occurrence of the protruding side groups, it can be concluded, that at least some of the side groups point out-of-plane and away from the surface. This also hinders the imaging of the molecular core. From the experimental data it is currently a challenge to distinguish between the type of side group and their orientations and, therefore, to precisely determine the molecular geometry on the surface. However, based on symmetric features in STM and NC-AFM images, a adsorption geometry is proposed for clover and trapezium types each. To confirm the proposed adsorption geometries, it is expected that a combination of DFT and NC-AFM calculations could resolve this open point.

The addition of copper to the PPIX on Ag(111) sample system leads to the formation of small clusters with a size of up to 7 nm, consequently, either the intermolecular or the molecule-surface interaction is modified due to the metal addition. STM and NC-AFM imaging of the clusters faced similar challenges as found already for imaging pristine PPIX on Ag(111). The flexibility of the side groups hinders a precise allocation of features observed in STM and NC-AFM images to the molecular structures, which in case of clusters is further exacerbated, as within the clusters single molecules cannot be clearly determined. As the molecular prophyrin cores cannot be imaged with high-resolution, it cannot be concluded if a coordinate bond has been formed based on SPM measurements. As described in section 6.3, clarification might be achieved by a variety of experiments: XPS measurements, heating experiments, or lateral manipulation. Another established

approach to observe metallation reaction with STM and AFM is changing the choice of molecule towards a porphyrin molecule without protruding side groups [29, 49].

6.5 Outlook: PPIX Adsorption on $CaF_2(111)$ Thin Film Surfaces

Molecular adsorption behaviour differs greatly for metal and insulating surfaces. One of the main influences on molecular growth mode are surface energies of the substrate (see section 2.3) [14]. Metal surfaces usually have a at least two times higher surface energy than insulating surfaces [56]. When a molecule adsorbs on a surface with a smaller surface energy, the molecule-surface interaction is weaker, which ultimately leads to dewetting [14].

Depositing PPIX on an insulating surface will result in a weaker interaction between both the porphyrin core as well as the molecular side groups and the surface in comparison to the interaction with the Ag(111) surface. As the surface energy $CaF_2(111)$ amounts to $470\,\mathrm{mJ\,m^{-2}}$ [180, 181], while Ag(111) has a surface energy of $1172\,\mathrm{mJ\,m^{-2}}$ [182], the $CaF_2(111)$ surface is chosen to investigate the effect of a weaker surface interaction on the behaviour of the molecular side groups on the $CaF_2(111)$ surface. But, as a first step, the question arises if the molecule adsorbs, and how it behaves on the $CaF_2(111)$ surface.

PPIX is deposited onto CaF_2 thin film samples held at room temperature as well as thin film samples cooled with liquid nitrogen. For both deposition temperatures STM overview images are shown in figure 6.7. Both images contain areas of CaF_2 and CaF_1 surface, which are decorated with bright protrusions of different sizes on both surfaces.

Due to the high defect density at the CaF_1 surface, molecules favour adsorption at the defect sides of the CaF_1 surface. This agrees with previous studies of PTCDA (perylenetetracarboxylic dianhydride) molecules, which adsorb at defect side of the CaF_1 surface [183]. As the adsorption at defect side is likely to influence the adsorption geometry as well as the behaviour of the side groups, in this work, PPIX adsorption will only be discussed for molecules adsorbed at the near-defect-free $CaF_2(111)$ areas.

Taking a closer look at the protrusions on $CaF_2(111)$ surfaces in figure 6.8, it is obvious that a variety of sizes exist. Examples of smaller protrusions are presented in 6.8a-c. These smaller protrusions have a size comparable to a single PPIX molecule, which is included in scale in figure 6.8h, thus, these protrusions are interpreted as single PPIX molecules adsorbed on the surface.

Other protrusions are significantly larger than the in scale PPIX model, these protrusions are interpreted as clusters of PPIX. Exemplary clusters are shown in figure 6.8d-f. The

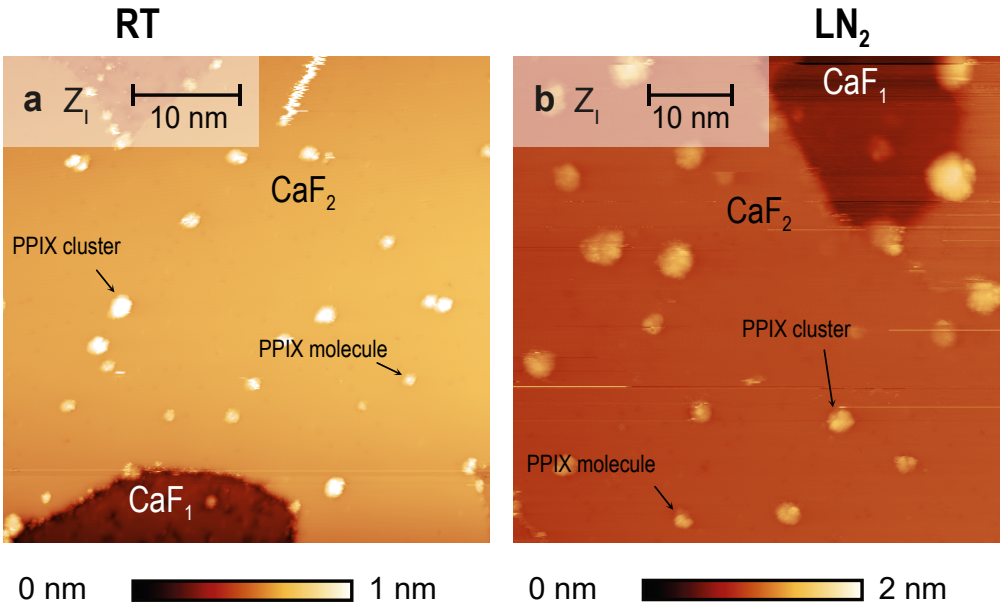

Figure 6.7: STM images of PPIX on CaF_2/CaF_1/Si(111). (a) Overview image with PPIX molecules and clusters on CaF_2 and CaF_1 areas after deposition onto room temperature sample. (b) Overview image of PPIX molecules and clusters after deposition onto the CaF_2 thin film sample cooled with liquid nitrogen. Imaging parameters: (a) $I = 100\,\text{pA}, U_S = -3\,\text{V}, T_S = 77\,\text{K}$, (b) $I = 100\,\text{pA}, U_S = -4.5\,\text{V}, T_S = 77\,\text{K}$.

number of molecules contributing to the cluster cannot be determined directly, as the structure of the protrusion has not been resolved. However, comparing the size of the protrusion to the size of an in scale PPIX molecule (see figure 6.8g) allows an estimation of the number of PPIX molecules within a single protrusion based on two assumptions: First, all molecules adsorb with the porphyrin core parallel to the underlying surface. Second, the molecules lie next to each other and do not overlap.

The cluster shown in figure 6.8d is the smallest cluster, of a size of about two PPIX molecules. A larger size is observed for the cluster shown in figure 6.8f, which exhibits a size of about four PPIX molecules.

Comparison of the PPIX on CaF_2 surfaces to PPIX adsorbed to Ag(111) (see section 6.2) shows that the PPIX molecules on CaF_2(111) surfaces exhibit neither of the three common shapes (clover, trapezium, paw type). However, in comparison to the Ag(111) surface, clusters occur without addition of a metal. This indicates, that the molecule-molecule interaction is stronger than the molecule-surface interaction on CaF_2(111) surfaces than on Ag(111) surfaces. This coincides with different surface energies of Ag(111) and CaF_2(111) surfaces.

Towards the question of the behaviour of the molecular side groups can be deduced that due to the weaker interaction to the surface, the molecular side groups might also show

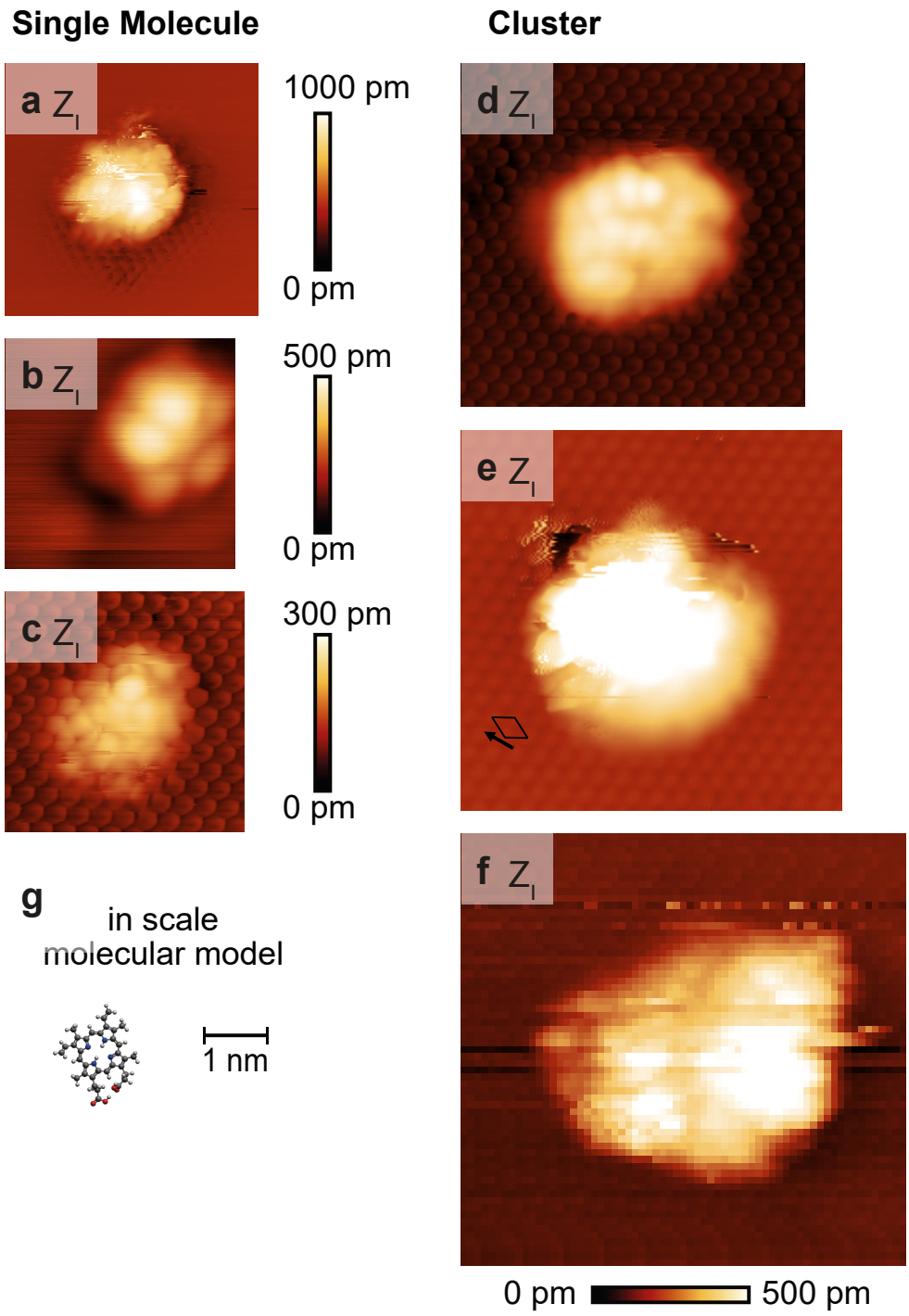

Figure 6.8: STM images of protrusions on $CaF_2(111)$ surfaces. (a-c) Protrusions of similar size of a porphyrin molecule. (d-f) Protrusions of increasing size interpreted as PPIX clusters. (g) A molecular model of PPIX including a scale bar of 1 nm in scale with the STM images (a-f). Imaging parameters: (a,c,d,f) $I = 100\,\text{pA}$, $U_S = -4.5\,\text{V}$, $T_S = 77\,\text{K}$, (b) $I = 5\,\text{pA}$, $U_S = -2.5\,\text{V}$, $T_S = 77\,\text{K}$, (e) $I = 100\,\text{pA}$, $U_S = -3\,\text{V}$, $T_S = 77\,\text{K}$.

less interaction to the underlying surface, which would allow more flexibility. This can explain why three types of molecule are recurringly observed on Ag(111), but no distinct type is observed on CaF_2(111) surfaces.
Therefore, it can be concluded, that the weak interaction of PPIX with the surface results in the formation of PPIX clusters. The molecular orientation of single molecules and single molecules in clusters has not been determined due to the high flexibility of the three dimensional side groups. Towards porphyrin adsorption on CaF_2(111) surfaces for metallation reactions, the molecule should be tweaked towards a slightly stronger molecule-surface interaction. An alteration of molecule-surface interaction can be achieved by three established approaches [184] (see section 2.3). First approach includes adding more functional groups like carboxylic acid to increase the molecule-surface interaction. Second, exchanging functional groups with other functional groups like halides or cyano moieties can alter the interaction type between molecule and surface. Third, changing the geometry of the functional groups can allow a more favourable adsorption geometry, resulting in a different molecule-surface interaction. Altering the prophyrin molecule towards a stronger molecule-surface interaction should aid with the reduction of cluster formation. Furthermore, the elimination of flexible side groups should facilitate imaging of a single molecule as well as determining the adsorbed geometry.

7 Quadruped Molecular Anchoring of Ferrocene Dicarboxylic Acid on $CaF_2(111)$ Bulk and Thin Film Surfaces

The pre-synthesised, commercially available metal-organic molecule 1,1'-ferrocene dicarboxylic acid (FDCA) is deposited to CaF_2 surfaces to obtain a metal-organic compound on an insulating surface.

Ferrocenes are members of the class of sandwich compounds, ferrocene was the first metal-organic molecule synthesised in 1951 [185, 186]. Ferrocene molecules consist of two cyclopentadienyl rings, which form coordinate bonds to the central iron atom, each ring has a hapticity (number of atoms coordinating) of five. A detailed discussion of the characteristics of coordinate bonds is presented in section 2.1. Ferrocene can undergo reversible redox reactions, therefore, they are widely utilised in electrochemistry as reference redox system [187].

Adding tailored anchor groups to ferrocene, makes them promising building blocks for functional molecular structures on surfaces.

Growing molecular films in the Frank-van-der-Merwe growth mode on insulating surfaces, a stronger molecule-substrate interaction is required than for molecules on metal surfaces due to the lower surface energy of the insulator[14]. This is often achieved by so called anchoring, as discussed previously in section 2.3. Anchoring describes the specific interaction between molecule and substrate via anchor groups, which are functional groups linking the molecule to the surface. Therefore, a ferrocene derivate containing two carboxylic acid moieties is chosen, specifically FDCA, where one carboxylic acid moiety is bound to each cyclopentadienyl ring.

So far, FDCA has been investigated on the insulating calcite(104) surface [20], as well as on conducting Ag(111), Au(111), Cu(110), and Cu_3N/Cu(110) surfaces [27]. Different adsorption geometries were found on the different surfaces: FDCA deprotonates on the

Cu(110) and Cu_3N/Cu(110) surfaces, the molecule adsorbs in an upright-standing position [27]. On Ag(111), Au(111), and calcite(104), FDCA molecules stay intact [27]. On the metal surfaces FDCA molecules form self-assembled patterns, while on calcite(104) the FDCA molecules form a (2×1) superstructure [20].

In this chapter anchoring of FDCA on CaF_2 surfaces is investigated with a focus set on the bonding motif formed between the anchor groups and CaF_2, as well as the molecular assembly of the FDCA molecules on the CaF_2 surface. Within this work a quadruped bonding motif is identified as cause for the anchoring. The molecules adsorb in two different orientations on the CaF_2 surface, which are linked to different adsorption geometries.

FDCA adsorption is investigated on both bulk and thin film CaF_2(111) surfaces using STM and NC-AFM, which are performed at 5 K, 77 K, and 300 K. Additional to the experimental results, DFT calculations are performed on the sample system of FDCA on CaF_2(111) to determine the bonding motif between the anchor group and the CaF_2(111) surface. With the aid of NC-AFM image calculations of different adsorption geometries obtained by DFT calculations, experimental and theoretical results can be combined.

The results of this chapter are published in two articles with the titles "Quadruped Molecular Anchoring to an Insulator: Functionalised Ferrocene on CaF_2 Bulk and Thin Film Surfaces" [188] and "Protruding hydrogen atoms as markers for the molecular orientation of a metallocene" [189].

Both publications are summarised in this section and are reprinted with permission in following sections 7.1 and 7.2.

Quadruped Molecular Anchoring to an Insulator:
Functionalised Ferrocene on CaF_2 Bulk and Thin Film Surfaces

Linda Laflör, Fabian A. Schlage, Lev Kantorovich, Philip J. Moriarty, Michael Reichling, Philipp Rahe

The Journal of Physical Chemistry C, American Chemical Society, 2020, 124, 18, 9900-9907, Copyright 2020 American Chemical Society

In this work, anchoring is demonstrated for FDCA to CaF_2(111) bulk and thin film surfaces using NC-AFM and STM measurements. On both CaF_2 bulk and thin film samples the formation of small islands consisting of a few molecules is observed. These molecular islands are stable at 5 K and also during room temperature measurements.

One key result of this study is the comparison of the adsorption characteristics of FDCA on bulk and thin film surfaces. Most importantly, no difference in the molecule adsorption is observed. Thus, results obtained on CaF_2 thin film surfaces can be transferred onto bulk crystals and the other way round. The investigation of thin film samples has the benefit of

a conductive sample, allowing different experimental techniques, such as STM, which are not possible on the bulk crystal.

Comparison of experimental data to DFT calculations indicates that the exceptional stability of the molecular islands stems from a robust quadruped bonding motif between the two carboxylic acid moieties and the CaF_2(111) surface. In detail, the hydrogen atom of each carboxylic acid moiety forms a hydrogen bond to the fluoride of the CaF_2 surface. Furthermore, a bond is formed between the oxygen of the carbonyl part of the carboxylic acid group and the calcium cation of the surface. This bonding motif results in a slightly tilted molecular geometry, which a majority of the FDCA molecules adopt. The molecules with this geometry adapt three different orientations following the threefold geometry of the CaF_2 surface.

A minority of FDCA molecules shows a different orientation on the CaF_2 surface by about 30°. This adsorption geometry can be explained by the energetically second-best DFT-optimised geometry, where one of the carboxylic acid groups is rotated by more than 180° and the ferrocene moiety adapts a partly staggered conformation.

Protruding hydrogen atoms as markers for the molecular orientation of a metallocene

Linda Laflör, Michael Reichling, Philipp Rahe
Beilstein J. Nanotechnology, 11, 1432-1438, 2020

A distinct dumbbell shape is observed as main feature for a single FDCA molecule in the experimental NC-AFM data conducted with a sharp, not functionalised tip. Using NC-AFM image calculations with the probe particle model enables to interpret the distinct dumbbell shape as caused by repulsive interaction between the NC-AFM tip and the top hydrogen of the cyclopentadienyl rings. The simulated and the experimental NC-AFM images show an excellent agreement at several tip-sample distances, both show a distinct dumbbell shape. Interaction with the chemically inert hydrogen atoms in the predominant repulsive regime leads to the suggestion that the chemical identity of the tip is not most important, however, a requirement is the sharpness of the tip to allow resolving the dumbbell shape. In combination with the molecular orientation, a strategy is proposed to determine the conformation of the ferrocene moiety on the CaF_2 surface by using the protruding hydrogen atoms as markers.

The DFT calculations are provided by Prof. Dr. Lev Kanotorovich and Dr. Philipp Rahe, which is gratefully acknowledged. Parts of experiments were performed at the groups of Prof. Dr. Michael Reichling and Prof. Dr. Philip J. Moriarty.

7.1 Quadruped Molecular Anchoring to an Insulator: Functionalised Ferrocene on CaF_2 Bulk and Thin Film Surfaces

7.1.1 Introduction

Motivated by applications in the fields of catalysis, molecular electronic devices, or molecular (opto-)electronics, there is now a large body of work available where the principles and strategies of molecular structure formation on surfaces have been studied. [190, 8] Molecular self-assembly and on-surface synthesis routes have been identified as promising approaches to form complex functional structures especially on metal surfaces. [190, 191] However, applications addressing the molecular conductivity or molecular charge state usually require insulating supports. [192, 193, 20, 194]

On-surface molecular assembly is subject to a quintessential competition between two key interactions, namely, molecule-molecule and molecule-substrate bonds. On metallic surfaces, these two interactions can often be well separated with tuning the molecule-molecule interaction by attachment of specific functional groups, while the molecule-substrate interaction can often be tailored independently by controlling the electronic hybridization or dispersion forces between the metallic surface and a molecular backbone. [190, 8] On insulator surfaces, in contrast, electronic hybridization is absent and dispersion forces are often not sufficient to hinder dewetting at room temperature. [11] Instead, molecular anchoring, where specific end groups bind the molecule to specific surface sites, has been identified as a route to structure formation and enabled the realization of advanced reaction routes on insulating supports. [14, 195, 196]

A key parameter for assessing molecular anchoring is the molecule-surface bond strength. [14] Thus, molecular assembly enabled by anchoring usually relies on surface-induced templating, where the molecular superstructure follows the geometry of the underlying surface lattice. [184] Successful examples of molecular anchoring, where molecules have been observed to form templated structures on insulator surfaces stable at room temperature, include molecules with cyano groups binding to step edges on KBr(001) [197], molecules with flexible cyano groups binding to KCl(001), [60] or molecules with carboxylic acid groups binding to calcite(104). [14, 16] On CaF_2(111) surfaces, a cooperative

anchoring mechanism to stabilise small molecular assemblies of cytosine has been identified, [198] while the molecule-surface bond between 3,4,9,10-perylenetetracarboxylic diimide (PTCDI), as well as chloro[subphthalocyaninato]boron(III) (SubPc) molecules, and CaF_2(111) has been found to be rather weak. [199, 200]

Functionalized ferrocene molecules are promising building blocks for functional structures as they link tailored anchor groups with an active center; plain ferrocene is, for example, widely used as a reference redox system in electrochemistry. [187] Ferrocene molecules functionalized by two carboxylic acid moieties, namely, 1,1'-ferrocenedicarboxylic acid (FDCA), have been investigated on calcite(104) [20] as well as on Ag(111), Au(111), Cu(110) and Cu_3N/Cu(110) surfaces [27] before. Deprotonation of the carboxylic acid groups has been observed on Cu(110) and Cu_3N/Cu(110) surfaces, leading to upright-standing molecules as a consequence of a strong molecule-surface interaction. [27] Instead, intact molecules are observed to arrange into a (2×1) superstructure on calcite(104), [20] while they form complex self-assembled patterns on Ag and Au surfaces [27].

In this study, we identify a quadruped molecular anchoring motif from the interaction of 1,1'-ferrocenedicarboxylic acid (FDCA) with CaF_2(111) surfaces of bulk crystals and thin films grown on Si(111). The anchoring allows for the formation of room-temperature stable assemblies, the observation of single isolated molecules at 300 K, and is a case study for a system exhibiting strong molecule-surface and weak molecule-molecule interactions. Results from non-contact atomic force (NC-AFM) and scanning tunnelling microscopy (STM) experiments are complemented by *ab-inito* calculations using density functional theory (DFT). The combination of these experimental and theoretical approaches unravels the molecular adsorption characteristics including details regarding the molecule-surface bond formation.

7.1.2 Methods

Sample preparation and scanning probe microscopy experiments were performed under ultrahigh vacuum conditions ($p < 5 \times 10^{-10}$ mbar) in four separate vacuum systems. An overview of the systems is given in Tab. 7.1.

Sample Preparation Thin film CaF_2 surfaces were prepared in two steps. First, flash cycles yield the (7×7) reconstruction on highly B-doped p-type Si(111) samples (Institute of Electronic Materials Technology, Warsaw, Poland). Next, CaF_2 material (cleanliness 99.9 %, Alfa Aesar) was deposited from an EFM3T e-beam evaporator (Focus GmbH, Huenstetten, Germany) on the Si(111) surface held at about 600 °C. The CaF_1 interface layer forms at this temperature and enables CaF_2 multilayer growth; further details can be found in ref [148].

system	type	mode	sample	T (K)
A	Omicron LT gen.II	NC-AFM, STM	thin film	5, 77
B	Omicron LT gen.III	NC-AFM	bulk	5
C	Omicron VT STM 25	STM	thin film	300
D	RHK Beetle VT AFM	NC-AFM	bulk	300

Table 7.1: Experimental Conditions Used within This Study (T: Measurement Temperature).

Bulk CaF_2 samples (Korth Kristalle, Altenholz, Germany) were prepared by mechanical cleaving in a vacuum after degassing the crystal and sample holder. [118] The sample was heated at about 330 K for 1 hbefore molecule deposition and NC-AFM experiments on system B, while it was directly used without heating on system D.
The $[1\,1\,\overline{2}]$ surface direction is determined experimentally as follows: CaF_2 bulk crystals are cleaved along another {111} plane after the experiments, and the $[1\,1\,\overline{2}]$ direction points toward the obtuse edge of the produced {111} surface. On the thin film samples, the CaF_2 $[1\,1\,\overline{2}]$ direction can be determined by inspecting the orientation of the (7×7) unit cell of silicon in STM as CaF_2 films are grown in type-B epitaxy. [148]
Molecule Evaporation Homebuilt Knudsen cells were filled with 1-1'-ferrocenedicarboxylic acid material (cleanliness 98 %, Alfa Aesar, Landau, Germany). The compound was degassed for several days for further purification before deposition. FDCA was evaporated at about 390 K on samples held at room temperature.
Scanning Probe Microscopy Low-temperature STM and NC-AFM measurements on thin film samples were performed at 5 and 77 K with an Omicron LT qPlus gen.II instrument (Scienta Omicron GmbH, Taunusstein, Germany) using a MATRIX control system (system A). Tuning-fork sensors in a qPlus configuration [90] with a W-tip and a separate tip wire were used in this system. Despite the presence of electrostatic background forces, NC-AFM experiments on thin film samples were performed at 0 V to exclude cross-talk between the NC-AFM and tunneling current signals. [201] Low-temperature NC-AFM experiments on bulk CaF_2 samples were performed with an Omicron LT qPlus gen.III instrument connected to a MATRIX control system (system B). qPlus sensors as supplied by the manufacturer were used in this system. Room-temperature STM data on CaF_2 thin film samples were acquired with an Omicron VT AFM 25 controlled by a MATRIX system and using W-tips (system C). Room-temperature NC-AFM measurements on bulk samples were performed using an RHK beetle-type AFM UHV 750 instrument (RHK Technology, Troy MI) operated by an RHK R9 control system (system D). Ar-sputtered Si cantilevers (type PPP-NCH from Nanosensors, Neuchâtel, Switzerland) with eigenfrequencies of around $f_0 \sim 300$ kHz were used in an optical beam-deflection configuration. For charge

compensation, a bias voltage of typically −5 V was applied to minimize the electrostatic background forces.

All experimental data were analyzed using Gwyddion. [120]

Density Functional Theory Calculations Calculations were performed with the CP2K (www.cp2k.org) code. [202] Mixed Gaussian and plane waves were used together with the MOLOPT short-range basis sets of double-ζ quality [203, 204] and Goedecker-Teter-Hutter (GTH) potentials [205] using the Perdew-Burke-Ernzerhof (PBE) generalized gradient approximation (GGA) functional [206] and the Γ point sampling. van-der-Waals interactions were included using the Grimme DFT-D3 dispersion correction, [113] as implemented in CP2K. Results were cross-checked using the nonlocal rVV10 method, [207] yielding systematically higher adsorption energies but similar molecular geometries. The basis-set superposition error is included in the adsorption energies and was calculated using the counterpoise method. [208] The adsorption energies were all calculated with respect to the staggered FDCA gas-phase geometry.

For the geometry optimization of single FDCA molecules, the $CaF_2(111)$ surface was modeled by a 5×5, 6-layer CaF_2 slab with the lowest CaF_2 layer fixed in the bulk geometry. Three CaF_2 triple layers (lowest triple layer fixed) and a 6×6 surface unit cell were used for calculating dimer geometries. The 1×10^{-4} Ha/Bohr force tolerance has been used in geometry optimization calculations.

The electron density difference is calculated as $\Delta\rho = \rho_{\text{slab+FDCA}} - \rho_{\text{slab}} - \rho_{\text{FDCA}}$, whereby $\rho_{\text{slab+FDCA}}$ is the electron density of the full system, while ρ_{slab} and ρ_{FDCA} denote the electron densities of the $CaF_2(111)$ slab and the FDCA molecule, respectively. CP-corrected dimer binding energies $E^{\text{CP}}_{\text{dimer}}$ are calculated as $E^{\text{CP}}_{\text{dimer}} = E^{\text{CP}}_{\text{dimer,total}} - E_{\text{slab}} - 2E_{\text{FDCA}}$ with the 2-body CP-corrected total dimer energy $E^{\text{CP}}_{\text{dimer,total}}$ and the energies of the separately geometry-optimized slab (E_{slab}) and FDCA (E_{FDCA}) subsystems. The energy gain/loss is calculated by comparison with two FDCA/$CaF_2(111)$ monomers: $E_{\text{diff}} = E^{\text{CP}}_{\text{dimer}} - 2E^{\text{CP}}_{\text{monomer}}$.

7.1.3 Results and Discussion

NC-AFM and STM experiments were performed in situ after depositing FDCA to a coverage between about 0.02 and 0.2 FDCA/nm^2 on bulk and thin film CaF_2 samples. The samples were held at room temperature during deposition; see Methods for further details. $CaF_2(111)$ surfaces are terminated by a layer of fluoride ions with F-Ca-F triple layers stacked along the (111) direction; see Fig. 7.1a. Bulk $CaF_2(111)$ surfaces were prepared by in situ cleaving, leading to surfaces with large, defect-free terraces. [139, 209] For the growth of CaF_2 thin films on Si(111), we chose preparation parameters, where CaF_2 multilayers grow on top of a CaF_1 interface layer, the latter being the result of an interface

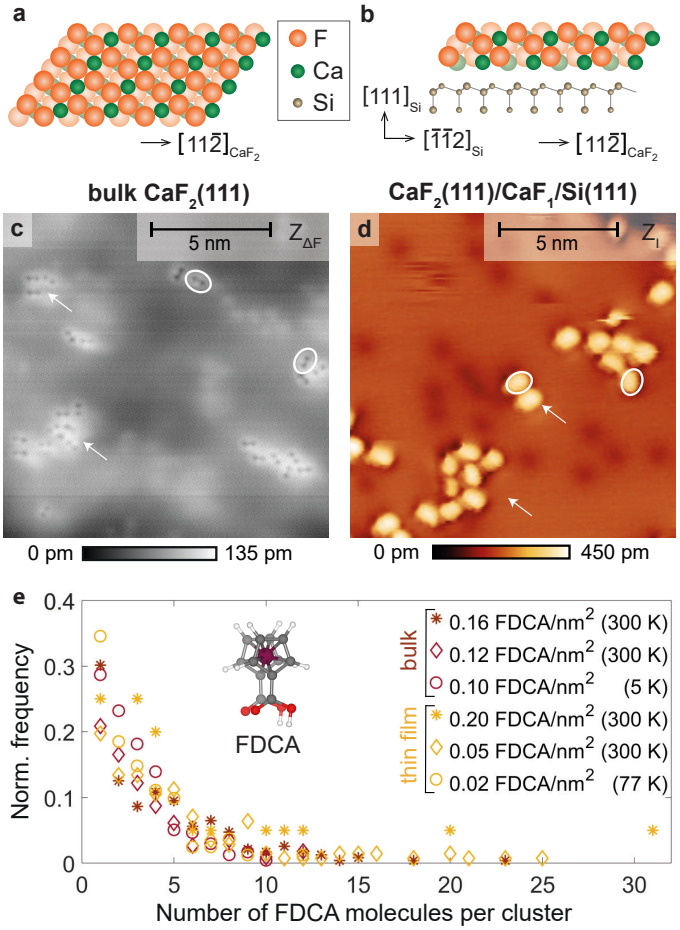

Figure 7.1: FDCA molecules deposited on bulk and thin film $CaF_2(111)$ surfaces. (a,b) Cross-sectional models of the bulk and thin film surface systems. (c) NC-AFM measurement on a bulk sample at 5 K and (d) STM measurement on a thin film sample at 300 K. (e) Normalized FDCA cluster size distribution for different $CaF_2(111)$ surfaces. Results for bulk crystal (thin film) samples are plotted in red (yellow). The respective coverage and measurement temperature are given in the legend. Molecular deposition was performed with the samples held at room temperature. Imaging conditions: (c) NC-AFM with qPlus sensor ($f_0 = 26\,641$ Hz) at $\Delta f = -5.5$ Hz, $U_S = 4$ V, $T_S = 5$ K; (d) STM at $I = 2$ pA, $U_S = -3$ V, $T_S = 300$ K.

reaction between CaF_2 molecules and the Si(111)-(7×7) surface. [148, 210, 158] Because of only a small lattice mismatch (0.6 % at 300 K) between CaF_2 and the underlying silicon, the atomic structures of the bulk and thin film (111) surfaces are virtually identical. Thus, the main difference between the $CaF_2(111)$ bulk and thin film surface is the presence of the underlying CaF_1 interface layer binding to the silicon surface for the thin film sample; see Fig. 7.1b where the structure of a single CaF_2 layer on $CaF_1/Si(111)$ is shown. Surfaces are usually prepared in a way that both $CaF_2/CaF_1/Si(111)$ and $CaF_1/Si(111)$ areas are present in the sample.

Atomic-size defects within the CaF_1 interface layer have been identified by high-resolution NC-AFM imaging, [148] while the CaF_2 layer is expected to be virtually defect-free. Therefore, we herein do not investigate the properties of FDCA molecules on the CaF_1 interface layer.

et 7.1c,d presents NC-AFM and STM data acquired on $CaF_2(111)$ bulk and thin film samples, respectively, where small clusters of molecules are revealed; exemplary clusters are marked by arrows. In NC-AFM imaging, the smallest unit observed within these clusters is a pair of dark depressions embedded in a bright halo, which we will herein refer to as dumbbells. Exemplary dumbbells are marked in Fig. 7.1c by white ellipses. Due to the large band gap of CaF_2, STM experiments can only be performed on the thin film samples. In the respective STM data, the smallest unit observed is an elliptic protrusion; two examples are marked in Fig. 7.1d. The dumbbell and elliptical shapes will, in the following, be identified as single FDCA molecules.

From a total of 347 and 243 clusters measured on bulk and thin film surfaces, respectively, at coverages ranging from 0.02 to 0.2 FDCA/nm^2, we extract the occurrence of the number of cluster-forming units having the dumbbell or elliptical shape with the results shown in Fig. 7.1e (data for bulk and thin film samples are shown in red and yellow, respectively). Under all conditions, namely, bulk and thin film samples investigated with NC-AFM and STM at 300, 77, or 5 K (see the Supporting information Figure S1 for a full data overview), we observe very small and stable FDCA assemblies, including the presence of single FDCA molecules. Specifically, the island size density distribution in Fig. 7.1(e) reveals no significant difference in the functional dependence of the normalized abundance of the island sizes for the different samples; for both surfaces, more than 85 % of the islands contain 10 or less molecules. The observation of similar distributions for the bulk and thin film surfaces suggests a negligible influence of the underlying CaF_1 interface layer on the assembly. As bulk $CaF_2(111)$ surfaces are known to exhibit an exceedingly low defect density, [139, 209] the similarity of the distribution functions for bulk and thin film surfaces furthermore suggests a similarly low defect density for the thin film CaF_2 layer. In contrast, mostly single FDCA molecules are found on the CaF_1 interface layer (data not shown), where a large number of defects have indeed been observed [148].

Finding similar adsorption properties for FDCA on $CaF_2(111)$ bulk and thin film samples is markedly different from studies performed for PTCDA on NaCl(001) and KBr(001) bulk and thin film surfaces. [211, 212, 213] In the latter examples, distinct differences in the on-bulk and on-thin film molecular structures have been observed.

Detailed NC-AFM and STM images of the same molecular cluster containing five of the aforementioned units are shown in Fig. 7.2a,b. There is a good match between the scaled ball-and-stick FDCA models (overlaid on the experimental data in Figure 7.2a,b)

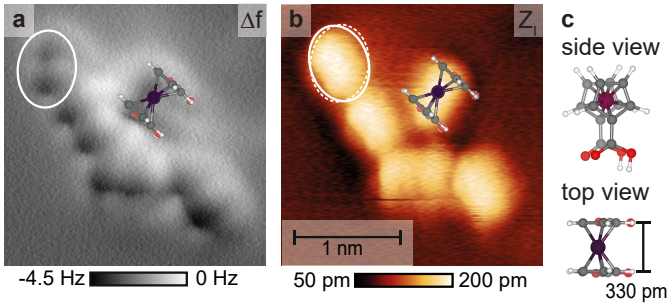

Figure 7.2: Imaging one FDCA cluster with NC-AFM and STM. (a,b) FDCA cluster formed by five molecules imaged in constant-height NC-AFM and constant-current STM. (a) Molecules appear as dumbbells in NC-AFM constant-height frequency-shift data. (b) Elliptical protrusions are apparent in STM data. A to-scale model of a single FDCA molecule is overlaid in the experimental data and a single FDCA molecule, which was manipulated while scanning, is marked. (c) Model of FDCA in eclipsed conformation. Imaging conditions: (a) constant-height NC-AFM image acquired with qPlus sensor ($f_0 = 26\,641$ Hz) at $U_S = 0$ V, $T_S = 77$ K. A 4 pixel averaging filter was applied to the image data; (b) STM at $I = 2$ pA, $U_S = -3$ V, $T_S = 77$ K.

and one dumbbell imaged in NC-AFM, as well as one elliptical protrusion imaged in STM. In particular, we measure from the images an average distance between the two dumbbell depressions in the NC-AFM data of (500 ± 100) pm, which is close to the separation of 330 pm between the two cyclopentadienyl (Cp) rings of a single FDCA molecule in the FDCA bulk structure (see Fig. 7.2c), but does not match the distance of about 900 pm between the Fe centers of the two nearest FDCA molecules in the bulk dimer structure. [214, 215] Thus, we identify one protrusion in STM as one single FDCA molecule, while the NC-AFM appearance of a single molecule is the dumbbell shape with two depressions surrounded by a bright halo. This interpretation is supported by the observation that a single feature can be manipulated by the scanning tip as it happened with the molecule marked in Fig. 7.2a,b within an image (not shown) acquired between the NC-AFM and STM data presented in Fig. 7.2.

To clarify the adsorption geometry and molecular orientation, we performed density functional theory (DFT)-based geometry optimization calculations (using the CP2K package [202]) for a single FDCA molecule adsorbed on a $CaF_2(111)$ slab in a total of eight FDCA/$CaF_2(111)$ starting geometries. (See Methods and the Supporting Information for more details.) The most stable adsorption geometry (geo 1) found across all investigated structures is shown in Fig. 7.3. The FDCA molecule takes an "eclipsed" conformation, where the two carboxylic acid groups point to the same direction. As a consequence, both Cp rings and carboxylic acid groups are located on top of each other. Although this eclipsed conformation is also adapted in the bulk structure, [215] we found for an isolated gas-phase FDCA molecule a preference for a partly "staggered" conformation, where the

rings are rotated by about 60° toward each other, with an energy gain of about −0.06 eV (see the Supporting Information, Figure S2).

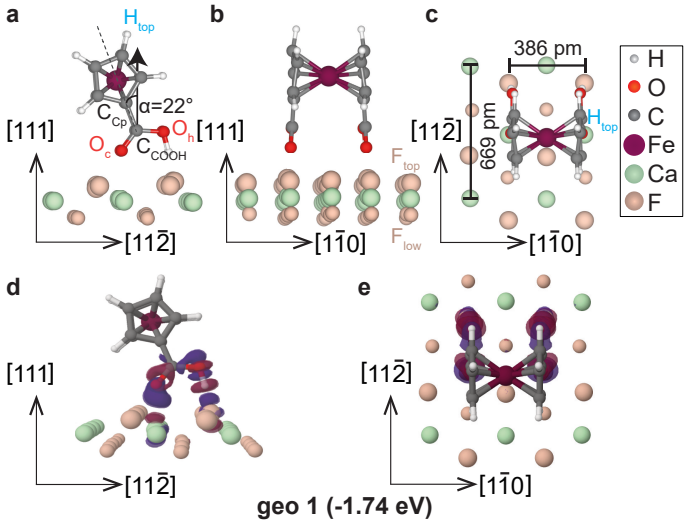

Figure 7.3: Adsorption geometry geo 1 of FDCA on $CaF_2(111)$. (a,b) Side and (c) top views of FDCA/$CaF_2(111)$ in the DFT-optimized geometry (for clarity, only the top CaF_2 layer is shown). (d) Side and (e) top views of the electron density difference with isosurfaces at $-0.015\,e/Å^3$ (red) and $0.015\,e/Å^3$ (blue).

In the minimum energy geometry geo 1, the carboxylic acid groups point toward the $CaF_2(111)$ surface and are in plane with the linked Cp rings. The carbonyl oxygens (O_c) are located on top of surface calcium ions, while the hydroxyl oxygen atoms (O_h) form bonds via the hydrogen atoms to top fluorine (F_{top}) surface atoms. The F_{top}-H-O_h distance of 2.52 Å is in good agreement with the distance expected for a moderate-to-strong hydrogen bond, [216] and the Ca-O_c distance of 2.40 Å points toward a more pronounced interaction. The geometry is furthermore favored by the approximate match between the O_h-O_c distance of 227 pm and the Ca-F_{top} distance of 281 pm, and the side and top views in Figure 7.3b,c reveal a close match between the FDCA bulk structure Cp ring distance of 330 pm with the $CaF_2(111)$ surface unit cell size along [1$\bar{1}$0] of 386 pm. An analysis of the electron density difference $\Delta\rho$ using isosurfaces of $\pm 0.015\,e/Å^3$ (e being the elementary positive charge) is shown in Figs. 7.3d,e. The bonding electron density is strongly localized at the carboxylic acid moieties and their nearby surface atoms, specifically along the two F_{top}-H-O_h and the two Ca-O_c bonds. The result of the molecule-surface interaction is a slightly tilted molecular geometry with an angle α of the C_{COOH}-C_{Cp} bond to the (111) surface normal of about 22°, as marked in Fig. 7.3a. Consequently, the ferrocene subunit protrudes from the surface, with the highest point above the surface plane occupied by the two top hydrogen atoms H_{top}, one from each Cp ring. The resulting quadruped binding motif, where one may imagine the molecule standing at 4 feet on the surface, explains

the experimental finding of room-temperature stable molecular adsorption as effectively a total of four entities bind rather independently, each in a favorable vertical geometry, to the $CaF_2(111)$ surface.

Next, by analyzing the molecular orientations and nearest-neighbor geometries we provide evidence that the molecular assembly is templated by the $CaF_2(111)$ surface. The $CaF_2(111)$ surface belongs to the planar space group $p3m1$, while the planar space group of only the topmost fluoride layer would be $p6mm$. As the DFT-calculated, energetically preferred FDCA geometry geo 1 includes interactions with F_{top} and Ca atoms, three equivalent adsorption positions on the surface following the 3-fold rotational $CaF_2(111)$ surface symmetry are expected. These equivalent orientations, which also include equivalent orientations due to the surface mirror symmetry, can be characterized by the alignment of the molecular Cp-Fe-Cp axis at 30, 150, and 270° with respect to the $[1\,1\,\bar{2}]$ direction; see Fig. 7.4a. However, as mirror-symmetric dumbbells (NC-AFM) or ellipses (STM) are typically observed in the experiments, the molecular orientations are only determined within the range of 0-180°, with the 270° orientation appearing at 90°. Thus, we expect to observe angles of 30, 90, and 150° for the Cp-Fe-Cp molecular axis from the experimental data. Due to the eclipsed Cp rings, the top hydrogen atoms (marked by blue circles in Fig. 7.4a) producing the dumbbell contrast are aligned with the Cp-Fe-Cp axis.

The orientations of a total of 962 FDCA molecules were determined using the orientations of the dumbbell (NC-AFM) and elliptical (STM) shapes and with respect to the $[1\,1\,\bar{2}]$ surface direction on bulk (788) and thin film (174) CaF_2 surfaces, yielding the angular distribution histograms shown in Fig. 7.4b. On thin film samples, molecules bound to step edges were ignored. No step edges were observed within the images on CaF_2 bulk samples. Across the range 0-180° we find three clear maxima for both surfaces at angles of 30, 90, and 150° (we estimate an error of ±2.5° for the angle measurement), in agreement with the expectation from the 3-fold surface symmetry and the optimum adsorption geometry. Additionally, three minor peaks with maxima at about 0, 60, and 120° can be identified in the bulk data. These peaks are not clearly apparent from the thin film surface data, however; we explain this by the reduced total number of orientations extracted from the thin film experiments.

The minor peaks can be explained by the energetically second-best DFT-optimized geometry geo 2 (see the Supporting Information Figure S3 for models of all further calculated geometries); the top and side views of the geometry are shown in Figure 7.4c,d. geo 1, the calculated adsorption energy is reduced by 0.16 eV. For this geometry geo 2, the carboxylic acid moiety A is found in a position very similar to the one in geo 1, namely, in plane with the close-by Cp ring binding to F_{top} and Ca surface atoms, while the other carboxylic acid moiety B is rotated by more than 180° around the C_{COOH}-C_{Cp} bond. In

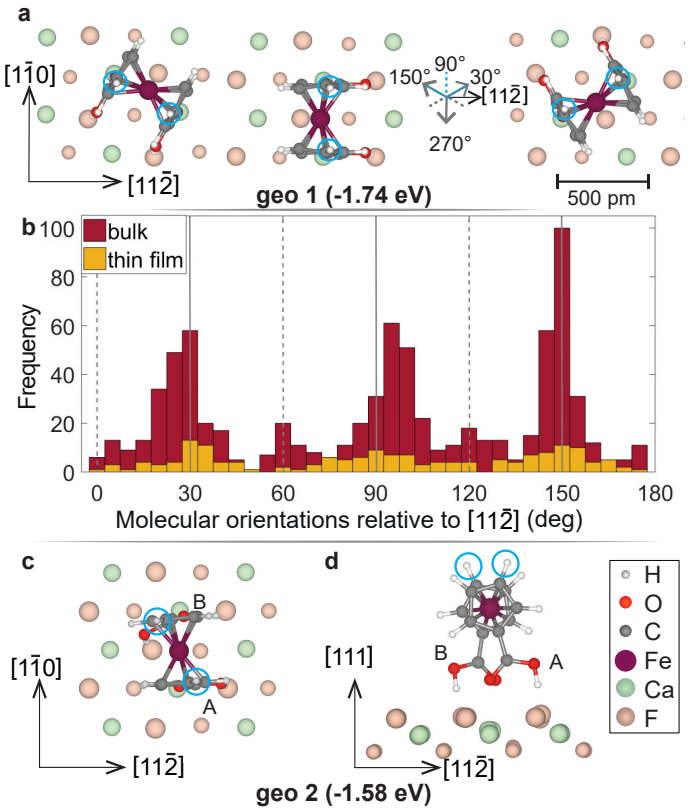

Figure 7.4: Analysis of molecular orientations. (a) Sketches of FDCA molecular orientations (geo 1) following the 3-fold rotational symmetry of the CaF_2(111) surface. (b) Frequency of experimentally measured orientations for bulk (thin film) samples plotted in red (yellow), clearly showing the expected orientations of 30, 90, and 150°. Orientations are analyzed with respect to the [1 1 $\bar{2}$] surface direction. (c) Top and (d) side-view of DFT-optimized less favorable (metastable) molecular geometry (geo 2), explaining the intermediate peaks at about 0, 60, and 120°.

particular, a bond between the carbonyl oxygen and the Ca surface atom is still present as in geo 1; however, the hydroxyl group moves toward the molecular center and binds to F_{top} underneath the molecular iron. As a consequence, the FDCA molecule adapts a partly staggered conformation with the Cp-Fe-Cp axis oriented at about 30° with respect to the [1 1 $\bar{2}$] direction. The staggered Cp rings also cause the protrusion of only one hydrogen atom per Cp ring into the vacuum; yet, due to the staggered ring orientation, the two protruding hydrogen atoms are at different ring positions. When drawing a line along these two hydrogen atoms, we find an angle of about 60° with respect to the [1 1 $\bar{2}$] directions, 30° off the hydrogen orientation found in geo 1, causing intermediate orientations. Thus, the flexibility of the FDCA molecule enables the experimental observation of at least two molecular geometries with their experimental occurrence frequency reflecting the order of the DFT-calculated adsorption energies. More importantly, however, we find a retention of the bond formation between the carboxylic acid moieties and the top-layer surface ions,

which additionally highlights the strong templating effect of the substrate.

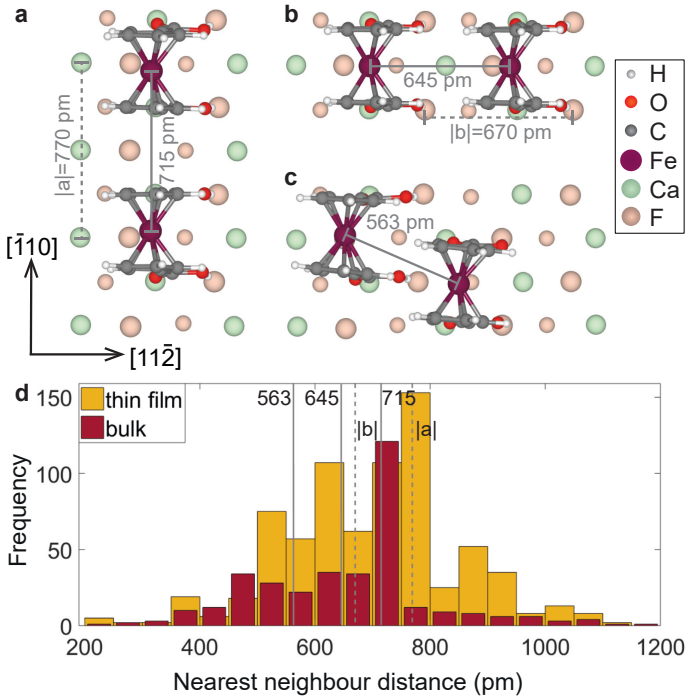

Figure 7.5: Analysis of molecular distances. (a-c) Top-views of DFT-optimized geometries for FDCA dimer arrangements. (d) Nearest-neighbor distance distribution extracted from NC-AFM and STM images. Results for bulk (thin film) samples are plotted in red (yellow). DFT-calculated dimer distances are indicated in (a)-(d) by solid gray lines. Dashed gray lines are used in all panels to indicate the size of a $(2\sqrt{2} \times \sqrt{2})$R45° superstructure.

Finally, a comparably small molecule-molecule interaction is identified from a DFT-based analysis of molecular dimers and an experimental measurement of the nearest-neighbor distances. Three molecular dimer geometries were considered with DFT using the optimum adsorption geometry geo 1 as the starting point with results presented in Fig. 7.5. Two FDCA molecules were arranged either along the $[\bar{1}10]$ (see Fig. 7.5a) or along the $[11\bar{2}]$ (see Fig. 7.5b) direction, as well as in a closely interlaced geometry (see Fig. 7.5c). We note that arranging molecules along $[\bar{1}10]$ separated by $a = 770$ pm and along $[11\bar{2}]$ with a spacing of $b = 670$ pm leads to a $(2\sqrt{2} \times \sqrt{2})$R45° superstructure. From the calculations, we find that the molecules in the dimer geometries move slightly together by about 55 pm for the $[\bar{1}10]$ dimer orientation (see Figure 7.5a), and by about 25 pm for a dimer along $[11\bar{2}]$(see Fig. 7.5b), while they move apart by more than 170 pm from a starting distance of 386 pm for the interlaced dimer geometry (see Fig. 7.5c). This geometrical rearrangement agrees with an analysis of the dimer binding energies, where we find an energy gain of about -0.08 and −0.14 eV for the $[\bar{1}10]$ and $[11\bar{2}]$ dimers, respectively, while the interlaced dimer is energetically unfavored with an energy loss of about 0.09 eV. For all geometries,

the quadruped molecule-surface anchoring motif remains with only minor geometrical rearrangements.

The dimer distances are very well reproduced by our experiments. A total of 352 (756) molecular pairs were measured on the bulk (thin film) surfaces, and we observe a clear accumulation of molecular separations at about 500-800 pm with a maximum of around 750 pm (we estimate an error of ±50 pm in all measurements); see Fig. 7.5d. Especially, the DFT-calculated dimer distances of 563, 645, and 715 pm as well as the sizes $|a| = 770$ pm and $|b| = 670$ pm of a $(2\sqrt{2} \times \sqrt{2})$R45° superstructure, lie within the experimental nearest-neighbor distance distribution.

Comparing the energy gain of up to −0.14 eV due to dimer formation with the adsorption energy of −1.74 eV due to the quadruped anchoring directly highlights a significantly stronger molecule-surface interaction than molecule-molecule interaction, in agreement with the experimental observations.

7.1.4 Conclusions

FDCA molecules on $CaF_2(111)$ bind to the top fluorine and top calcium surface atoms via their carboxylic acid moieties, forming F-HO hydrogen as well as Ca-O bonds in a quadruped geometry. The bond formation is facilitated by an excellent match of the molecular moiety dimensions with the surface lattice sizes and leads to an upright, slightly tilted molecular geometry with firm anchoring to the surface. The majority of FDCA molecules is found to adapt this geometry, with three different molecular orientations following the 3-fold rotational symmetry of the $CaF_2(111)$ surface. However, an energetically second-best molecular geometry, where one molecular carboxylic acid moiety is rotated by about 180°, is present as a minority population. The quadruped molecular adsorption geometry at equivalent lattice sites on the surface is maintained when considering molecular dimers in DFT; weak molecule-molecule interactions cause only slight molecular relaxations. The calculated dimer distances are in agreement with the experimentally observed nearest-neighbor distance distribution. No nucleation at surface defect sites on $CaF_2(111)$ terraces was found, and no differences between adsorption on bulk and thin film surfaces were apparent in the experimental data. The latter observation is in full agreement with DFT calculations, where surface ion displacements and electron density differences revealed a confinement of the molecule-substrate interaction to mostly the first CaF_2 substrate layer.

In conclusion, we identified a strong templating effect facilitated by a quadruped anchoring motif for the FDCA/$CaF_2(111)$ system. The robustness of the anchoring mechanism is evidenced by the observation of small molecular clusters and single molecules stable at room

temperature, observed on both bulk CaF_2(111) and thin film CaF_2/CaF_1/Si(111) surfaces. The room-temperature stability together with the possibility for structure formation on device-relevant CaF_2 thin films [146] makes this system highly relevant for applications. Thus, our findings open the door to advanced molecular adsorption and reaction studies, exploiting the anchoring motif found here on CaF_2(111). The vertical arrangement of carboxylic acid groups to form a strong molecule-surface bond could further be exploited to anchor larger functional structures or to grow self-assembled monolayers on an optically transparent insulator surface.

7.1.5 Supporting Information

Geometry optimization; FDCA gas-phase geometries; adsorption geometries geo 4 to geo 8 of FDCA on CaF_2(111); and DFT-calculated adsorption energy E_ads and adsorption angles α and α' of FDCA on CaF_2(111)(PDF)

7.1.5.1 NC-AFM and STM data

In addition to the images shown in the main text Fig. 1, we present examples of NC-AFM imaging performed at room temperauture on CaF_2 bulk samples (Fig. 7.6(c)) and STM imaging at low temperatures on thin film samples (Fig. 7.6(b)). These and comparable images from other sample locations are used for the statistical analysis of the cluster sizes (main text Fig. 1), molecular orientations (main text Fig. 4), and nearest-neighbour distances (main text Fig. 5).

7.1.5.2 Geometry optimisation

A total of eight starting geometries using several upright-standing as well as flat-lying FDCA molecules were chosen for the geometry optimisation with CP2K. Among these geometries we chose several positions of the carboxylic acid groups on the CaF_2(111) surface and used both eclipsed and staggered molecular conformations (see Fig. 7.7 for the two FDCA gas-phase conformations). The adsorption energies were all calculated with respect to the staggered gas phase geometry. These calculations resulted in a total of seven different final geometries which can be classified by several geometric properties: First, the FDCA molecule can exhibit either a **staggered** or an **eclipsed** conformation. Second, it can be identified which part of the **functional group** is located nearby which species of the surface (F_{top}, F_{low} or Ca). We also consider whether the carboxylic acid moieties are **in or out of plane** with the attached cyclopentadienyl (Cp) ring. Third, we identify the **molecular tilt** by determining the angle between the surface normal $\vec{e}_z = \vec{e}_{(111)}$ and the bond between C_{COOH} and C_{Cp} within the FDCA molecule (see also Fig. 7.8). This angle is

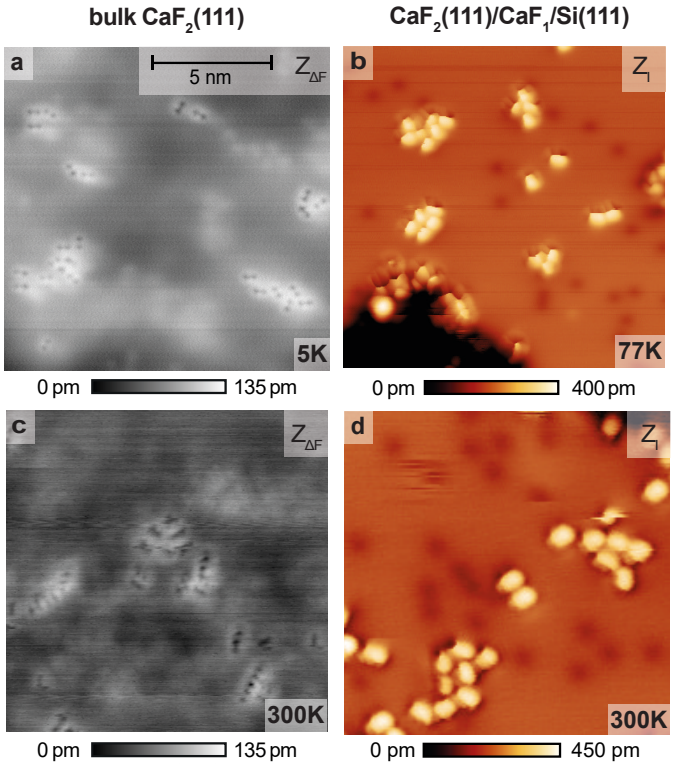

Figure 7.6: Measurements on bulk and thin film samples in NC-AFM and STM mode and at different temperatures. a) NC-AFM image acquired on a bulk sample using a qPlus sensor ($f_0 = 26\,641$ Hz, $\Delta f = -5.5$ Hz, $U_S = 4$ V, $T_S = 5$ K). b) STM image acquired on a CaF_2/CaF_1/Si(111) thin film sample ($I = 2$ pA, $U_S = -3$ V, $T_S = 77$ K). c) NC-AFM image acquired on a bulk CaF_2(111) surface using a silicon cantilever ($f_0 = 300\,042$ Hz, $\Delta f = -15.4$ Hz, $T_S = 300$ K). d) STM image acquired on a CaF_2/CaF_1/Si(111) thin film sample ($I = 2$ pA, $U_S = -3$ V, $T_S = 300$ K).

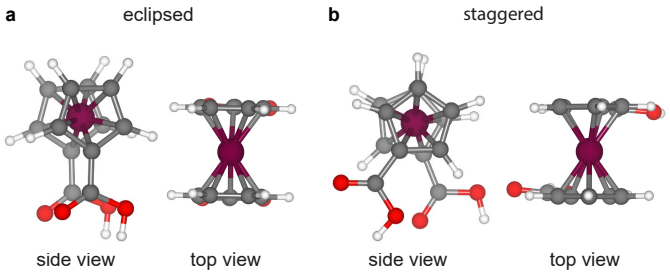

Figure 7.7: FDCA gas-phase geometries. Side and top views of a) eclipsed and b) staggered FDCA conformations (the energy difference between these conformations in the gas phase is about 0.06 eV). The staggered conformation represents the DFT-optimised lowest-energy gas-phase configuration.

determined for both carboxylic acid moieties of FDCA indicated as α and α' in table 7.2 together with the adsorption energies E_{ads}. Similar angles ($\alpha \approx \alpha'$) highlight a symmetric adsorption geometry.

Table 7.2: DFT calculated adsorption energy E_{ads} and adsorption angles α and α' of FDCA on CaF_2(111).

	E_{ads} (eV)	α (deg)	α' (deg)
geo 1	-1.74	22	22
geo 2	-1.58	16	-12
geo 3	-1.58	16	-12
geo 4	-1.38	68	24
geo 5	-1.29	40	40
geo 6	-1.24	74	74
geo 7	-1.19	24	2
geo 8	-1.06	60	60

In addition to the geometries geo 1 and geo 2 presented in the main text, a total of six further starting geometries were chosen with the results geo 4 to geo 8 shown in Fig. 7.8. Although started with different geometries, geo 2 and geo 3 converge to adsorption geometries, which are identical as a consequence of the surface mirror-symmetry. Therefore, geo 3 is not reproduced in Fig. 7.8.

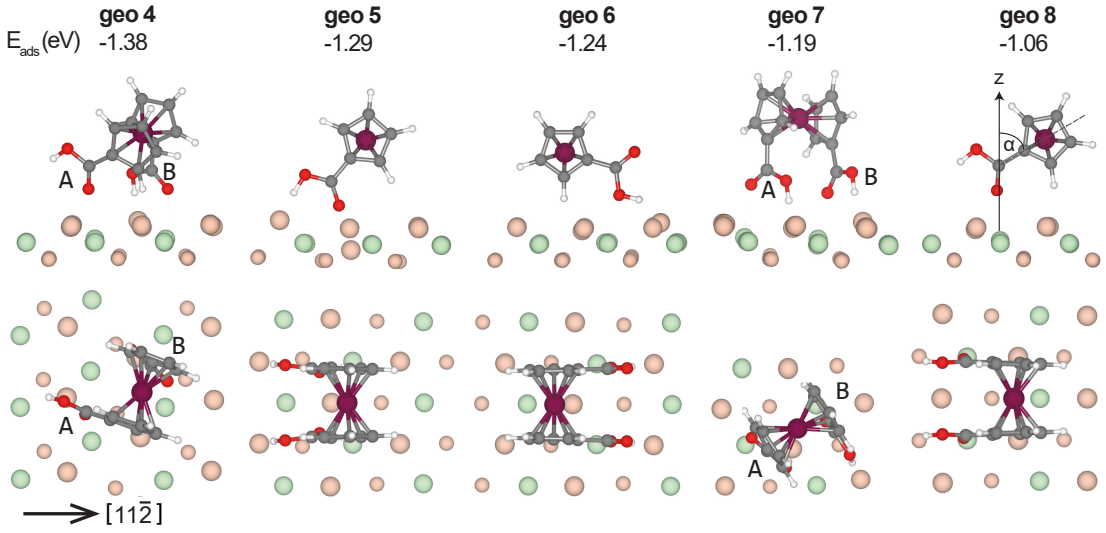

Figure 7.8: Adsorption geometries geo 4 to geo 8 of FDCA on CaF_2(111). Side (top row) and top (bottom row) views of the DFT-optimised geometries.

Small displacemens of the surface ions nearby the FDCA molecule are found from the DFT calculations. In the case of **geo 1**, the two F_{top} atoms (binding to O_h) and the two Ca atoms (binding to O_c) move slightly outwards towards the molecule while the top fluorides adjacent of O_c are pushed inwards. Only minute displacements are found within the second CaF_2 layer and virtually no changes are present from the third triple layer onwards.
For **geo 4**, a geometry was found where only one carbonyl group of carboxylic acid

moiety A (see Fig. 7.8) points towards the surface calcium ion with the hydroxyl group pointing away from the surface. The second carboxylic acid moiety adapts a geometry similar to the one of **geo 1**. The angle of the carboxylic acid moiety A of 24° is close to the angle of **geo 1**, while the angle of moiety B amounts to 68°. The molecule is distorted when compared to the eclipsed gas phase geometry.
The FDCA molecule in **geo 5** was initially placed with the hydroxyl group pointing to the lower fluoride anion, which appears to be highly unfavoured. As a result of the geometry optimisation, this is the geometry where both hydroxyl groups as well as the carbonyl groups are pointing to top fluorides, with F_{top} nearby O_c being pushed into the surface. The molecule is tilted with respect to the surface normal by the angle of 40°.
The molecule shown in **geo 6** is lying rather flat on the surface, with an eclipsed conformation. Therefore, the adsorption angles $\alpha = \alpha'$ of 74° are the largest among all investigated geometries. Here, two hydrogen bonds are formed with top fluoride anions, while the molecular carbonyl groups point away from the surface. In **geo 7**, carboxylic acid group A is in a similar geometry as in geo 1, also highlighted by the similar angle of 24°. Regarding carboxylic acid group B, however, the hydroxyl group is slightly rotated around the $O_{hydroxy}$-$C_{carboxy}$ bond axis, and the hydrogen is not exactly underneath the oxygen atom, but instead points towards the molecular centre, specifically to the top fluoride of the adjacent row. This results in an upright standing position with an angle α' of just 2°.
For **geo 8**, a geometry of a lying molecule, similar to geo 6 but with the carbonyl group binding to the surface, was identified.

7.1.6 Acknowledgements

Financial support by the German Research Foundation (DFG) via grant RA2832/1-1 and from the People Programme (Marie Curie Actions)of the European Union's Seventh Framework Programme (FP7/2007-2013) under Research Executive Agency (REA) Grant No. 628439is gratefully acknowledged.
P.R. thanks Samuel Jarvis (Lancaster University, U.K.) and Matthew Watkins (University of Lincoln, U.K.) for the most helpful advice on CP2K, the CP2K-UK project for strong support, and David Abbasi-Pérez (King's College London, U.K.) for the most helpful assistance on calculating and presenting electron density differences. Computing time was granted by the University of Osnabrück via DFG project 239246210.

7.2 Protruding Hydrogen Atoms as Markers for the Molecular Orientation of a Metallocene

Reprinted (adapted) with permission from Protruding hydrogen atoms as markers for the molecular orientation of a metallocene, Linda Laflör, Michael Reichling, Philipp Rahe, Beilstein J. Nanotechnology, 11, 1432-1438, 2020 Copyright 2020 Beilstein Journal.

7.2.1 Introduction

It is still a challenge to determine the precise adsorption geometry of three-dimensional (3D) molecules on surfaces. While spectroscopic methods such as X-ray standing wave [217] or photoelectron diffraction [218] can precisely determine the location of atomic species in ordered molecular systems on surfaces [219], scanning probe methods are commonly employed for the investigation of both ordered and unorderd molecular systems as well as of individual and isolated species [192, 220, 14]. For example, two different non-planar isomers of dibenzo[a,h]thianthrene molecules could be identified by high-resolution non-contact atomic force microscopy (NC-AFM) [221, 110]. Furthermore, the imaging of hydrogen atoms attached to propellane molecules with CO functionalised tips was suggested to enable the identification of three-dimensional molecules [127]. Very recently, a combination of NC-AFM and automated structure detection has been able to resolve the orientation of small organic 3D molecules from NC-AFM data [173]. Adapting these approaches to a broad range of 3D molecules bears the strong potential not only to gain insight into the on-surface adsorption properties of molecules, but also to unravel the intramolecular geometry.

A prototypical class of molecules with a hindered rotation determines different conformers is the metallocene family. These molecules consist of a central metal atom sandwiched between two rotatable cyclopentadienyl (C_5H_5, Cp) rings. The limiting cases of the ring orientations are known as *eclipsed* and *staggered* conformers. For ferrocene, the rotational barrier between these conformers amounts to only 0.04 eV in the gas phase [222][223][224], while for substituted ferrocenes the energy barriers determined in the gas phase amount up to 0.2 eV [225][226][227]. In solution, barriers of up to 0.7 eV are measured [228][229] and for ionised derivates calculations yielded rotational barriers of up to 1.4 eV [230].

From this class of molecules we investigate the ferrocene derivate 1,1'-ferrocene dicarboxylic acid (FDCA), a ferrocene functionalised with two carboxylic acid moieties. This molecule has been analysed before on Ag(111), Cu(110), and Cu_3N/Cu(110) surfaces [27] as well as on the insulator surfaces calcite(104) [20] and CaF_2(111) [188]. An eclipsed ferrocene conformation was found to be predominant on the metallic surfaces [27] and on

calcite(104) [20]. On CaF_2(111) surfaces, density functional theory (DFT) calculations revealed an optimum geometry of the eclipsed conformer in a nearly upright-standing, slightly tilted fashion, as well as a staggered conformer in an energetically less favourable geometry with one rotated carboxylic acid moiety [188]. These geometries, referred to as *geo 1* and *geo 2*, are depicted in 7.9(a),(b). The molecule-surface bond, with a binding energy for *geo 1* calculated to be -1.74 eV, is surprisingly strong [188]. Due to the tilted molecular orientations, both geometries have two hydrogen atoms as the topmost unit protruding the surface. However, the orientation with respect to the CaF_2(111) surface lattice differs for the two geometries.

In this work we investigate the NC-AFM contrast formation of FDCA molecules on CaF_2(111) surfaces. A distinct dumbbell shape has been observed in both topography and constant-height imaging modes at low temperature experiments (5 K and 77 K) with qPlus sensors as well as at room temperature using silicon cantilevers [188]. Although the NC-AFM tips were not functionalised, i.e. not specifically terminated with atoms or molecules for imaging, we find a very good agreement between the experimental data and probe particle model (PPM) [106] calculations using CO and Xe tips. Our analysis suggest that contrast formation is governed by repulsion between the tip and the hydrogen atoms serving as markers for the molecular conformation.

7.2.2 Methods

Scanning probe microscopy experiments were performed on CaF_2(111) bulk and CaF_2/CaF_1/Si(111) thin film samples under ultra-high vacuum conditions ($p < 5 \times 10^{-10}$ mbar) in two separate systems equipped with appropriate facilities for in-situ sample preparation.

Bulk CaF_2 crystals (Korth Kristalle, Altenholz, Germany) were cleaved in vacuum [118] after degassing the crystal and sample holder. To reduce residual charge on the surface [231], the sample was heated at about 330 K for one hour prior to the deposition of the ferrocene molecules and NC-AFM experiments. Thin CaF_2 films were prepared by deposition of CaF_2 (cleanliness 99.9 %, Alfa Aesar, Kandel, Germany) from an EFM3T e-beam evaporator (Focus GmbH, Huenstetten, Germany) on freshly prepared Si(111)-(7×7) surfaces held at about 930 K. Silicon substrates were highly B-doped p-type Si(111) samples (Institute of Electronic Materials Technology, Warsaw, Poland) with the (7×7) reconstruction prepared by flash-cycles. Further details on the thin film growth and properties can be found in Refs. [148, 188, 158, 210].

Deposition of 1,1'-ferrocene dicarboxylic acid (cleanliness 98 %, Alfa Aesar, Kandel, Germany) on samples held at room temperature was accomplished by sublimation from

home-built Knudsen cells heated to about 390 K.

For bulk samples, the $[1\,1\,\bar{2}]$ surface direction was determined by cleaving the crystal after the NC-AFM experiments along a (111) plane other than the surface plane. For thin film samples, the orientation of the Si(111)-(7×7) unit cell was measured by scanning tunnelling microscopy (STM) and the $[1\,1\,\bar{2}]$ direction determined by considering the B-type epitaxy of the CaF_2/CaF_1/Si(111) thin films samples, see Ref. [188] for further details.

STM and NC-AFM experiments were conducted at low temperatures (5 K and 77 K) in two separate systems. Experiments on bulk crystals were performed using an Omicron LT qPlus gen.III instrument (ScientaOmicron GmbH, Taunusstein, Germany), while experiments on thin films used a ScientaOmicron LT qPlus gen.II machine, both operated with a MATRIX controller. W-tips attached to tuning fork sensors in qPlus configuration [90] were used in both systems, yet, for the measurements on thin film samples home-built sensors were fabricated with a separate tunnelling current wire to exclude cross-talk between the NC-AFM and tunnelling current signals [201], while sensors as supplied by the manufacturer were used for measurements on bulk CaF_2 samples. Sensors were excited to oscillation amplitudes between about 0.15 nm and 0.8 nm. Both instruments were equipped with an atom-tracking system for drift measurement and compensation [232]. All experimental data were analysed using Gwyddion [120].

The probe particle model (PPM) [106] was used for simulating NC-AFM imaging contrast. Neutral oxygen and xenon atoms were used as probe particles and frequency-shift Δf data were calculated for an oscillation amplitude of 0.5 nm. Lateral and vertical stiffness were chosen as 0.5 N/m and 20 N/m, respectively. FDCA molecular models in the DFT-optimised geometries (using *geo 1* and *geo 2* from Ref. [188], see 7.9(a,b)) were arranged along the CaF_2 $[1\,1\,\bar{2}]$ direction, resembling one molecular row of the $(2\sqrt{2} \times \sqrt{2})$R45° superstructure that was observed in the experiments. All simulated Δf data are shown with a colour code representing a strong attractive tip-surface interaction as bright and a weak attractive or repulsive interaction as dark to allow direct comparison with the experimental data. We refer to this representation as "inverted colour scale".

7.2.3 Results and Discussion

Figures 7.9(c) and (d) show examples of the prevalently-observed dumbbell-shaped appearance of FDCA molecules on CaF_2(111) surfaces [188] for NC-AFM measurements performed at 5 K and 77 K on bulk and thin film samples, respectively.Previously, no difference in the molecular properties when comparing adsorption on CaF_2(111) bulk and thin film surfaces has been observed [188].

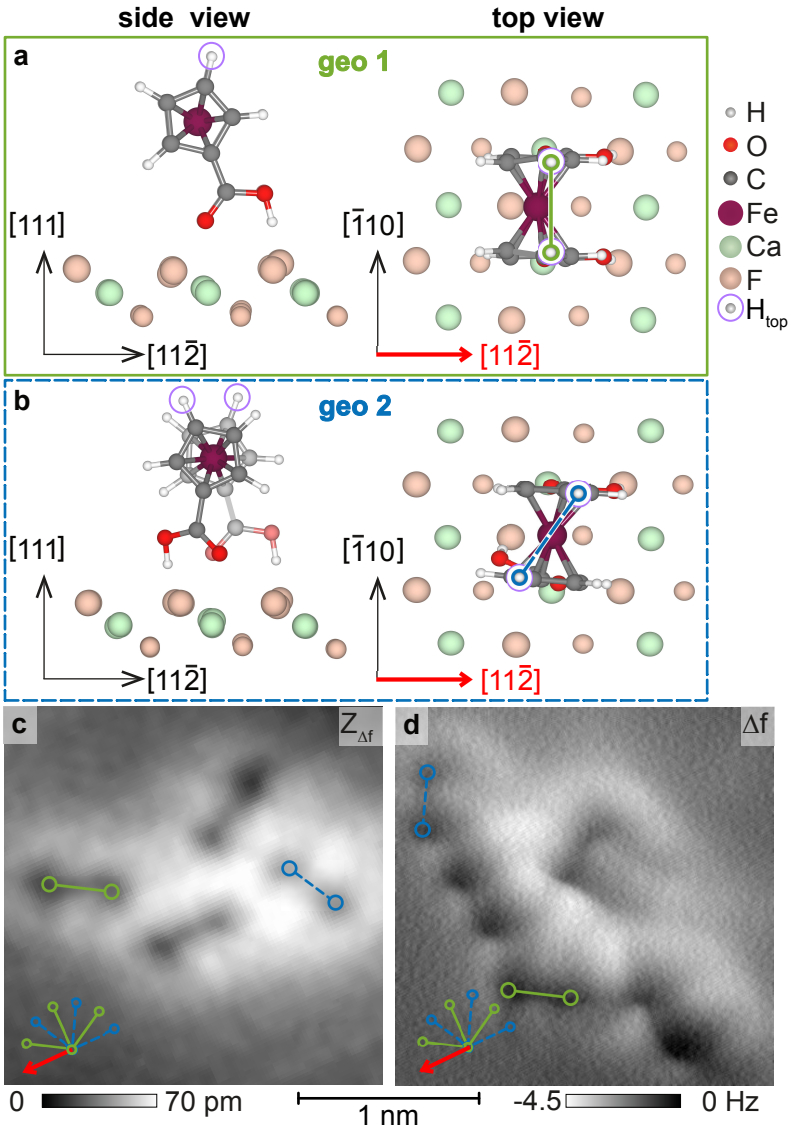

Figure 7.9: **Dumbbell shape of single FDCA molecules.** Quadruped binding motif of FDCA on $CaF_2(111)$ (adapted from Ref. [188]) of (a) *geo 1* and (b) *geo 2*. Dumbbell shape of FDCA molecules (c) on bulk $CaF_2(111)$ measured by NC-AFM in topography mode and (d) on a thin film $CaF_2(111)$ surface measured in the constant height mode (adapted from Ref. [188]). The orientations of the two geometries *geo 1* and *geo 2* are marked by solid green and dashed blue lines, respectively, and are included in all images with the respective orientation. (A five pixel averaging filter was applied to reduce noise within the frequency shift image. An inverted colour scale is used for the constant-height Δf NC-AFM data to match the topography appearance.)

The distance-dependency of the imaging contrast was analysed for constant-height data where frequency-shift images were acquired at different tip-sample distances, see 7.10(b) to (e). Data were acquired above a region where several FDCA molecules were arranged along the $[1\,1\,\overline{2}]$ direction (see STM data in 7.10(a)), with a molecular separation determined by the $CaF_2(111)$ lattice periodicity of 669 pm. Upon step-wise reducing the tip-surface distance, the experimental NC-AFM contrast evolves from an elliptic shape caused by attractive tip-sample interactions (panel b) into ring-like structures, followed by the dumbbell shape (panel c). Further reduction of the tip-sample distance then results in the evolution of a sharp line (one example marked by an arrow in panel d), which suggests a relaxation of the front tip apex in agreement with earlier observations in organic [111, 233] or inorganic [234, 235] systems. For the smallest tip-sample separation, two short, elongated dark segments (see markers in panel e) evolve on one side of a sharp line connecting the weights of the dumbbells.

For an interpretation of the NC-AFM contrast, we run simulations based on the probe particle model [106] for three molecules aligned along $[1\,1\,\overline{2}]$, each molecule being in the DFT-optimised adsorption geometry *geo 1* [188], as shown in 7.10(o) and (p). We use Lennard-Jones parameters for CO and Xe tips, a neutral probe particle, and stiffness values of $(k_x, k_y, k_z) = (0.5, 0.5, 20)\,\mathrm{N/m}$, yielding the results for CO reproduced in Figures 7.10(f) to (i) and for Xe in Figures 7.10 (k)-(n) at the same heights.

Both series of images exhibit a remarkable similarity to the experimental data: the change from the ellipse to the dumbbell shape is reproduced as well as the evolution of a sharp line connecting the two dumbbell weights (panels h and l). The characteristic contrast features appear in the simulations at different heights for the different tips, a finding which we attribute to the different van-der-Waals radii of CO and xenon. From a comparison with the molecular geometry we can confidentially assign the dark weights of the dumbbell to repulsive interactions with the top hydrogen atoms H_{top} (see 7.9(a)). The bright halo around these two weights is in turn caused by attractive forces acting between the tip and other atoms of the FDCA molecule. Thus, the PPM simulations allow the assignment of the dumbbell shape to a single FDCA molecule and, in turn, the orientation of the dumbbell precisely defines the axis between the top hydrogen atoms. Additionally, the asymmetry that evolves at close tip-sample distances is reproduced by the simulations, especially the two small, elongated dark segments marked by small triangles in panel (e). In the calculations, these dark segments are due to repulsive interactions with the lower-lying hydrogen atoms of the Cp rings, similar to the lines across the top bond of the Cp ring observed in previous measurements of FDCA on Cu(110) and Cu_3N/Cu(110) surfaces [27]. We note that the location of these dark segments is here linked to the surface orientation by the molecular geometry, where the expected match with the experimental results is

fulfilled.

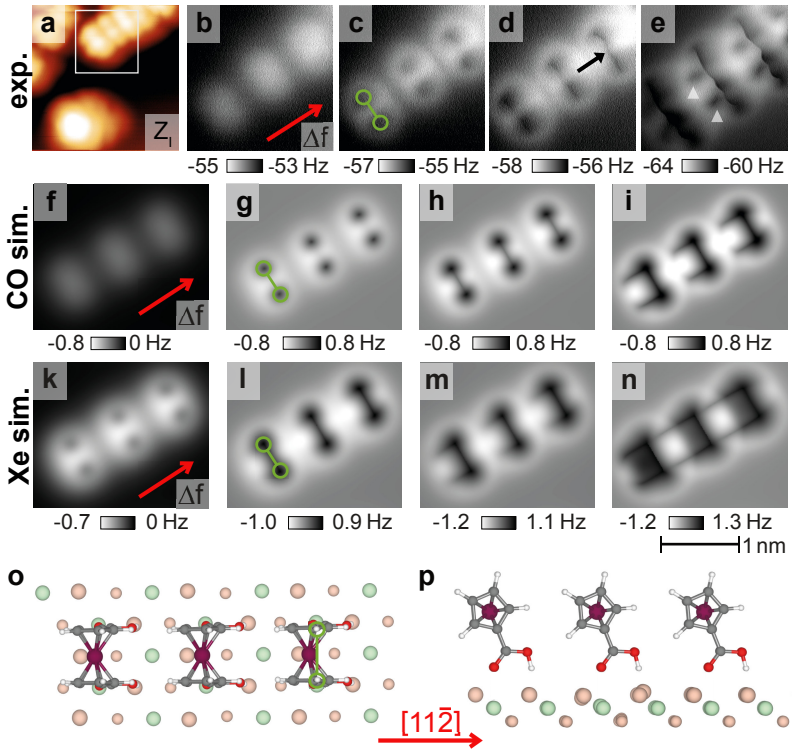

Figure 7.10: **High-resolution NC-AFM imaging and simulation.** Experimental and simulated frequency-shift images of a single molecular row along the [1 1 $\bar{2}$] direction (red arrows). Exemplary molecules are marked by a green dumbbell. (a) Experimental STM image ($U = 4$ V, $I_t = 2$ pA). (b) to (e) Experimental constant-height NC-AFM data ($f_0 = 24\,363$ Hz, $Q_0 \sim 6000$, $A_0 = 0.27$ nm). Frequency shift ranges are shown below each image (inverted colour scales are used); a four pixel averaging filter was applied to reduce noise within the frequency shift images. A slight tilt of the constant-height plane leads to a small modulation along the row.). (f) to (i) Simulated NC-AFM images using a CO tip model. (k) to (n) Simulated NC-AFM images for a Xe tip model positioned with the tip backbone positioned at the same heights as for the CO image calculations. (o) and (p) Structure of the simulation cell with each molecule in the single-molecule DFT-optimised geometry *geo 1* [188].

The good match between the key features in experiments and calculations is remarkable as measurements were not performed with a specifically prepared tip. The accidental functionalisation of the tip might have occurred through the adsorption of a FDCA molecule to the tip with the carbonyl moiety facing the surface., This would be in line with earlier NC-AFM experiments of NTCDI adsorbed on Ag-terminated silicon surfaces [102]. In the latter case, the observation of submolecular contrast similar to images acquired with CO-terminated tips has been explained by a tip-adsorbed NTCDI molecule with a CO-like carboxylic oxygen pointing towards the sample [102]. In the present experiments, a similar

mechanism with one of the FDCA carbonyl groups pointing towards the sample is plausible. However, the agreement between experiment and simulation might also reflect a more general feature of repulsive mode imaging. While the tip-surface interaction force curves in the attractive region differ significantly from each other for different tip-terminating species, the force curves in the repulsive region are so steep that differences in their details have only minor influence on the NC-AFM contrast. Hence, the NC-AFM contrast observed for imaging with different tip terminations differs only by the distance of the onset of certain features as found for the simulations with CO and xenon tips. In either case, the interaction with the top hydrogen atoms is found to be localised and repulsive and serves as a marker for the hydrogen atom position.

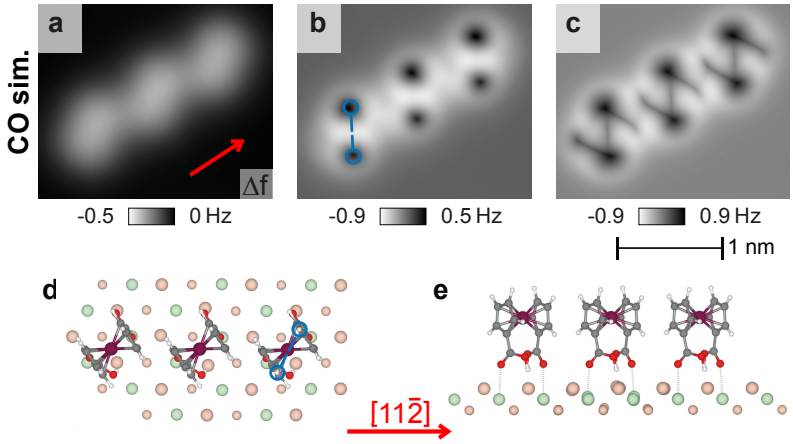

Figure 7.11: **NC-AFM image calculation for a [11$\bar{2}$] row of FDCA molecules in *geo 2*.** (a) to (c) constant-height frequency-shift Δf data (inverted colour scale used) simulated at decreasing tip-sample distances for a row of FDCA molecules, each in *geo 2*. The red arrows mark the [11$\bar{2}$] direction and the dashed blue line (forming an angle of 60° with the [11$\bar{2}$] direction) the molecular orientation for *geo 2*. (d) Top and (e) side views of the simulation cell using *geo 2* from Ref. [188].

A previous analysis of the molecular orientations highlighted the presence of a minority population of FDCA molecules exhibiting the adsorption geometry *geo 2* with a partly staggered molecular conformation [188]. The protruding hydrogen atoms align in this geometry along a different direction with respect to *geo 1* due to the partly staggered conformation of the Cp rings. The corresponding PPM image calculations with identical simulation parameters as before for a CO tip are shown in 7.11. Although the molecular row still proceeds along the [11$\bar{2}$] direction, the orientation of the dumbbell shape differs: The angle between the dumbbell-connecting line and the [11$\bar{2}$] direction reduces from 90° (*geo 1* in 7.10) to 60° (*geo 2* in 7.11). This is a direct consequence of the partly staggered conformation which moves the top hydrogen atoms to these positions. At further reduced

distances (see 7.11(c)), lines both along the position of the top Cp bonds and along the iron centre of the FDCA molecule are again revealed.

Experimental examples for the different orientations are given in 7.9(c) and (d). Due to the three-fold rotational symmetry of the $CaF_2(111)$ surface, a total of six orientations, three for each geometry, are possible and included as sketches in the lower left corners with solid green and dashed blue lines marking the orientation of *geo 1* and *geo 2*, respectively. Molecules of both geometries oriented along one of the possible angles are present in the experimental images, two examples for each geometry are marked. The experimental contrast is similar to the pattern of a single molecule within the calculated images in 7.10(h) and (m) for *geo 1* and 7.11(b) for *geo 2*.

7.2.4 Summary and Conclusions

We have investigated the origin of the dumbbell shape, which is observed when imaging FDCA molecules on $CaF_2(111)$ surfaces with NC-AFM. Based on a comparison of experimental constant-height frequency-shift data with image calculations using the probe particle model, we identify repulsive interactions between the tip and the topmost hydrogen atoms of the Cp rings of single FDCA molecules as the fundamental cause for the dumbbell shape. Due to the strong molecule-surface bond, molecules are usually not manipulated while scanning in this repulsive mode. We found tips prepared by standard procedures to be mostly stable and sharp enough to locally enter the repulsive regime. Following the vision of Ref. [127], the measurement of the two hydrogen atom positions with respect to the orientation of the $CaF_2(111)$ lattice allows us to identify the ferrocene conformer and the molecular orientation on the surface. The experimental observation of the dumbbell shape suggests that the prerequisite of a stable tip during repulsive interactions with the hydrogen atoms can easily be fulfilled, even at room temperature. This is in line with previous findings of stable tips for sub-molecular resolution imaging at 77 K [102, 100] and 300 K [236]. Due to the predominant repulsive interactions with the chemically rather intert hydrogen atoms, we speculate that the chemical identity of the tip is therefore of second-rank. Still, the tip has to be sharp enough to allow a resolving capacity of the dumbbell-shape.

This is a demonstration for identifying hydrogen atoms in a 3D molecule with non-functionalised tips as well as the use of hydrogen atoms as markers for the molecular geometry. As the method introduced here is based on an universal imaging mechanism and widely applicable experimental procedures, we expect that the introduced method will allow the identification of other conformers and especially give further insights into adsorption geometries of complex 3D molecules.

The work further underlines the general applicability of repulsive mode imaging of molecules independent of a specific tip termination such as CO that is hitherto the standard tip for this imaging mode. We propose that high resolution repulsive mode imaging of hydrogen atoms is possible with a variety of tips if the following three preconditions are fulfilled: (1) The molecule is sufficiently strongly bonded to the substrate to withstand manipulation due to lateral forces exerted by the approaching tip. (2) The tip atomic arrangement is characterised by a deep minimum of total energy preventing a rearrangement of tip atoms or disintegration if the tip is strained by the interaction with the molecule. (3) The tip end is atomically sharp. The third condition implies the stabilisation of the tip terminating atom by one or very few bonds directed towards the tip apex. Such a bond will always exhibit sufficient lateral elasticity to yield a sharp contrast feature when the tip terminating atom passes a molecular protrusion.

7.2.5 Acknowledgements

We are indebted to Philip J. Moriarty (University of Nottingham, UK) for supporting part of the experiments and for comments on the manuscript.

7.2.6 Funding

Financial support by the German Research Foundation (DFG) via grant RA2832/1-1 and from 222 the People Programme (Marie Curie Actions) of the European Union's Seventh Framework Pro223 gramme (FP7/2007-2013) under Research Executive Agency (REA) Grant No. 628439 are grate224 fully acknowledged. Computing time was granted by the University of Osnabrück via DFG project 225 239246210.

7.3 Conclusions

Summarising this chapter, the deposition of a metal-organic compound to an insulating surface has been performed successfully. The FDCA molecules adsorb on both bulk and thin film $CaF_2(111)$ surfaces in an equal manner, eliminating any doubts on the influence of the underlying CaF_1/Si(111) sample on the molecular adsorption. Furthermore, investigating FDCA adsorption on CaF_2 surfaces allowed not only a deep understanding of the anchoring motif, but also the imaging mechanism. The anchoring follows a firm quadruped bonding motif, where both carboxylic acid moieties point towards the surface and form two bonds each. One between the carbonyl oxygen and the calcium cation and a hydrogen bond between the hydroxyl part and the fluoride anion. This motif was confirmed with DFT calculations, being one of the few examples to combine theory with experiments regarding the anchoring mechanism.
Based on the DFT calculations and with the help of PPM, insights on the imaging mechanism of this rigid three dimensional molecule could be gained. Measuring in the repulsive regime without a specifically terminated tip, results in imaging the top most hydrogen as dark dumbbells. Based on this the orientation of the FDCA molecules can be determined regarding the $CaF_2(111)$ surface. Two types of adsorbed molecules are observed, as they show two different orientations regarding the $[1\,1\,\overline{2}]$ surface direction. These two adsorption geometries match the two energetically most favourable adsorption configurations in DFT, *geo*1 and *geo*2.
Therefore, this chapter showed not only a successful introduction of a metal-organic compound with an intramolecular coordinate bond to an insulator, but gave valuable insights on anchoring and imaging of molecules.

8 Towards Metal Coordination Networks on Surfaces

While on-surface networks can be stabilised by several interaction types (see chapter 2.4), here, I would like to concentrate on two bond types: hydrogen bonds and coordinate bonds. These are the ones responsible for intermolecular bond formation in trimesic acid (TMA, cf. figure 8.1a) networks. I will investigate the bond formation of TMA on Au(111), aiming to lay foundations for coordinate bonds between TMA and iron on an insulating surface. For this purpose, first, pure TMA is investigated on Au(111) in section 8.3 to gain deeper understanding of hydrogen-bonded networks with STM and NC-AFM. A deeper understanding of the intermolecular features in NC-AFM images at the hydrogen bond position, will help to distinguish between hydrogen and coordinate bonds (see section 8.3.3). Second, TMA on Au(111) will be heated to investigate the influence of thermal activation, (section 8.4.1). This experiment is repeated on surfaces, which have been exposed to Fe alloying in prior experiments (sections 8.4.2, 8.4.3). Third, TMA and iron are co-deposited onto the Au(111) to examine the influence of iron on the self-assembly (section 8.5). Deposition order and temperatures are varied to inspect their influences on coordinate bond formation in section 8.5.1. The intermolecular contrast of the TMA and iron self-assembly is investigated regarding the intermolecular bonding in section 8.5.2.

8.1 Introduction

TMA has been studied intensively on conducting surfaces [237] and a first study exists on an insulator, namely calcite(104) [184]. For both metal and insulator surfaces, TMA forms networks via dimeric and trimeric hydrogen bonds (see figure 8.1b,c). While on various metal surfaces both hydrogen bond types result in extensive networks, on calcite dimeric bonds form only small fragments of a network, which is explained by a lattice mismatch hindering successful anchoring. Trimeric bonded networks on calcite are similar to the ones observed on metal surfaces. This will be elucidated in section 8.1.1.
A coordinate bond between TMA and a metal has been established on metal surfaces

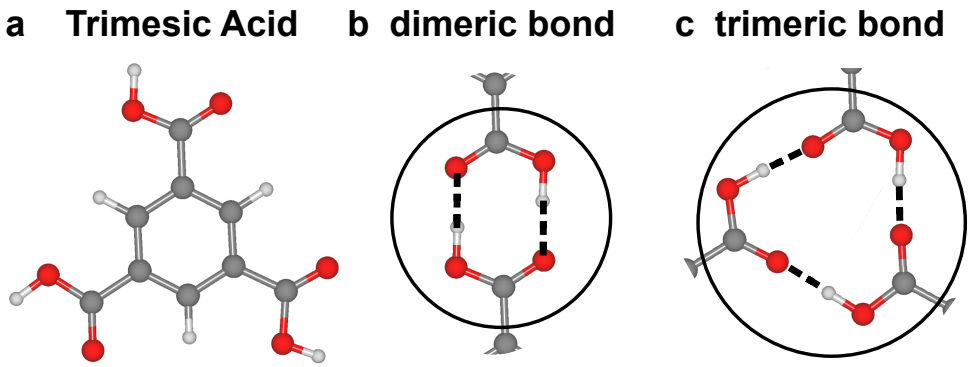

Figure 8.1: Ball and stick model of (a) trimesic acid, schematic of (b) a dimeric and (c) a trimeric bond (carbon - grey, oxygen - red, hydrogen - white), recreated following Zhou et al. [238].

[239, 240, 241, 242, 243], but has not been formed on an insulating surface to the best of my knowledge. Nevertheless, the lattice mismatch of the dimeric bonded network fragments on calcite(104) allows the suggestion that introducing coordinate bonds will elongate the bond length and result in a better lattice agreement between calcite(104) surface and the TMA network. This could result in a long-range ordered metal-organic network. Therefore, the aim of this work is to produce a metal-organic network with TMA on Au(111), in order to gain knowledge on the coordination network formation. This will lay a base for transferring this knowledge onto the calcite(104) surface.

8.1.1 Hydrogen-Bonded TMA Networks

Hydrogen bonds are non-covalent, electrostatic interactions between a hydrogen bond donor and a hydrogen bond acceptor [38]. The hydrogen bond donor consists of a hydrogen atom, covalently bound to a high electronegative atom such as a halogen, chalcogen, or pnictogen atom. Examples of hydrogen bond donors are hydroxyl moieties, the hydroxyl part of carboxylic acids, or amines. The hydrogen bond acceptor consists of an electronegative atom, containing at least one lone electron pair. Examples for hydrogen bond acceptors are halogens, amines, and the carbonyl oxygen of carboxylic acids. Hydrogen bonds are typically linear, the angle between the bond donor, the hydrogen atom and the bond acceptor usually amounts to 180 ° [38]. For that reason, the arrangement of functional groups influences the possibility of hydrogen bond formation. Different arrangements of functional groups at small building blocks can result in different geometries via hydrogen bonds. An exemplary functional group engaging in hydrogen bond formation is carboxylic acid, which can act either as bond donors or acceptors, or as both donor and acceptor simultaneously.

A good example for a molecule functionalised with several carboxylic acid moieties is TMA. The $C_3{}^h$ symmetric molecule, depicted in figure 8.1a, consists of a benzene ring substituted with three carboxylic acid moieties at the 1, 3, and 5 positions.
For hydrogen-bonded TMA networks on conducting surfaces, several ordered assemblies are observed. These assemblies are based on solely two hydrogen bonding motifs: Dimeric and trimeric bonding motifs [244]. In case of the dimeric bonding motif, two parallel hydrogen bonds are formed between two carboxylic acid moieties, this is depicted in figure 8.1b. The trimeric bonding motif is shown in figure 8.1c. It consists of three molecules, interacting via one carboxylic acid each, forming three hydrogen bonds. The three hydrogen bonds are arranged in a circular bonding motif [244]. Based on these bonding motifs several ordered structures are formed. The dominating structures on Au(111) surfaces are the honeycomb (HON; also sometimes described as chicken wire), and several sizes of flower structures, as well as the close-packed structure [244, 245, 246, 247, 248, 249].
HON consists of only dimeric bonds, while the close-packed structure contains only trimeric bonds. A combination of dimeric and trimeric bonds in different ratios is required for the different sized flower structures. The abundance of each structure depends on the surface coverage, although local fluctuations of the TMA coverage can occur, which results in simultaneous occurrence of the different structure types [244].

Honeycomb Network

At lower coverages up to roughly 0.6 ML, HON is observed as dominating structure [244]. As HON is bound via dimeric bonds only, the HON network consists of six molecules with hexagonal pores, each pore with a diameter of 1.1 nm on Au(111) [244]. The unit cell of HON is depicted in 8.2a. HON networks are known to mainly orient along the Au(111) $[\bar{2}11]$ surface direction, where the HON is either tilted by $(4 \pm 1)^\circ$ or $(30 \pm 1)^\circ$ regarding the $[\bar{2}11]$ surface direction [250]. However, other HON orientations are also observed, but less frequent [250]. When two domains meet, a domain wall separates the differently orientated HON networks. Here, rows of bow-tie structure are found, examples are given in chapter 8.3.

Host-Guest Systems of the HON Network

Porous networks, like the HON network or the flower structures, can be used as host-guest systems [237], where molecules are introduced into the pores. The HON pores on Au(111) are known to host single TMA molecules. This will be relevant for predicting the coverage of TMA on the surface and therefore discussed in more detail. TMA as guest molecule sits at a non-central position inside the pore and interacts preferentially

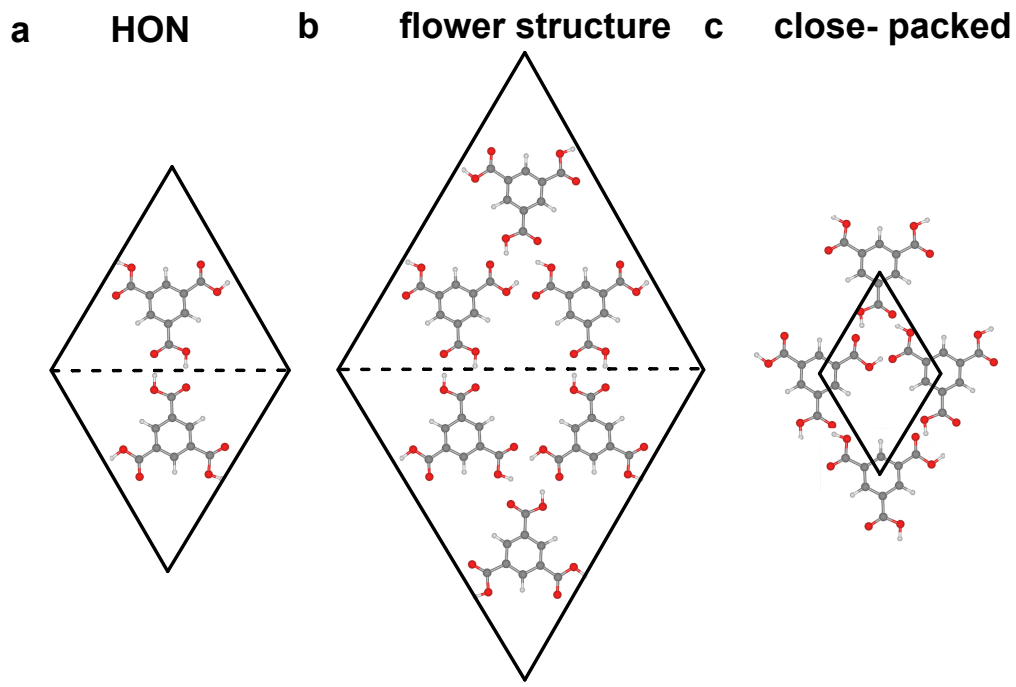

Figure 8.2: Schematics of the unit cells of different TMA assemblies: (a) honeycomb's, (b) the smallest flower structure's and (c) close-packed structure's unit cell - recreated following Ye et al. [244].

via two hydrogen bonds with two neighbouring TMA molecules. Energetically sightly less favourable is an adsorption position, where the guest TMA interacts with two TMA molecules of the pore interacting directly with each other [251]. Beside TMA molecules, several other organic and inorganic molecules have been introduced as guests to HON pores [245, 251, 252, 253, 254], but to the best of my knowledge metal atoms or clusters have not yet been introduced as guests. The pore size remains stable for all introduced guests, therefore, the dimeric bonding motif is not influenced by guest molecules.

Flower Structures

At a coverage larger than 1.04 molecules/nm^2, different sized flower structures occur. They are formed by a combination of trimeric and dimeric bonding motifs. The smallest flower structure unit cell consists of six molecules, it is depicted in figure 8.2b. In this unit cell, three molecules are connected via trimeric bond in each unit cell half. The two unit cell halfs are connected via dimeric bonds. For larger flower structures the number of dimeric and trimeric bonds is increased [244]. Similarly to the HON, the size of the hexagonal pore embedded in the different sized flower structures has a pore diameter of 1.1 nm. The distance between two pores depends on the unit cell size of the flower structure [244]. Examples of flower structures are given in chapter 8.3.1.

Close-Packed Structure

The third structure, the close-packed structure is defined by the trimeric bonding motif only see figure 8.2c. The close-packed structure is found at a coverage of about 1 ML or 1.34 molecules/nm^2 [244]. The most prominent feature is the equally oriented molecules, the carboxylic acid moieties are all aligned in the same three directions.

TMA on an Insulating Surface

So far, all examples of hydrogen-bonded TMA networks that have been discussed in this chapter, have been implemented on conducting surfaces. On insulating surfaces the data situation is scarce for hydrogen-bonded TMA networks. To the best of my knowledge, the only experiments published were conducted on calcite(104) [184]. Two types of networks are observed on calcite(104): a close-packed structure and fragments of HON network. The close-packed structure is described as a nearly hexagonal ordered phase (in the publication referred to as close-packed flower motif). It shows a strong templating effect, as the lattice of the nearest-neighbour distance matches the calcite lattice [184]. The HON network (in the publication referred to as chicken-wire motif) is only observed as fragments. The fragments are oriented along the $[\overline{42}61]$ direction by $\pm(18.0\pm0.2)^\circ$. The HON networks are short ranged due to a lattice mismatch. This is likely to hinder the anchoring of the carboxylic acid moieties to the calcite(104) surface, probably due to the protruding oxygen atoms of the surface [184]. For the HON network only one TMA molecule can adsorb in a position where all three carboxylic acid moieties have the ability to anchor to the underlying calcite surface. The extended HON network, however, misses this anchoring abilities due to the lattice mismatch. This makes this adsorption geometry energetically less favourable [184].

8.1.2 Coordinate Bonds with TMA

Staying with the example of TMA, the three carboxylic acid moieties act as possible reactive ligands for coordinate bonding. Therefore, the TMA molecule has up to six sites for coordinate bonds via the carboxylic acid moiety. Additionally, coordination can occur via the benzene ring. Metal coordination to TMA has been observed with Co on Au(111) [243], Fe on Cu(100) [241, 242], as well as Cu and Fe on Cu(110) [239, 240]. In the following, the different coordinate bonds formed with TMA will be discussed, for a more detailed elucidation on coordinate bonds in general, please see chapter 2.

In presence of cobalt, TMA forms either complexes or undergoes partial deprotonation depending on the surface temperature. At 200 K, TMA sits on top of cobalt atoms , coordination occurs via the benzene ring, and no signs of deprotonation are observed [243].

At 300 K, the carboxylic acid moieties are partly deprotonated and TMA forms unordered assemblies, a formation of a coordinate bond is not observed [243]. On Cu(100) TMA forms chiral, square planar, clover-like complexes with iron adatoms at room temperature. The complexes consist of four, deprotonated TMA molecules coordinating to a central iron atom. Each molecule coordinates via one carboxylate moiety with an unidentate bond to the central iron atom [241, 242]. Heating the sample system to 350 K causes growth of the clover-like complex. One carboxylate moiety forms one additional coordinate bond to an iron metal centre. To this metal centre two TMA molecules coordinate via one carboxylate moiety. At this position, a bonding motif of three TMA molecules coordinating via one oxygen each to the iron atom is observed [241]. Heating the sample system further to 400 K results in connecting the motifs formed at 350 K, forming larger clusters leading to a larger structure [241].
On Cu(110) TMA molecules form ordered 1D chains with copper adatoms as well as with co-deposited iron [239, 240]. In both cases TMA is deprotonated [239]. In case of coordination to copper, each TMA molecule connects to two Cu dimers resulting in linear chains. Each molecule forms one coordinate bond via one oxygen of one carboxylate moiety each. The ratio of TMA:Cu amounts to 1:2. In case of coordination to iron, coordination centre is a single Fe atom. The remainder bonding is equivalent to the metal-organic network formed with copper. The ratio of TMA:Fe amounts to 1:1. The 1D order probably stems from the missing row reconstruction of the Cu(110) surface [239].

Deprotonation of TMA

TMA is osberved to deprotonate in the presence of some metal adatoms (Ag, Cu, Fe, Co) and on the surfaces Cu(111) and Pd(111) [255, 243, 249, 256, 257, 258]. Deprotonation is often caused by strong molecule-metal interaction or requires elevated temperatures [237]. For most coordinated TMA molecules, TMA is known to deprotonate. Then, coordinate bonds are observed between carboxylate ligands and metal centres. For some sample systems ordered phases are obtained [249, 256, 257]. In combination with cobalt TMA deprotonates at room temperature, forming densely arranged, unordered structures [243].

8.1.3 Identification of Coordinate Bonds

To identify coordinate bonds in SMONs mostly two techniques have been used so far: both XPS and STM have determine coordinate and covalent bonds in metal-organic compounds. Here, I'll focus on STM only. However, both techniques are only feasible on conducting samples. This limitation can be avoided by applying another technique: AFM. Few high-resolution NC-AFM images have been taken on metal-organic molecules and networks resolving coordinate bonds [259, 260, 261, 262]. This will be discussed later on in this section.

Coordinate bonds have been identified with STM. However, the coordinate bonds or the metal centre of the coordinate bond are imaged differently throughout different sample systems. In some cases, the metal centre of a coordinate bond is depicted as bright protrusion. Examples are TMA coordinated to Fe on Cu(100) [242] or TMA coordinated to copper dimers on Cu(110) [239]. However, in some cases the metal centre of the coordinate bond is not depicted as protrusion. One example is Fe and TMA chains on Cu(110) [239], however, a similar structure with Cu is imaged as protrusion. The different imaging of Fe and Cu on Cu(110) can be explained by a reduced density of electrons in the metal's s state of the metal atom not imaged as protrusion [239]. Fe coordinated to TMA on Cu(110) and Cu(100) is also imaged differently, the most obvious difference is the underlying substrate. Yet, the coordination geometry differs on the two surfaces as well. On Cu(110) four TMA molecules coordinate to the Fe centre, while only two coordinate on Cu(100) [239, 242]. While the STM contrast of Fe is not discussed in both publications, the different coordination geometries might have an impact on the local density of state of the metal, which then can result in the differences observed by STM. Albeit, the fact that metal atoms are possibly not imaged in STM exacerbates the clear identification of coordinate bonds.

Another metal-organic compound, which has been identified with STM is TMA coordinated to Co on Au(111). After depositing both metal and TMA to the 200 K Au(111), TMA is observed to adsorb partly on top of Co adatoms. These molecules appear brighter in STM than the neighbouring molecules, who are not coordinated to the cobalt [243]. In this specific example the large amount of unreacted molecules allows an easy identification of the reacted ones.

AFM is another technique to identify coordinate bonds, especially on insulators, where STM and XPS cannot be performed. Highest resolution AFM images are obtained with functionalised tips. So far, few examples exist for NC-AFM with CO functionalised tips of metal-organic compounds. The examples can be grouped into two systems: compounds with chelat ligands (see chapter 2.1) and molecules interacting with a neighbouring metal adatom. Prominent example systems of chelat ligands are porphyrin and phthalocyanine

molecules, which are metallised in the ring centre. These have been discussed in chapter 6. Few examples exist of metals coordinating to a single or several non-cyclic molecules being investigated with NC-AFM: Au and PTCDA [261], Cu and 2,6-dimethylnaphthalene [259], Au and graphdyine nano wires [260], Au-phenanzine [262], and Au-heptacene [263]. Copper forms coordinate bonds with 2,6-dimethylnaphthalene on Cu(111), resulting in metal-organic chains. In NC-AFM the molecules are connected by bond-like features, the C-Cu-C bond is imaged as one bright line. The copper atom is not imaged as separate protrusion [259]. The remaining examples are molecules coordinating to gold. Gold as metal centre is imaged as bright, round protrusion in NC-AFM for all given examples [260, 262, 263]. In case of graphdyine two lines are imaged between the protrusion of the gold adatom and the carbon-carbon triple bonds [260]. Similar are the results of phenanzine, where gold coordinates to the tertiary amine atoms two molecules. The gold atom is imaged as one protrusion, and bonds are imaged as lines connecting both molecules to the metal centre [262]. For heptacene and gold no lines are observed connecting the protrusion of the metal to the organic ligand [263]. These example unifies that the principles of contrast formation underlying the imaging of the coordinate bond as well as the metal centre itself have not been discussed. Comparing these examples, the imaged features appear to differ for the different metal atoms (Cu and Au). This might be assigned to different atomic properties, like atomic radii, resulting in different tip-sample interaction. Summarising, coordinate bonds have successfully been identified with NC-AFM. However, different imaged features are observed for different metal centres. So far, the differences in imaging contrast have not been elucidated. Hence, understanding the contrast formation of intermolecular interactions, coordinate bonds or other, will help distinguishing different intermolecular interactions and identifying coordinate bonds.

8.2 Iron Deposition on Au(111)

In this section, I investigate the deposition of Fe on pristine Au(111) surfaces. The section starts with a literature overview (section 8.2.1). It is followed by the conducted experiments in section 8.2.2. In this section room temperature deposition of iron is investigated, as well as iron deposition onto heated samples investigating near-surface alloy formation.

8.2.1 Literature Overview

Iron, being the fourth most abundant element in the earth's crust, is most commonly found in oxidised form, usually +2, +3, and +6. Additional oxidation states of -2, -1, 0, +1, +4, and +5 do exist and iron can therefore form a vast range of compounds [38]. When iron

occurs as a solid, it forms a body-centred cubic structure [33]. It is the second most used metal for SMONs [22]. Iron has been extensively grown on metal surfaces.

Iron forms islands, when grown on Au(111) at room temperature [33, 34]. The nucleation of iron islands begins at the elbows of the herringbone reconstruction on Au(111) at coverages as low as 0.1 ML [34]. Islands formed at the pinched side of the elbows show a diamond shape, while the ones formed at the bulged elbow site exhibit a triangular shape [32]. The edges of the islands with triangular shape are aligned with the $\langle 1\bar{1}0 \rangle$ of the underlying Au(111) surface [34]. Both island types are atomically flat [33]. Increasing coverage leads to a growth of both island types. At about 0.4 ML the beginning of second-layer island growth is observed [32]. Further increasing Fe coverage results in a further growth of first- and second-layer islands. From a coverage of about 0.6 ML onwards, first-layer islands begin to coalesce [32]. First- and second-layer iron islands form a superstructure on the Au(111) surface, a square rhomboid structure. The following layers grow in bcc crystal structure. [33, 34, 264]. This allows an easy determination of iron coverage. The square rhomboid structure of the iron island unit cell has a side length of 0.288 nm, which results in a density of 0.072 nm^2/atom [34]. Therefore, the coverage c_{ML} of 13.9 atoms/nm^2 amounts to one monolayer of iron (ML) within the first-layer.

Another aspect to consider is the process of alloying at elevated temperatures. Despite the widely quoted statement that thermal activation of alloying of the Fe/Au(111) is initiated at temperatures of above 573 K [265, 266], a newer study from 2008 has indicated that the activation of iron diffusion into the top surface layers of Au(111) already occurs at 400 K forming a near-surface alloy [35]. Furthermore, diffusion of iron atoms into the Au(111) bulk crystal starts at 500 K, forming an iron-gold alloy. This was underlined by low energy ion scattering as well as XPS [35]. To the best of my knowledge no STM data has been published so far for Fe/Au(111) alloys.

An example of an alloy formation being studied with STM is zinc alloying with the Au(111) surface. In contrast to Fe beginning to alloy at 400 K, Zn starts to alloy with the Au(111) surface at 105 K. The deposition was carried out at a surface temperature of 105 K. Zinc atoms start island growth at the herringbone elbows, comparable to the results found for iron on Au(111) [267]. Atom exchange begins between zinc adatoms and gold surface atoms at 105 K. This is deduced from a slight herringbone distortion. After deposition of zinc to Au(111) surface at room temperature, two types of alloys have been observed. First, a zinc-gold alloy grows at the Au(111) step edges in finger-like peninsulas [267]. At this point, the herringbone reconstruction is highly disturbed. Second, the metal exchange of single zinc adatoms at the Au(111) surface is noted mainly at the elbow sides by dark spots in the respective STM images. The contrast results from chemical contrast arising from the different electronic properties of the metals. Heating the Zn/Au(111) sample system to

temperatures of 350 K and above results in the formation of a sub-surface alloy, which has been confirmed by XPS measurements [267].

8.2.2 Experiments on Au(111)

In this section, the adsorption of iron deposited on both the room temperature as well as the heated Au(111) sample is investigated. First, iron deposited at room temperature is investigated. These experiments act as control, that the previously described growth of iron is achieved. Furthermore, the room temperature experiments allow the determination of iron coverage at different sample positions. These values are set as expected coverages. In the second experiment, the impact of heating the Au(111) sample to 383 K during the iron deposition is investigated regarding the iron adsorption. The formation of an iron and gold alloy is investigated. Iron is deposited onto an Au(111) sample of a size of roughly 5 mm × 6.5 mm, while the spot size of the EFM3T has a diameter of 14 mm. Measurements to determine the iron coverage have been conducted at six different positions on the Au(111) sample, as illustrated in the graphic in figure 8.3. These measurements have been performed after one Fe deposition with a flux of 2.23 nA and a deposition time of 80 min. Multiple overview images of a size of up to 200 nm × 200 nm have been acquired at each of the positions. To determine the local coverage c (in atoms/nm^2) in the experiments, the surface area of the islands A_{island} (in nm^2) is measured, as well as the size of the image A_{image}. Based on the A_{island} and the coverage of one monolayer (c_{ML} = 13.9 atoms/nm^2) the number of iron atoms in one image is determined and the coverage c is calculated by.

$$c = \frac{A_{island} \cdot c_{ML}}{A_{image}} \tag{8.1}$$

To determine the deposited monolayer (ML) of iron, the local iron coverage $c(atoms/nm^2)$ and the coverage of one monolayer (c_{ML}) are used.

$$ML = \frac{c}{c_{ML}} \tag{8.2}$$

In the experiments, a sub-monolayer coverage is obtained at every position at the Au(111) sample for a flux of 2.23 nA and 80 min deposition time. The results are shown in figure 8.3. Across the sample, the coverage varies by a factor 100.
The iron coverage amounts to a minimum at position VI (c.f. tab. 8.1) with 0.1 atoms/nm^2 (0.007 ML). As imaged in figure 8.3b, the previously described nucleation at the herringbone elbows can be observed at position VI. The nucleation centres are imaged as small protrusions. The highest coverage is obtained at position III, which amounts to 9.2 atoms/nm^2 (0.661 ML), see figure 8.3c and table 8.1. In figure 8.3c iron islands on

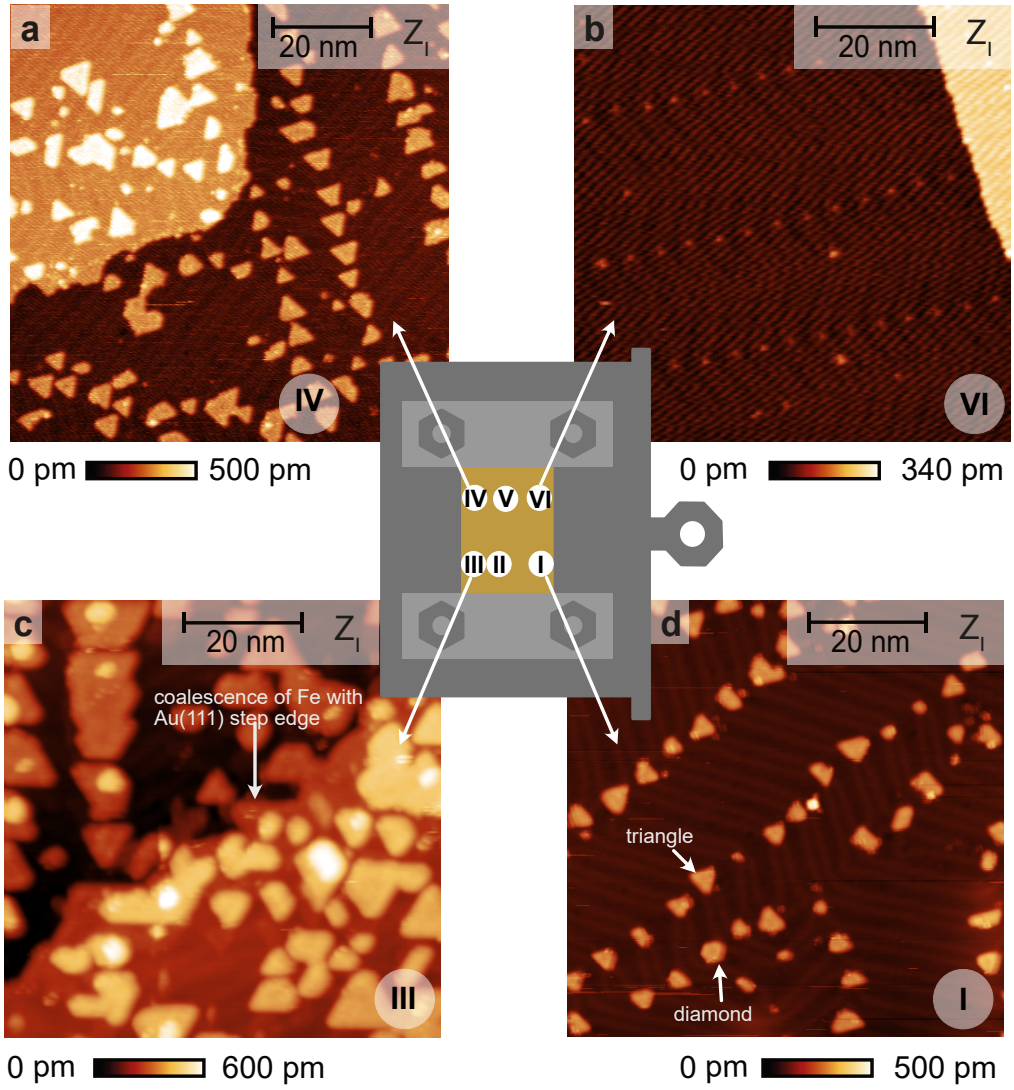

Figure 8.3: Deposited iron islands on Au(111) surface. Schematic of sample holder including the investigated areas on the sample system in the centre. Images (a-d) all taken after the same deposition, (a) area IV with a coverage of 0.247 ML, (b) area VI with a coverage of 0.007 ML, (c) area III with a coverage of 0.661 ML, and (d) area I with a coverage of 0.068 ML. Due to the previously described technical issues in chapter 3.2, severe disturbances limit the imaging quality in region IV, and VI. Imaging parameters: (a,b) $I = 50\,\text{pA}$, $U_S = -25\,\text{mV}$, $T_S = 4.6\,\text{K}$; (c) $I = 500\,\text{pA}$, $U_S = -5\,\text{mV}$, $T_S = 4.6\,\text{K}$; (d) $I = 500\,\text{pA}$, $U_S = 5\,\text{mV}$, $T_S = 4.6\,\text{K}$; Deposition parameters: Flux:2.23 nA, $t = 80\,\text{min}$.

Au(111) and an Au(111) step edge is imaged. At this point, coalescence of the islands starts occurring. Initiating second-layer growth is also observed at a coverage of 0.661 ML. The iron islands do also coalesce with the Au(111) step edge, an example is marked in figure 8.3c. These results match the previous results described in literature (see chapter 8.2.1). The large differences in coverage are most likely a result of a small misalignment of the EFM3T and the deposition position of the manipulator arm. This results in

Table 8.1: Determined Fe coverage. The flux is listed for the different depositions. The deposition time is given in minutes. Sample position is listed in the next column, with the positions matching the positions illustrated in figure 8.3. Iron coverages are listed as atoms/nm^2 (c) and monolayers (c_{ML}). The expected coverages (c_{exp}) for iron and TMA experiments are deduced from the coverage at position I for pure iron.

Flux [nA]	Time [min]	Position	T [K]	c [atoms/nm^2]	c_{ML} [ML]	c_{exp} [ML]
	Pure Iron					
2.23	80		298			
		Position I		1.0 ± 0.1	0.068 ± 0.001	
		Position II		6.7 ± 0.1	0.482 ± 0.001	
		Position III		9.2 ± 0.1	0.661 ± 0.001	
		Position IV		3.4 ± 0.1	0.247 ± 0.001	
		Position V		1.2 ± 0.1	0.084 ± 0.001	
		Position VI		0.1 ± 0.1	0.007 ± 0.001	
5.1	80	Position I	383	3.6 ± 2.4	0.26 ± 0.17	0.15
	Iron and TMA	Position I				
2.23	80		298	1.0 ± 0.4	0.07 ± 0.03	0.07
2.23	80		298	0.9 ± 0.4	0.06 ± 0.03	0.07
2.68	80		298	2.5 ± 1.1	0.18 ± 0.08	0.08
1.6	60		298	2.5 ± 1.6	0.2 ± 0.1	0.17
2.5	80		338	8.4 ± 2.2	0.6 ± 0.2	0.08
5.1	80		383	3.6 ± 1.1	0.3 ± 0.1	0.15

a iron gradient across the Au(111) surface. The iron coverage at position I amounts to 1 atoms/nm^2 (0.068 ML), where triangular and diamond shaped islands are observed. Both island types are highlighted in figure 8.3d. Most islands are observed at the elbow sites of the Au(111)'s herring bone reconstruction. The following experiments are all conducted at position I, as the coverage is the most suitable at this position. Therefore, the coverage at position I is set as calibration for later experiments. It allows determination of the expected coverage for different deposition parameters. The expected coverage c_{exp}, determined from the deposition parameters, requires a conversion factor. This is determined by the experimentally ascertained coverage at position I $c_{ML-pos.I}$, divided by the theoretically ascertained coverage $c_{theo-pos.I}$ for given deposition parameters. The conversion factor is multiplied with the theoretically determined coverage $c_{ML-theo}$ for the experimental parameters of the deposition.

$$c_{exp} = c_{ML-theo} \frac{c_{ML-pos.I}}{c_{theo-pos.I}} \tag{8.3}$$

The theoretical coverage can be determined by rate r and time of deposition t.

$$c_{ML-theo} = \frac{3}{r}\frac{t}{60min} \tag{8.4}$$

Rate and flux have a linear correlation, which ultimately allows the determination of the expected coverage depending on flux, deposition time and the conversion factor.

$$r = 9 \cdot 10^{-5} flux + 2 \cdot 10^{-5} \tag{8.5}$$

Both expected coverages and experimental results of depositions with TMA are given in table 8.1. Comparing the expected coverages with the experimentally determined coverage of combined iron and TMA experiments shows that the expected coverage matches the measured coverages reasonably well. Exemptions are deposition of iron onto heated Au(111) surface. The experimental coverage is up to a tenfold higher than the expected coverage. The overestimation can be correlated to the alloying occurring at increase temperature. As described in the following section, identification of iron is not conclusive and the proposed areas allocated to iron, might be alloys. Therefore, the coverage for deposition onto heated surfaces, needs to be considered with caution. Additionally, during parallel deposition of TMA and iron, the molecules and metal atoms seem to form mixed material islands. This might lead to an overestimation of the iron coverage, as the size of the mixed islands will be larger than for pure iron.
In summary, Fe deposition onto room temperature Au(111) has been performed successfully. The coverage dependent stages of iron growth on Au(111) have been reproduced. The formation of triangular and diamond shaped islands has been observed, as well as the coalesce and second-layer growth at higher coverages.

8.2.2.1 Formation of a Fe/Au(111) Near-Surface Alloy

As later experiments with TMA and Fe require deposition of Fe onto a heated Au(111) sample, the experiments are conducted without TMA first. Kahn et al. identified the formation of a near-surface alloy at 400 K with XPS [35], in this paragraph I investigate the beginning alloying process with STM. The Au(111) sample is heated to 383 K during Fe deposition. In comparison to room temperature deposition, Au(111) surface and iron are impacted by the elevated temperature, which is shown in the STM overview image in figure 8.4. The image shows several step edges, which are frayed, an example is highlighted in green in figure 8.4a. The terraces themselves show a disturbed herring bone reconstruction, which is indicated in figure 8.4a and b. The herringbone reconstruction does not show the characteristic 120° elbows, but various angles. The domain walls of the herringbone

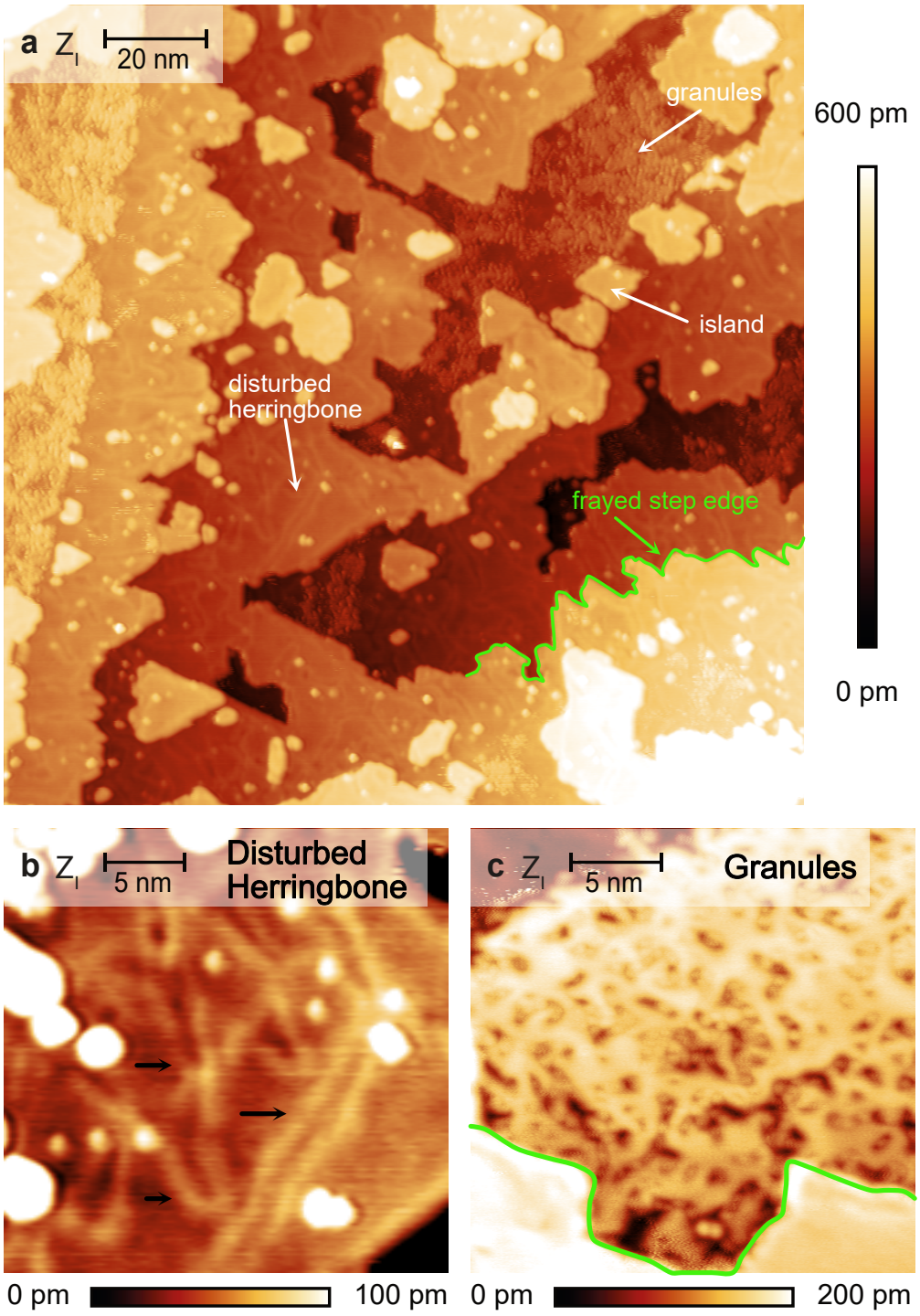

Figure 8.4: Fe deposited onto a 383 K Au(111) surface (a) STM overview image of Fe/Au(111) surface. Exemplary island, region with disturbed herringbone and granules are indicated, a frayed step edge is highlighted in green. (b) Detail image of an area with disturbed herring bone. Exemplary disturbed herringbone reconstruction indicated by black arrows. (c) Detail image of a granule region at a frayed step edge highlighted in green. Imaging parameters: (a-c) $I = 100\,\mathrm{pA}$, $U_S = 1\,\mathrm{V}$, $T_S = 78.2\,\mathrm{K}$.

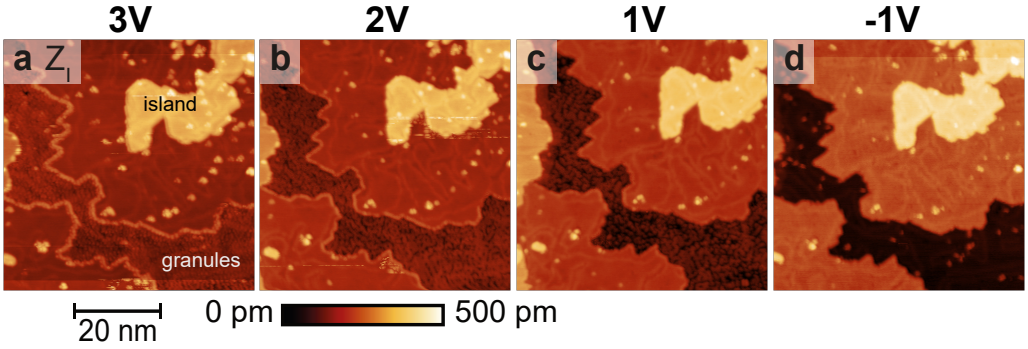

Figure 8.5: Fe/Au(111) alloy at different bias voltages: (a) $U_S = 3\,\mathrm{V}$, (b) $U_S = 2\,\mathrm{V}$, (c) $U_S = 1\,\mathrm{V}$, (d) $U_S = -1\,\mathrm{V}$. Imaging parameters: (a-d) $I = 100\,\mathrm{pA}$, $T_S = 78.2\,\mathrm{K}$.

reconstruction do not run parallel most of the time. Another characteristic of Fe deposited onto the heated Au(111) sample are features here referred to as granules. Granules are areas of a layer of an undefined assembly covering the terrace. Examples of the granules are highlighted in figure 8.4a and c. Furthermore, islands are observed on all terraces, an exemplary one is also indicated in figure 8.4a. As larger islands can also be observed, the distinction between large island and terrace is sometimes unclear. Changing the imaging parameters gives insight on structural differences between islands and terraces. At larger bias voltages (2 V, 3 V) a decoration of the step edges is observed for terraces only (see figure 8.5a,b). At these positions the step edges appear much brighter than the terrace. The island's step edge, however, does not appear brighter at said bias voltages. This leads to the suggestion that the terraces are decorated with iron or an alloy and the islands are not. Measuring the at negative bias voltages, step edges of islands and terraces are imaged identical. However, at negative bias voltages STM does not image granules, which are imaged throughout the images at positive bias voltage.

A clear allocation of the observed characteristics to iron, Au(111), or an Fe/Au(111) alloy is not possible. Therefore, the described observations are compared to the results of Zn/Au(111) alloy [267]. The disturbed herringbone reconstruction has also been observed for Zn/Au(111), in this case it is caused by a replacement of Au surface atoms with Zn atoms. The finger like extension of the step edges is allocated to the formation of a Zn/Au alloy [267].

Based on the observations and the comparison with the Zn/Au(111) alloy, I suggest that the islands are a homogeneous compound, likely of iron or an alloy of unknown chemical composure. The terraces consist most likely of Au(111) with Au atoms exchanged with Fe atoms, causing the disturbance of the herring bone. The step edges are decorated with either iron or an alloy. The granules are most likely an alloy as well, as this kind of behaviour, as far as I know, has not been observed for pristine iron on gold. The exact

chemical composition of the possibly different alloy cannot be distinguished from the STM data.

8.3 TMA Assembly on Au(111)

In the following sections, STM and NC-AFM experiments of TMA on Au(111) will be presented. First, experiments with TMA deposited onto the sample held at room temperature are analysed in section 8.3.1. Here, the formation of different assemblies is examined. Second, the possibility of guest molecules in the HON pore is investigated and guest molecules are introduced by co-depositing CO molecules (see section 8.3.2). Third, a closer look is taken at the hydrogen bond of the carboxylic dimer in a HON network (section 8.3.3).

8.3.1 Room Temperature Deposition of TMA on Au(111)

As described in section 8.1, TMA is known to assemble in several different assemblies on Au(111) after room temperature deposition. In this work, it is confirmed that several different assemblies can occur simultaneously, due to local coverage differences on an Au(111). This is shown in the overview image of 94.5 nm × 94.5 nm, acquired at a coverage of 0.3 molecules/nm^2 in figure 8.6a, where HON networks, two types of flower structures, and close-packed structure are observed. This matches the previously described results, where local coverage differences have been described to result in simultaneously occurring assemblies [244].

For all observed assemblies, the TMA molecules are imaged alike for voltages of ±1 Vin STM imaging. Each molecule exhibits a triangular shape, where the triangle apexes can be allocated to the carboxylic acid moieties of TMA [244]. This is illustrated by placing a TMA model onto the imaged TMA molecule in figure 8.6b. Despite, increasing the voltage to 2.7 V has been reported to result in a different contrast [250].

As shown in figure 8.6a, the predominant structure is the HON network, where purely dimeric bonds cause the long range ordered assembly. An amplified image of HON network is displayed in figure 8.6c.

Another group of assemblies observed are flower structures. The size of the flower structures can vary with the number of molecules connected via trimeric bonds. Examples of different sized flower structures are reproduced in figure 8.6d and e: 6 molecules per unit cell in 8.6d, and 12 molecules per unit cell in 8.6e.

The close-packed structure is also observed in these experiments. This structure is formed by only trimeric bonds form intermolecular interaction. A close-packed structure is

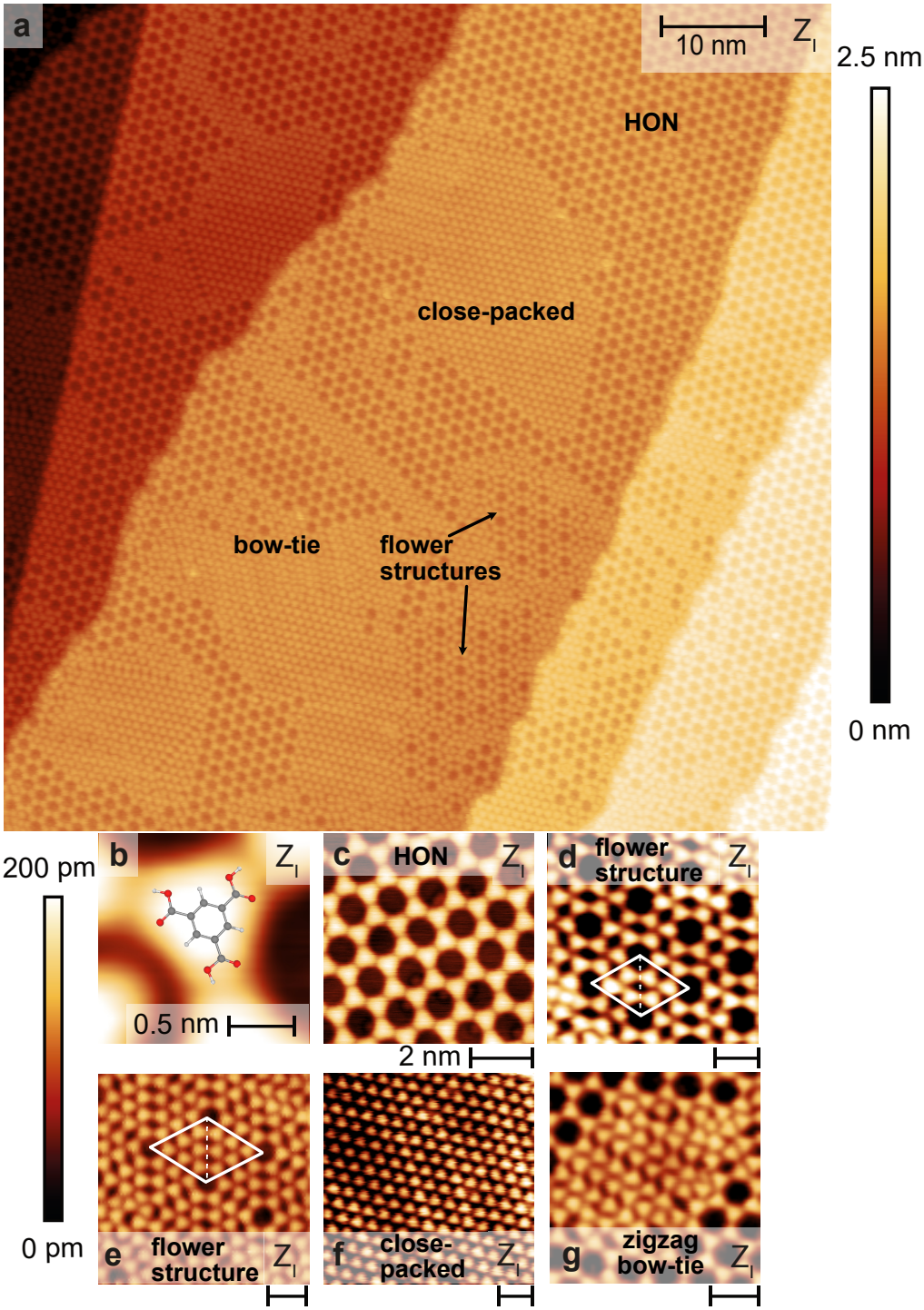

Figure 8.6: Variety of TMA unit cells observed on Au(111) after room temperature deposition. (a) Overview STM image of TMA molecules covering several, neighbouring gold terraces showing various TMA assemblies. (b) Schematic of a single TMA molecule placed on an STM image. (c) A close up of a honey comb network. (d-e) Different sizes of flower structure. (f) Close-packed TMA molecules. (g) A bow-tie arrangement of TMA molecules. $c_{TMA} = 0.3\,\text{mols/nm}^2$ Imaging parameters: (a,c,e,f) $I = 50\,\text{pA}, U_S = 50\,\text{mV}, T_S = 4.6\,\text{K}$; (b) $I = 5\,\text{pA}, U_S = 50\,\text{mV}, T_S = 4.6\,\text{K}$, (d,g) $I = 50\,\text{pA}, U_S = 500\,\text{mV}, T_S = 4.6\,\text{K}$.

depicted in 8.6f. These structures match the structures reported in literature before [244].

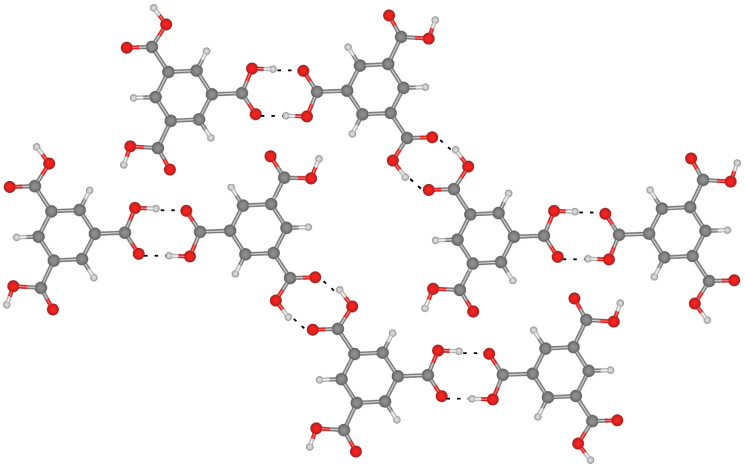

Figure 8.7: Schematic of the zigzag bow-tie structure, potential hydrogen bonds are indicated by dashed lines.

Additional to the structures reported so far in literature, another structure is observed in these experiments. As shown in figure 8.6g, it is a densely arranged, pore less structure. In the following, the term densely arranged area will be the term to describe poreless assemblies, who have no defined structure (yet). Due to its shape the structure will now be referred to as zigzag bow-tie, as the triangle apex of two molecules point towards each other. A proposed structure of the zigzag bow-tie structure is shown in figure 8.7. This structure was determined by aligning molecular models on top of several STM images. The main characteristic of the zigzag bow-tie structure are the two dimeric bonded TMA molecules, which resemble a bow-tie. Therefore, this motif will also be called bow-tie motif. One bow-tie motif is connected to the next molecule via dimeric bond forming another bow-tie motif. The next row of molecules is slightly shifted forming another zigzag row. The zigzag bow-tie structure resembles the assembly observed at domain walls, where two differently orientated HON networks interlace. However, the zigzag bow-tie structure shows larger structures than previously observed for domain walls.

In conclusion, in this work most of the TMA networks on Au(111) at room temperature deposition described by Ye et al. [244] have been confirmed. Moreover, the zigzag bow-tie structure, a densely arranged structure consisting of dimeric bound TMA molecules, is observed. The zigzag bow-tie structure matches the assembly observed at domain walls of two adjacent HON domains, where the HON is displaced. Nevertheless, so far larger ordered networks of zigzag bow-tie structures have not been reported to the best of my knowledge.

8.3.2 Guest Molecules in HON Pores: TMA and CO Molecules

Porous networks like the HON network are known to host guests. In this section only HON network will be discussed only regarding hosting guest molecules. Here, TMA molecules are spotted to act as guest molecules inside the HON pores. An example of an empty HON pores is given in figure 8.8a. An example of a HON pore filled with a TMA guest molecule is given in figure 8.8b. Here, the molecule is absorbed non-central in the HON forming intermolecular interaction between the carboxylic acid moieties, which matches the host-guest geometry observed by Ibenskas et al. [251]. In this work, 5 % of HON pores are filled with a guest TMA molecule. Furthermore, alien molecules can be introduced as guests to the HON pore [245, 251, 252, 253, 254]. Here, I investigate the addition of CO via dosing into the cold scan head. The HON network and flower, and close-packed structures described previously remain intact during the deposition. CO is observed on areas of the pristine Au(111) as well as inside HON pores. This is depicted in figure 8.8c, where three out of four pores are filled with one CO molecule each. Two adsorption geometries are observed for the CO guest molecule in figure 8.8c: It adsorbs either at the dimeric hydrogen bond, the position, where both triangular apexes meet (highlighted with a white arrow), or at the base of the triangle, between both carboxylic acid moieties of one TMA molecule (highlighted with a yellow arrow). In summary, the occasional filling of the HON pore with TMA molecules is confirmed, which matches the results in literature very well [251]. Additionally, CO deposited onto the cold sample results in CO acting as guest molecule.

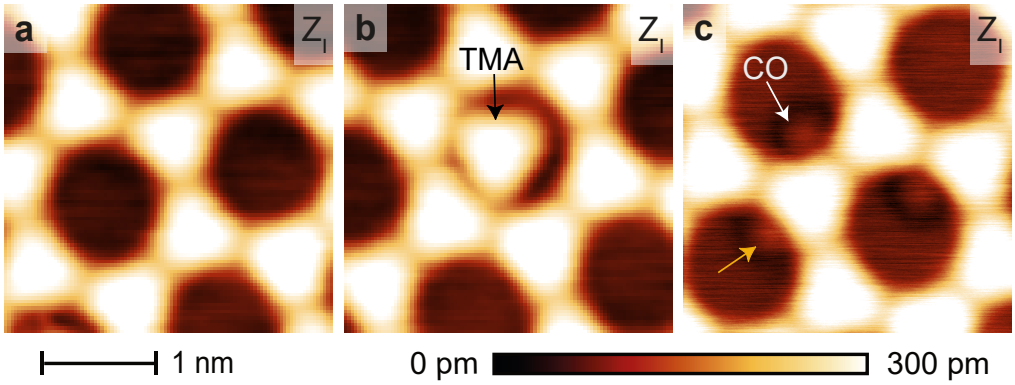

Figure 8.8: Images of HON pores. All images are displayed in the same size. (a) Empty HON pores, (b) one HON pore hosting a TMA molecule, (c) three HON pores hosting one CO molecule each. Imaging parameters: $I = 5\,\text{pA}$, $U_S = 50\,\text{mV}$, $T_S = 4.6\,\text{K}$.

8.3.3 Constant-Height NC-AFM imaging the Honeycomb Network and Mapping the Interaction Forces between CO Tip and the Honeycomb Network

This section focuses on imaging the carboxylic acid dimer of the honeycomb network with constant-height NC-AFM imaging using CO functionalised tips. In addition to constant-height images, systematic force mapping of the HON network is conducted to determine total and site-specific interaction forces between CO tip and different positions within the HON network: Site-specific interaction forces are acquired at the possibilities of the carbon atoms of both the benzene ring and the carboxylic acid group, as well as the bond between the two carbon atoms. Plus, the interaction force between the CO tip and the benzene ring centre is investigated. But, especially, an emphasis is set on the hydrogen-bonded intermolecular region, namely the region of the carboxylic acid dimer.

8.3.3.1 Constant-Height NC-AFM Images of TMA Molecules and the Honeycomb Structures

While TMA molecules exhibit a triangular shape in STM images (see section 8.3.1, figure 8.9a), the molecular structure is uncovered in a much higher detail with high-resolution NC-AFM images in constant-height mode.

$\Delta f(z)$ curves (figure 8.9b) are acquired at three different positions: the benzene ring centre, the centre of the carboxylic acid dimer ($R_2^2(8)$), and the HON pore. At the HON pore position an overall attractive $\Delta f(z)$ curve is acquired. Between the benzene ring centre and the tip repulsive interaction is observed from a tip sample distance of about z_p=75 pm. The interaction between tip and sample at $R_2^2(8)$ centre is attractive until a very small tip-sample interaction is reached. Constant-height NC-AFM data shown in figure 8.9c,d is in agreement with the frequency shift curves. The HON pores are imaged with attractive interaction for all tip-sample distances. The imaged features at the TMA molecule positions are strongly dependent on the tip-sample distance. In figure 8.9d, the HON network is imaged in constant-height mode, while z_p is increased from bottom to top. The total z_p range amounts to 74 pm, within the $\Delta f(z)$ curves the z_p range is marked in grey (see figure 8.9b). The z_p range is deduced from the $\Delta f(z)$ curves at the HON pore by comparing the Δf values in the HON pore within image 8.9d to the values of the $\Delta f(z)$ curve. Based on the distant-dependent imaging of the TMA molecules in the HON network, a decrease of the tip-sample distance results in the observation of three key changes in the imaging: First, the benzene ring exhibits a doughnut-like shape at larger tip-sample distances. This doughnut-like shape is defined by a nearly circular protrusion with a depression in the centre. In comparison, in the work of Zahl et al., the benzene

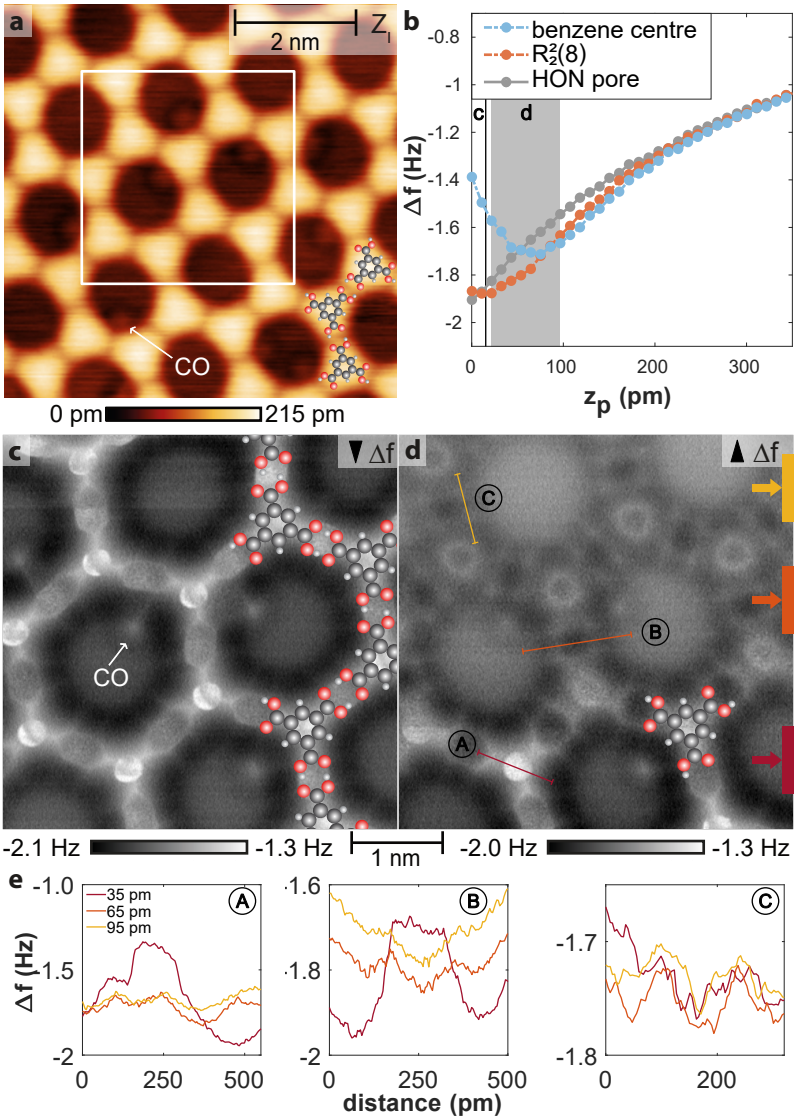

Figure 8.9: (a) STM and (c,d) constant-height NC-AFM images of HON networks, scan directions are indicated by small black triangles. (d) The tip-sample distance is increased from bottom to top by about 74 pm (deduced from $\Delta f(z)$ curves in (b)), to highlight the distance-dependent imaging contrast. (e) Line scans at different tip-sample distances along (A) the benzene ring; as well as (B) perpendicular, and (C) parallel to the hydrogen-bonded carboxylic dimer. Imaging parameters, (a) STM: $I = 5\,\text{pA}$, $U_S = 50\,\text{mV}$, (c,d) NC-AFM: $f_0 = 26\,172\,\text{Hz}$, $U_S = 0\,\text{V}$, All: $T_S = 4.6\,\text{K}$.

ring of TMA molecules expresses a more triangular shape, which is explained due to electrostatic attractive behaviour of the carboxylic acid moieties towards the benzene ring [268].

In this work, when decreasing the tip-sample distance, the benzene ring is imaged as a disc-like protrusion with sharp edges. The transition from doughnut- to disc-like shape can be observed in the line scans performed across the benzene ring, shown in figure 8.9e.

At 95 pm and 65 pm, a depression is clearly visible at the benzene centre, the line scan of the benzene ring does not show a depression at the ring centre at 35 pm. A step of roughly half the total height is observed at one side of the protrusion of the benzene ring, this is allocated to the carbon of the carboxylic acid moiety. The transition from doughnut- to disc-like shape has also been observed upon tip-sample distance reduction at the hexagonal facet of fullerene molecules [269]. The transition has been explained by tip relaxation due to the repulsive tip-sample interaction [269].

Second, the oxygen atoms of the carboxylic acid moieties are imaged as round, repulsive protrusions at a larger tip-sample distance of about 95 pm. Reducing the tip-sample distance to about 35 pm results in the sharpening of the features to a triangular shape between the oxygen atoms and the carbon atom of the carboxylic acid moiety ($C_{carbonyl}$). Here, I would like to emphasize that both oxygen atoms of the carboxylic acid moiety are imaged identically, however, chemically they are different: The hydroxyl oxygen atom is covalently bound to $C_{carbonyl}$ and the hydrogen atom via one bond each, while the carbonyl oxygen atom is bound to the $C_{carbonyl}$ atom via a double bond. The observation of both oxygen atoms being imaged identically and the observation of single protrusions at the oxygen positions, as well as sharp lines at the oxygen-carbon bond position matches observations made for bis-(parabenzoicacid) molecules on Au(111) with CO and Xe tips [74]. However, the single repulsive features have been observed with the CO tip and sharp triangular features at bond position have been reported for NC-AFM measurements with a Xe tip [74]. The difference observed in the Δf contrast, when imaging with the different terminated tips, is explained by the electrostatic interaction, as the CO tip is negatively and the Xe tip is positively charged [74].

Third, at larger distances, no repulsive features are observed at the hydrogen bond positions. Sharp lines evolve at the hydrogen bond position upon reducing the tip-sample distance. The results at larger tip-sample distances match the results observed for TMA on Cu(111), where also no repulsive features are observed at the hydrogen bond positions [268]. While it is established that electron density exists at the hydrogen bond position, which can also result in bond-like features in high-resolution NC-AFM [94], sharp features have also been explained as a result of the summation of electron densities of non-interacting molecules, resulting in a repulsive interaction with the tip [109].

The line scans (B) and (C) shown in figure 8.9e are extracted along the carboxylic dimer from figure 8.9d. Line scan (B) proceeds vertically to the hydrogen bond, and line scan (C) proceeds along the O-H-O axis. Line scans (B) show differences depending on the tip-sample distance: For larger distances, larger frequency shifts are observed at the oxygen position, and a lower value is observed at the dimer centre. At smaller tip-sample distance, the line scan clearly shows higher frequency shifts at the carbobxylic dimer area. Line

scan (C) surprisingly does not show distinct differences for different tip-sample distances, as based on the different contrasts at the oxygen position one would expect differences within the line scans.

8.3.3.2 Interaction Force Maps

Additional to constant-height NC-AFM images, systematic distance-dependent force measurements are performed between the CO functionalised tip and the HON network. In the next paragraph, a short description of the acquisition and process of the force measurements is given. This is followed by an analysis of the site-specific measurements.

Methods

First, distance-dependent force measurements are performed along two lines (red and blue) as highlighted in figure 8.10a. Along both lines, force measurements are acquired along a z_p range of 510 pm at a small tip-sample distance. Additionally, three long-range curves are acquired, covering a total z_p range of 5 nm. Second, drift vectors along all three directions are determined for the residual drift. For this purpose, the grid of the HON is aligned within the constant-height NC-AFM image in figure 8.10a. The data are drift corrected by shearing the image, the slice data is drift corrected by translating subparts of the images and shearing the slice data. The void areas within the constant-height NC-AFM image are filled with average Δf values of the background.

Frequency shift curves are extracted at ten different positions as marked in figure 8.10a: Positions above atoms of the TMA molecule are marked with circles, bond positions and intermolecular positions are marked with crosses, positions in the HON pore are marked with stars. Third, the frequency shift curves ($\Delta f(z_p)$) are translated to force curves ($F(z_p)$) via the Sader-Jarvis formula [270], the results are shown in figure 8.10d. The force curves show an overall attractive interaction between tip and sample, with minima around 500 pN.

A variety of long- and short-ranged forces contribute to the total force. While short-range forces include chemical interactions, long-ranged forces include for example van-der-Waals interactions (see chapter 3.1.2). The long-ranged forces include background forces between the surface and the mesoscopic tip. To eliminate the background forces, additional to the curves taken at positions of the TMA molecule or the hydrogen-bonded dimer area, two curves are taken within the HON pore. Both curves without molecular contribution show long-range forces. These force curves (grey) are then used for the *"on-minus-off"* approach [271], where the respective curves are subtracted from the data set. The site-specific force curves are shown in figure 8.10e.

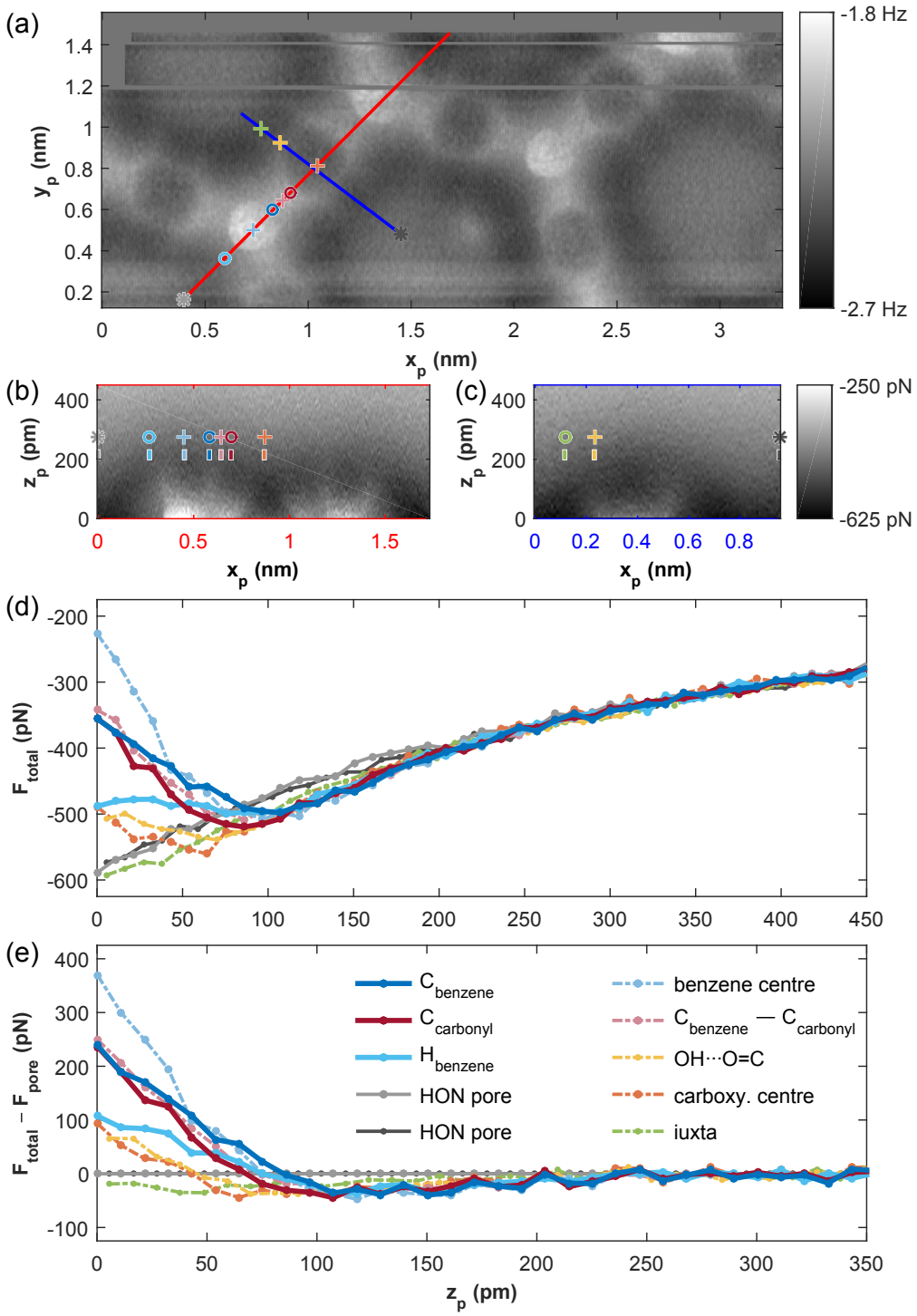

Figure 8.10: Distance-dependent force measurements using a CO tip. (a) NC-AFM image as reference with the positions of X-Z force measurements marked (red and blue line). X-Z force measurements (b) along (red) and (c) across (blue) the carboxylic acid dimer. Circles (crosses) mark the atom (bond and intermolecular position) positions of the force curves. (d) Total and (e) site-specific extracted from the X-Z force measurements (b,c). Savitzky-Golay filter is applied to force data along z_p (window size: 21 pixel, being equivalent to 10.7 pm), 3 pixel average is applied to force curves along x_p in (d,e).

Site-Specific Forces

The site-specific force curves are interpreted as interaction between the CO tip and the TMA molecule, as the influence of the Au(111) sample, as well as the influence of the mesoscopic tip is eliminated by subtracting the force curves of the HON pore. For all force curves, the attractive regime is rather weak, with a maximum of about 50 pN at a tip-sample distance of 100 pm. The magnitude of the attractive interaction agrees with calculations of attractive van-der-Waals interaction between a CO tip and a molecule, specifically for the example of azines [109]. When the tip-sample distance is reduced, repulsive interactions occur at almost all positions, with the so called iuxta position, which is directly next to the hydrogen bond of the carboxylic acid dimer, being the only exception.

The strongest repulsion is observed at the benzene centre position (light blue dashed line), with a maximum repulsive force of about 350 pN.

At the σ bond position (rose dashed line), which is the bond between the carbon atom of the benzene ring and the carbon of the carboxylic acid group, the repulsion is weaker compared to the benzene ring centre. However, in a similar range as for the σ bond, site-specific forces are observed at the force measured at the atomic position of the carbon of the benzene ring ($C_{benzene}$, dark blue solid line), as well as the carbon of the carboxylic acid group ($C_{carbonyl}$, dark red solid line). At the smallest tip-sample distance the repulsive forces at the three positions ($C_{benzene}$, $C_{carbonyl}$, σ bond), show a similar quantity of about 250 pN. However, at an intermediate tip-sample distance of about 25 pm-100 pm, differences occur at the three sites. The site-specific force at the $C_{benzene}$ position is more repulsive than at the σ bond position, where a higher repulsion is observed than at the $C_{carbonyl}$ position.

The $C_{carbonyl}$ has two oxygen atoms, which are covalently bound. These oxygen atoms are electronegative in comparison to the carbon atoms, resulting in a positive polarisation of the $C_{carbonyl}$. As the CO tip has a negatively charged cloud in front of the oxygen atom [112], a stronger attraction is expected between the CO tip and the positively polarised $C_{carbonyl}$. This is in alignment with the observation that a more attractive interaction occurs between CO-tip and $C_{carbonyl}$.

The repulsive force at the hydrogen position of the benzene ring (light blue solid line) is smaller than the forces measured at the other atomic positions, while the maximum repulsive force at the $H_{benzene}$ is comparable to the forces measured at the hydrogen bond position (yellow dashed line) and the carboxylic acid dimer centre (orange dashed line) at about 100 pN. However, the repulsive force at the hydrogen atom position rises at a tip-sample distance of about 100 pm, but the curve has a very flat slope. The repulsive forces at the hydrogen bond position and the dimer centre start to increase at about 70 pm.

The repulsion measured at the hydrogen bond position is likely amplified by the deflection of the CO tip towards the void region of the HON pore, as the electron density is expected

to be lower at the HON pore.
When further inspecting the forces measured at the hydrogen bond position (yellow dashed line) and at the centre of the carboxylic dimer (orange dashed line), very similar force magnitudes are found at both positions. The similarity of both force curves, is surprising at first, as a higher electron density is expected at the hydrogen bond position than at the carboxylic acid dimer centre. The higher electron density would be expected to result in a higher repulsion at the hydrogen bond position.
One possible explanation, why similar forces are observed at both the hydrogen bond position and the carboxylic acid dimer position, can be given by the negatively charged cloud in front of the CO tip [112]: Repulsion occurs between tip and the increased electron density of the hydrogen bond. However, similar repulsion at a small tip-sample distance at the carboxylic acid dimer position can be caused by an additive effect of the surrounding electron density of the hydrogen bonds on both sides.
Nevertheless, a difference of forces at both positions is apparent in the slice data in figure 8.10c: At the position of the hydrogen bonds white filaments are found. These filaments extend outwards from the position of the hydrogen bond, and show a tilted shape. This shapes creates a difficulty to identify the filaments presence in the vertical force curve at the hydrogen bond position. Still, in the NC-AFM image these filaments are imaged as sharp lines at a small tip-sample distances.

8.3.3.3 Summary

Summarising, with high-resolution NC-AFM imaging of the HON network the structure of the TMA molecules and the intermolecular regions are identified. NC-AFM images show features at the benzene ring and the carboxylic acid positions, as well as intermolecular features at the carboxylic acid dimer. However, the contrast observed is strongly distance dependent. The benzene ring is imaged as doughnut like shape at a large tip-sample distance, upon tip-sample distance reduction the contrast transitions to a disc-like shape. The contrast observed at a larger tip-sample distance matches in the majority of observations with the results of the HON on Cu(111) by Zahl et al. [268], however, on Cu(111), the benzene ring expresses a more triangular shape. The transition from doughnut shape to disc-like shape is in agreement with the observations of imaging fullerene molecules [269]. At the carboxylic acid group positions, point-like features are imaged at the oxygen positions, when imaging with a larger tip-sample distance. At a smaller tip-sample distance, triangular features are imaged at the carboxylic acid position. So far, the point-like protrusions have been observed when imaging with a CO tip, and the sharp, triangular features are observed with a Xe tip. [74]. Repulsive intermolecular contrast is only observed, when imaging at small tip-sample distances. The intermolecular contrast at

larger tip-sample distances is in agreement with NC-AFM measurements of the HON network on Cu(111) surface [268].
The site-specific forces show repulsive forces at a small tip-sample distance at all positions of the TMA molecule and the hydrogen-bonded carboxylic dimer position. Electrostatic interactions contribute to the site-specific forces, caused by the electronegative charged cloud in front of the CO tip. The electronegative CO tip is attracted by the positively polarised $C_{carbonyl}$ and repelled by electron dense regions such as the hydrogen-bond or when surrounded by electron dense areas, like at the carboxylic acid dimer position.

8.4 Thermally Induced Assembly Changes and the Influence of Fe Contaminations

In the following section, two factors are investigated regarding the influence on the TMA assembly: Heating of TMA on Au(111) and residual Fe contaminations in the Au(111) sample including heating experiments. The influence of heating on the TMA assembly is investigated by warming the sample system up to 383 K. This will be done, as later experiments with iron will require heating.
Due to the alloying process of iron with Au(111) (see section 8.2.2), iron contaminations of the Au(111) cannot be excluded in samples exposed to Fe in previous experiments. By repeating the heating experiments on a previously alloyed, and then cleaned sample, the presence of residual iron contaminations can be determined. The influence of residual Fe atoms in the Au(111) sample is investigated towards the TMA assembly in dependency of contamination density (see sections 8.4.2 and 8.4.3).
Hence, experiments are conducted on three different samples: Au(111) without prior Fe deposition, Au(111) with one Fe deposition at 383 K, and Au(111) with several cycles of Fe deposition including deposition onto heated surfaces. These will be abbreviated in this chapter as followed: pristine Au(111), Au(111)-Fe1, Au(111)-FeX. All Au(111) samples are cleaned prior the experiments by sputter and anneal cycles as described in section 4.1.1.

8.4.1 Heating TMA on Pristine Au(111) Sample

In this section, TMA is deposited onto the pristine Au(111) sample at room temperature. Then, the sample is heated to 348 K for another 10 min. As a next heating step the sample is warmed to 383 K for 10 min. After both heating steps the sample is allowed to cool down to 333 K and then the sample is placed into the scan head, which is cooled with liquid nitrogen to 78.3 K.

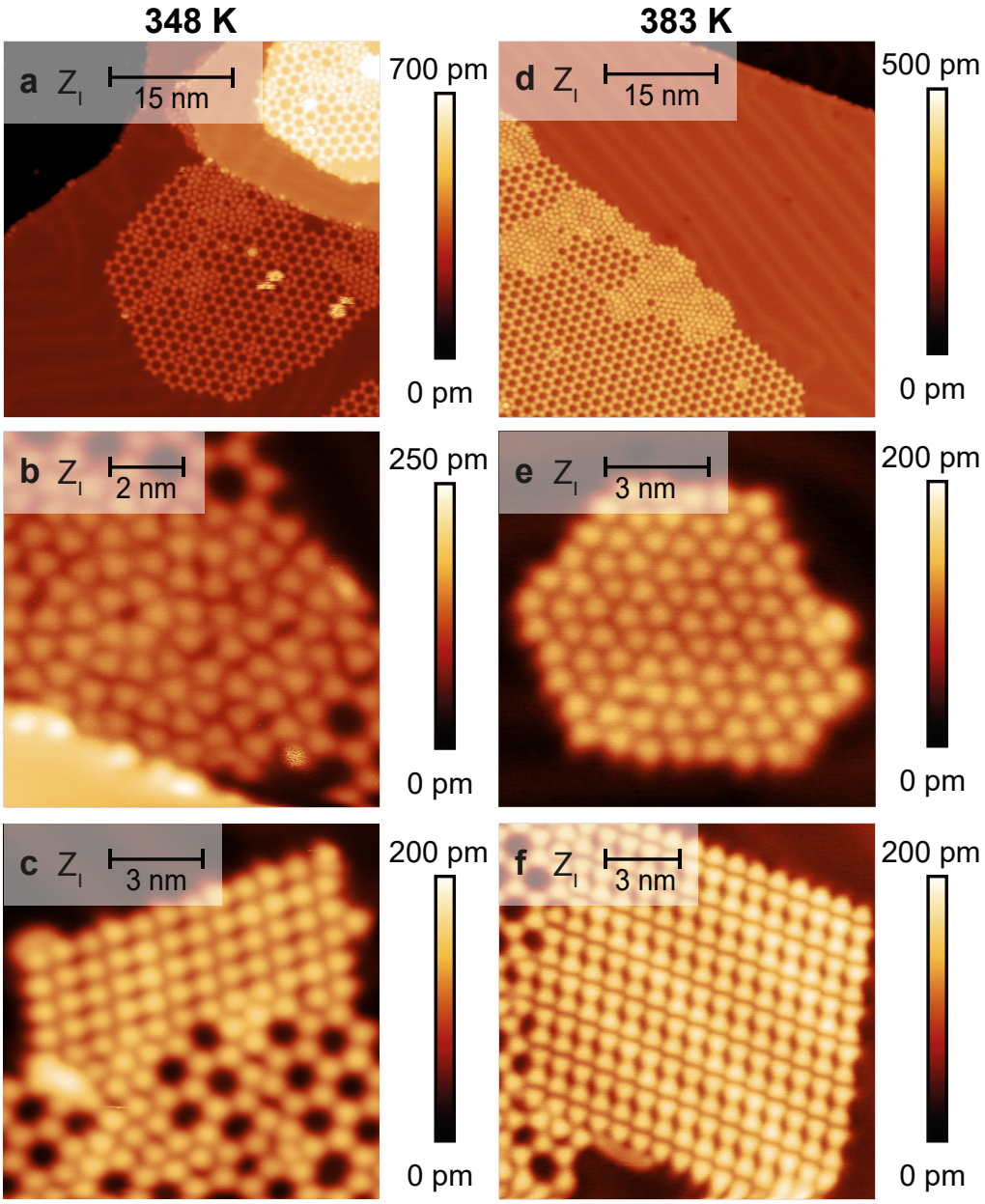

Figure 8.11: STM images of TMA on pristine Au(111) after heating the system to 348 K (a-c) and 383 K (d-f). (a) Overview image of TMA on pristine Au(111) after heating to 348 K showing Au(111) surface, HON and densely arranged areas. (b) Densely arranged areas at step edges. (c) Parallel bow-tie structure, HON and densely arranged areas. (d) Overview image of the sample after annealing to 383 K showing Au(111) surface, HON, and densely arranged areas. (e) Image of a densely arranged TMA island. (f) Parallel bow-tie structure. Imaging parameters: $I = 100\,\text{pA}$, $U_S = -500\,\text{mV}$, $T_S = 78.3\,\text{K}$.

As first step the sample has been heated to 348 K. Similar to room-temperature experiments, TMA forms large areas of HON networks, which are shown in figure 8.11a. The HON is interrupted by densely arranged areas without long range order. An example of such an

unordered area is given in figure 8.11b. Additionally, to the unordered, densely arranged areas, a new assembly can be observed. An example is given in figure 8.11c. It is mostly observed on the edge of either HON or unordered areas. The main characteristic of this area is the bow-tie motif. The dimeric bonded molecules form linear rows with the two carboxylic acid moieties not interacting in the dimeric bond are facing the next molecule arranged in a bow-tie motif. The neighbouring row of TMA molecules is arranged in parallel, therefore the structure is now called "parallel bow-tie" structure. The parallel bow-tie structures differs from the zigzag bow-tie structure observed at room temperature. A proposed bonding motif of the parallel bow-tie is given in figure 8.12. As described

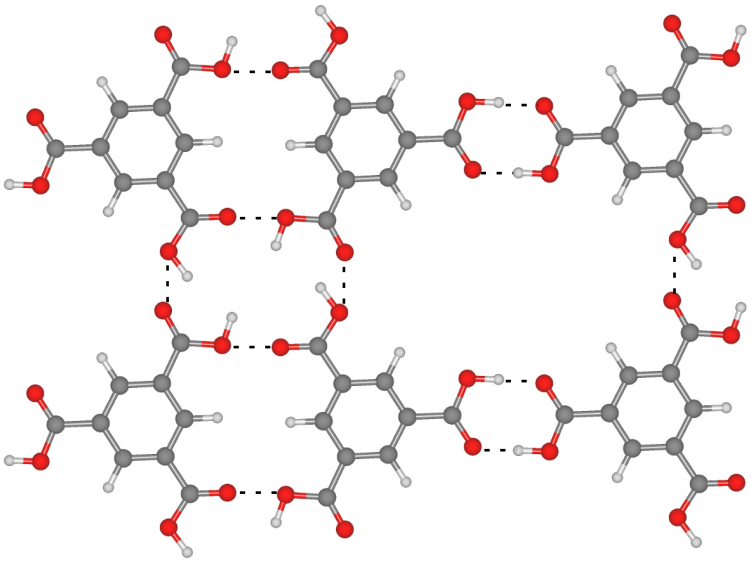

Figure 8.12: Proposed bonding motif of the parallel bow-tie structure, hydrogen atoms are positioned based on the HON network calculations. Different positions of hydrogen atoms are likely. Potential hydrogen bonds are indicated by dashed lines.

previously, the bow-tie motif consists of the dimeric bond. Here, the bow-tie motifs are connected most likely by two hydrogen bonds formed by four carboxylic acid moieties, as indicated in the illustration by dashed lines. The rows of connected bow-tie motifs are connected via one hydrogen bond per TMA molecule. This results in a maximum of possible hydrogen bonds. The rows of parallel bow-tie structures are terminated by TMA molecules with a single carboxylic acid group not engaged in a bow-tie motif.

As second step, the sample is heated to 383 K. Results are similar to the ones observed after heating to 343 K. The results after heating to 383 K are shown in the STM images in figure 8.11d-f. TMA forms large areas of HON, which is again interrupted by unordered, densely arranged areas. These are also uniquely observed as islands on the bare Au(111) terrace, without neighbouring TMA networks or step edges, an example of an island is given in figure 8.11e. Parallel bow-tie structure is also observed after this heating step (see figure 8.11f).

Summarising, heating TMA on the pristine Au(111) surface, results in HON and two new assemblies: The parallel bow-tie structure and unordered, densely arranged areas.

8.4.2 Heating TMA on a Sample Exposed to Fe Once

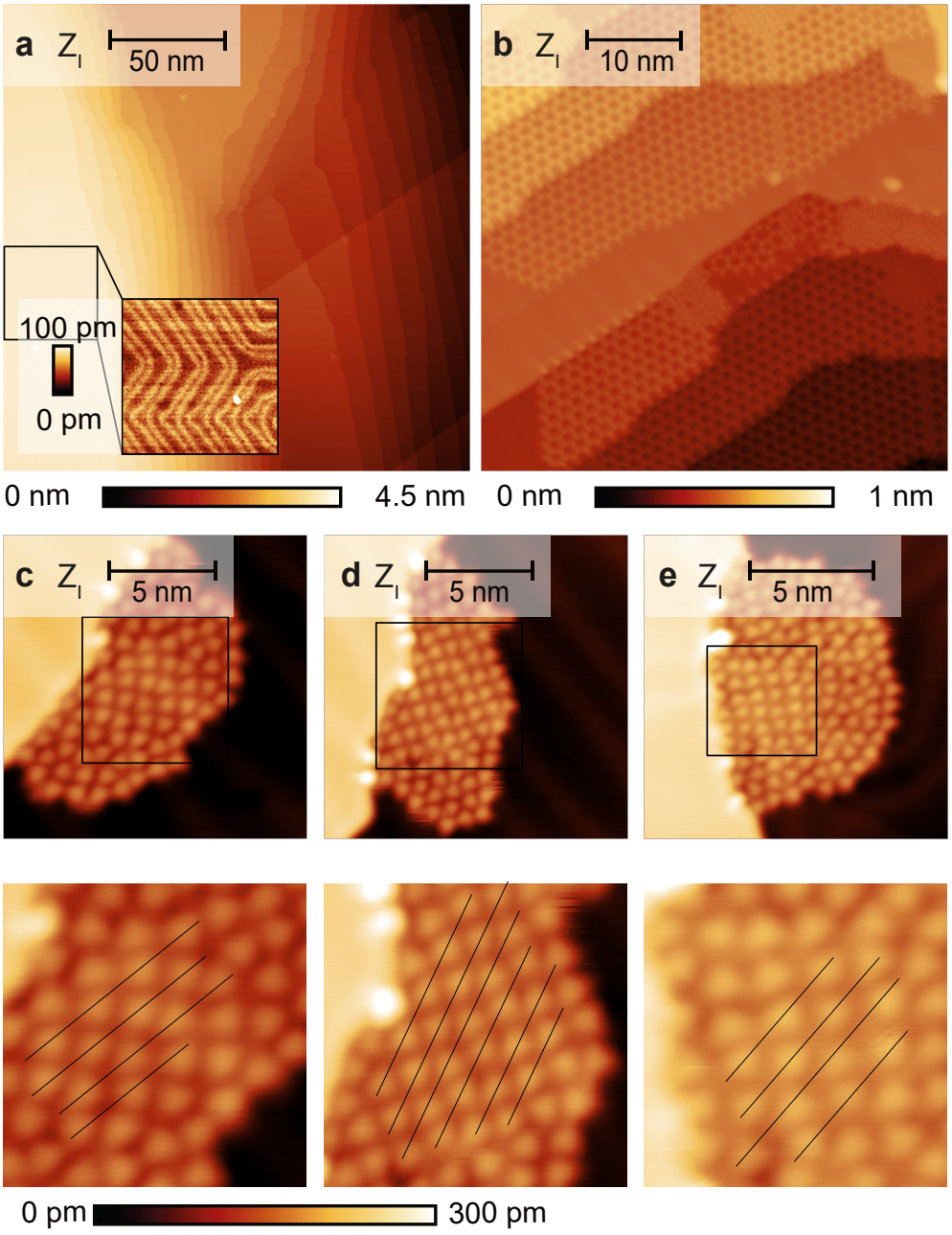

Figure 8.13: TMA on Au(111)-Fe1 heated to 383 K. (a) Au(111)-Fe1 prior the TMA experiments, zoomed in on the herringbone reconstruction in the inset (b) STM overview image of TMA on Au(111)-Fe1 showing HON network and densely arranged areas. (c-e) Densely arranged areas with ordered and unordered areas magnified areas are indicated by a black triangle within the images. Imaging parameters: (a) $I = 100\,\mathrm{pA}, U_S = -1\,\mathrm{V}, T_S = 78.3\,\mathrm{K}$, (b-e) $I = 1\,\mathrm{nA}, U_S = -1\,\mathrm{V}, T_S = 78.3\,\mathrm{K}$.

In the experiments of this section TMA is deposited on Au(111)-Fe1. The Au(111)-Fe1 surface, as shown in figure 8.13a, does not show any abnormalities compared to pristine Au(111) (e.g. figure 4.1). The herringbone reconstruction shows the characteristic features like the parallel domain walls and elbows described in section 4.1.1.
In figure 8.13b an overview image of TMA deposited on Au(111)-Fe1 and heated to 383 K is shown. The image shows large HON networks. Similar to experiments on the pristine Au(111) sample, the HON network is interrupted by densely arranged areas. Taking a closer look at these densely arranged areas one observes mostly unordered assembly. However, within the islands of unordered TMA molecules small areas with ordered arrangements are found in figure 8.13c-e. These areas share that the molecules are aligned in rows, and within these rows the molecules have the same orientation. The rows are indicated by lines in the excerpts of the island images.

8.4.3 Heating TMA on a Sample Repeatedly Exposed to Fe and Heated Several Times

In this section TMA is deposited onto an Au(111)-FeX sample. The sample has been exposed to iron several times including two heating experiments. The experiments have been performed in three steps: First, the sample is allowed to sit at room temperature for 2 h. Second, the sample is heated to 348 K for 10 min. Third, the sample is heated to 383 K for 10 min. As heating to 348 K resulted in an interim stage, this step is only described briefly as the last subsection.

8.4.3.1 Step One: Sample for 2 h at 300 K

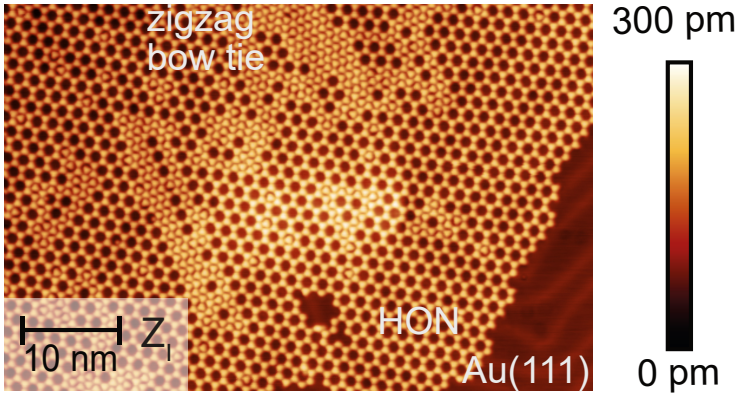

Figure 8.14: TMA on Au(111) after 2 h at room temperature. Au(111)-FeX, HON, and zigzag bow-tie structures are labelled. Imaging parameters, STM: $I = 100\,\text{pA}$, $U_S = 500\,\text{mV}$,$T_S = 4.6\,\text{K}$.

TMA on Au(111) is placed in the preparation chamber to sit at room temperature (300 K) for two hours. This experiment allows to investigate if the time period of the sample

being at room temperature has any impact on the molecular assemblies. After this step, large areas of HON networks are observed as well as the close-packed and zigzag bow-tie structure (cf. figure 8.14). Only occasionally one of the flower structures is observed. This indicates a restructuring towards HON networks, as this is not only the predominant structure at this state, but also as the other assemblies occur only occasionally. To quantify these results a total of roughly 0.5 μm^2 has been analysed and only four times flower structures have been observed. Zigzag bow-tie structures are observed more often. In previous measurement without prolonged time at room temperature flower structures were more common than zigzag bow-tie structures. Consequently, the prolonged time at room temperature causes restructuring to favoured HON, close-packed and zigzag bow-tie structures. The possibility of Fe contaminations does not impact the TMA assembly in this step.

8.4.3.2 Final Step: Heating the Sample System to 383 K

After leaving the sample at 300 K for two hours, and after heating the sample to 348 K for 10 min the sample system is heated to 383 K for 10 min. This final heating step aims to investigate the influence of heating in the presence of possible Fe contaminations on assembly formation. Looking at the TMA/Au(111)-FeX sample system, one observes bare Au(111) areas, as well as two different assemblies of TMA molecules. One is the previously described HON network (see figure 8.15a), the other one is a densely arranged area, showing an ordered arrangement of TMA molecules. It is now referred to as UC110. An example of UC110 is given in figure 8.15c. It differs from both bow-tie structures, as well as the close-packed structure described in section 8.3 and 8.4.1. The HON network is

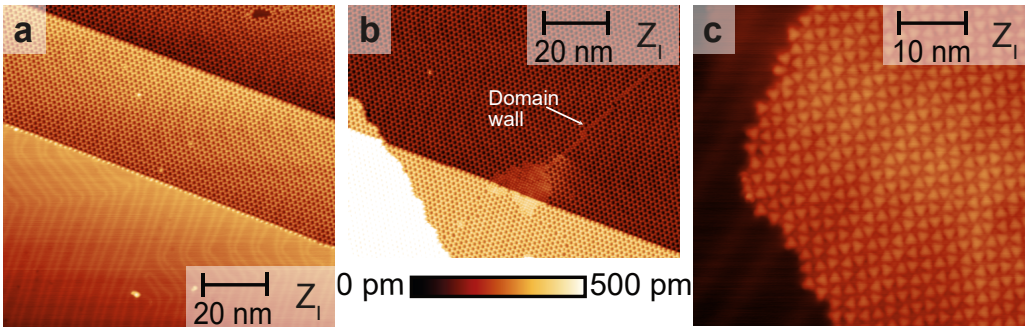

Figure 8.15: Overview images of TMA on Au(111)-FeX after heating the system to 383 K. (a) Large areas of Au(111) surface with undisturbed herringbone reconstruction as well as near perfect HON spanning over two Au(111) terraces. (b) Densely arranged area at step edges surrounded by HON. Domain wall is indicated by a white arrow. (c) Densely arranged area abut on Au(111) surface. Imaging parameters: $I = 100\,\text{pA}$, $U_S = 500\,\text{mV}$, $T_S = 4.6\,\text{K}$.

spanning nearly disturbance-free over multiple gold terraces (cf. figure 8.15a, b), indicating that the formation of dimeric hydrogen bonds, causing the HON structure, is predominant and thermally favoured.

The densely arranged UC110 areas are either surrounded by HON or are located at step edges (cf. figure 8.15b). The UC110 islands can also begin at the HON or step edge, but terminate on the Au(111) terrace (cf. figure 8.15c). The UC110 areas often occur at domain walls. an example is given in figure 8.15b. An UC110 island has not been observed without neighbouring to the step edge or the HON network.

A STM image of the UC110 area obtained with a CO tip is shown in figure 8.16a, and an image with higher resolution is reproduced in figure 8.16b. One can recognise an ordered structure. Looking at the single molecules in figure 8.16b, TMA is no longer imaged as triangular protrusion, but it is imaged in a petal like shape due to the CO-functionalised tip. The characteristics of the petal shape are a circular centre and three equally sized lobes.

These simplify the determination of the molecular the orientation. The molecules show different orientations. After eight molecules, the alignment of the molecules repeats itself. One orientation is highlighted with green dots in figure 8.16a. The repetitive pattern allows the determination of a unit cell. A total of eight molecules are in the unit cell.

The molecules in the unit cell show a different orientations, with molecules 4 and 7 (purple and grey) having the same orientation. Examples of the UC110 are marked in figure 8.16a and b. The unit cell is determined by measuring orientations and molecule positions of 40 unit cells. The average uncertainty of the orientation of each molecules amounts to 4°, and of the molecular centre position 0.03 nm. The model of the unit cell of UC110 is given in 8.16c. The extended UC110 has a shape of a parallelogram of two molecules times 9 molecules with angles of 47.4° ± 1° and 132.6±1° , this depiction is chosen to display proposed bonds between molecular rows. Therefore, the molecules marked in the same colour will be distinguished for descriptive reasons only, the top row is marked by numbers only (e.g. 1), while the bottom row is indexed with the matching number and a dash (e.g. 1'). This nomenclature is implemented, as top row molecules often interact with bottom row molecules. Therefore a discrimination is necessary to describe the intermolecular features.

Looking closer at the unit cell, the orientation of the molecules allows different arrangements of bonds. These bonds can be partly confirmed by constant-height AFM images. As shown in figure 8.16d constant-height images are only obtained of fractions of the UC110, not of a whole unit cell. Putting these fractions together for UC110, 28 bond-like features can be identified between the oxygen atoms.

With 24 carboxylic acid moieties involved in the bonding pattern, a maximum of 24 hydrogen atoms are available for hydrogen bonds, assuming no deprotonation is occurring,

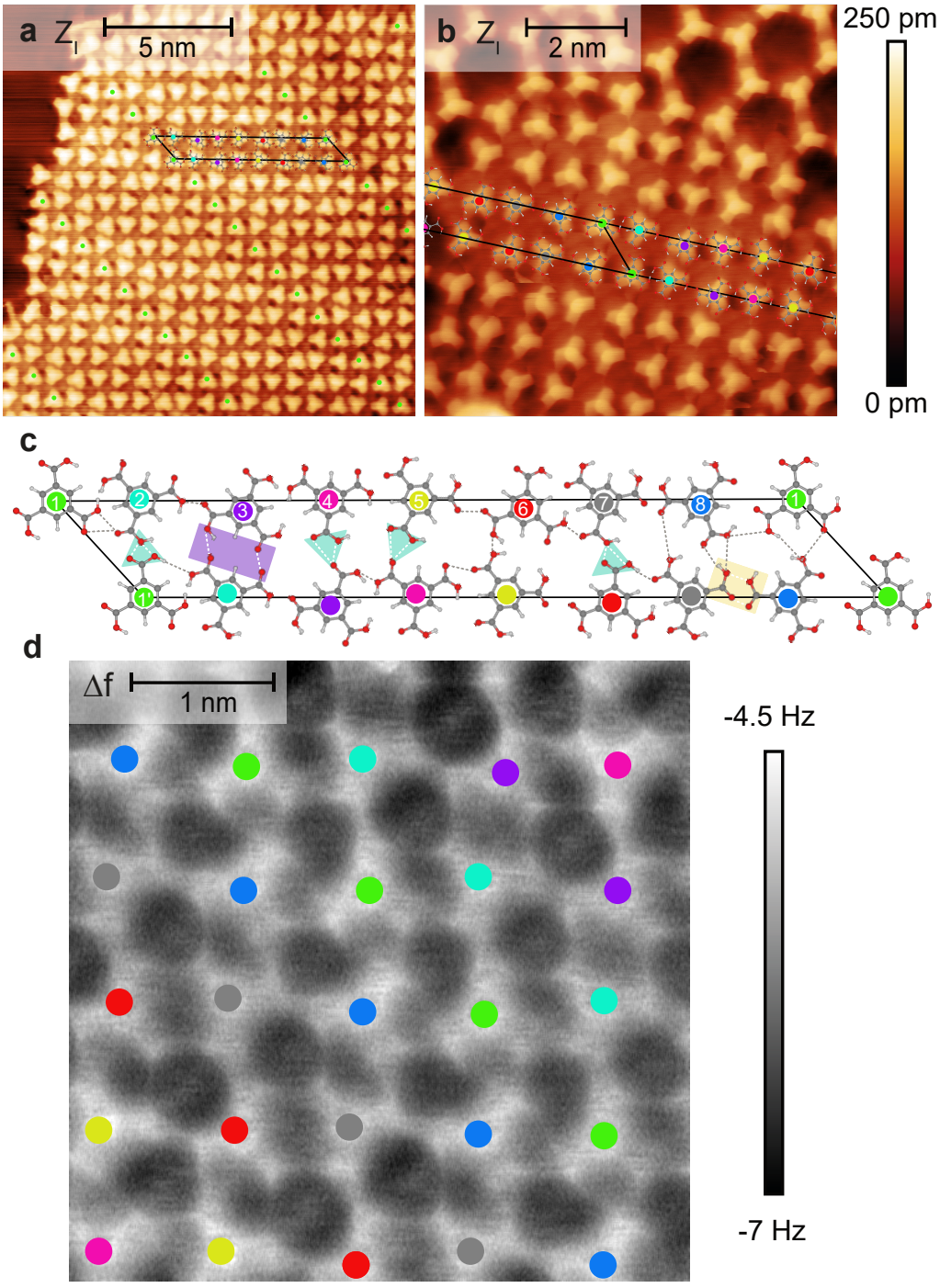

Figure 8.16: Densely arranged area of UC110 structure, (a) STM overview image with one unit cell marked fully, periodicity indicated by green circles placed in molecules' centre. (b) Close up of UC110 and adjacent HON taken as STM image. (c) Schematic of UC110 with molecules numbered, observed intermolecular features indicated by dashed lines, and exemplary bonding motifs highlighted: Triangular motif (turquoise triangle), rectangular motif (purple rectangle), and open dimeric motif (yellow rectangle). (d) NC-AFM constant-height image, molecules of UC110 marked with coloured circles. Imaging parameters: (a,b) $I = 100\,\mathrm{pA}$, $U_S = 500\,\mathrm{mV}$, $T_S = 4.6\,\mathrm{K}$, AFM: (d) $\Delta f = -5.5\,\mathrm{Hz}$, $U_S = 0\,\mathrm{V}$, $f_0 = 26\,462\,\mathrm{Hz}$, $T_S = 4.6\,\mathrm{K}$.

which has been observed for heated TMA on Ag(111) [249]. This leaves four bond-like features unexplained.
For all bonding patterns the interaction of multiple carboxylic acid moieties forms a loose arrangement of several carboxylic moieties creating chains. So far STM and AFM do not allow discrimination of the oxygen atoms of the carboxylic acid moiety. In the schematic, in figure 8.16c, the hydrogen atoms are only indicated at possible positions. Each carboxylic acid moiety can be rotated around the C-C bond by 180 °. This will change hydrogen bond donor and acceptors, as well as allow and forbid bonds in certain combinations. As there are 576 possible combinations within the chain-like bonding situation, these will not be discussed in detail. However, it is important to keep in mind, that the four bonds, which cannot be explained by hydrogen bonds, can occur at various positions.
Additional to hydrogen bonds two possibilities exist, which could explain the total number of intermolecular features imaged: Coordinate bonds and artefact imaging, also known as apparent bonds. This will be elucidated in the discussion in section 8.4.4. Based on the imaged intermolecular contrast, several bonding motifs are identified to occur several times in the UC110, these are named and listed in table 8.2.

Table 8.2: Bonding motifs in the UC110.

bonding motif	colour code
open dimeric	yellow
rectangular	purple
triangular	turquoise

First, the open dimeric bond, is located between molecules 7 and 8 and highlighted by a yellow rectangle in figure 8.15c. The TMA molecules point to one another, but in comparison with a bow-tie motif, the oxygen atoms of one side are closer to one another, than on the other side. This reminds of an assembly described by Payer et al., where heating TMA causes deprotonation on Ag(111) surfaces [249]. Nevertheless, the surrounding bonding patterns, do not match the deprotonation patterns on Ag(111). Therefore, deprotonation is neither proven nor excluded for UC110.
The second bonding motif is named rectangular motif. It is highlighted in purple. It consists of two molecules (2' and 3) face each other with the base of the molecules' triangle, so one oxygen of each carboxylic acid group points towards the ones of the adjacent TMA molecule. Two carboxylic acid moieties of each molecule are in this pattern, but only one oxygen of each moiety is involved in the bonding motif. Two bonds are observed in this motif.
Third, the triangular bonding motif exists between two carboxylic acid moieties. Both oxygen atoms of one carboxylic acid moiety interact with the same oxygen atom of the

neighbouring TMA molecule. This bonding motif can be observed between molecules 1' and 2 or 4 and 5 and is marked by a turquoise triangle.

8.4.3.3 Interim Step: Heating the Sample System to 348 K

In the interim stage, the TMA/Au(111) system, is heated to 348 K for 10 min. As depicted in figure 8.17a huge areas of the gold terraces are covered by the HON network and a densely arranged area. This is similar to the results of the experiment at 383 K.
In comparison to the densely arranged areas at 383 K, the area here can be divided into ordered areas and into a transition region. The transition region is observed at the border between ordered part of the densely arranged area and the HON network. In the transition region, bow-tie motifs are regularly spotted, though they do not form larger ordered structures, but occur in small clusters. In figure 8.17 b and c exemplary bow-tie motif are highlighted in light blue, while an exemplary adjacent HON pore is outlined in dark blue. The bow-tie phase is interrupted by seemingly unordered TMA molecules. The combination of small clusters of bow-tie and unordered molecules surround ordered assemblies in the centre of the areas. Looking closer at the ordered assemblies of densely arranged areas, repetitive structures are observed. Three unit cells are identified in these areas. The unit cells contain, one, three, and four molecules and are respectively named UC75-1, UC75-3, and UC75-4
In the following, the different unit cells of these measurements are described. In figure 8.17b two unit cells, UC75-1 and UC75-3, are identified. UC75-3 is highlighted in pink, and periodicity is marked by black lines. In UC75-3 three molecules are arranged in a parallelogram shape with a density of $(1.7 \pm 0.1)\,\mathrm{mols/nm^2}$, which is more dense than the HON structure (with a density of $(0.8 \pm 0.1)\,\mathrm{mols/nm^2}$). As indicated by white arrows in the image, UC75-3 exists in two orientations, which are rotated by 180 ° (cf. figure 8.17b,d). The different orientations are separated by rows of two molecules each time. These molecules separating UC75-3 form yet another unit cell UC75-1, which is indicated in grey. The symmetry operation to obtain the different unit cells involves mirroring along the mirror plane indicated by a dashed, grey line, which occurs to halve the UC75-3.
The UC75-4 is marked green in figure 8.17c, it is a unit cell of four molecules. The unit cell has a shape of a parallelogram. The periodicity is indicated by black lines. UC75-4 appears to be undisrupted by any other unit cells. The density of $(1.7 \pm 0.1)\,\mathrm{mols/nm^2}$ for UC75-4 is identical to UC75-3, both unit cells have a parallelogram shape. The orientation of each molecule is determined by analysing the orientation of the triangle apexes. When comparing both unit cells from right to left, the first three molecules in the row are rotated identical, which is the point where UC75-3 starts its repetitive pattern, but UC75-4 inserts a fourth molecule of a different orientation.

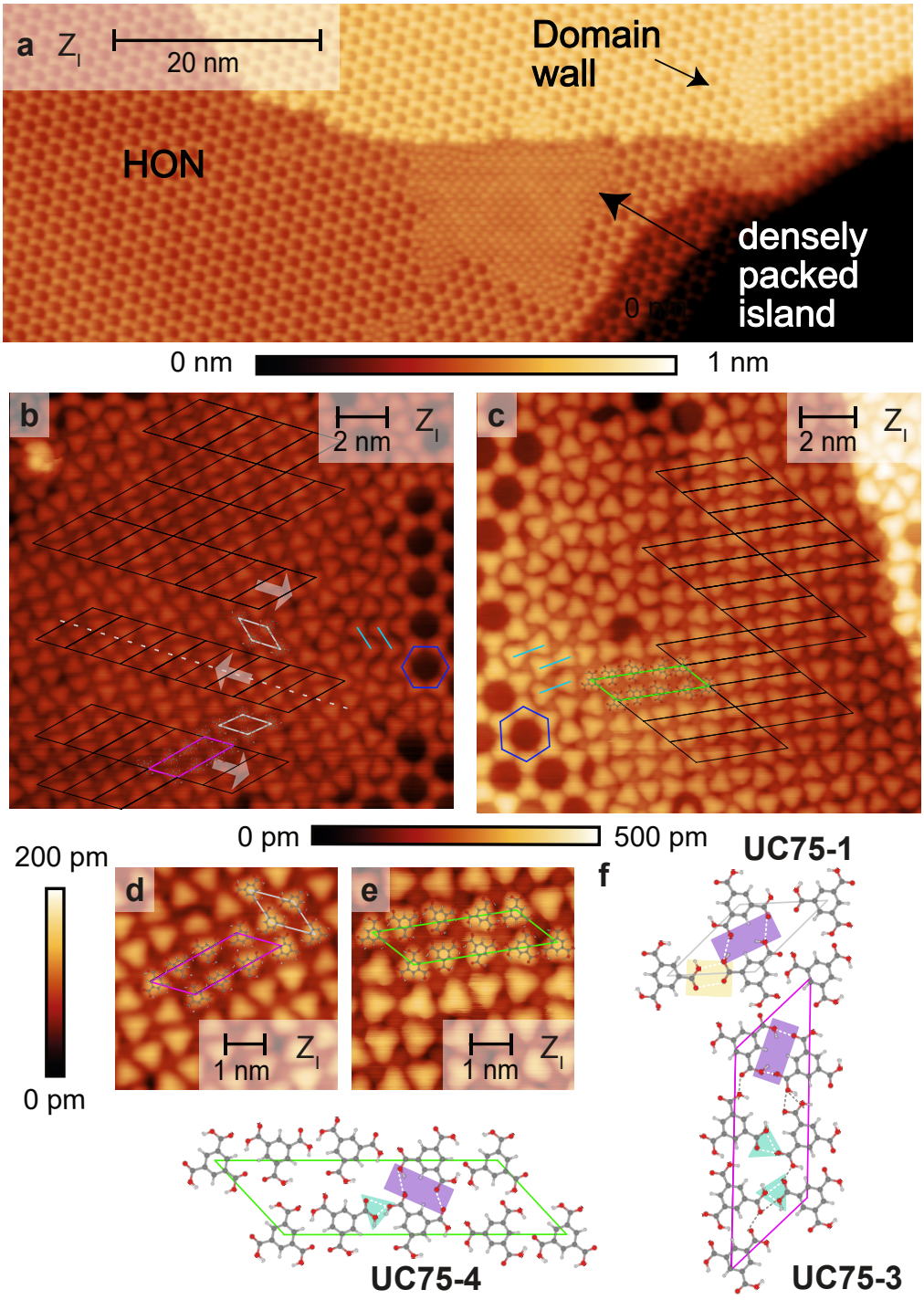

Figure 8.17: New assemblies after heating to 348 K: (a) Overview image of heated TMA/Au(111)-FeX surface system, with HON networks with different directions separated by domain walls and a densely arranged area. (b,c) Densely arranged areas, with exemplary HON pores are highlighted in dark blue and bow-tie motifs in light blue. Unit cells of ordered structures are highlighted in pink and grey (b) and in green (c). In both cases unit cells are surrounded by an unordered transition phase. Close-ups on unit cells in (d) and (e) Schematics of these three unit cells are depicted in (f) Imaging parameters: STM (a-e) $I = 100\,\text{pA}, U_S = 500\,\text{mV}, T_S = 4.6\,\text{K}$.

For all three unit cells one cannot identify any dimeric or trimeric bonding motifs, which were the exclusive bonding motifs at room temperature measurements. Instead, the bonding motif already observed for UC110 are identified. The chain like character of the bonding motif is observed for all three unit cells, as is the rectangular bonding motif. The triangular bonding motif is observed for UC75-3 and UC75-4. The open dimeric bonding motif is observed in UC75-1 only (see figure 8.17).

8.4.4 Discussion

Summarising, the surface looks undisturbed throughout the different Au(111) samples. Step edges and herringbone reconstruction are observed for all three samples. Iron contamination can not be identified by STM images of the Au(111) samples. Heating experiments give insight on the presence of Fe contaminations, as different molecular assemblies are observed for the different samples. The heating experiments of TMA on pristine Au(111), Au(111)-Fe1, and Au(111)-FeX show distinct HON networks, as well as densely arranged areas. The densely arranged areas can be divided into ordered and unordered areas. Unordered densely arranged areas can be observed for heating experiments on pristine Au(111), Au(111)-Fe1 and after heating to 348 K on Au(111)-FeX.

Ordered densely arranged areas are observed for all three surfaces, after every heating step. However, the structure of the ordered areas differs between the surfaces.

On pristine Au(111) after both heating steps, a so called parallel bow-tie structure is observed, as well as the close-packed structure. Both structures can be explained fully by hydrogen bonds. However, for the parallel bow-tie structure interaction with subjacent gold atoms cannot be excluded. This has previously been observed for molecules with carboxylic acid moieties. Here, the formation of coordinate bonds towards excess gold adatoms of the Au(111) is known. An example is 6,6'-(1,4-buta-1,3-diynyl)bis(2-naphthoic acid), where the sample is heated to 397 K and the molecules undergo covalent coupling to form dimers, which is followed by the formation of a coordination complex, where four dimers form coordinate bonds to two gold atoms, forming a rectangular array [272]. As the parallel bow-tie structure is observed on pristine Au(111), iron contamination can be excluded as cause for this structure.

On Au(111)-Fe1 ordered densely arranged areas have been identified. Molecules of the same orientation are aligned in rows. No repetitive order of the rows is observed. In contrast to Au(111)-Fe1, the densely arranged areas formed after heating on Au(111)-FeX show long-range order at both heating steps. Different unit cells have been identified on Au(111)-FeX. The unit cells show different bonding motifs than the observed motifs at room temperature (dimeric and trimeric bonding motifs) and on pristine Au(111) after

heating.
Taking a closer look at the bonding motifs of UC75-1, -3, and 4, as well as UC110, three motifs have been identified: open dimeric, triangular and rectangular. These are only observed on samples previously exposed to Fe and alloying experiments. This leads to the suggestion, that they are caused by Fe contaminations in the Au(111) sample. Fe contaminations are most likely to cause two different reactions with TMA: First deprotonation, second coordination. Different arguments strengthen the possibility of either reaction type: The open dimeric bonding motif, observed for UC75-1 and UC110, resembles the bonding motif found for annealed TMA on Ag(111) [249]. On Ag(111) the open dimeric bonding motif is explained by partially deprotonated TMA molecules.
Nevertheless, deprotonation as single cause for the new unit cell seems unlikely, as partial deprotonation alone would allow even less bonds to be formed. The UC110 shows 28 intermolecular features in constant-height NC-AFM images. A maximum of 24 bonds could be explained by hydrogen bonds if no deprotonation occurred, which leads to another explanation: the formation of coordinate bonds. As UC110 only occurs on samples with prior Fe alloying experiments, coordinate bonding is likely to occur to iron contaminations of the Au(111) sample and less likely to subjacent gold atoms. Therefore, a possible reaction with near-surface alloyed iron could result in coordinate bond formation causing these unit cells.
Another explanation to imaging more bonds than actually possible with hydrogen bonds is that two atoms close to each other can cause repulsion of the CO tip. It will be imaged like a bond, though there is none. This effect has been described by Ellner et al. and is explained in more detail in chapter 3.1 [109].
However, due to the lack of knowledge of the number of Fe contaminations and the true number of intermolecular interactions in UC110, neither the number of coordinate bonds, or hydrogen bonds, nor their position can be determined.
In conclusion, Fe contaminations occur after prior alloying processes, even though three sputter anneal cycles have been performed after the alloying. Further confirmation, and quantitative analysis of Fe contaminations in the gold bulk requires another analysis technique. XPS looks most promising, similar to experiments by Khan et al. [35].
The formation of the unordered densely arranged areas occurs on all samples. Therefore the formation of these assemblies is caused either by deprotonation or coordination with subjacent gold atoms. The formation of the different unit cells on samples exposed to Fe in prior experiments, allows to allocate the formation of these to the presence of Fe. Fe can either cause deprotonation or coordinate bond formation.

8.5 Reactions of TMA with Iron on Au(111)

In this section, the reaction of TMA with iron is examined on an Au(111) surface. Aim of these experiments is the manufacturing of coordinate bonds between iron and TMA, resulting in a SMON.

8.5.1 Influence of Deposition Order and Temperature

To test the best reaction parameters, deposition order as well as Au(111) surface temperature during deposition are varied. Therefore, varying sequences of deposition order are probed. This is followed by depositing both TMA molecules and iron atoms to surfaces of elevated temperatures. First, room temperature deposition of iron is followed by deposition of different ratios of TMA. Second, TMA is deposited onto the Au(111) room temperature sample, followed by iron deposition. Third, TMA and iron are deposited in parallel to Au(111) surfaces at elevated temperatures (338 K, 383 K).

8.5.1.1 Room Temperature Deposition

First, iron is deposited onto the clean Au(111) surface and then TMA is added. A coverage of TMA of 0.16 mols/nm^2 is measured, resulting in a TMA:Fe ratio of 1:6 (cf. table 8.1). Depicted in figure 8.18a-c, iron islands form at the herringbone elbows, just as expected from the previous experiments. The TMA molecules are observed to cluster around the iron islands as a densely arranged area, which will be looked into more closely later on.
Second, doubling the amount of TMA to 0.36 mols/nm^2 resulted in a TMA:Fe ratio of 1:3. A growth of the densely arranged areas surrounding the iron islands is observed (cf. 8.18d). The size of the iron islands remains the same. This is deduced from the iron coverage (cf. table 8.1). A large quantity of the TMA molecules accumulates in a densely arranged manner comparable to the previous deposition. However, a HON structure is observed occasionally at the molecules' island edges (cf. 8.18e,f).
Third, the deposition order is interchanged, precisely, TMA is deposited first, followed by iron (cf. 8.18g-i). Iron islands are also observed, but they are mainly found on the side of terraces covered with TMA. Only a few small islands are spotted surrounded by TMA. The islands are marked by white arrows in figure 8.19a. A TMA:Fe ratio of 1:9 is received. The TMA molecules accumulate in both structures observed previously: HON and densely arranged areas, which are indicated in figure 8.19a. The HON is much more abundant than in previous measurements, the densely arranged areas are distributed across the terraces, often beginning at iron islands. Additionally, irregularly shaped holes are observed in the TMA assemblies, where bare Au(111) surface is surrounded by TMA molecules, these

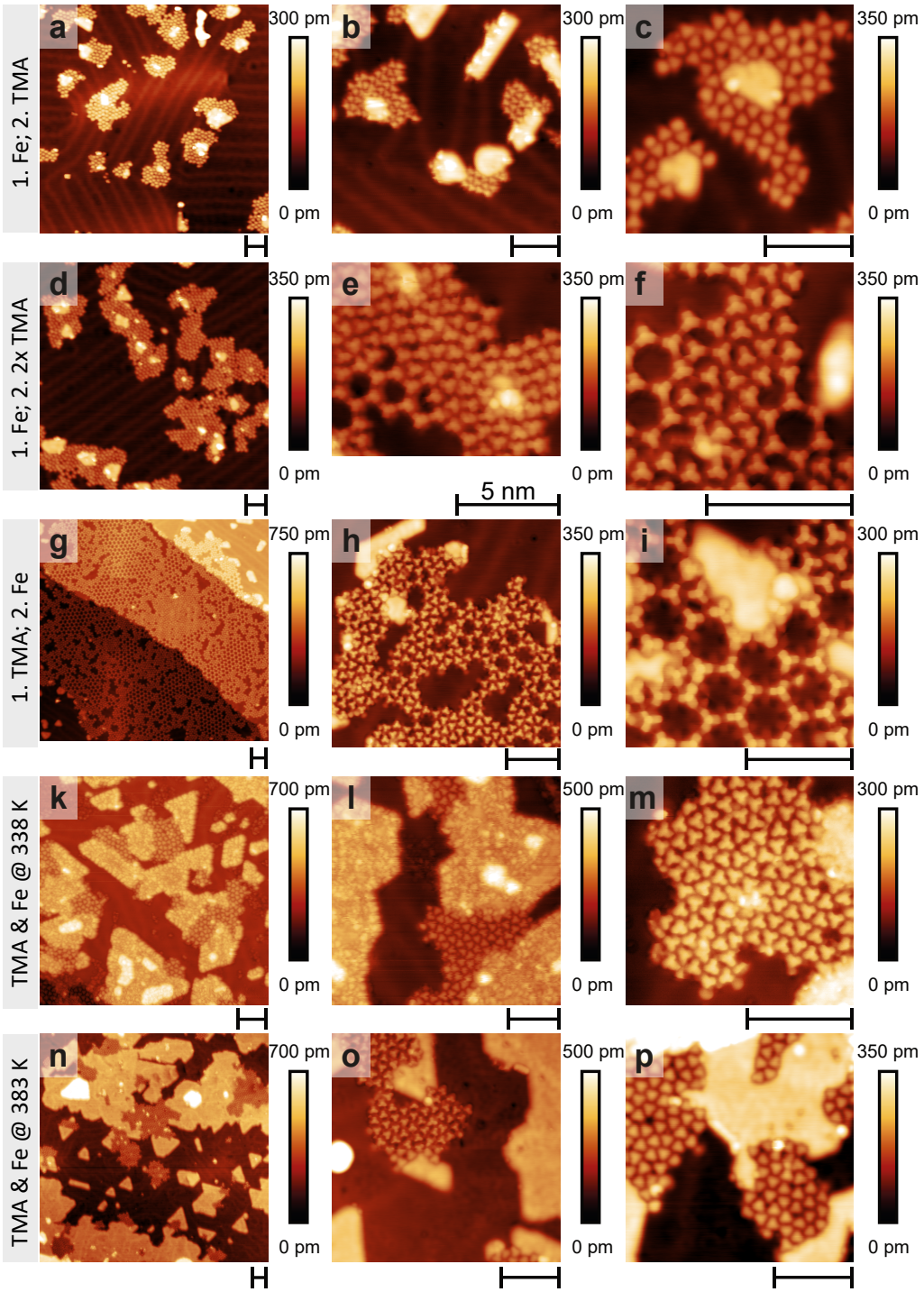

Figure 8.18: STM images of varying deposition sequences and coverages of TMA and iron onto Au(111). (a-c) Deposition of iron followed by TMA deposition, (d-f) the amount of TMA is doubled. (g-i) TMA is deposited first, followed by iron deposition. (k-m) Parallel deposition to 338 K warm surface and (n-p) to 383 K warm surface; 5 nm scale bars are added to all images; Imaging parameters: (a-i; n-p): $I = 50\,\text{pA}$, $U_S = -25\,\text{mV}$, (k,l): $I = 5\,\text{pA}$, $U_S = -100\,\text{mV}$ (m): $I = 50\,\text{pA}$, $U_S = -5\,\text{mV}$, $T_S = 4.6\,\text{K}$.

areas are marked by a grey arrow in figure 8.19a.

Possibility of Desorption

This leads to the question, are the blank Au(111) areas in between TMA assemblies caused by desorption of TMA molecules? Regarding this question, an area of mainly densely arranged areas and pristine Au(111) is determined, which is surrounded by HON network. As large areas of HON network are expected after room temperature deposition and long time exposure, the expected coverage of molecules for HON network is known. This can be compared with the counted molecule coverage. The example given in figure 8.19b has an expected number of 568 TMA molecules, while the counted number of molecules amounts to 541. This amounts to less than a 5 % difference. This proposition was tested on several areas of the sample. All results lie within a 5 % error. The deviation can be explained by the other structures of TMA occurring at room temperature. They have a more dense assembly and would result in a slightly higher coverage than expected. Therefore, no evidence for TMA desorption is observed. In summary, for both deposition orders densely

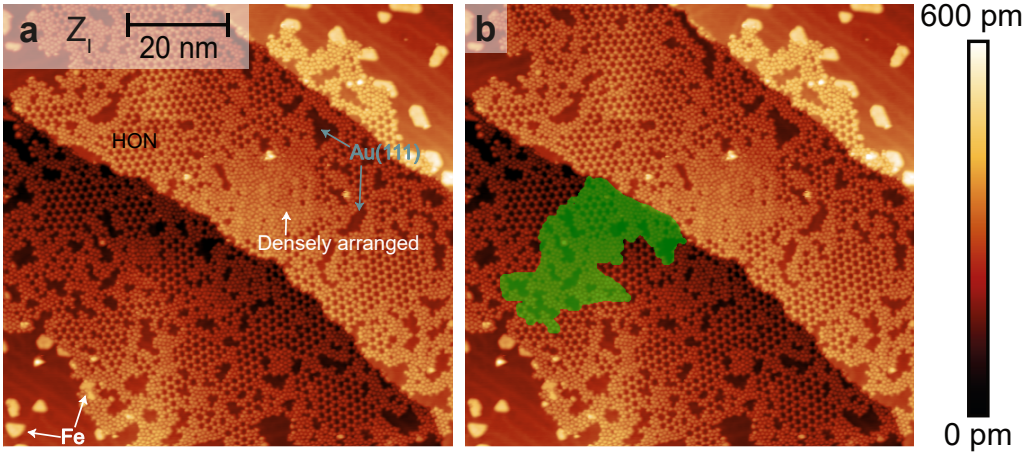

Figure 8.19: Composition of TMA and iron on Au(111) after the stepwise deposition of TMA followed by iron. Exemplary densely arranged assembly of TMA are marked by a white arrow, the areas of bare gold surrounded by TMA are marked by grey arrows, islands of iron are indicated with white arrows. In b an area is marked to determine the coverage at not HON sites. Imaging parameters: $I = 50\,\mathrm{pA}, U_S = -25\,\mathrm{mV}, T_S = 4.6\,\mathrm{K}$.

arranged areas of TMA are observed. As these densely arranged areas have not occurred on pristine Au(111) at room temperature, they are likely caused by the iron. The order of depositing both reactants as well as the TMA:Fe ratio strongly influences the assembly formation. While a high abundance of iron on the surface results in densely arranged areas of TMA, a lower abundance of iron allows an occurrence of HON. This might result from a lack of iron atoms on positions further away from the iron islands, which would indicate that diffusion of the iron atoms is limited or that the previously deposited TMA

molecules shield the iron from new TMA molecules added to the surface. This might cause an inhibition of the reaction, which has formed these densely packed areas. For TMA deposited prior to iron a high abundance of HON network is observed as well as large areas of pristine Au(111) surrounded by HON. As desorption has been excluded, reorganisation of the TMA molecules is likely to occur. The high abundance of HON can be explained by missing interaction with iron. This would explain, why iron atoms or clusters are not observed as guests in the HON, as this results in a reassembly of TMA.
To obtain a maximum of interaction between iron and TM,A a higher coverage of iron is important. Additionally, for a increasing the likeliness of molecules and iron atoms to interact during deposition, a parallel deposition might be advantageous. Parallel deposition will therefore be used during the heating experiments.

8.5.1.2 Deposition at Elevated Temperatures

Next, TMA and iron are deposited in parallel onto the heated Au(111) surface. First, the surface temperature was raised to 338 K. On the first look in figure 8.18k, the formation of iron islands and densely packed TMA resembles the room temperature deposition of first iron deposition followed by TMA. Taking a closer look at figure 8.18l, the iron islands are of an irregular texture. The iron islands have an uneven surface. This could result from the formation of a mixture of TMA and iron, which would explain the extraordinary high iron coverage (cf. table 8.1). As previously described in chapter 8.2.2, small granules are spotted at the Au(111)'s surface, which are imaged as light protrusions and are usually found at the mixed iron islands. The densely arranged TMA areas seem uninfluenced by the mixed islands as well as the the alloy formation with the Au(111) surface.
Last, depositing molecules and metal to the 383 K warm Au(111) surface also results in densely arranged TMA areas, but the Au(111) and iron islands are affected by the elevated temperature. However, the densely arranged islands are sometimes locked in what supposedly is an Au(111) terrace. Similar to the alloy formation described in section 8.2.2.1, the features of the alloy formation are observed in this experiments: First, the herringbone reconstruction of the Au(111) surface is highly disturbed. Second, the typical elbows are also not imaged. Furthermore, many black impurities are spotted in the Au(111) surface (figure 8.18n,o. The densely arranged areas of TMA appear unaffected by the alloy formation.

8.5.2 High-Resolution Imaging of TMA/Fe/Au(111) Sample System

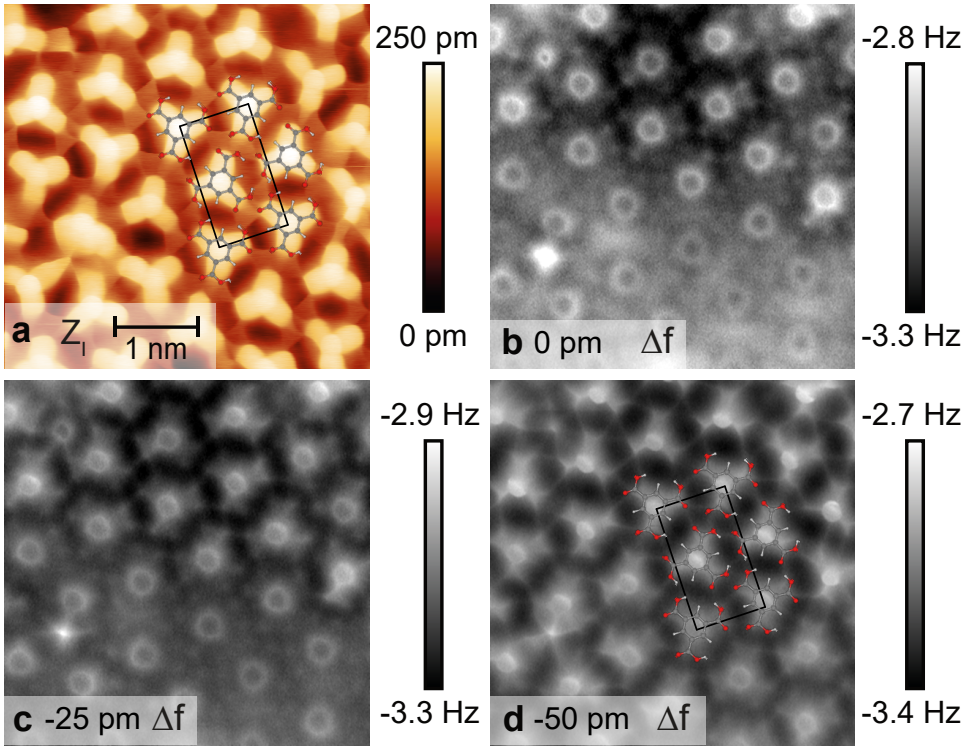

Figure 8.20: Imaging UC-Fe: (a) STM image of UC-Fe, (b-d) constant-height NC-AFM images. STM $I = 50\,\text{pA}, U_S = -25\,\text{mV}, T_S = 4.6\,\text{K}$, AFM: $\Delta f = -3\,\text{Hz}, U_S = 0.65\,\text{mV}, f_0 = 26\,461\,\text{Hz}, T_S = 4.6\,\text{K}$.

Regardless of the deposition order or surface temperature during deposition, a densely arranged area of the TMA molecules is observed. Parts of the densely arranged area are unordered, while other areas show an ordered arrangement. The ordered arrangement (see figure 8.20a) consists of TMA rows, which are alternating rotated by 180°. A unit cell can be determined for the long-range arrangement, a sketch of the unit cell is included in the STM and NC-AFM images in figure 8.20a and d. This unit cell is observed for all deposition sequences and temperatures, and in the following will be abbreviated as UC-Fe. The depicted UC-Fe is obtained after the parallel deposition at 383 K, examples of UC-Fe for different deposition methods can be spotted in the STM images in figures 8.18c, f, and l. The UC-Fe contains two molecules, it has a rectangular shape and a size of 880 pm×1530 pm. The position of the TMA molecules can be determined from the STM and AFM images. In STM the petal shape of the TMA molecules allows the determination of the orientation of the molecules. In NC-AFM images (figure 8.20b-d) a more precise determination of the molecular orientation is possible.

The extended unit cell depicted in figure 8.20a consists of six molecules. These are

arranged in a rectangular fashion of 2×3 molecules. In figure 8.20a UC-Fe is marked by the ball and stick models of the molecules and a black rectangle. Of the six molecules four are oriented in the same direction, the other two are rotated by 180 °.
As the UC-Fe is obtained only in the presence of iron, and occurs regardless of the probed deposition parameters, in conclusion iron influences the formation the unit cell. To determine, if intermolecular coordination exists within the UC-Fe, in depth analysis of STM and NC-AFM images is required. Taking a closer look at the STM images no intermolecular features are imaged that indicate the presence of iron. Furthermore, single molecules do not appear brighter in STM, which was observed for the adsorption of TMA on top of cobalt [243]. Therefore, further investigation are required to determine the role of Fe in the UC-Fe formation. As a next step, constant-height NC-AFM images are taken with a CO functionalised tip. The constant-height images of the TMA molecules in UC-Fe area in figure 8.20b-d match the previous described constant-height imaging of TMA HON network in section 8.3.3.2. The single TMA molecules are imaged with the features being strongly distance dependet. The benzene rings and the oxygen atoms can be clearly identified at the different tip-sample distances, at which constant-height NC-AFM images are performed.
At small tip-sample distances, repulsive intermolecular features are observed beginning from the oxygen positions of one carboxylic acid moiety to another molecule's carboxylic acid moiety. In total, ten sharp lines are imaged connecting the carboxylic acid groups. These sharp lines resemble bond-like features.
These bond-like features cannot be allocated towards a specific intermolecular interaction directly. There are three options for the intermolecular bonding situation at the intermolecular feature position: First option is the intermolecular interaction via hydrogen bonds. However, hydrogen bonds can only form a maximum of six intermolecular bonds, simply due to the presence of six carboxylic acid groups in the UC-Fe. Second, there is the option for coordinate bonds with iron of the carboxylic acid moiety or the carboxylate, if deprotonation occurs. Third option, the bond-like features are only imaged artefacts as the short atom distance can result in imaging apparent bonds, though no chemical bond exists.

8.5.2.1 Unit Cell Averaging

With the aim to better understand the bonding motif of the UC-Fe, the contrast has to be enhanced. This is achieved by averaging several unit cells with Matlab. In the example given in figure 8.21a five unit cells are averaged. The averaged images allow a more precise allocation of the imaged bonds to specific positions in the unit cell.
To investigate the properties of the imaged bonds, and therefore, to figure out if coordinate bonds are the reason for the bonding motif, one needs to determine the length and

orientation of each bonds. This requires the exact positions of the oxygen atoms of each

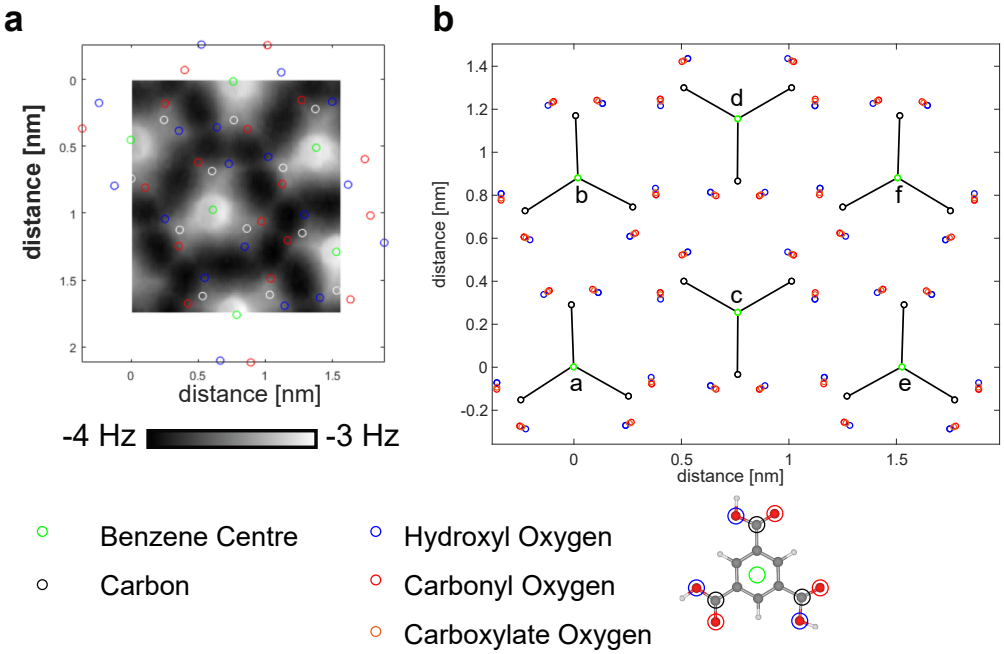

Figure 8.21: Optimising of UC-Fe: (a) Averaged image of one unit cell with indicated atomic positions. (b) Optimised model of UC-Fe, including the carboxylic carbon positions, the benzene centre, and possible oxygen positions: Hydroxyl oxygen in blue, carbonyl oxygen in red, carboxylate oxygen in yellow. A model of protonated TMA is depicted, where coloured circles are added to identify the atoms.

moiety.

Therefore, a model of the UC-Fe is required. To obtain the model depicted in figure 8.21, the orientation of each carboxylic acid moiety is surveyed for several molecules by drawing a line along the C-C bond. The intersection of the elongated C-C bond lines allows the determination of the centre of the benzene rings within the unit cell. Orientations and molecule centres of several molecules are overlayed, resulting in averaged orientations and centre positions. Based on the averaged orientations and benzene ring centre positions the TMA molecules can be placed in the unit cell. The molecular models allow the determination of the positions of all TMA atoms. Carboxylic acid's carbon atoms (white/black) as well as the molecules' centre positions (green) are placed on the averaged constant-height image in figure 8.21a.

The orientation of the carboxylic acid group has not been determined from the imaged constant-height images, the unit cells model needs to be given for both orientations. Additionally, the position of the oxygen atoms is given for the case of deprotonation (carboxylate oxygen, orange), as this is known to occur for TMA in the presence of metal adatoms [243, 249, 255, 256, 257, 258]. For the oxygen atoms, the different bound

oxygen atoms have to be considered (hydroxyl (blue), carbonyl (red), carboxylate (orange)). These oxygen positions differ for each oxygen type. Within figure 8.21a one possible configuration, within figure 8.21 b all configurations are included.
To optimise the overlap of atom positions to the image, a mirror axis is introduced along the centres of the TMA molecules c and d, which resulted in an even better match. However, the mirror axis is only mirroring the carbon positions of the benzene ring and the carboxylic acid moieties. Mirroring the oxygen atoms is not possible, when the molecule is still protonated, as the bond lengths and angles differ for the carbonyl (red) and the hydroxyl (blue) oxygen. This can be illustrated at molecule d in the model in figure 8.21b. The mirror axis runs vertically along the carboxylic acid carbon (black) and benzene ring centre (green) line. Mirroring at this position the oxygen atoms of the down pointing moiety cannot occur without loosing chemical properties. Therefore, the optimised model does only consider carbon positioning for the mirroring process.
Summarising the model, the centres of the benzene rings are indicated as green circles, the carbon atoms of the carboxylic acid moiety as black circles, and the hydroxyl oxygen atoms in blue as well as the carbonyl oxygen atoms in red. The carboxylate's oxygen atoms are indicated as orange circles. They sit at a position between the hydroxyl and carbonyl oxygen atoms.

8.5.2.2 Bond Lengths

In figure 8.22a ten the intermolecular features connecting the oxygen atoms are indicated on the optimised model. Five different intermolecular feature positions are observed, as well as five mirrored bond-like features (indicated with a dash). The intermolecular features will be described as bonds in the latter, however, the reason for contrast formation has still to be confirmed. Comparing the bonding motif formed in UC-Fe with the bonding motif of UC110 (described in chapter 8.4.3.2), there are few similarities. The chain like properties are similar, the different carboxylic acid moieties are all linked. The UC110's triangular bonding motif is comparable to the motif in UC-Fe formed by bonds 1 and 2 as well as bonds 4 and 5. Nevertheless, combined with bond 3 the motif is unique. Additional to the imaged bonds, two distances are highlighted between oxygen atoms (indicated by orange lines and letters). At these positions no intermolecular features are imaged in the constant-height AFM mode.
Based on the oxygen positions the oxygen-oxygen distance can be determined for the imaged bonds 1 to 5 and the positions without intermolecular features at positions A and B. The distances for the imaged bonds 1-5 and the distances A and B are given in figure 8.22c. For the distance between the oxygen atoms the chemically different oxygen atoms of the carboxylic acid moieties have to be considered (hydroxyl, carbonyl, carboxylate). This

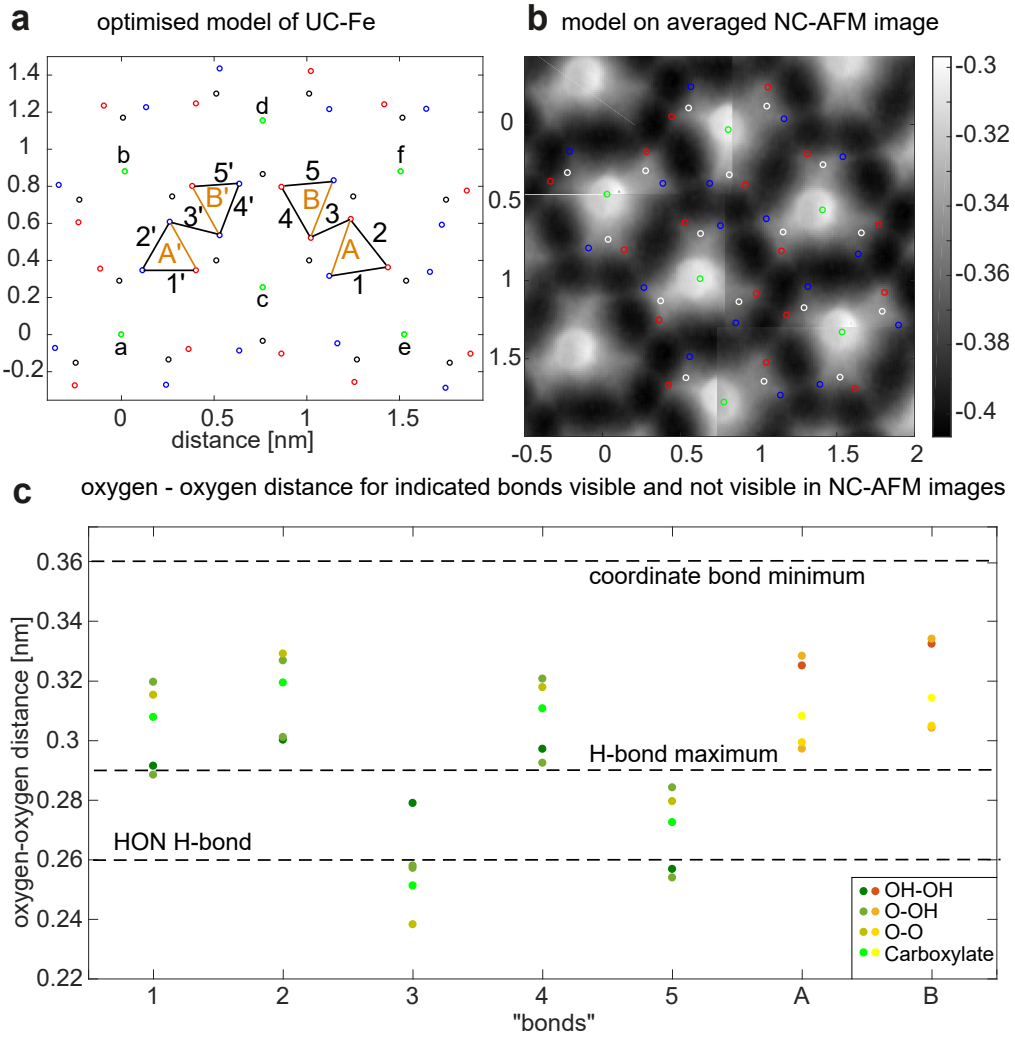

Figure 8.22: Bond motif in UC-Fe. (a) Schematic of UC-Fe with intermolecular features seen in NC-AFM, indicated in black and numbered, and distances between oxygen atoms without intermolecular features in NC-AFM in orange and labelled with letters. (b) schematic model on averaged NC-AFM images. (c) oxygen-oxygen distances given for all observed bonds (green) and exemplary not observed bonds (orange) for possible oxygen combinations.

results in five possible combinations of the different types of oxygen atoms: The distance between two hydroxyl oxygen atoms (marked in dark green and dark orange). There are two distances between hydroxyl oxygen and carbonyl oxygen (marked in green and orange), as the geometry is different for the two conformers. For example bond 1 in figure 8.22a molecule c binds via the hydroxyl oxygen to the carbonyl oxygen of molecule e, if the hydroxyl group of molecule e was instead involved in the bond, the geometry would be different, resulting in a different bond length. Additionally, there is the distance between two carbonyl oxygen atoms (light green and yellow, 8.22c). And last, the distance between two carboxylate oxygen atoms is given (neon green and neon yellow). Not depicted are

combinations of protonated carboxylic acid moieties and carboxylate moieties. This would give another four combinations, where the distances lie within the range of the previously given combinations. With the oxygen-oxygen distances for the ten bond-like features the possibilities of intermolecular hydrogen bonds and intermolecular coordinate bonds are elucidated.

Hydrogen bonds may vary in length, the typical oxygen-oxygen distance in liquids amounts to 240 pm to 290 pm [273]. The oxygen-oxygen distance in hydrogen bonds between a carboxylic acid and a carboxylate is typically around 240 pm [274]. The oxygen-oxygen distance of the HON dimer amounts to 260 pm and is plotted in 8.22c as dashed line. In the distance range of 240 pm to 290 pm lie all conformer combinations of bonds 3 and 5, as well as one of the O-OH combinations for bond 1. However, while both bonds 1 and 1' can have O-OH combinations, these have to stem from different configurations, because otherwise the unit cell would be broken. This results that the two different O-OH values have to be considered for a O-OH hydrogen bond at bonds 1 and 1'. While the oxygen-oxygen distance of one O-OH amounts to about 290 pm, the other configuration, with a distance of about 320 pm, is too long for a hydrogen bond. Therefore, it is unlikely a hydrogen bond exists at bond 1, as well as bonds 2, and 4. For this reason, there has to be another explanation, what causes the intermolecular interaction at position 1, 2, and 4.

The excess of iron could allow different reactions. On the one hand deprotonation of the molecules may occur. If this would happen, fewer possibilities of hydrogen bonds would exist and hydrogen bonds could explain fewer imaged bonds. On the other hand, the formation of a coordination complex with iron as coordination centre and TMA as ligand is possible for the protonated as well as for the deprotonated molecules. Iron is known to form metal-organic compounds with organic molecules equipped with carboxylic acid moieties. TMA and iron form 1D chains on Cu(110) surfaces, the oxygen-oxygen distance amounts to 390 pm. As this is only one possible coordination geometry, oxygen-oxygen distances from substances in solution will be compared.

The oxygen-oxygen distance of carboxylate ligands and iron distances for a planar coordination geometry are recorded to range between 360 pm and 450 pm, which are distances acquired in solution [275, 276, 277]. Most coordination complexes lie in this range of distance [278]. The measured oxygen-oxygen distances of UC-Fe are far below the ones for planar coordination complexes. Therefore, a planar coordination geometry cannot exist at bond positions 1,2, and 4. Nevertheless, to exclude that the intermolecular features at bond positions 1 to 5 are in fact imaged artefacts, so called apparent bonds, oxygen-oxygen distances A and B, where no intermolecular features are observed, are investigated. Those distances (A and B) stretch from 300 pm to 330 pm. As there is no bond-like feature imaged in this distance range, it can be assumed that bonds imaged in or larger than this

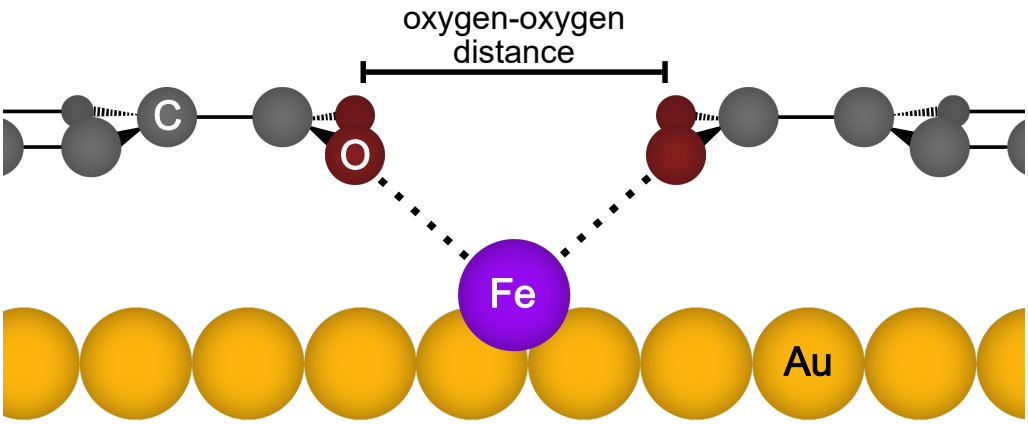

Figure 8.23: Sketch of a possible three dimensional coordination geometry of with iron (purple) subjacent to the trimesic acid (grey and red) molecules on the gold (yellow) surface.

distance range have to be real intermolecular bonds, as the distance-dependent overlap of charge density can be excluded. Based on that assumption, bonds 1, 2, and 4 can be verified as real bonds. While the bonds 3 and 5 have to be taken into consideration for apparent bonds, as they might be explainable by the distance effect.
Summarising, the insights obtained from the oxygen-oxygen distances: the imaging of apparent bonds is not occurring for an oxygen-oxygen distance longer than 300 pm. In conclusion, bonds longer than 300 pm have to be real chemical bonds, while bonds imaged at positions with an oxygen-oxygen distance shorter than 300 pm can either stem from real chemical bonds or from apparent bond imaging.
Therefore, the bonds can be categorised into bonds with an oxygen-oxygen distance longer than 300 pm and bonds with an oxygen-oxygen distance shorter than 300 pm. Four imaged bonds (3,5(')) are in the category shorter than 300 pm. Within the length of these bonds hydrogen bonds as well as apparent bonds are possible.
Six imaged bonds (1,2,4 (')) are in the category larger than 300 pm. As, at this oxygen-oxygen distance, no intermolecular feature is observed between other oxygen atoms (A,B), these six bonds stem from real chemical bonds. While the oxygen-oxygen distance is too long for hydrogen bonds, they are also too short for a planar coordination geometry. However, due to the fact that the UC-Fe only occurs in the presence of iron and similar bonds have been observed for TMA on Au(111)-FeX surfaces, it can be suggested that another coordination geometry is formed. An explanation is the formation of a three dimensional coordination geometry. As shown in the schematic in figure 8.23 where the iron atom is lying in a subjacent position or substitutes a gold atom and the oxygen atoms form a coordinate bond to the iron underneath. This geometry reduces the oxygen-oxygen

distance, which could then be in alignment to the oxygen-oxygen distances observed for bonds 1,2, and 4 (’). This argumentation is reinforced by the alloying experiments in section 8.2.2.1, where near-surface alloy begins to form at 338 K. Therefore, it is concluded that the UC-Fe is with a very high likeliness indeed a result of a metal-organic network formation and three dimensional intermolecular bonds are present.

8.6 Conclusions

In this chapter, long-range ordered networks of TMA on Au(111) have been successfully reproduced at room temperature. Additional to the structures observed by Ye et al., a zigzag bow-tie structure has been observed. Combining constant-height NC-AFM imaging with systematic force maps of the HON network deepened the understanding of imaging the dimeric hydrogen bond. Constant-height NC-AFM imaging of TMA molecules allowed high-resolution images of the molecular shape: benzene ring, atomic positions of oxygen atoms, and intermolecular interaction at hydrogen bond position have been imaged with features strongly depending on the tip-sample distance. The observed features are in agreement with previous reported contrasts for TMA molecules [268]. Mapping the site-specific forces between the CO tip and the molecule revealed a strong influence of electrostatic interaction, namely, the negatively charged cloud of the CO tip on the imaging contrast of electron dense regions, as well as the positively polarized $C_{carbonyl}$.
Heating pure TMA on pristine Au(111) revealed the formation of densely arranged areas in defect-free HON terraces. The densely arranged areas can be divided into unordered and ordered areas. The ordered areas are described as parallel bow-ties. These assemblies are uniquely observed after annealing of TMA on pristine Au(111).
Heating experiments of TMA are repeated after iron exposure to and alloying with the Au(111) sample, which has been cleaned by sputter and anneal cycles (Au(111)-Fe1, Au(111)-FeX). After the heating procedure on the previously iron exposed surface large areas of HON are observed, as well as ordered and unordered densely arranged areas. The densely arranged areas show different structures after different heating temperatures and iron exposures prior the experiments. After multiple iron exposures different sized unit cells are observed. These unites the unique observation on surfaces exposed to iron and alloying. This leads to the conclusion, iron contaminates the Au(111) surface even after three sputter and anneal cycles. The iron contaminations likely induce a reaction with TMA, probably deprotonation or coordination, resulting in structural changes of the TMA assembly. The different sized unit cells contain similar bonding patterns. These differ drastically from the dimeric and trimeric bonds of room temperature measurements.
Next, TMA and iron have been deposited on Au(111). Throughout different preparation

protocols densely arranged areas are formed, which contain both ordered and unordered areas. Additionally, for some preparation protocols HON is observed, which usually can be associated to experiments with limited iron diffusivity. The ordered areas throughout all preparation protocols unifies the same structure. It is described by the unit cell UC-Fe. The UC-Fe shows a unique bonding motif different than the structures observed without iron, however, similar bonding patterns are observed for ordered structures formed on surfaces with iron contaminations (UC75-1, -3, -4; UC110). In conclusion, iron is involved in the structure formation for said unit cells. With the help of constant-height imaging ten intermolecular features are observed. Based on the considerations regarding the oxygen-oxygen distance, these features can be categorised into bond-like features with an oxygen-oxygen distance shorter than 300 pm and oxygen-oxygen distances longer than 300 pm. While the shorter bond-like features can either originate from hydrogen bonds or are as apparent bonds, the longer bonds are suggested with strong evidence to stem from a three dimensional coordination geometry to subjacent iron atoms.

9 Conclusions

Metal-organic compounds provide unique functionalities including chargeability [20], magnetism [19], or optoelectricity [21]. Thus, these materials are highly promising for the fabrication of nano scale devices via the bottom-up approach. This approach is often conducted on surfaces, due to the benefits of a controlled, two dimensional environment and the availability of real-space investigations with scanning probe microscopy. However, to fully exploit the properties of the metal-organic compounds, decoupling from the underlying surface is required. While this decoupling can be achieved by insulating surfaces, these surfaces have significantly lower surface energies, which often results in weak adsorption and dewetting of adsorbates on insulating surfaces.

Within this thesis, three approaches are followed towards the fabrication of metal-organic assemblies on insulating surfaces: (1) the deposition and assembly of pre-synthesised metal-organic molecules, (2) the on-surface synthesis of individual metal-organic molecules, and (3) the on-surface formation of metal-organic networks via coordinate bonds.

For approach (1), namely the deposition and assembly of pre-synthesised metal organic molecules, ferrocene dicarboxylic acid (FDCA) is deposited on insulating CaF_2 bulk and CaF_2/CaF_1/Si(111) thin film surfaces. FDCA is a metallocene complex, which consists of two cyclopentadienyl (C_5H_5) rings coordinated to an iron centre. Each cyclopentadienyl ring is functionalised with a carboxylic acid (COOH) group. Single FDCA molecules are imaged as bright protrusions in STM and with a distinct dumbbell shape in NC-AFM. The molecules form small clusters on CaF_2 bulk and thin film surfaces. The small clusters are observed at low and room temperature due to firm anchoring. This firm anchoring of the carboxylic acid moieties to the CaF_2(111) surface is caused by a "quadruped" anchoring mechanism. This mechanism is revealed based on experimental data and DFT calculations: Each carboxylic acid group anchors both via a hydrogen bond to a fluoride of the CaF_2 surface and via a bond between the carbonyl oxygen atom and a calcium cation of the surface. The molecules adsorb in a slightly tilted geometry, therefore two hydrogen atoms (one of each cyclopentadienyl ring) are the topmost atoms. Based on the features observed in NC-AFM images it is found that the dumbbell shape results from imaging

these two hydrogen atoms. Based on finding two different orientations of the dumbbells relative to the $\langle 11\bar{2} \rangle$ surface directions of $CaF_2(111)$, two different adsorption geometries are identified, namely, adsorption of a staggered and of an eclipsed molecule. These two geometries are in alignment with the two energetically most favourable adsorption geometries within the DFT calculations.

Towards approach (2), the on-surface synthesis of individual metal-organic molecules, the metallisation of porphyrin molecules is approached using the basic building block of heme and chlorophyll, namely protoporphyrin IX (PPIX) molecules. PPIX is a porphyrin derivative with eight side groups, having four methyl (CH_3), two ethylene (C_2H_3), and four propionic acid ($C_3O_2H_5$) moieties covalently bound to the porphyrin core. Each group can have a number of configurations due to the flexibility of the bonds. The metallisation reaction is attempted with copper on both Ag(111) and $CaF_2(111)$ thin film surfaces and monitored with STM and NC-AFM.

First, STM and AFM imaging of PPIX on Ag(111) revealed single molecules, which are imaged in STM as protrusions of different shapes. Three shapes appear recurringly, they are here denoted as 'clover', 'trapezium', and 'paw'. The different shapes are explained by different conformers, which can form on the surface due to the flexibility of side groups of PPIX. With high-resolution NC-AFM images of the three shapes, the flexible side groups pointing out of the molecular plane are imaged as bright protrusions. Due to the out-of-plane geometry and the flexibility of the side groups, the molecular PPIX core could not be imaged with NC-AFM on Ag(111). Nearly symmetric arrangements of features are observed for clover and trapezium shape in NC-AFM images. Based on the NC-AFM features of the side groups and consideration of the flexibility of the side groups, orientations of PPIX molecules are suggested for clover and trapezium shapes.

Second, PPIX is observed to form small clusters on Ag(111) in combination with Cu. The molecular side groups remain flexible as multiple features are observed within the clusters using NC-AFM. Due to the flexibility of the side groups, a precise allocation based on STM and NC-AFM imaging data of PPIX molecules and Cu atoms within a cluster is difficult. However, as the clusters are only observed in the presence of Cu, a change in either the molecule-molecule interaction or the molecule-substrate interaction is caused by the Cu atoms. This could stem from metallation of the porphyrin molecule, intermolecular coordination, molecular deprotonation, or van-der-Waals interaction.

Third, an outlook for studying PPIX on an insulator surface is given by imaging PPIX on CaF_2 thin film surfaces. Clusters are observed on the CaF_2 surface for molecular deposition at about 300 K or about 100 K. This indicates that the molecule-substrate interaction is relatively weak and anchoring occurs to be weaker than for the case of FDCA on $CaF_2(111)$.

Fourth, the mobility of Cu on CaF_2 thin films is studied by tip induced displacement and heating. Here, tip induced displacement is investigated by scanning the same sample area for several times in STM mode. A reduction of the number of clusters is observed after four scan cycles, while the remaining clusters grow in size. Stepwise heating of Cu on CaF_2 surfaces up to 573 K also results in a reduction of cluster density, while the height of the single clusters increases. Thus, both experiments indicate a low barrier for lateral mobility. This makes Cu suitable as educt for future reactions, as a high mobility increases the chances of a reaction occurring.

For approach (3), the on-surface formation of metal-organic networks via coordinate bonds, trimesic acid (TMA) and iron are codeposited on Au(111) surfaces. TMA is a small organic molecule consisting of a benzene ring with three carboxylic acid groups at positions 1, 3, and 5.

First, the adsorption of Fe on Au(111) revealed at submonolayer room temperature deposition triangular and diamond shaped Fe islands. The formation of islands is in agreement with the Volmer-Weber growth reported for this sample system [32, 33, 34]. After Fe deposition on Au(111) samples heated to 338 K and 383 K, STM images present frayed step edges of the Au(111) surface in combination with island and granules formation, as well as a strongly distorted herringbone reconstruction. These observations indicate the formation of an iron-gold near-surface alloy.

Second, the deposition of TMA molecules on Au(111) surfaces yield different hydrogen-bonded structures as observed with STM: the honeycomb network, the set of flower structures, close-packed structure, and a zigzag bow-tie. While the former three structures have been observed in previous studies [244], the zigzag bow-tie structure has only been reported at domain walls, here the zigzag bow-tie is found to form larger assemblies. The zigzag bow-tie consists of rows of dimeric hydrogen-bonded molecules.

The honeycomb network structure is studied in detail with constant-height NC-AFM imaging and force mapping using a CO functionalised tip. The constant-height images of the HON network show a strong distance dependency of the imaged features of the molecules. In particular, the features at the oxygen position change from round protrusions to sharp triangular features at the position of the carboxylic acid group. Mapping the site-specific forces at different positions in the honeycomb network show distinct differences in short-range repulsive interactions and the importance of electrostatic interaction between CO tip and sample. An exemplary difference is observed between the carbon atom of the carboxylic acid group and carbon of the benzene ring. The positively polarised carboxylic acid carbon shows a less repulsive interaction with the CO tip than the interaction between tip and the carbon atom of the benzene ring. This selected example reveals the influence of

the electrostatic interaction between the negatively charged cloud in front of the CO tip and the molecule.
Third, the codeposition of Fe and TMA on Au(111) surfaces in different deposition order and at different sample temperature leads to the formation of a densely arranged ordered structure as observed with STM and NC-AFM imaging. In NC-AFM images, intermolecular bond-like features connecting the oxygen positions of the carboxylic acid groups are furthermore observed. A rectangular unit cell containing two TMA molecules and ten intermolecular features is found. An analysis of the oxygen-oxygen distance is performed to determine the respective bonding character of these ten positions. This analysis revealed that the oxygen-oxygen distance at the position of four of the ten intermolecular features are shorter than 300 pm, which can either be due to hydrogen bonds or imaging artefacts caused by close atom proximity, also known as apparent bond contrast [111]. In contrast, the oxygen-oxygen distances for the other six intermolecular features are longer than 300 pm. These are too long for hydrogen bonds, are unlikely apparent bonds, but are furthermore too short for a planar coordinate bond with Fe. This leads to the conclusion that a three dimensional coordination geometry exists, where the Fe lies subjacent to the TMA molecules. This model is in agreement with the observed near-surface alloying of Fe on the Au(111) surface. Therefore, it can be concluded that the approach of metal-organic network formation provides long-range ordered metal arrays.

It is envisioned that the results of this thesis can be used within promising next steps towards nano scale devices: After small metal-organic clusters of FDCA molecules have been formed on the insulating CaF_2 surface and quadruped anchoring has been identified as root for stable adsorption, it is now possible to investigate the properties and functionalities of FDCA. By substitution of the iron centre with different metals, the properties of and the interaction between different metallocenes can be exploited. Possible future experiments include probing the electronic properties of the molecular clusters, like the storage of charges, as well as in general the optoelectronic properties of metal-organic compounds on insulating surfaces towards applications in solar cells or light emitting diodes. Further experiments investigating the magnetic properties of the metal-organic compounds can aid in pushing the field of novel information storage and processing, as in the quantum cellular automata.

Bibliography

[1] Kulisch, W. *Nanotechnologie für Einsteiger : Herstellung und Eigenschaften von Kohlenstoff-Nanostrukturen;* Wiley-VCH Verlag GmbH & Co. KGaA: Weinheim, Germany, 2016.

[2] Wolf, E. L. *Nanophysik und Nanotechnologie : Eine Einführung in die Konzepte der Nanowissenschaften;* Wiley-VCH Verlag GmbH & Co. KGaA: Weinheim, Germany, 2015.

[3] Rubahn, H.-G. *Nanophysik und Nanotechnologie;* Vieweg+Teubner Verlag, 2002.

[4] Feynman, R. P. *Engineering and Science* **1960**, *23*(5), 22–36.

[5] Bates, K. A.; Rothschild, M.; Bloomstein, T. M.; Fedynyshyn, T. H.; Kunz, R. R.; Liberman, V.; Switkes, M. *IBM Journal of Research and Development* **2001**, *45*(5), 605–614.

[6] Xia, Y.; Whitesides, G. M. *Annual Review of Materials Science* **1998**, *28*, 153–184.

[7] Yoon, K. Y.; Dong, G. B. *Materials Chemistry Frontiers* **2020**, *4*(1), 29–45.

[8] Kühnle, A. *Curr. Opin. Coll. Interf. Sci.* **2009**, *14*, 157–168.

[9] Shen, Q.; Gao, H. Y.; Fuchs, H. *Nano Today* **2017**, *13*, 77–96.

[10] Eigler, D.; Schweizer, E. *Nature* **1990**, *344*, 524–526.

[11] Burke, S. A.; Topple, J. M.; Grütter, P. *J. Phys.: Condens. Matter* **2009**, *21*(42), 423101.

[12] Bauer, E. *Zeitschrift für Kristallographie* **1958**, *110*, 372–394.

[13] Langlais, V. J.; Schlittler, R. R.; Tang, H.; Gourdon, A.; Joachim, C.; Gimzewski, J. K. *Physical Review Letters* **1999**, *83*(14), 2809–2812.

[14] Rahe, P.; Kittelmann, M.; Neff, J. L.; Nimmrich, M.; Reichling, M.; Maass, P.; Kühnle, A. *Adv. Mater.* **2013**, *25*(29), 3948–3956.

[15] Paris, C.; Floris, A.; Aeschlimann, S.; Neff, J.; Kling, F.; Kühnle, A.; Kantorovich, L. *Communications Chemistry* **2018**, *1*(1), 66.

[16] Paris, C.; Floris, A.; Aeschlimann, S.; Kittelmann, M.; Kling, F.; Bechstein, R.; Kühnle, A.; Kantorovich, L. *J. Phys. Chem. C* **2016**, *120*(31), 17546–17554.

[17] Ataman, E.; Andersson, M. P.; Ceccato, M.; Bovet, N.; Stipp, S. L. S. *The Journal of Physical Chemistry C* **2016**, *120*(30), 16597–16607.

[18] Hoff, B.; Gingras, M.; Peresutti, R.; Henry, C. R.; Foster, A. S.; Barth, C. *The Journal of Physical Chemistry C* **2014**, *118*(26), 14569–14578.

[19] Manna, P.; Tripuramallu, B. K.; Bommakanti, S.; Das, S. K. *Dalton Transactions* **2015**, *44*(6), 2852–2864.

[20] Rahe, P.; Steele, R. P.; Williams, C. C. *Nano Lett.* **2016**, *16*, 911–916.

[21] Xu, H.; Chen, R. F.; Sun, Q.; Lai, W. Y.; Su, Q. Q.; Huang, W.; Liu, X. G. *Chemical Society Reviews* **2014**, *43*(10), 3259–3302.

[22] Dong, L.; Gao, Z.; Lin, N. *Progress in Surface Science* **2016**, *91*(3), 101–135.

[23] Schuller, L.; Haapasilta, V.; Kuhn, S.; Pinto, H.; Bechstein, R.; Foster, A. S.; Kuhnle, A. *Journal of Physical Chemistry C* **2016**, *120*(27), 14730–14735.

[24] Zhang, Y.; Schulz, F.; Rytting, B. M.; Walters, C. C.; Kaiser, K.; Metz, J. N.; Harper, M. R.; Merchant, S. S.; Mennito, A. S.; Qan, K. N.; Kushnerick, J. D.; Kilpatrick, P. K.; Gross, L. *Energy & Fuels* **2019**, *33*(7), 6088–6097.

[25] Miwa, K.; Imada, H.; Kawahara, S.; Kim, Y. *Physical Review B* **2016**, *93*(16), 165419.

[26] Leber, R.; Wilson, L. E.; Robaschik, P.; Inkpen, M. S.; Payne, D. J.; Long, N. J.; Albrecht, T.; Hirjibehedin, C. F.; Heutz, S. *Chemistry of Materials* **2017**, *29*(20), 8663–8669.

[27] Berger, J.; Kośmider, K.; Stetsovych, O.; Vondráček, M.; Hapala, P.; Spadafora, E. J.; Švec, M.; Jelínek, P. *J. Phys. Chem. C* **2016**, *120*(38), 21955–21961.

[28] Zhao, Y.; Yuan, B.; Li, C.; Zhang, P.; Mai, Y.; Guan, D.; Li, Y.; Zheng, H.; Liu, C.; Wang, S.; Jia, J. *Chemphyschem* **2019**, *20*(18), 2394–2397.

[29] Gottfried, J. M. *Surface Science Reports* **2015**, *70*(3), 259–379.

[30] Shubina, T. E.; Marbach, H.; Flechtner, K.; Kretschmann, A.; Jux, N.; Buchner, F.; Steinruck, H.-P.; Clark, T.; Gottfried, J. M. *Journal of the American Chemical Society* **2007**, *129*(30), 9476–9483.

[31] Gambardella, P.; Stepanow, S.; Dmitriev, A.; Honolka, J.; de Groot, F. M. F.; Lingenfelder, M.; Sen Gupta, S.; Sarma, D. D.; Bencok, P.; Stanescu, S.; Clair, S.; Pons, S.; Lin, N.; Seitsonen, A. P.; Brune, H.; Barth, J. V.; Kern, K. *Nature Materials* **2009**, *8*(3), 189–193.

[32] Donati, F.; Mairov, A.; Casari, C. S.; Passoni, M.; Bassi, A. L. *Surface Science* **2012**, *606*(7-8), 702–710.

[33] Voigtlander, B.; Meyer, G.; Amer, N. M. *Surface Science* **1991**, *255*(3), L529–L535.

[34] Stroscio, J. A.; Pierce, D. T.; Dragoset, R. A.; First, P. N. *Journal of Vacuum Science & Technology a-Vacuum Surfaces and Films* **1992**, *10*(4), 1981–1985.

[35] Khan, N. A.; Matranga, C. *Surface Science* **2008**, *602*(4), 932–942.

[36] Mortimer, C. *Chemie*, Vol. 9. Auflage; Thieme Verlag: Stuttgart, 2006.

[37] Janiak, C.; Meyer, H.-J.; Gudat, D.; Kurz, P. *Riedel Moderne Anorganische Chemie;* De Gruyter, 2018.

[38] Holleman, A. F.; Wiberg, E. *Lehrbuch der Anorganischen Chemie;* Walter de Gruyter: Berlin, New York, 1995.

[39] Harriman, A.; Richoux, M. C.; Neta, P. *Journal of Physical Chemistry* **1983**, *87*(24), 4957–4965.

[40] Diller, K.; Klappenberger, F.; Marschall, M.; Hermann, K.; Nefedov, A.; Woll, C.; Barth, J. V. *Journal of Chemical Physics* **2012**, *136*(1), 014705.

[41] Cheng, Z.; Du, S.; Guo, W.; Gao, L.; Deng, Z.; Jiang, N.; Guo, H.; Tang, H.; Gao, H.-J. *Nano Research* **2011**, *4*(6), 523–530.

[42] Bai, Y.; Buchner, F.; Wendahl, M. T.; Kellner, I.; Bayer, A.; Steinruck, H.-P.; Marbach, H.; Gottfried, J. M. *Journal of Physical Chemistry C* **2008**, *112*(15), 6087–6092.

[43] Di Santo, G.; Castellarin-Cudia, C.; Fanetti, M.; Taleatu, B.; Borghetti, P.; Sangaletti, L.; Floreano, L.; Magnano, E.; Bondino, F.; Goldoni, A. *Journal of Physical Chemistry C* **2011**, *115*(10), 4155–4162.

[44] Doyle, C. M.; Krasnikov, S. A.; Sergeeva, N. N.; Preobrajenski, A. B.; Vinogradov, N. A.; Sergeeva, Y. N.; Senge, M. O.; Cafolla, A. A. *Chemical Communications* **2011**, *47*(44), 12134–12136.

[45] Li, Y.; Xiao, J.; Shubina, T. E.; Chen, M.; Shi, Z.; Schmid, M.; Steinrück, H.-P.; Gottfried, J. M.; Lin, N. *Journal of the American Chemical Society* **2012**, *134*(14), 6401–6408.

[46] Cirera, B.; de la Torre, B.; Moreno, D.; Ondracek, M.; Zboril, R.; Miranda, R.; Jelinek, P.; Ecija, D. *Chemistry of Materials* **2019**, *31*(9), 3248–3256.

[47] Gonzalez-Moreno, R.; Sanchez-Sanchez, C.; Trelka, M.; Otero, R.; Cossaro, A.; Verdini, A.; Floreano, L.; Ruiz-Bermejo, M.; Garcia-Lekue, A.; Martin-Gago, J. A.; Rogero, C. *Journal of Physical Chemistry C* **2011**, *115*(14), 6849–6854.

[48] Goldoni, A.; Pignedoli, C. A.; Di Santo, G.; Castellarin-Cudia, C.; Magnano, E.; Bondino, F.; Verdini, A.; Passerone, D. *Acs Nano* **2012**, *6*(12), 10800–10807.

[49] Buchner, F.; Flechtner, K.; Bai, Y.; Zillner, E.; Kellner, I.; Steinruck, H. P.; Marbach, H.; Gottfried, J. M. *Journal of Physical Chemistry C* **2008**, *112*(39), 15458–15465.

[50] Chemisorption and physisorption. Book, I. G. **2002**.

[51] Chen, B. W. J.; Kirvassilis, D.; Bai, Y. H.; Mavrikakis, M. *Journal of Physical Chemistry C* **2019**, *123*(13), 7551–7566.

[52] Vericat, C.; Vela, M. E.; Benitez, G. A.; Gago, J. A. M.; Torrelles, X.; Salvarezza, R. C. *Journal of Physics: Condensed Matter* **2006**, *18*(48), R867–R900.

[53] Rowan, S. J.; Cantrill, S. J.; Cousins, G. R. L.; Sanders, J. K. M.; Stoddart, J. F. *Angewandte Chemie-International Edition* **2002**, *41*(6), 898–952.

[54] Northrop, B. H.; Zheng, Y. R.; Chi, K. W.; Stang, P. J. *Accounts of Chemical Research* **2009**, *42*(10), 1554–1563.

[55] Barth, J. V.; Costantini, G.; Kern, K. *Nature (London, United Kingdom)* **2005**, *437*(7059), 671–679.

[56] Rahe, P.; Lindner, R.; Kittelmann, M.; Nimmrich, M.; Kühnle, A. *Physical Chemistry Chemical Physics* **2012**, *14*(18), 6544–6548.

[57] Pawlak, R.; Nony, L.; Bocquet, F.; Olson, V.; Sassi, M.; Debierre, J. M.; Loppacher, C.; Porte, L. *Journal of Physical Chemistry C* **2010**, *114*(20), 9290–9295.

[58] Ataman, E.; Andersson, M. P.; Ceccato, M.; Bovet, N.; Stipp, S. L. S. *The Journal of Physical Chemistry C* **2016**, *120*(30), 16586–16596.

[59] Jia, Q.; Hu, Z.-X.; Ji, W.; Burke, S. A.; Gao, H.-J.; Grütter, P.; Guo, H. *Phys. Chem. Chem. Phys.* **2016**, *18*(16), 11008–11016.

[60] Amrous, A.; Bocquet, F.; Nony, L.; Para, F.; Loppacher, C.; Lamare, S.; Palmino, F.; Cherioux, F.; Gao, D. Z.; Canova, F. F.; Watkins, M. B.; Shluger, A. L. *Adv. Mater. Interf.* **2014**, *1*(9), 1400414.

[61] Kittelmann, M.; Rahe, P.; Gourdon, A.; Kühnle, A. *ACS Nano* **2012**, *6*(8), 7406–7411.

[62] Kittelmann, M.; Rahe, P.; Kühnle, A. *Journal of Physics-Condensed Matter* **2012**, *24*(35), 354007–354013.

[63] Rahe, P.; Nimmrich, M.; Kühnle, A. *Small* **2012**, *8*(19), 2969–2977.

[64] Meier, T.; Pawlak, R.; Kawai, S.; Geng, Y.; Liu, X. S.; Decurtins, S.; Hapala, P.; Baratoff, A.; Liu, S. X.; Jelinek, P.; Meyer, E.; Glatzel, T. *Acs Nano* **2017**, *11*(8), 8413–8420.

[65] Stepanow, S.; Lin, N.; Barth, J. V. *Journal of Physics: Condensed Matter* **2008**, *20*(18), 184002.

[66] Lin, T.; Shang, X. S.; Adisoejoso, J.; Liu, P. N.; Lin, N. *Journal of the American Chemical Society* **2013**, *135*(9), 3576–3582.

[67] Shi, Z.; Liu, J.; Lin, T.; Xia, F.; Liu, P. N.; Lin, N. *Journal of the American Chemical Society* **2011**, *133*(16), 6150–6153.

[68] Lin, T.; Kuang, G. W.; Wang, W. H.; Lin, N. A. *Acs Nano* **2014**, *8*(8), 8310–8316.

[69] Seitsonen, A. P.; Lingenfelder, M.; Spillmann, H.; Dmitriev, A.; Stepanow, S.; Lin, N.; Kern, K.; Barth, J. V. *Journal of the American Chemical Society* **2006**, *128*(17), 5634–5635.

[70] Lin, T.; Kuang, G.; Shang, X. S.; Liu, P. N.; Lin, N. *Chemical Communications* **2014**, *50*, 15327–15329.

[71] Urgel, J. I.; Schwarz, M.; Garnica, M.; Stassen, D.; Bonifazi, D.; Écija, D.; Barth, J. V.; Auwärter, W. *Journal of the American Chemical Society* **2015**, *137*(7), 2420–2423.

[72] Binnig, G.; Quate, C.; Gerber, C. *Physical Review Letters* **1986**, *56*(9), 930–933.

[73] Binnig, G.; Rohrer, H. *Surface Science* **1983**, *126*(1), 236–244.

[74] van der Lit, J.; Di Cicco, F.; Hapala, P.; Jelínek, P.; Swart, I. *Physical Review Letters* **2016**, *116*(9), 096102.

[75] Scheuerer, P.; Patera, L. L.; Simbürger, F.; Queck, F.; Swart, I.; Schuler, B.; Gross, L.; Moll, N.; Repp, J. *Physical Review Letters* **2019**, *123*(6), 066001.

[76] Purckhauer, K.; Weymouth, A. J.; Pfeffer, K.; Kullmann, L.; Mulvihill, E.; Krahn, M. P.; Muller, D. J.; Giessibl, F. J. *Scientific Reports* **2018**, *8*, 9330.

[77] Binnig, G.; Rohrer, H.; Gerber, C.; Weibel, E. *Physical Review Letters* **1983**, *50*(2), 120–3.

[78] Meyer, G.; Neu, B.; Rieder, K. H. *Applied Physics a-Materials Science & Processing* **1995**, *60*(3), 343–345.

[79] Voigtländer, B. *Scanning Probe Microscopy*, NanoScience and Technology; Springer-Verlag: Berlin, 2015.

[80] Binnig, G.; Rohrer, H.; Gerber, C.; Weibel, E. *Applied Physics Letters* **1982**, *40*(2), 178–180.

[81] Binnig, G.; Rohrer, H. *Reviews of Modern Physics* **1987**, *59*(3), 615–625.

[82] Brillouin, L. *Comptes Rendus de l'Académie des Sciences* **1926**, *183*, 24–26.

[83] Kramers, H. A. *Zeitschrift für Physik* **1926**, *39*, 828–840.

[84] Wentzel, G. *Zeitschrift für Physik* **1926**, *38*, 518–529.

[85] Bardeen, J. *Physical Review Letters* **1961**, *6*(2), 57–58.

[86] Tersoff, J.; Hamann, D. R. *Physical Review B* **1985**, *31*(2), 805–813.

[87] Morgenstern, K.; Lorente, N.; Rieder, K.-H. *Physica Status Solidi B-Basic Solid State Physics* **2013**, *250*(9), 1671–1751.

[88] Bartels, L.; Meyer, G.; Rieder, K. H. *Applied Physics Letters* **1997**, *71*(2), 213–215.

[89] Voigtländer, B. *Atomic Force Microscopy*, NanoScience and Technology; Springer Nature: Cham, Switzerland, 2nd ed., 2019.

[90] Giessibl, F. J. *Appl. Phys. Lett.* **1998**, *73*(26), 3956–3958.

[91] Giessibl, F. J. *Review of Scientific Instruments* **2019**, *90*(1), 011101.

[92] London, F. *Transactions of Faraday Society* **1936**, *332*, 8.

[93] Debye, P. J. W.; Debye, P. J. W. *Polar molecules*, Vol. 172; Dover New York, 1929.

[94] Ellner, M.; Pou, P.; Pérez, R. *Physical Review B* **2017**, *96*(7), 075418.

[95] Gross, L.; Mohn, F.; Moll, N.; Liljeroth, P.; Meyer, G. *Science* **2009**, *325*(5944), 1110–1114.

[96] Hanssen, K. O.; Schuler, B.; Williams, A. J.; Demissie, T. B.; Hansen, E.; Andersen, J. H.; Svenson, J.; Blinov, K.; Repisky, M.; Mohn, F.; Meyer, G.; Svendsen, J.-S.; Ruud, K.; Elyashberg, M.; Gross, L.; Jaspars, M.; Isaksson, J. *Angewandte Chemie-International Edition* **2012**, *51*(49), 12238–12241.

[97] Fatayer, S.; Poddar, N. B.; Quiroga, S.; Schulz, F.; Schuler, B.; Kalpathy, S. V.; Meyer, G.; Perez, D.; Guitian, E.; Pena, D.; Wornat, M. J.; Gross, L. *Journal of the American Chemical Society* **2018**, *140*(26), 8156–8161.

[98] Kichin, G.; Wagner, C.; Tautz, F. S.; Temirov, R. *Physical Review B* **2013**, *87*(8), 081408.

[99] Mohn, F.; Schuler, B.; Gross, L.; Meyer, G. *Applied Physics Letters* **2013**, *102*(7), 073109.

[100] Yesilpinar, D.; Schulze Lammers, B.; Timmer, A.; Amirjalayer, S.; Fuchs, H.; Mönig, H. *Nanoscale* **2020**, *12*(5), 2961–2965.

[101] Hauptmann, N.; Gonzalez, C.; Mohn, F.; Gross, L.; Meyer, G.; Berndt, R. *Nanotechnology* **2015**, *26*(44), 445703.

[102] Sweetman, A. M.; Jarvis, S. P.; Sang, H.; Lekkas, I.; Rahe, P.; Wang, Y.; Wang, J.; Champness, N. R.; Kantorovich, L.; Moriarty, P. *Nat. Commun.* **2014**, *5*, 3931.

[103] Dürig, U. *Appl. Phys. Lett.* **1999**, *75*(3), 433–435.

[104] Gross, L.; Schuler, B.; Pavliček, N.; Fatayer, S.; Majzik, Z.; Moll, N.; Pena, D.; Meyer, G. *Angewandte Chemie-International Edition* **2018**, *57*(15), 3888–3908.

[105] Weymouth, A. J.; Hofmann, T.; Giessibl, F. J. *Science* **2014**, *343*(6175), 1120–1122.

[106] Hapala, P.; Kichin, G.; Wagner, C.; Tautz, F. S.; Temirov, R.; Jelínek, P. *Phys. Rev. B* **2014**, *90*(8), 085421.

[107] Gajdos, M.; Eichler, A.; Hafner, J. *Journal of Physics-Condensed Matter* **2004**, *16*(8), 1141–1164.

[108] de Oteyza, D. G.; Gorman, P.; Chen, Y. C.; Wickenburg, S.; Riss, A.; Mowbray, D. J.; Etkin, G.; Pedramrazi, Z.; Tsai, H. Z.; Rubio, A.; Crommie, M. F.; Fischer, F. R. *Science* **2013**, *340*(6139), 1434–1437.

[109] Ellner, M.; Pou, P.; Perez, R. *Acs Nano* **2019**, *13*(1), 786–795.

[110] Pavliček, N.; Herranz-Lancho, C.; Fleury, B.; Neu, M.; Niedenführ, J.; Ruben, M.; Repp, J. *Physica Status Solidi B-Basic Solid State Physics* **2013**, *250*(11), 2424–2430.

[111] Hämäläinen, S. K.; van der Heijden, N.; van der Lit, J.; den Hartog, S.; Liljeroth, P.; Swart, I. *Physical Review Letters* **2014**, *113*(18), 186102.

[112] Ellner, M.; Pavliček, N.; Pou, P.; Schuler, B.; Moll, N.; Meyer, G.; Gross, L.; Peréz, R. *Nano Letters* **2016**, *16*(3), 1974–1980.

[113] Grimme, S.; Antony, J.; Ehrlich, S.; Krieg, H. *J. Chem. Phys.* **2010**, *132*(15), 154104.

[114] Temmen, M. *Abbildung von Graphen und CaF2(111) mittels hochauösender Nicht-Kontakt-Rasterkraftmikroskopie* Phd thesis, **2016**.

[115] Lübbe, J. *Cantilever properties and noise figures in high-resolution non-contact atomic force microscopy* Phd thesis, **2012**.

[116] Schnieder, H. *Entwicklung der Präparation schockgefrorener Proben für die Nichtkontakt-Rasterkraftmikroskopie* Phd thesis, **2013**.

[117] Baurichter, R. *Laborbericht zur Temperaturkalibration der Probenheizstation im UHV-System* Studienarbeit, **2022**.

[118] Tröger, L.; Schütte, J.; Ostendorf, F.; Kühnle, A.; Reichling, M. *Rev. Sci. Instrum.* **2009**, *80*(6), 063703.

[119] Rahe, P. *The calcite(10-14) surface: a versatile substrate for molecular self-assembly* Thesis, **2011**.

[120] Nečas, D.; Klapetek, P. *Cent. Eur. J. Phys.* **2011**, *10*(1), 181–188.

[121] Perdereau, J.; Biberian, J. P.; Rhead, G. E. *Journal of Physics F-Metal Physics* **1974**, *4*(5), 798.

[122] Heyraud, J. C.; Metois, J. J. *Surface Science* **1980**, *100*(3), 519–528.

[123] Tanishiro, Y.; Kanamori, H.; Takayanagi, K.; Yagi, K.; Honjo, G. *Surface Science* **1981**, *111*(3), 395–413.

[124] Wöll, C.; Chiang, S.; Wilson, R. J.; Lippel, P. H. *Physical Review B: Condensed Matter and Materials Physics* **1989**, *39*(11), 7988–91.

[125] Darling, S. B.; Rosenbaum, A. W.; Wang, Y.; Sibener, S. J. *Langmuir* **2002**, *18*(20), 7462–7468.

[126] Barth, J. V.; Brune, H.; Ertl, G.; Behm, R. J. *Physical Review B* **1990**, *42*(15), 9307–9318.

[127] Kawai, S.; Nishiuchi, T.; Kodama, T.; Spijker, P.; Pawlak, R.; Meier, T.; Tracey, J.; Kubo, T.; Meyer, E.; Foster, A. S. *Science Advances* **2017**, *3*(5), e1603258.

[128] Wang, C. R.; Mueller, B. H.; Hofmann, K. R. *Nanotechnology* **2003**, *14*(11), 1192–1196.

[129] Wang, C. R.; Bierkandt, M.; Paprotta, S.; Wietler, T.; Hofmann, K. R. *Applied Physics Letters* **2005**, *86*(3), 033111.

[130] Watanabe, K.; Hirayama, H. *Surface Science* **1994**, *317*(3), L1125–L1128.

[131] Aldahhak, H.; Hogan, C.; Lindner, S.; Appelfeller, S.; Eisele, H.; Schmidt, W. G.; Dahne, M.; Gerstmann, U.; Franz, M. *Physical Review B* **2021**, *103*(3), 035303.

[132] Oura, K.; Lifshits, V.; Saranin, A.; Zotov, A.; Katayama, M. *Surface Science An Introduction;* Springer: Berlin, 2010.

[133] Takayanagi, K.; Tanishiro, Y.; Takahashi, S.; Takahashi, M. *Surface Science* **1985**, *164*(2-3), 367–92.

[134] Giessibl, F. J. *Science (Washington, D. C.)* **1995**, *267*(5194), 68–71.

[135] Takayanagi, K.; Tanishiro, Y.; Takahashi, M.; Takahashi, S. *Journal of Vacuum Science & Technology, A: Vacuum, Surfaces, and Films* **1985**, *3*(3, Pt. 2), 1502–6.

[136] Stich, I.; Payne, M. C.; Kingsmith, R. D.; Lin, J. S.; Clarke, L. J. *Physical Review Letters* **1992**, *68*(9), 1351–1354.

[137] Golan, G.; Axelevitch, A.; Gorenstein, B.; Manevych, V. *Microelectronics Journal* **2006**, *37*(9), 910–915.

[138] Letz, M.; Parthier, L. *Physical Review B* **2006**, *74*(6), 064116.

[139] Barth, C.; Foster, A. S.; Reichling, M.; Shluger, A. L. *J. Phys.: Condens. Matter* **2001**, *13*(10), 2061–2079.

[140] Heggemann, J.; Laflör, L.; Rahe, P. *Review of Scientific Instruments* **2021**, *92*(5).

[141] Pieper, H. H. *Morphology and electric potential of pristine and gold covered surfaces with the uorite structure* Phd thesis, **2012**.

[142] Atkins, P. W.; de Paula, J. *Physikalische Chemie;* Wiley-VCH Verlag GmbH&Co: Weinheim, 4 ed., 2006.

[143] Heim, K. R.; Coyle, S. T.; Hembree, G. G.; Venables, J. A.; Scheinfein, M. R. *Journal of Applied Physics* **1996**, *80*(2), 1161–1170.

[144] LaBella, V. P.; Shusterman, Y.; Schowalter, L. J.; Ventrice, C. A. *Journal of Vacuum Science & Technology a-Vacuum Surfaces and Films* **1998**, *16*(3), 1692–1696.

[145] Sokolov, N. S.; Suturin, S. M.; Krichevtsov, B. B.; Dubrovskii, V. G.; Gastev, S. V.; Sibirev, N. V.; Baranov, D. A.; Fedorov, V. V.; Sitnikova, A. A.; Nashchekin, V.; Sakharov, V. I.; Serenkov, I. T.; Shimada, T.; Yanase, T.; Tabuchi, M. *Physical Review B* **2013**, *87*(12), 125407.

[146] Illarionov, Y. Y.; Banshchikov, A. G.; Polyushkin, D. K.; Wachter, S.; Knobloch, T.; Thesberg, M.; Mennel, L.; Paur, M.; Stöger-Pollach, M.; Steiger-Thirsfeld, A.; Vexler, M. I.; Walt, M.; Sokolov, N. S.; Mueller, T.; Grasser, T. *Nature Electronics* **2019**, *2*(6), 230–235.

[147] Watanabe, M.; Suemasu, T.; Muratake, S.; Asada, M. *Appl. Phys. Lett.* **1993**, *62*.

[148] Rahe, P.; Smith, E. F.; Wollschlager, J.; Moriarty, P. J. *Physical Review B* **2018**, *97*(12), 125418.

[149] Lucas, C. A.; Loretto, D.; Wong, G. C. L. *Physical Review B* **1994**, *50*(19), 14340–14353.

[150] Harada, J.; Takahashi, I.; Itoh, Y.; Sokolov, N. S.; Yakovlev, N. L.; Shusterman, Y.; Alvarez, J. C. *Journal of Crystal Growth* **1996**, *163*(1-2), 31–38.

[151] Sokolov, N. S.; Alvarez, J. C.; Shusterman, Y. V.; Yakovlev, N. L.; Overney, R. M.; Itoh, Y.; Takahashi, I.; Harada, J. *Applied Surface Science* **1996**, *104*, 402–408.

[152] Sokolov, N. S.; Alvarez, J. C.; Gastev, S. V.; Shusterman, Y. V.; Takahashi, I.; Itoh, Y.; Harada, J.; Overney, R. M. *Journal of Crystal Growth* **1996**, *169*(1), 40–50.

[153] Olmstead, M. A.; Bringans, R. D. *Journal of Electron Spectroscopy and Related Phenomena* **1990**, *51*.

[154] Wang, C. R.; Muller, B. H.; Hofmann, K. R. *Surface Review and Letters* **2003**, *10*(4), 605–610.

[155] Olmstead, M. A.; Uhrberg, R. I. G.; Bringans, R. D.; Bachrach, R. Z. *Physical Review B* **1987**, *35*(14), 7526–7532.

[156] Saranin, A. A.; Lifshits, V. G.; Ignatovich, K. V.; Bethge, H.; Kayser, R.; Goldbach, H.; Klust, A.; Wollschlager, J.; Henzler, M. *Surface Science* **2000**, *448*(2-3), 87–92.

[157] Olmstead, M. A.; Uhrberg, R. I. G.; Bringans, R. D.; Bachrach, R. Z. *Journal of Vacuum Science & Technology B* **1986**, *4*(4), 1123–1127.

[158] Olmstead, M. A In *Thin Films: Heteroepitaxial Systems*; Liu, W. K., Santos, M. B., Eds.; World Scientific: Singapore, 1999; Vol. 15; book section 5.

[159] Venables, J. A.; Spiller, G. D. T.; Hanbücken, M. *Reports on Progress in Physics* **1984**, *47*(4), 399–459.

[160] Pakarinen, O. H.; Barth, C.; Foster, A. S.; Nieminen, R. M.; Henry, C. R. *Physical Review B (Condensed Matter and Materials Physics)* **2006**, *73*(23), 235428.

[161] Wollschläger, J. *Applied Physics A: Materials Science & Processing* **2002**, *75*(1), 155–166.

[162] Wang, C. R.; Müller, B. H.; Hofmann, K. R. *Thin Solid Films* **2002**, *410*(1-2), 72–75.

[163] Smeu, M.; Guo, H.; Ji, W.; Wolkow, R. A. *Physical Review B* **2012**, *85*(19), 195315.

[164] Wang, C. R.; Muller, B. H.; Bugiel, E.; Hofmann, K. R. *Journal of Vacuum Science & Technology, A: Vacuum, Surfaces, and Films* **2004**, *22*(5), 2182–2187.

[165] Muller, B. H.; Wang, C. R.; Hofmann, K. R.; Bierkandt, M.; Deiter, C.; Wollschlager, J. *Surface Science* **2003**, *532*, 633–638.

[166] Sumiya, T. *Applied Surface Science* **2000**, *156*(1-4), 85–96.

[167] Voet, D.; Voet, J. G. *Biochemistry;* John Wiley and Sons: New York USA, 4 ed., 2011.

[168] Jarvis, S. P. *International Journal of Molecular Sciences* **2015**, *16*(8), 19936–19959.

[169] Gross, L.; Schuler, B.; Pavliček, N.; Fatayer, S.; Majzik, Z.; Moll, N.; Pena, D.; Meyer, G. *Angewandte Chemie-International Edition* **2018**, *57*(15), 3888–3908.

[170] Mateo, L. M.; Sun, Q.; Liu, S.-X.; Bergkamp, J. J.; Eimre, K.; Pignedoli, C. A.; Ruffieux, P.; Decurtins, S.; Bottari, G.; Fasel, R.; Torres, T. *Angewandte Chemie-International Edition* **2020**, *59*(3), 1334–1339.

[171] Kawai, S.; Krejci, O.; Nishiuchi, T.; Sahara, K.; Kodama, T.; Pawlak, R.; Meyer, E.; Kubo, T.; Foster, A. S. *Science Advances* **2020**, *6*(9), 8913.

[172] Zhong, Q.; Hu, Y.; Niu, K.; Zhang, H.; Yang, B.; Ebeling, D.; Tschakert, J.; Cheng, T.; Schirmeisen, A.; Narita, A.; Müllen, K.; Chi, L. *Journal of the American Chemical Society* **2019**, *141*(18), 7399–7406.

[173] Alldritt, B.; Hapala, P.; Oinonena, N.; Urtev, F.; Krejci, O.; Canova, F. F.; Kannala, J.; Schulz, F.; Liljeroth, P.; Foster, A. S. *Science Advances* **2020**, *6*(9), eaay6913.

[174] Hauke, C. M.; Bechstein, R.; Kittelmann, M.; Storz, C.; Kilbinger, A. F.; Rahe, P.; Kühnle, A. *ACS Nano* **2013**, *7*(6), 5491–5498.

[175] Kaiser, K.; Gross, L.; Schulz, F. *Acs Nano* **2019**, *13*(6), 6947–6954.

[176] Schuler, B.; Meyer, G.; Pena, D.; Mullins, O. C.; Gross, L. *Journal of the American Chemical Society* **2015**, *137*(31), 9870–9876.

[177] Schuler, B.; Zhang, Y. L.; Collazos, S.; Fatayer, S.; Meyer, G.; Perez, D.; Guitian, E.; Harper, M. R.; Kushnerick, J. D.; Pena, D.; Gross, L. *Chemical Science* **2017**, *8*(3), 2315–2320.

[178] Mistry, A.; Moreton, B.; Schuler, B.; Mohn, F.; Meyer, G.; Gross, L.; Williams, A.; Scott, P.; Costantini, G.; Fox, D. J. *Chemistry-a European Journal* **2015**, *21*(5), 2011–2018.

[179] Kong, H. H.; Wang, L. K.; Sun, Q.; Zhang, C.; Tan, Q. G.; Xu, W. *Angewandte Chemie-International Edition* **2015**, *54*(22), 6526–6530.

[180] Gilman, J. J. *Journal of Applied Physics* **1960**, *31*, 2208–18.

[181] Puchin, V. E.; Puchina, A. V.; Huisinga, M.; Reichling, M. *Journal of Physics-Condensed Matter* **2001**, *13*(10), 2081–2094.

[182] Vitos, L.; Ruban, A. V.; Skriver, H. L.; Kollar, J. *Surface Science* **1998**, *411*(1-2), 186–202.

[183] Rahe, P. *Beilstein Journal of Nanotechnology* **2020**, *11*, 1615–1622.

[184] Rahe, P.; Nimmrich, M.; Kühnle, A. *Small* **2012**, *8*(19), 2968–2968.

[185] Kealy, T. J.; Pauson, P. L. *Nature* **1951**, *168*(4285), 1039–1040.

[186] Miller, S. A.; Tebboth, J. A.; Tremaine, J. F. *Journal of the Chemical Society* **1952**, (Feb), 632–635.

[187] Gritzner, G.; Kuta, J. *Pure Appl. Chem.* **1984**, *56*(4), 461.

[188] Laflör, L.; Schlage, F. A.; Kantorovich, L.; Moriarty, P. J.; Reichling, M.; Rahe, P. *The Journal of Physical Chemistry C* **2020**, *124*(18), 9900.

[189] Laflör, L.; Reichling, M.; Rahe, P. *Beilstein Journal of Nanotechnology* **2020**, *11*, 1432–1438.

[190] Barth, J. V. *Annual Review of Physical Chemistry* **2007**, *58*, 375–407.

[191] Maurer, R. J.; Ruiz, V. G.; Camarillo-Cisneros, J.; Liu, W.; Ferri, N.; Reuter, K.; Tkatchenko, A. *Prog. Surf. Sci.* **2016**, *91*(2), 72–100.

[192] Barth, C.; Foster, A. S.; Henry, C. R.; Shluger, A. L. *Adv. Mater.* **2011**, *23*(4), 477–501.

[193] Bombis, C.; Ample, F.; Lafferentz, L.; Yu, H.; Hecht, S.; Joachim, C.; Grill, L. *Angew. Chem. Int. Ed.* **2009**, *48*(52), 9966–9970.

[194] Steurer, W.; Fatayer, S.; Gross, L.; Meyer, G. *Nat. Commun.* **2015**, *6*, 8353.

[195] Para, F.; Bocquet, F.; Nony, L.; Loppacher, C.; Féron, M.; Cherioux, F.; Gao, D. Z.; Federici Canova, F.; Watkins, M. B. *Nat. Chem.* **2018**, *10*(11), 1112–1117.

[196] Lindner, R.; Kühnle, A. *ChemPhysChem* **2015**, *16*(8), 1582–1592.

[197] Maier, S.; Fendt, L.-A.; Zimmerli, L.; Glatzel, T.; Pfeiffer, O.; Diederich, F.; Meyer, E. *Small* **2008**, *4*(8), 1115–1118.

[198] Schütte, J.; Bechstein, R.; Rohlfing, M.; Reichling, M.; Kühnle, A. *Phys. Rev. B* **2009**, *80*(20), 205421.

[199] Loske, F.; Reichling, M.; Kühnle, A. *Jpn. J. Appl. Phys.* **2011**, *50*(8), 08LB07.

[200] Loske, F.; Reichling, M.; Kühnle, A. *Chem. Commun.* **2011**, *47*(37), 10386–10388.

[201] Majzik, Z.; Setvín, M.; Bettac, A.; Feltz, A.; Cháb, V.; Jelínek, P. *Beilstein J. Nanotechnol.* **2012**, *3*, 249–259.

[202] Hutter, J.; Iannuzzi, M.; Schiffmann, F.; VandeVondele, J. *WIREs Comput. Mol. Sci.* **2014**, *4*(1), 15–25.

[203] VandeVondele, J.; Hutter, J. *J. Chem. Phys.* **2007**, *127*(11), 114105.

[204] Lippert, G.; Hutter, J.; Parrinello, M. *Theor. Chem. Acc.* **1999**, *103*(2), 124–140.

[205] Krack, M. *Theor. Chem. Acc.* **2005**, *114*(1), 145–152.

[206] Perdew, J. P.; Burke, K.; Ernzerhof, M. *Phys. Rev. Lett.* **1996**, *77*(18), 3865–3868.

[207] Sabatini, R.; Gorni, T.; de Gironcoli, S. *Phys. Rev. B* **2013**, *87*(4), 041108.

[208] Boys, S. F.; Bernardi, F. *Mol. Phys.* **1970**, *19*(4), 553–566.

[209] Foster, A. S.; Barth, C.; Shluger, A. L.; Reichling, M. *Phys. Rev. Lett.* **2001**, *86*(11), 2373–2376.

[210] Wollschläger, J. In *Recent Research Developments in Applied Physics*; Pandalai, S., Ed.; Transworld Research Network: Trivandrum, India, 2002; Vol. 5-II; pages 621–695.

[211] Loppacher, C.; Zerweck, U.; Eng, L. M.; Gemming, S.; Seifert, G.; Olbrich, C.; Morawetz, K.; Schreiber, M. *Nanotechnology* **2006**, *17*(6), 1568–1573.

[212] Kunstmann, T.; Schlarb, A.; Fendrich, M.; Wagner, T.; Möller, R.; Hoffmann, R. *Phys. Rev. B* **2005**, *71*(12), 121403.

[213] Such, B.; Goryl, G.; Godlewski, S.; Kolodziej, J. J.; Szymonski, M. *Nanotechnology* **2008**, *19*(47), 475705.

[214] Palenik, G. J. *Inorg. Chem.* **1969**, *8*(12), 2744.

[215] Takusagawa, F.; Koetzle, T. F. *Acta Crystal. Sec. B* **1979**, *35*(DEC), 2888–2896.

[216] Steiner, T. *Angew. Chem. Int. Ed.* **2002**, *41*(1), 48–76.

[217] Woodruff, D. P. *Reports on Progress in Physics* **2005**, *68*(4), 743.

[218] Woodruff, D. P. *Journal of Electron Spectroscopy and Related Phenomena* **2002**, *126*(1), 55–65.

[219] Hauschild, A.; Temirov, R.; Soubatch, S.; Bauer, O.; Schöll, A.; Cowie, B. C. C.; Lee, T. L.; Tautz, F. S.; Sokolowski, M. *Physical Review B* **2010**, *81*(12), 125432.

[220] Hoffmann-Vogel, R. *Reports on Progress in Physics* **2017**, *81*(1), 016501.

[221] Pavliček, N.; Fleury, B.; Neu, M.; Niedenführ, J.; Herranz-Lancho, C.; Ruben, M.; Repp, J. *Physical Review Letters* **2012**, *108*(8), 086101.

[222] K., B. R.; Haaland, A. *Journal of Organometallic Chemistry* **1966**, *5*(5), 470.

[223] Haaland, A.; Nilsson, J. E. *Acta Chemica SCANDINAVICA* **1968**, *22*, 2653–2670.

[224] Coriani, S.; Haaland, A.; Helgaker, T.; Jørgensen, P. *ChemPhysChem* **2006**, *7*, 245–249.

[225] Sorriso, S. *Journal of Organometallic Chemistry* **1979**, *179*, 205–213.

[226] Nowik, I.; Herber, R. H. *Inorganica Chimica Acta* **2000**, *310*, 191–195.

[227] Almenningen, A.; Haaland, A.; Samdal, S. *Journal of Organometallic Chemistry* **1979**, *173*, 293–299.

[228] McCulloch, B.; Brubaker, C. H. J. *Organometallics* **1984**, *3*, 1707–1711.

[229] Shen, L.-H.; Okoroator, M. O.; Brubaker, C. H. J. *Organometallics* **1986**, *7*(4), 825–829.

[230] Xue-Bin, W.; Bing, D.; Hin-Koon, W.; Lai-Sheng, W. *Angewandte Chemie International Edition* **2005**, *44*(37), 6022.

[231] Barth, C.; Pakarinen, O. H.; Foster, A. S.; Henry, C. R. *Nanotechnology* **2006**, *17*(7), 128–136.

[232] Rahe, P.; Schütte, J.; Schniederberend, W.; Reichling, M.; Abe, M.; Sugimoto, Y.; Kühnle, A. *Review of Scientific Instruments* **2011**, *82*(6), 063704.

[233] Peng, J.; Guo, J.; Hapala, P.; Cao, D.; Ma, R.; Cheng, B.; Xu, L.; Ondráček, M.; Jelínek, P.; Wang, E.; Jiang, Y. *Nature Communications* **2018**, *9*(1), 122.

[234] Labidi, H.; Koleini, M.; Huff, T.; Salomons, M.; Cloutier, M.; Pitters, J.; Wolkow, R. A. *Nature Communications* **2017**, *8*, 14222.

[235] Sweetman, A.; Jarvis, S. P.; Rashid, M. A. *Beilstein Journal of Nanotechnology* **2016**, *7*, 937–945.

[236] Iwata, K.; Yamazaki, S.; Mutombo, P.; Hapala, P.; Ondracek, M.; Jelinek, P.; Sugimoto, Y. *Nature Communications* **2015**, *6*, 7766.

[237] MacLeod, J. *Journal of Physics D: Applied Physics* **2019**, *53*(4), 043002.

[238] Zhou, Q. Y.; Li, Y. B.; Li, Q.; Wang, Y. B.; Yang, Y. L.; Fang, Y.; Wang, C. *Nanoscale* **2014**, *6*(14), 8387–8391.

[239] Classen, T.; Fratesi, G.; Costantini, G.; Fabris, S.; Stadler, F. L.; Kim, C.; de Gironcoli, S.; Baroni, S.; Kern, K. *Angewandte Chemie - International Edition* **2005**, *44*(38), 6142–6145.

[240] Classen, T.; Lingenfelder, M.; Wang, Y.; Chopra, R.; Virojanadara, C.; Starke, U.; Costantini, G.; Fratesi, G.; Fabris, S.; de Gironcoli, S.; Baroni, S.; Haq, S.; Raval, R.; Kern, K. *Journal of Physical Chemistry A* **2007**, *111*(49), 12589–12603.

[241] Spillmann, H.; Dmitriev, A.; Lin, N.; Messina, P.; Barth, J. V.; Kern, K. *Journal of the American Chemical Society* **2003**, *125*(35), 10725–10728.

[242] Messina, P.; Dmitriev, A.; Lin, N.; Spillmann, H.; Abel, M.; Barth, J. V.; Kern, K. *Journal of the American Chemical Society* **2002**, *124*(47), 14000–14001.

[243] Iancu, V.; Braun, K.-F.; Schouteden, K.; Van Haesendonck, C. *Physical Review Letters* **2014**, *113*(10), 106102.

[244] Ye, Y. C.; Sun, W.; Wang, Y. F.; Shao, X.; Xu, X. G.; Cheng, F.; Li, J. L.; Wu, K. *Journal of Physical Chemistry C* **2007**, *111*(28), 10138–10141.

[245] MacLeod, J. M.; Ivasenko, O.; Perepichka, D. F.; Rosei, F. *Nanotechnology* **2007**, *18*(42), 424031.

[246] Griessl, S.; Lackinger, M.; Edelwirth, M.; Hietschold, M.; Heckl, W. M. *Single Molecules* **2002**, *3*(1), 25–31.

[247] Dmitriev, A.; Lin, N.; Weckesser, J.; Barth, J. V.; Kern, K. *The Journal of Physical Chemistry B* **2002**, *106*(27), 6907–6912.

[248] Baviloliaei, M. S.; Diekhöner, L. *Physical Chemistry Chemical Physics* **2014**, *16*(23), 11265–11269.

[249] Payer, D.; Comisso, A.; Dmitriev, A.; Strunskus, T.; Lin, N.; Wöll, C.; DeVita, A.; Barth, J. V.; Kern, K. *Chemistry-a European Journal* **2007**, *13*(14), 3900–3906.

[250] Iancu, V.; Braun, K.-F.; Schouteden, K.; Van Haesendonck, C. *Langmuir* **2013**, *29*(37), 11593–11599.

[251] Ibenskas, A.; Simenas, M.; Kizlaitis, K. J.; Tornau, E. E. *Journal of Physical Chemistry C* **2019**, *123*(6), 3552–3559.

[252] Yan, L. H.; Kuang, G. W.; Lin, N. *Chemical Communications* **2018**, *54*(75), 10570–10573.

[253] Li, W.; Jin, J.; Leng, X.; Lu, Y.; Liu, X.; Wang, L. *The Journal of Physical Chemistry C* **2016**, *120*(23), 12605–12610.

[254] Velpula, G.; Teyssandier, J.; De Feyter, S.; Mali, K. S. *ACS Nano* **2017**, *11*(11), 10903–10913.

[255] Lin, N.; Payer, D.; Dmitriev, A.; Strunskus, T.; Wöll, C.; Barth, J. V.; Kern, K. *Angewandte Chemie International Edition* **2005**, *44*(10), 1488–1491.

[256] Svane, K. L.; Baviloliaei, M. S.; Hammer, B.; Diekhoner, L. *Journal of Chemical Physics* **2018**, *149*(16), 164710.

[257] Lipton-Duffin, J.; Abyazisani, M.; MacLeod, J. *Chemical Communications* **2018**, *54*(60), 8316–8319.

[258] Ibenskas, A.; Simenas, M.; Kizlaitis, K. J.; Tornau, E. E. *Journal of Physical Chemistry C* **2020**, *124*(20), 11212–11220.

[259] Telychko, M.; Su, J.; Gallardo, A.; Gu, Y.; Mendieta-Moreno, J. I.; Qi, D.; Tadich, A.; Song, S.; Lyu, P.; Qiu, Z.; Fang, H.; Koh, M. J.; Wu, J.; Jelinek, P.; Lu, J. *Angewandte Chemie-International Edition* **2019**, *58*(51), 18591–18597.

[260] Shan, H.; Mao, Y.-h.; Zhao, A.-D. *Chinese Journal of Chemical Physics* **2019**, *32*(5), 620–624.

[261] Mohn, F.; Repp, J.; Gross, L.; Meyer, G.; Dyer, M. S.; Persson, M. *Physical Review Letters* **2010**, *105*(26), 266102.

[262] Albrecht, F.; Neu, M.; Quest, C.; Swart, I.; Repp, J. *Journal of the American Chemical Society* **2013**, *135*(24), 9200–9203.

[263] Urgel, J. I.; Hayashi, H.; Di Giovannantonio, M.; Pignedoli, C. A.; Mishra, S.; Deniz, O.; Yamashita, M.; Dienel, T.; Ruffieux, P.; Yamada, H.; Fasel, R. *Journal of the American Chemical Society* **2017**, *139*(34), 11658–11661.

[264] Allmers, T.; Donath, M. *New Journal of Physics* **2009**, *11*, 103049.

[265] Engelbrecht, J. A. A.; Vermaak, J. S.; Snyman, H. C. *Thin Solid Films* **1978**, *48*(1), 127–132.

[266] Engelbrecht, J. A. A.; Snyman, H. C. *Thin Solid Films* **1979**, *59*(3), 345–352.

[267] Schüttler, K. M.; Bansmann, J.; Engstfeld, A. K.; Behm, R. J. *Journal of Chemical Physics* **2020**, *152*(12), 124701.

[268] Zahl, P.; Yakutovich, A. V.; Ventura-Macias, E.; Carracedo-Cosme, J.; Romero-Muniz, C.; Pou, P.; Sadowski, J. T.; Hybertsen, M. S.; Perez, R. *Nanoscale* **2021**, *13*(44), 18473–18482.

[269] Gross, L.; Mohn, F.; Moll, N.; Schuler, B.; Criado, A.; Guitián, E.; Peña, D.; Gourdon, A.; Meyer, G. *Science* **2012**, *337*(6100), 1326–1329.

[270] Sader, J. E.; Jarvis, S. P. *Applied Physics Letters* **2004**, *84*(10), 1801–1803.

[271] Sweetman, A.; Stannard, A. *Beilstein Journal of Nanotechnology* **2014**, *5*, 386–393.

[272] Held, P. A.; Gao, H.-Y.; Liu, L.; Mück-Lichtenfeld, C.; Timmer, A.; Mönig, H.; Barton, D.; Neugebauer, J.; Fuchs, H.; Studer, A. *Angewandte Chemie-International Edition* **2016**, *55*(33), 9777–9782.

[273] Herschlag, D.; Pinney, M. M. *Biochemistry* **2018**, *57*(24), 3338–3352.

[274] Lin, J.; Pozharski, E.; Wilson, M. A. *Biochemistry* **2017**, *56*(2), 391–402.

[275] Hohenberger, J.; Ray, K.; Meyer, K. *Nature Communications* **2012**, *3*, 720.

[276] Qin, J.; Perera, R.; Lovelace, L. L.; Dawson, J. H.; Lebioda, L. *Biochemistry* **2006**, *45*(10), 3170–3177.

[277] Domazetis, G.; James, B. D. *Organic Geochemistry* **2006**, *37*(2), 244–259.

[278] Nimmermark, A.; Ohrstrom, L.; Reedijk, J. *Zeitschrift Fur Kristallographie-Crystalline Materials* **2013**, *228*(7), 311–317.

Acknowledgements

Here, I would like to thank all people supporting me in completing this thesis.
First and foremost, I am truly grateful to Philipp Rahe for the opportunity to carry out this exiting, rather chemical, research project. Thank you for always finding time for discussions and answering questions. You have constantly shown interest in my work and encouraged me to bring in my ideas and opinions. Your involvement and help throughout the years, especially with all the lab quarrels, has been invaluable.
Here, I would like to thank Michael Reichling, Martin Steinhart, and Carola Meyer for their membership in my thesis examination committee.
I also thank the members of both AG Rahe and Reichling. You have welcomed me to Osnabrück. Your ongoing support, advice, and times out of the lab has made my time in Osnabrück a lot more enjoyable. Here, shout out to Daniel for many fun adventures outside of the physics world. To Jonas, Tim, and Max, I would like to express my thank for your countless discussions and helping out in the lab. At this point, I would also like to thank Michael Reichling for the opportunity, and Fabian and Bob for their help doing measurements in the RHK lab. I am also grateful for the opportunity to conduct experiments in the labs of Angelika Kühnle, then located at the Johannes-Gutenberg Universität Mainz. Furthermore I would like to thank the bachelor students Paul and Rostislaw for their committed works.
Additionally, I am thankful for the support I found in other university departments, especially the members of the Mentoring group and of the Fachschaft für Promovierende. Here, a special thanks to Franziska, Julia and Katharina for the digital, daily home office meetings during those crazy corona times.
Furthermore, I am most grateful for the ongoing support from my friends and family.
I am especially thankful to my parents Hildegard and Ralf, and my sister Marie for encouraging me to keep going. Thank you that I can always rely on you! Finally, my deepest thanks go to Nils. Thank you for always being by my side, for being understanding and cheering for me even in the most stressful times.

Scientific contributions

Refereed publications

- **L. Laflör**, M. Reichling, P. Rahe:
  Protruding hydrogen atoms as markers for the molecular orientation of a metallocene
  Beilstein Journal of Nanotechnology, 11, 1432, (2020)

- **L. Laflör**, F. A. Schlage, L. Kantorovich, M. Reichling, P. Rahe:
  Quadruped Molecular Anchoring to an Insulator: Functionalized Ferrocene on CaF_2 Bulk and Thin Film Surfaces
  Journal of Physical Chemistry C, 124, 18, 9900 (2020)

- J. Heggemann, **L. Laflör**, P. Rahe:
  Double sample holder for efficient high-resolution studies of an insulator and a metal surface
  Review of Scientific Instruments, 92, 053705 (2021)

Conference contributions

- **Comparing bulk with thin film dielectric: Ferrocene dicarboxylic acid on CaF_2(111) surfaces** (Poster)
  L. Laflör, F. A. Schlage, M. Reichling, P. J. Moriarty, P. Rahe
  663rd WE-Heraeus-Seminar on Dynamics and Structure Formation, Bad Honnef, Germany, 25-28 February 2018

- **Comparison of bulk and thin film materials: Ferrocene dicarboxylic acid on CaF_2(111) surfaces** (Talk)
  L. Laflör, F. A. Schlage, M. Reichling, P. J. Moriarty, P. Rahe
  21st NC-AFM, Porvoo, Finland, 17-21 September 2018

- **Anchoring of Ferrocene Dicarboxylic Acid molecules on CaF_2(111) bulk and thin film surfaces** (Poster)
  L. Laflör, F. A. Schlage, M. Reichling, P. J. Moriarty, P. Rahe
  2019 Chemical Reactions at Surfaces, Gordon Research Conference, Ventura, USA, 17-22 February 2019

- **NC-AFM imaging of molecules with flexible side groups using CO functionalised tips** (Poster)
  L. Laflör, P. Rahe
  22nd NC-AFM, Regensburg, Germany, 29 July- 2 August 2019

- **Mapping the axial interaction forces with a carboxylic acid dimer** (Poster)
  L. Laflör, J. Heggemann, P. Rahe
  23rd NC-AFM, Nijmegen, Netherlands, 31 July- 5 August 2022

- **The search for iron: NC-AFM imaging of the trimesic acid-iron self-assembled networks on Au(111)** (Talk)
  L. Laflör, P. Rahe
  23rd NC-AFM, Nijmegen, Netherlands, 31 July- 5 August 2022

Erklärung über die Eigenständigkeit der erbrachten wissenschaftlichen Leistung
Ich erkläre hiermit, dass ich die vorliegende Arbeit ohne unzulässige Hilfe Dritter und ohne Benutzung anderer als der angegebenen Hilfsmittel angefertigt habe. Die aus anderen Quellen direkt oder indirekt übernommenen Daten und Konzepte sind unter Angabe der Quelle gekennzeichnet.
Bei der Auswahl und Auswertung folgenden Materials haben mir die nachstehend aufgeführten Personen in der jeweils beschriebenen Weise unentgeltlich geholfen.

1. DFT & PPM Rechnungen in Kapitel 7 wurden von Lev Kantorovich und Philipp Rahe durchgeführt

Weitere Personen waren an der inhaltlichen materiellen Erstellung der vorliegenden Arbeit nicht beteiligt. Insbesondere habe ich hierfür nicht die entgeltliche Hilfe von Vermittlungs- bzw. Beratungsdiensten (Promotionsberater oder andere Personen) in Anspruch genommen. Niemand hat von mir unmittelbar oder mittelbar geldwerte Leistungen für Arbeiten erhalten, die im Zusammenhang mit dem Inhalt der vorgelegten Dissertation stehen.
Die Arbeit wurde bisher weder im In- noch im Ausland in gleicher oder ähnlicher Form einer anderen Prüfungsbehörde vorgelegt. Osnabrück, den 18.08.2022

.....
Datum/Unterschrift